



**HAL**  
open science

# Comportement de matériaux illuminés par des sources laser multi-kW

Thomas Lafargue

► **To cite this version:**

Thomas Lafargue. Comportement de matériaux illuminés par des sources laser multi-kW. Energie électrique. HESAM Université, 2023. Français. NNT : 2023HESAE021 . tel-04496284

**HAL Id: tel-04496284**

**<https://pastel.hal.science/tel-04496284>**

Submitted on 8 Mar 2024

**HAL** is a multi-disciplinary open access archive for the deposit and dissemination of scientific research documents, whether they are published or not. The documents may come from teaching and research institutions in France or abroad, or from public or private research centers.

L'archive ouverte pluridisciplinaire **HAL**, est destinée au dépôt et à la diffusion de documents scientifiques de niveau recherche, publiés ou non, émanant des établissements d'enseignement et de recherche français ou étrangers, des laboratoires publics ou privés.

ÉCOLE DOCTORALE SCIENCES DES MÉTIERS DE L'INGÉNIEUR  
Institut de Mécanique et d'Ingénierie - TREFLE

# THÈSE

présentée par : **Thomas Lafargue-Tallet**  
soutenue le : **6 Mars 2023**

pour obtenir le grade de : **Docteur**

préparée à : **École Nationale Supérieure d'Arts et Métiers**

Discipline : **Section CNU 60**

Spécialité : **Énergétique**

## Étude du comportement de matériaux illuminés par des sources laser de fortes puissances

THÈSE DIRIGÉE PAR :  
**Emmanuelle ABISSET-CHAVANNE**

ET CO-ENCADRÉE PAR :  
**Raymond PEIFFER et Christophe PRADERE**

**Jury**

**M. Cyril CALIOT**

**Mme. Mouna EL HAFI**

**M. Franck ENGUEHARD**

**M. Lionel MERLAT**

**M. Matthieu POMMIES**

**M. Alain SOMMIER**

Chargé de Recherche, CNRS

Professeure des Universités

Professeur des Universités

Docteur, Institut Saint-Louis,

Docteur, Alphanov

Ingénieur de recherche, CNRS

Président

Rapporteur

Rapporteur

Examinateur

Invité

Invité

T  
H  
È  
S  
E





À Syntiche

---

# Remerciements

Cette thèse est le fruit d'un travail de trois ans au sein du laboratoire de recherche I2M. Un parcours marqué par la bonne ambiance, un enthousiasme généralisé et des montagnes russes émotionnelles. Je souhaite adresser ici mes remerciements à toutes les personnes qui m'ont apporté leur aide et leur soutien pendant ces trois années.

Je remercie également tous les membres du jury, en particulier Franck ENGUEHARD et Mouna EL HAFI, rapporteurs de ce manuscrit ainsi que Cyril CALIOT président du jury.

Je remercie très chaleureusement Raymond PEIFFER, sans qui je n'aurais jamais engagé ce travail, merci pour tous les conseils prodigués dans le travail et la vie de tous les jours.

Un grand merci à Emmanuelle ABISSET-CHAVANNE et Christophe PRADERE, pour l'aide et les conseils apportés dans la bonne humeur. Merci également à Alain SOMMIER, pour tous les conseils pratiques, son pragmatisme et son implication dans les manips. Chacun de vous m'a apporté des compétences complémentaires tout au long de cette thèse, merci pour tout ce que j'ai appris à vos côtés.

Je tiens à remercier tous les permanents de l'équipe I2M-TIFC : Jean-Christophe BATSALE, Marie-Marthe GROZ, Andrzej KUSIAK, Jean-Luc BATTAGLIA, Stephane CHEVALIER et Jeremie MAIRE. Les discussions scientifiques que l'on a pu avoir tout au long de ma thèse m'ont permis de découvrir et de m'améliorer dans de nombreux domaines.

J'ai une pensée amicale pour service thermique de MBDA, notamment Marie DE BATS qui m'a accueilli dans son équipe et donné de nombreux conseils. Merci à Maximilian TAILLANDIER pour toutes ces conversations autour du laser et les bons moments partagés. Merci aussi à Eric DUCLOUX et Jérôme FIRTION présents pendant la réalisation du VTF.

Je remercie tous mes colocataires de la salle de manips. On a partagé de bons moments ensemble,

## REMERCIEMENTS

---

aligné pas mal de faisceaux et écrit beaucoup d'équations le tout dans une bonne ambiance: Yannick BAFANGA, Coline BOURGES, Marine GARCIA, Théo CHAVATTE, Clément CHASSAIN, Kevin KRAUSE, Malo LECORGNE, Théodore KELLER , Alejandro MATEOS CANSECO, Hugo BOUE, merci à tous ! Hamza Abderezak AOUALI, merci pour tous ces débats !

Un grand merci à toute l'équipe d'ALPhANOV, pour les efforts réalisés pendant, mais aussi avant la thèse : Benoit APPERT-COLLIN, Matthieu POMMIES, Charly REGNAULT, Adrien CAUSSE, Kilian SANFINS, ARNAUD BEAUMADIER, Matthias PORTELLANO, Patrick MOREAU, Pierre DASINIERES, Florent HUSSON, Florent DARRE, Matthieu VALENTIN. J'ai une pensée particulière pour l'équipe de la première heure du VTF : Emmanuel CHALUMEAU et Adèle MORISSET.

Je tiens à remercier les gestionnaires du laboratoire, en particulier Muriel EZAN BORE, pour sa gentillesse et son aide dans les différentes démarches administratives. Merci également Mesdames Azita AHMADI SENICHAULT, Florence DUVILLE et Céline KOVACS pour leur sympathie et leurs encouragements.

Je remercie également ma famille, mes parents et ma sœur. Vous m'avez encouragé et soutenu, merci pour tout.

Enfin, Syntiche, je ne te remercierais jamais assez pour ton soutien et ta patience (il en fallait...). Tu as été là dans les moments de joie (manips qui marchent / modèles qui collent) et les moments plus compliqués (manips loupés / modèles qui ne collent pas / Rédaction). Merci de m'avoir remonté le moral et redonné le sourire. C'est avec toute ma reconnaissance que je te dédie ce travail.

## REMERCIEMENTS

---

## REMERCIEMENTS

---

# Résumé

Que ce soit dans les fibres optiques qui permettent un accès pratique à l'information en ligne, dans la chirurgie, l'usinage, la gravure de semi-conducteur, les imprimantes... les sources laser font aujourd'hui partie de notre quotidien. Mais qu'est-ce qui les rend unique ? La réponse est simple si l'on considère le laser comme un concentré de lumière. Or, concentrer la lumière, est dans l'imaginaire collectif souvent relié à des effets dévastateurs (Siège de Syracuse, Star Wars, ...). Les premiers fonds de recherche dédiés à l'étude de l'arme laser date des années 70 (DARPA – Excalibur Project). Dans le cadre d'un projet à moyen/long terme de recherche et développement d'armes laser de fortes puissances, MBDA France en coopération avec ALPhANOV, développe des essais autour d'un laser continu de haute puissance pour quantifier la vulnérabilité des cibles.

La vulnérabilité laser fait référence à la susceptibilité d'un système, d'un appareil ou d'un matériau d'être endommagé par l'exposition à un rayonnement laser. La vulnérabilité au laser varie en fonction de la longueur d'onde, de la puissance et de la durée de l'exposition au rayonnement, ainsi que des caractéristiques du système ou du matériau exposé. Le travail présenté dans cette thèse a pour objectif de développer des outils permettant de quantifier la vulnérabilité des cibles illuminées par un laser de forte puissance.

Le travail doctoral s'articule autour de plusieurs problématiques distinctes. La première porte sur la quantification spatio-temporelle des réflexions du laser au contact de la matière, sources de possibles dommages collatéraux. Dans un second temps, l'obtention de cartographies de températures est une étape clé pour déterminer l'état de la cible, car les effets du laser sont majoritairement thermiques. Pour finir, la détermination des variations spatio-temporelle du flux absorbé par la cible permettent d'identifier pour ensuite prédire les élévations de température et donc l'état de la cible. Chacune des thématiques étudiées a fait l'objet d'une première étude sans dynamique thermique pour construire et valider des méthodes appliquées, dans un second temps, lors d'illuminations laser de fortes



puissances.

En conclusion, les méthodes proposées dans cette thèse, à savoir un dispositif expérimental de mesures de champs de réflectivités bidirectionnelles, le développement d'une nouvelle approche de mesures de températures sans contact appelée Active-Thermo-Reflectometry ainsi que des méthodes de fluxmétrie, permettent de quantifier la vulnérabilité des cibles illuminées par des sources laser de fortes puissances.

Mots-clés : Conditions Extrêmes, Thermographie Infra Rouge, Méthode Inverses, Imagerie, Hautes températures, Hauts flux, Réflexion, Absorption, BRDF

RESUME

---

RESUME

---

# Abstract

Whether used in fibre optics for convenient online access to information, surgery, machining, semiconductor etching or printers, laser sources are now part of our everyday lives. But what makes them unique? The answer is simple, if you think of a laser as a concentrate of light. In the collective imagination, concentrating light is often associated with devastating effects (Siege of Syracuse, Star Wars, etc.). The first research funds dedicated to the study of laser weapons date back to the 1970s (DARPA - Excalibur Project). As part of a medium/long-term project to research and develop high-power laser weapons, MBDA France, in cooperation with ALPhANOV, is developing tests using a high-power continuous laser to quantify the vulnerability of targets.

Laser vulnerability refers to the susceptibility of a system, device or material to be damaged from exposure to laser radiation. Laser vulnerability varies according to the wavelength, power and duration of exposure to the radiation, as well as the characteristics of the system or material exposed. The aim of the work presented in this thesis is to develop tools for quantifying the vulnerability of targets illuminated by a high-power laser.

The doctoral work focuses on several distinct research axis. The first concerns the spatio-temporal quantification of laser reflections on contact with matter, which are a source of possible collateral damage. Secondly, obtaining temperature maps is a key step in determining the state of the target, as the effects of the laser are mainly thermal. Finally, determining the spatial and temporal variations of the absorbed flux by the target makes it possible to identify and then predict temperature rises and therefore the state of the target. Each of these axis studied was the subject of an initial study without thermal dynamics in order to develop and validate methods that were then applied under high-power laser illuminations.

In conclusion, the methods proposed in this thesis, namely, an experimental device for measuring

## ABSTRACT

---

bidirectional reflectivity fields, the development of a new approach to non-contact temperature measurement called Active-Thermo-Reflectometry, and fluxmetry methods, enable the vulnerability of targets illuminated by high-power laser sources to be quantified.

Keywords :Extreme conditions, Infrared thermography, Inverse methods, Imaging Systems, High temperatures, High flux, Reflection, Absorption, BRDF

# Contents

<b>Remerciements</b>	<b>5</b>
<b>Résumé</b>	<b>9</b>
<b>Abstract</b>	<b>13</b>
<b>List of tables</b>	<b>21</b>
<b>List of figures</b>	<b>28</b>
<b>1 Introduction</b>	<b>29</b>
1.1 Societal & industrial context . . . . .	30
1.2 Context of this thesis . . . . .	32
<b>2 Background of radiative heat transfer</b>	<b>35</b>
2.1 Introduction . . . . .	36
2.2 Fundamentals of thermal radiation . . . . .	36
2.3 Definition of a black body . . . . .	37
2.4 Useful radiometry quantities . . . . .	38
2.5 Planck’s law . . . . .	39
2.6 Wien’s displacement law . . . . .	42
2.7 Stefan–Boltzmann law . . . . .	42
2.8 Black bodies and real bodies: radiative properties and Kirchhoff’s law . . . . .	44
2.8.1 Link between emissivity and reflectivity for opaque media . . . . .	47
2.8.2 Different kinds of opaque materials . . . . .	47
2.9 Conclusion . . . . .	48
<b>3 Optical characterisation of a opaque metallic material over infrared wavelengths</b>	<b>49</b>
3.1 Context . . . . .	50

## CONTENTS

---

3.2	Introduction to BRDF measurement . . . . .	51
3.3	BRDFs in the IR spectral range . . . . .	52
3.3.1	Devices for measuring BRDFs . . . . .	53
3.4	Methods for characterising BRDFs . . . . .	54
3.4.1	Experimental set-up . . . . .	54
3.4.2	Presentation of the studied samples and wavelength . . . . .	56
3.4.3	Qualitative BRDF acquisition and data processing . . . . .	57
3.4.4	Presentation of the collimation part of the set-up . . . . .	61
3.4.5	Optical path of the incident beam . . . . .	61
3.4.6	Optical path of the reflected beam . . . . .	65
3.4.6.1	Imaging system . . . . .	65
3.4.6.2	From pixel-based images to BRDF images . . . . .	65
3.5	Set-up and method validation . . . . .	70
3.6	Analysis of the set-up, method capacities and limits . . . . .	73
3.7	Implementation of the multi-spectral BRDF measurement system . . . . .	74
3.8	Conclusions regarding infrared multi-spectral data based on qualitative BRDFs . . . . .	79
<b>4</b>	<b>Absolute temperature measurement with an IR camera by active thermo-reflectometry (ATR)</b> . . . . .	<b>81</b>
4.1	Introduction . . . . .	83
4.2	Contactless temperature measurements with an IR camera . . . . .	83
4.3	Introduction to the IR sensor . . . . .	85
4.3.1	Difference sensors . . . . .	85
4.3.2	Sensor characteristics . . . . .	86
4.3.3	Sensor and wavelength sensitivity . . . . .	87
4.3.4	Conclusions regarding IR sensors . . . . .	87
4.4	State of the art of the radiative measurement of temperature . . . . .	89
4.4.1	Radiative measurement of temperature: emission . . . . .	89
4.4.1.1	Presentation of the passive method . . . . .	91
4.4.1.2	Presentation of the active method . . . . .	92
4.4.2	Radiative measurement of temperature: reflection . . . . .	94
4.4.3	Conclusions regarding the analysis of the state of the art of temperature measurement by IR technology . . . . .	94
4.5	Experimental set-up of ATR . . . . .	95
4.6	From images to temperature fields: black body calibration . . . . .	98
4.6.1	Experimental set-up for black body calibration . . . . .	99

## CONTENTS

---

4.6.2	Black body calibration model . . . . .	102
4.6.3	InSb high-temperature calibration . . . . .	105
4.6.4	InSb low-temperature calibration . . . . .	107
4.6.5	Sensitivity to camera noise . . . . .	109
4.6.6	Conclusions regarding the black body calibration . . . . .	111
4.7	Presentation of ATR . . . . .	112
4.7.1	Radiative balance . . . . .	112
4.7.2	Introducing the Fresnel model . . . . .	114
4.7.3	Illustration of the model for numerical cases . . . . .	115
4.7.4	Presentation of ATR . . . . .	119
4.7.5	Numerical validation of ATR . . . . .	121
4.8	Validation of ATR on heterogeneous samples at ambient temperatures . . . . .	124
4.8.1	Stainless steel sample . . . . .	124
4.8.2	Three-layer aluminium sample . . . . .	129
4.8.3	Conclusions regarding static measurement . . . . .	132
4.9	Conclusions regarding temperature measurement with infrared thermography . . . . .	133
<b>5</b>	<b>From quantitative thermal imaging to spatio-temporal heat flux estimation</b> . . . . .	<b>135</b>
5.1	Introduction . . . . .	136
5.2	Direct and inverse problems . . . . .	137
5.3	Generation of numerical direct problems . . . . .	139
5.3.1	Analytical approach . . . . .	139
5.3.1.1	Direct thermal diffusion problem in 2D . . . . .	139
5.3.1.2	Direct thermal diffusion problem in 3D . . . . .	143
5.3.2	Introduction to the finite volume method (FVM) applied to thermal diffusion in 2D . . . . .	146
5.4	Inverse method for a quantitative spatio-temporal estimation of the heat flux - FVM-based approach . . . . .	148
5.4.1	Estimation of the 2D heat source based on the FVM . . . . .	148
5.4.1.1	Description of the method . . . . .	148
5.4.1.2	Global correlation parameter study . . . . .	153
5.4.1.3	Application on numerical data . . . . .	153
5.4.1.4	Conclusions regarding heat source estimation in 2D heat diffusion based on the FVM . . . . .	157
5.4.2	Towards a 3D estimation . . . . .	157
5.4.3	Conclusions regarding the FVM-based spatio-temporal heat flux estimation . . . . .	159



## CONTENTS

---

5.5	Description of the inverse method for the quantitative spatial and temporal estimation of an excitation flux - an analytical approach . . . . .	160
5.5.1	Mathematical description of the inverse method for the time and space estimation of heat flux . . . . .	160
5.5.2	Spatio-temporal heat flux estimation for 3D thermal conduction . . . . .	163
5.5.2.1	Impulse response . . . . .	163
5.5.2.2	Application to the numerical 3D problem . . . . .	164
5.5.2.3	Conclusions regarding analytical spatio-temporal heat flux estimation . . . . .	167
5.6	General conclusions regarding heat flux estimation . . . . .	168
<b>6</b>	<b>Application to multi-KW laser-material interaction</b>	<b>171</b>
6.1	Introduction . . . . .	172
6.2	Presentation of the VTF . . . . .	172
6.3	Towards dynamic measurement of the BRDF . . . . .	174
6.3.1	Context . . . . .	174
6.3.2	Presentation of the experimental set-up . . . . .	176
6.3.3	Data acquired during the trials . . . . .	176
6.3.4	Measurement of the incident beam . . . . .	182
6.3.5	From pixel-based acquisition to dynamic BRDF-based images . . . . .	186
6.3.6	Dynamic BRDF measurements . . . . .	186
6.3.7	Summary of dynamic BRDF measurement . . . . .	190
6.4	Application of ATR for dynamic cases . . . . .	191
6.4.1	Introduction . . . . .	191
6.4.2	Experimental set-up and sample description . . . . .	191
6.4.3	Method reminders . . . . .	193
6.4.4	Application of the ATR method during 4 kW continuous laser-material interaction . . . . .	195
6.4.5	Summary of ATR temperature measurement during HEL illumination . . . . .	201
6.5	Heat flux measurement during HEL material interaction . . . . .	203
6.5.1	Reminders regarding the inverse method . . . . .	203
6.5.2	Modelling the heat transfer . . . . .	204
6.5.3	Estimation of the absorbed heat flux under HEL illumination . . . . .	208
6.5.3.1	Experimental set-up . . . . .	208
6.5.3.2	Case of a front-painted aluminium plate . . . . .	210
6.5.3.3	Case of a bare aluminium plate . . . . .	217
6.5.4	Summary of heat flux reconstruction . . . . .	222
6.6	Chapter summary . . . . .	222

## CONTENTS

---

<b>7 Conclusion and perspectives</b>	<b>223</b>
7.1 Conclusion . . . . .	223
7.2 Perspectives . . . . .	224
<b>8 Annexe reflection</b>	<b>241</b>

## CONTENTS

---

# List of Tables

2.1	Description of the infrared spectrum. . . . .	37
4.1	Measured effective reflectivity of the stainless steel sample. . . . .	126
4.2	Measured effective reflectivity of the aluminium three-part sample. . . . .	131
5.1	Thermal properties of AL2024. . . . .	139
5.2	Geometry for the 2D and 3D direct problems. . . . .	139
6.1	Steps of the ATR method for multiple experimental times. . . . .	197
6.2	Thermal properties of AL2024. . . . .	210

## LIST OF TABLES

---

# List of Figures

1.1	Selected examples of luminous weapons in fiction and legend: a) lightsaber, (b) Death Star, (c) heat vision of Superman and (d) the Archimedes mirror. . . . .	31
1.2	Illustration of a laser system: (a) left-side view of an NKC-135 airborne laser [1] and (b) MBDA showcased HELMA-P laser anti-drone system mounted on an Arqus Sherpa armored vehicle [2]. . . . .	32
1.3	Schematic representation of the different zones of interest during HEL illumination and PhD objectives. . . . .	33
2.1	Schematic of the electromagnetic wave spectrum [3]. . . . .	36
2.2	Kirchhoff Law presentation. . . . .	38
2.3	Introduction to hemispherical/directional radiative quantities. . . . .	39
2.4	Black body radiative intensity function of the wavelength for different temperatures. . . . .	40
2.5	Study of Planck's law as a function of the temperature for two wavelengths (4 and 10 $\mu m$ ): (a) temperature function of black body radiative intensity and (b) derivative of the black body radiative function of the temperature intensity. . . . .	41
2.6	Theoretical relative error in temperature measurement with a 10% underestimation of Planck's law for 2 wavelengths (4 $\mu m$ and 10 $\mu m$ ). . . . .	42
2.7	Relation between Planck's and Wien's laws. . . . .	43
2.8	Schematic of the optical balance on semi-transparent media illuminated by an incident electromagnetic wave. . . . .	45
2.9	Description of a real body. . . . .	48
3.1	Schematic of specular, diffuse and glossy reflections. . . . .	50
3.2	Geometrical definition of a BRDF angle and its associated coordinates. . . . .	52
3.3	Illustration of the bases for BRDF experimental measurement: (a) goniometer [4], (b) kaleidoscope [5] and (c) off-axis parabolic mirror [6]. . . . .	54
3.4	Schematic showing the OAPM's focusing property. . . . .	55
3.5	Schematic of the experimental set-up - XY view. . . . .	56
3.6	Description of the surface condition: (a) definition of the surface roughness and (b) illustration of the grinding process (image from the company Luxalp). . . . .	57

LIST OF FIGURES

---

3.7	Measured sample 4 surface topography. . . . .	58
3.8	Representation of BRDF acquisition. . . . .	59
3.9	BRDF acquisition flowchart with images captured at their corresponding steps. . . . .	60
3.10	Optical schema of the collimation optical assembly. . . . .	61
3.11	Scheme of the OAPM: $F_e = 50.8$ mm, $F_p = 25.4$ mm, and the mirror diameter is 76.2 mm. . . . .	62
3.12	Description of the mirror surface points. . . . .	63
3.13	Theoretical OAPM corresponding angle. . . . .	64
3.14	Schematic of the OAPM's ( $F_e=50.8$ mm and $d=76.2$ mm) cross section and the maximum angle. . . . .	64
3.15	Schematic of the imaging system. . . . .	65
3.16	Identifying the position of the OAPM centre. The centre of the white box corresponds to the centre of the OAPM. . . . .	66
3.17	Computed pixel coordinates $\theta$ . . . . .	67
3.18	Reconstruction of the mirror in real space from the images. . . . .	68
3.19	Computation of the pixel vertex and pixel area. . . . .	69
3.20	Evolution of the solid angle along the OAPM. . . . .	69
3.21	Theoretical Lambertian and specular BRDFs. . . . .	70
3.22	Validation on the mirror. . . . .	71
3.23	Partial validation on the Infragold. . . . .	72
3.24	Normalised measured BRDFs of the mirror. . . . .	72
3.25	Illustration of pixels below the threshold of 1 DL after image subtraction. . . . .	73
3.26	IR spectrum normalised sensitivity of a monochromator associated with an IR InSb camera. . . . .	74
3.27	Normalised BRDFs with highlighted polar and azimuthal angles for samples 1, 4 and 5 ( $Ra = 0.05 \mu m$ , $Ra = 0.4 \mu m$ and $Ra = 0.8 \mu m$ ) at 4000 nm. . . . .	75
3.28	Sample 4 ( $Ra = 0.4 \mu m$ ) normalised BRDFs at different wavelengths. . . . .	76
3.29	Illustration of the used profile line. . . . .	77
3.30	Sample 4 normalised BRDFs for several wavelengths. . . . .	78
3.31	Sample 4 normalised BRDFs for different wavelengths. . . . .	79
4.1	Schematic representation of contactless temperature measurements on an opaque surface. . . . .	84
4.2	Schematic representation of any infrared scene on opaque media, focusing on the sensor. . . . .	85
4.3	Sensitivity of different sensors as a function of wavelength (translated from [7]). . . . .	87
4.4	Schematic representation of contactless temperature measurements on an opaque surface <b>with a focus on the radiative balance</b> . . . . .	89

LIST OF FIGURES

---

4.5	Illustration of the apparent temperature for a real body as a function of emissivity and temperature. . . . .	90
4.6	Schematic representation of the experimental set-up. . . . .	96
4.7	Schematic representation of any infrared scene on opaque media, with a focus on the calibration. . . . .	98
4.8	Schematic representation of black body calibration. . . . .	99
4.9	Typical black body calibration image. . . . .	101
4.10	Schematic representation of the data acquisition. . . . .	103
4.11	Presentation of calibration data. . . . .	104
4.12	Linear fit description of the InSb high-temperature calibration. . . . .	105
4.13	Slope coefficient fitting for InSb high-temperature calibration. . . . .	106
4.14	Projection of the fit atop the data. . . . .	106
4.15	Linear fit description. . . . .	107
4.16	Slope coefficient fitting for InSb low-temperature calibration. . . . .	108
4.17	Projection of the fit atop the data. . . . .	108
4.18	Relative difference. . . . .	109
4.19	Relative measured camera deviation. . . . .	110
4.20	Computed error from temperature measurements due to camera noise. . . . .	110
4.21	Presentation of the numerical study: (a) emissivity field, (b) histogram of emissivity. . . . .	115
4.22	The surrounding radiant flux density is detected by the camera through a perfect mirror, (a) and (b), or through the heterogeneous sample, (c) and (d), in a homogeneous irradiation configuration (290 K), (a) and (c), and in a heterogeneous irradiation case, (b) and (d). . . . .	117
4.23	Radiative flux leaving ( $\dot{q}_s^l$ ) the sample (300 K) with different black body equivalent temperatures of the surrounding scene: (a) uniform at 290 K; (b) uniform at 300 K; (c) uniform at 350 K; (d) heterogeneous case. . . . .	118
4.24	Simulated camera response (step 2 of ATR) for a heterogeneous sample (a) and a reference mirror (b): (a.1) radiative image from the sample $\dot{q}_{s,1}$ ; (a.2) radiative image from the illuminated sample $\dot{q}_{s,2}$ ; (a.3) difference between both images $\dot{q}_{s,2} - \dot{q}_{s,1}$ ; (b.1) radiative image from the mirror $\dot{q}_{m,1}$ ; (b.2) radiative image from the illuminated mirror $\dot{q}_{m,2}$ ; (b.3) difference between both images $\dot{q}_{m,2} - \dot{q}_{m,1}$ . . . . .	122
4.25	Illustration of the ATR method (a) normal reflectivity $\tilde{\rho}_{E,s}^\perp$ ; (b) emissivity $(1 - \tilde{\rho}_{E,s}^\perp)$ ; (c) sample emittance $\dot{q}_s^e$ ; (d) sample black body emittance $\dot{q}_s^b$ . . . . .	123
4.26	Presentation of the stainless steel sample with two surface treatments: (1) rough (untreated) and (2) laser polished. . . . .	124



LIST OF FIGURES

---

4.27	Camera measurements (step 2 of ATR) on the (a) stainless steel sample, where the left side is the rough surface and the right is the laser-polished surface, and (b) for the reference mirror. (a.1) raw sample measurement $\dot{q}_{s,1}$ ; (a.2) illuminated sample $\dot{q}_{s,2}$ ; (a.3) difference $\dot{q}_{s,2} - \dot{q}_{s,1}$ ; (b.1) raw mirror measurement $\dot{q}_{m,1}$ ; (b.2) illuminated mirror $\dot{q}_{m,2}$ ; (b.3) difference $\dot{q}_{m,2} - \dot{q}_{m,1}$ . . . . .	125
4.28	Measured sample radiative properties (step 4): (a) reflectivity $\tilde{\rho}_{Fs}^\perp$ ; (b) emissivity $(1 - \tilde{\rho}_{Fs}^\perp)$ . . . . .	126
4.29	Measured stainless steel sample emittance: (a) $\dot{q}_s^e$ (b) $\dot{q}_s^b$ . . . . .	127
4.30	Sample temperature distribution ( $^\circ\text{C}$ ): (a) temperature map; (b) histogram of temperatures for ATR and emissivity correction methods. The room temperature is measured to be $21.3^\circ\text{C}$ . . . . .	128
4.31	Presentation of the three-layer aluminium sample: (1) raw surface, (2) painted black, and (3) speckled. . . . .	129
4.32	Camera measurements (step 2 of ATR) (a) on the three-layer aluminium and (b) for the reference mirror. (a.1) Raw sample measurement $\dot{q}_{s,1}$ ; (a.2) illuminated sample $\dot{q}_{s,2}$ ; (a.3) difference $\dot{q}_{s,2} - \dot{q}_{s,1}$ ; (b.1) raw mirror measurement $\dot{q}_{m,1}$ ; (b.2) illuminated mirror $\dot{q}_{m,2}$ ; (b.3) difference $\dot{q}_{m,2} - \dot{q}_{m,1}$ . . . . .	130
4.33	Measured sample radiative properties (step 4): (a) reflectivity $\tilde{\rho}_{Fs}^\perp$ ; (b) emissivity $(1 - \tilde{\rho}_{Fs}^\perp)$ . . . . .	130
4.34	Measured emittance of the three-layer aluminium sample: (a) sample's emittance $\dot{q}_s^e$ (b) sample's black body emittance $\dot{q}_s^b$ . . . . .	131
4.35	Sample temperature distribution ( $^\circ\text{C}$ ): (a) temperature map; (b) histogram of temperatures for the ATR and emissivity correction methods. The room temperature is measured as $23.2^\circ\text{C}$ . . . . .	132
5.1	Heat flux description. . . . .	136
5.2	Elementary schematic of direct and inverse problems. . . . .	138
5.3	Obtained temperature fields on the rear face at different time steps: (a) $t=0.5$ s, (b) $t=1$ s, (c) $t=2$ s and (d) $t=3$ s. . . . .	142
5.4	Illustration of the obtained temperature fields on the rear face at different time steps: (a) $t=0.5$ s, (b) $t=1$ s, (c) $t=2$ s and (d) $t=3$ s. . . . .	145
5.5	Illustration of a portion of the 2D grid used for discretisation. . . . .	146
5.6	Description of the inverse method based on the finite volume approach in 2D cases. . . . .	152
5.7	Behaviour of the $C_{global}$ function of (a) $C_{VT,\Delta T}$ , (b) $C_{VT,h}$ and (c) $C_{VT,h}$ . . . . .	153
5.8	Behaviour of the $C_{global}$ function of (a) $C_{VT,\Delta T}$ , (b) $C_{\Delta T,h}$ and (c) $C_{VT,h}$ . . . . .	154
5.9	Diffusivity estimation: (a) mean estimated thermal diffusivity and (b) number of thermal diffusivity estimations. . . . .	155
5.10	Histogram of thermal diffusivity estimation. . . . .	155
5.11	Volumetric heat source estimation: (a) maximum estimated volumetric heat source over time and (b) estimated power of each character as a function of time. . . . .	156
5.12	Relative error of heat flux estimation. . . . .	156

## LIST OF FIGURES

---

5.13	Illustration of a portion of the 3D grid used for discretisation. . . . .	157
5.14	Decomposition of heat sources: (a) heat flux function of time and (b) thermal response of the system. . . . .	160
5.15	Imposed heat flux description. . . . .	164
5.16	Maximum identified power for different regularisation factors ( $\nu$ ). . . . .	165
5.17	Estimated power on each letter and over the total surface as a function of time. . . . .	166
5.18	Measured computational times as a function of the regularisation factor ( $\nu$ ). . . . .	167
6.1	Experimental set-up for the characterisation of HEL radiation scattered from a solid surface. . . . .	173
6.2	Experimental set-up for the characterisation of HEL radiation scattered from a solid surface. . . . .	177
6.3	Numerical illustration of the incident power density for a laser power of 4 kW and a beam diameter of 30 mm (numerical data): (a) Gaussian beam and (b) top hat beam. . . . .	178
6.4	Sample behaviour at different time steps under top hat and Gaussian illumination. . . . .	179
6.5	BRDF behaviour at different time steps under top hat and Gaussian illumination. . . . .	181
6.6	Spatial filter used during data processing: blue corresponds to pixels outside the panel, and yellow corresponds to pixels inside the panel. . . . .	182
6.7	Experimental set-up developed to calibrate the incident beam. . . . .	183
6.8	Typical image acquired during the calibration process. . . . .	183
6.9	Experimental curves of image discrete integration as a function of laser power for multiple ITs. . . . .	184
6.10	Fitting of the slope coefficient and intercept. . . . .	185
6.11	Projection of the identified fit atop the experimental data. . . . .	185
6.12	Considered geometry for identifying the pixel location and the corresponding to the solid angle . . . . .	187
6.13	Illustration of measured polar coordinates. . . . .	188
6.14	Measured solid angle cartography. . . . .	188
6.15	Measured BRDFs with top hat illumination (time step $t=1.8, t=2, t=5$ s) and Gaussian illumination (time step $t=0.3, t=0.7, t=0.9$ and $t=1.4$ s). . . . .	189
6.16	Schematic representation of the experimental set-up. . . . .	192
6.17	Surface roughness measurements. . . . .	193
6.18	Sample presentation: (a) rear face after polishing and before the trial, (b) rear face after the trial, (c) front face before the trial and (d) front face after the trial. . . . .	193
6.19	Camera calibration curves for multiple ITs. . . . .	195
6.20	Calibration for (a) $\dot{q}_{s,1}$ , (b) $\dot{q}_{s,2}$ and (c) $\dot{q}_{s,2} - \dot{q}_{s,1}$ . . . . .	196
6.21	Measured reflectivity: (a) reflectivity field measured at the beginning, (b) temporal plot of reflectivity for different pixels. . . . .	198

## LIST OF FIGURES

---

6.22	DL correction: (a) temporal plot of the raw DL, (b) temporal plot of the corrected DL, (c) last image of the raw DL, (d) last image of the corrected DL. . . . .	199
6.23	DL correction: (a) temporal plot of apparent temperature, (b) temporal plot of corrected temperature, (c) last image of the apparent temperature, (d) last image of the corrected temperature. . . . .	200
6.24	Error obtain though the application of ATR method: (a) DL error without correction, (b) DL error with correction, (c) temperature error without correction, (d) temperature error with correction. . . . .	201
6.25	Thermal problem positioning. . . . .	205
6.26	Thermal problem positioning. . . . .	209
6.27	Illustration of the clamping system: (a) image in visible light (front face) and (b) raw image captured by the IR camera. . . . .	209
6.28	Measured laser beam spatial repartition of (a) the measured beam and (b) a profile of the cross section. . . . .	210
6.29	Laser temporal profile and the measured maximum temperature on each pixel. . . . .	211
6.30	a) Temporal temperature profile for the central pixel and (b) cross section of temperature across the centre row of the sample. . . . .	212
6.31	Estimated power ( $Q(t)$ ) as a function of time. . . . .	213
6.32	Estimated power: $Q(x, y, t = 1)$ . . . . .	214
6.33	Cross section of the estimated power: $Q_{xy}(t = 1)$ . . . . .	215
6.34	a) Excitation temporal profile for the calibration and (b) image of the maximum measured temperature. . . . .	217
6.35	Temperature temporal profile of the central pixel. . . . .	218
6.36	Illustration of the temperature field: (a) maximum measured temperature and (b) cross section of the temperature field for different time steps. . . . .	218
6.37	Spatial estimation of the absorbed power at (a) $t=0.2$ s, (b) $t=1$ s, (c) $t=2$ s and (d) $t=3$ s. . . . .	220
6.38	Temporal behaviour of the absorbed power. . . . .	221
6.39	Sample absorbance as a function of time. . . . .	221
8.1	Measured samples surface topography . . . . .	241
8.2	Measured Multi-Spectral BRDFs on sample 1 . . . . .	242
8.3	Measured Multi-Spectral BRDFs on sample 2 . . . . .	243
8.4	Measured Multi-Spectral BRDFs on sample 3 . . . . .	244
8.5	Measured Multi-Spectral BRDFs on sample 4 . . . . .	245
8.6	Measured Multi-Spectral BRDFs on sample 5 . . . . .	246
8.7	Measured Multi-Spectral BRDFs on sample 6 . . . . .	247

# Chapter 1

## Introduction

### Table of Contents

---

<b>1.1</b>	<b>Societal &amp; industrial context</b> . . . . .	<b>30</b>
<b>1.2</b>	<b>Context of this thesis</b> . . . . .	<b>32</b>

---

### 1.1 Societal & industrial context

Whether for fibre optics that allow convenient access to online information, in printers, in cars (lidar) or for cutting sheet metal, for example, laser sources are now part of our daily lives. However, what makes them so unique? The answer is simple when we consider what a laser is: concentrated light.

Laser radiation is first and foremost a spatial, temporal and spectral concentration of photons. The spatial aspect refers to the photons all sharing the same direction, and the temporal aspect refers to photons being coherent and oscillating in phase with each other at a given wavelength. It is easy to understand that this concentrated energy offers infinite possibilities, which is one of the most striking features of this invention. When Albert Einstein described the principle of stimulated emission for the first time in 1917 (without being able to prove it experimentally), he did not propose any specific applications. Nevertheless, this principle has led to the aforementioned presence of lasers that are now integral to modern technology.

One specific application, high-powered lasers, involves concentrating large amounts of light energy, which can cause devastating effects. This can be seen in the multitude of stories including laser weapons, for example, Superman's laser heat waves from his eyes (1933) or the Death Star from the Star Wars saga, which projects a laser beam (1977) (see Figure 1.1).

However, the idea of concentrating light to make a weapon is much more ancient. In 237 BC, Archimedes himself is said to have made a mirror to focus sunlight to sink ships that were attacking the city of Syracuse.

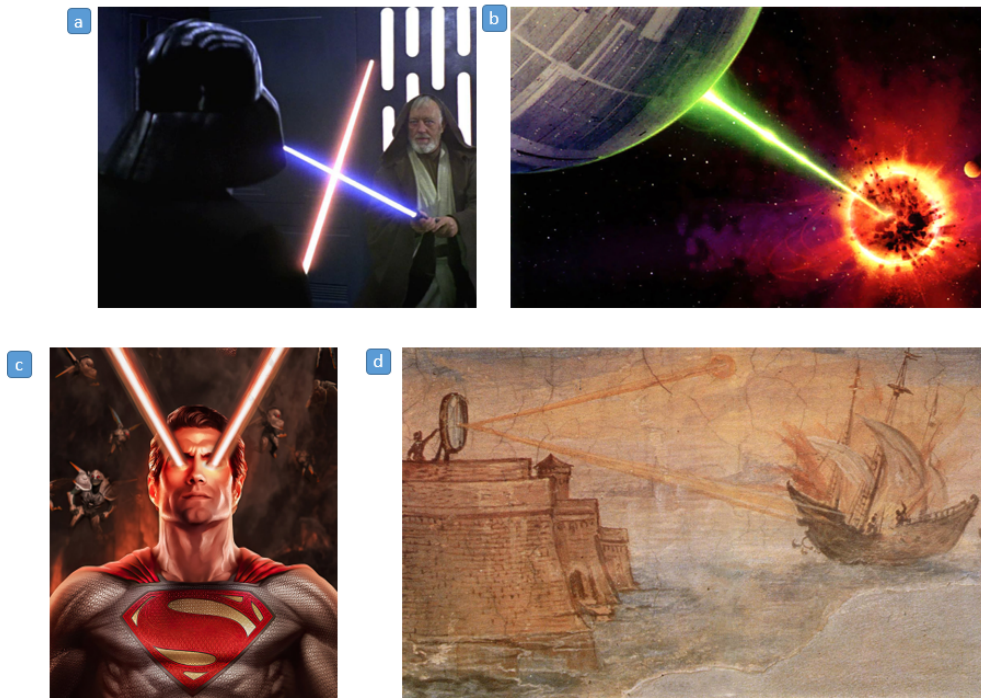


Figure 1.1: Selected examples of luminous weapons in fiction and legend: a) lightsaber, (b) Death Star, (c) heat vision of Superman and (d) the Archimedes mirror.

This common trope came to life at the beginning of the Cold War, when the first studies and prototypes were realised [8]. In the 1970s, after a series of field validations of high-powered ground-based CO<sub>2</sub> lasers, the United States launched its first anti-structure laser weapon proof-of-concept program called the Airborne Laser Lab (ALL), the origin of the airborne laser (ABL), a 480 kW CO<sub>2</sub> laser mounted on a Boeing NKC-135 tanker aircraft [9, 10, 11]. During its 11 years of operation, this proof of concept was used to destroy several AIM-9 missiles as well as drones. The laser was retired in 1984 and has been on display at the Air Force Museum at Wright Patterson Air Force Base since 1988. Since then, many developments have taken place in different countries in different applications (naval, air and land).

One of the major difficulties in the use of such a system towards military applications is understanding target vulnerability. In conventional systems, missiles take a predictable amount of time to reach their target, which is then destroyed nearly instantaneously upon contact. In contrast, lasers travel at light speed and are able to hit their targets essentially instantly. The effects of lasers are mainly thermal, requiring a certain amount of time for the target to degrade (burn/deform). The



Figure 1.2: Illustration of a laser system: (a) left-side view of an NKC-135 airborne laser [1] and (b) MBDA showcased HELMA-P laser anti-drone system mounted on an Arqus Sherpa armored vehicle [2].

difficulty is to determine in advance whether the target system will be defeated.

## 1.2 Context of this thesis

This thesis topic is part of a project for the research and development of multi-kW laser weapons. Following the diversification of threats in the modern world and the risks of laser illumination, MBDA France is acquiring a test facility for continuous high-powered lasers. The general objective of MBDA France is to have the capacity to quantify the vulnerability of these targets. Specifically, studies are performed through target illumination tests for different applications (materials, technologies). The overall scientific objective of the project is to determine the following for high-powered continuous lasers:

- knowledge and understanding of laser–matter interactions,
- experimental characterisation of the phenomena involved using original imaging methods (IR imaging, innovative multifunctional sensing, etc.),
- development of inverse methods for the estimation of optical and thermophysical properties.

Given a relevant material's family of interest, different degradation mechanisms are involved, which can be thermal, thermomechanical, thermochemical, or even a combination of these.



## 1.2. CONTEXT OF THIS THESIS

The main motivation of this thesis is to quantify the radiative balance between the power absorbed by the material under illumination and the reflected power. This quantification addresses both local and global scales, as the excitation modes that are produced lead to very pronounced gradients. For the experimental part, bench capacity for high-powered laser excitation has already been developed, including all aspects related to laser safety [12].

The work presented in this thesis focuses on the development of experimental techniques for multi-parameter/multi-spectral characterisation techniques and numerical methods to obtain the desired parameters. From a schematic point of view, laser ablation or high-energy laser (HEL) beam interactions with matter can be summarised according to the following diagram (Figure 1.3). The illuminated area involves complex problems, with variations in thermophysical properties, phase changes, oxidation, etc., whereas the rest of the target is mainly subjected to thermal diffusion. The starting point of this thesis assumes that no measurement can be done in the illuminated part. Consequently, the challenge lies in determining the behaviour of the illuminated area by studying its surroundings.

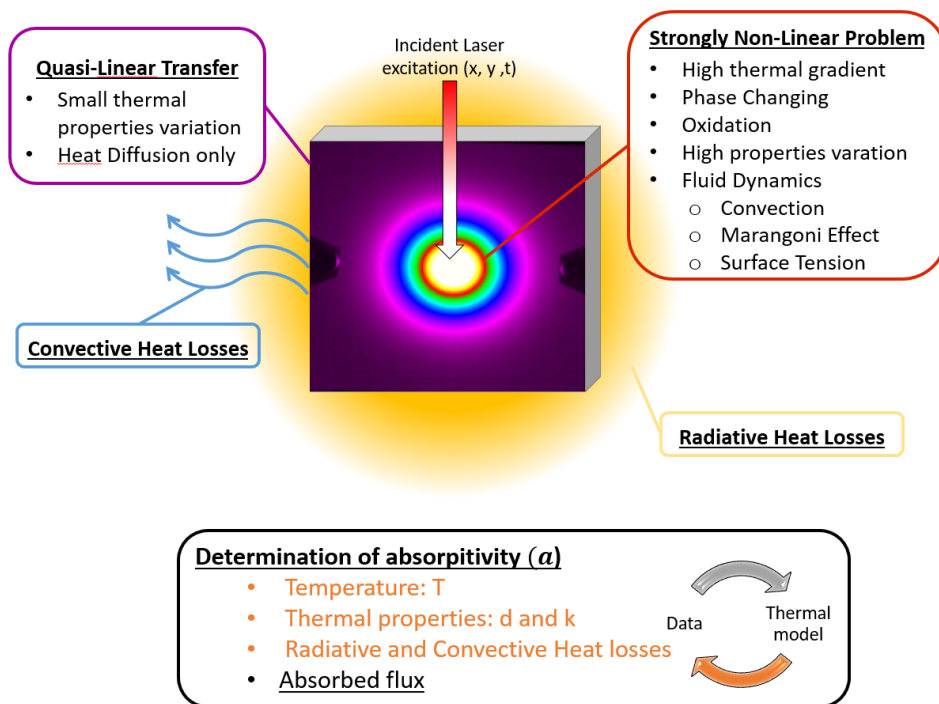


Figure 1.3: Schematic representation of the different zones of interest during HEL illumination and PhD objectives.



## 1.2. CONTEXT OF THIS THESIS

---

To achieve the objectives of the thesis and to remove the current barriers, the work is organised along the following four axes:

- Experimental and numeric development of methods for measuring reflection fields

This work relies on rich literature [13, 14] addressing in the visible range to determine the reflection field of lasers impacting opaque materials in the infrared range. This is a new avenue for the I2M-TREFLE laboratory. While the laboratory has great experience working with transmission [15, 16, 17, 18, 19, 20, 21], measuring reflection fields necessitates extending the team's primary topic and introduces related challenges.

- Experimental and numeric development of methods for measuring temperature fields with an infrared camera

The idea is to superimpose a spectral signal reflected by the surface on its own emission. This superposition would allow the reflection coefficient to be characterised simultaneously with the emission coefficient. Related techniques, which are described in the literature [22, 23], are adapted here in real time and for imaging.

- Analytical development and applying inverse methods to measure the heat flux actually absorbed by the sample

In areas far from the laser's impact, the thermal properties of the material behave relatively linearly. This allows the use of inverse techniques that were recently developed at I2M-TREFLE. Combined with thermal imaging, this enables the complete characterisation of possibly anisotropic materials [24, 25, 26, 27, 28, 29, 30].

- Application of various proposed methods under HEL illumination

At this stage, the different methods studied at the laboratory scale or by numerical studies is tested under extreme conditions.

# Chapter 2

## Background of radiative heat transfer

### Table of Contents

---

<b>2.1</b>	<b>Introduction</b>	<b>36</b>
<b>2.2</b>	<b>Fundamentals of thermal radiation</b>	<b>36</b>
<b>2.3</b>	<b>Definition of a black body</b>	<b>37</b>
<b>2.4</b>	<b>Useful radiometry quantities</b>	<b>38</b>
<b>2.5</b>	<b>Planck's law</b>	<b>39</b>
<b>2.6</b>	<b>Wien's displacement law</b>	<b>42</b>
<b>2.7</b>	<b>Stefan–Boltzmann law</b>	<b>42</b>
<b>2.8</b>	<b>Black bodies and real bodies: radiative properties and Kirchhoff's law</b>	<b>44</b>
2.8.1	Link between emissivity and reflectivity for opaque media	47
2.8.2	Different kinds of opaque materials	47
<b>2.9</b>	<b>Conclusion</b>	<b>48</b>

---

## 2.1 Introduction

This chapter introduces fundamental radiative laws and quantities necessary for understanding this thesis.

## 2.2 Fundamentals of thermal radiation

The electromagnetic spectrum describes all electromagnetic radiation classified by frequency, wavelength or energy. Infrared radiation (IR), with wavelengths ranging from a few microns to several millimetres, is only a small part of the electromagnetic spectrum, which ranges from infinitely small ( $< 10^{-15} m$ ) to long waves of greater than several tens of kilometres (see Figure 2.1).

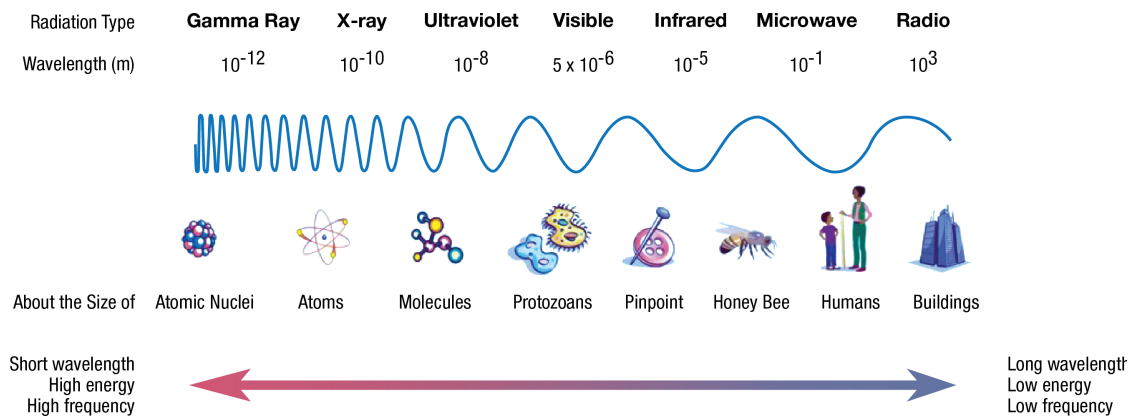


Figure 2.1: Schematic of the electromagnetic wave spectrum [3].

The thermal radiation carries energy  $E$  (J). The Planck–Einstein relation (see Eq. 2.1) describes the link between the amount of energy and the wavelength.

$$E = h\nu = \frac{hc}{\lambda} \quad (2.1)$$

where  $h$  is the Planck constant ( $h \approx 6.626 \times 10^{-34} m^2 \cdot kg \cdot s^{-1}$ ),  $c$  is the speed of light ( $c \approx 3 \times 10^9 m \cdot s^{-1}$ ) in air,  $\lambda$  is the wavelength ( $\mu m$ ) and  $\nu$  is the frequency (Hz).

Just as electromagnetic waves have a wide domain of wavelengths, they carry vastly different amounts of energy. Thermal radiation may be defined as electromagnetic waves that are emitted by a medium solely due to its temperature. This definition limits the range of wavelengths of importance

### 2.3. DEFINITION OF A BLACK BODY

---

for heat transfer between  $0.1 \mu m$  and  $100 \mu m$ . IR radiation consists of 3 distinct bands. The boundaries of each band depend on conventions that vary according to the user. The IR camera user community tends to define the infrared wavelength based on the camera sensor spectral range [7], whereas the optical community has other markers; for example, the ISO 20473:2007 standard for "Optics and Photonics" defines the IR spectrum (see Table 2.1). In this manuscript, the camera-user-based distinction is used.

	Short-wavelength ( $\mu m$ )	Mid-wavelength ( $\mu m$ )	Far-wavelength ( $\mu m$ )
Camera user	0.8 - 2	2 - 5	7-13
Optical community	0.78 - 3	3 - 50	50 -5000

Table 2.1: Description of the infrared spectrum.

### 2.3 Definition of a black body

When an electromagnetic wave impinges upon a surface (solid or liquid surface, particle or bubble), the wave may be reflected (either partially or totally), and the rest of the wave penetrates into the medium. While passing through the medium, the wave may continuously be attenuated. If the wave is completely attenuated, the medium is considered opaque. If the wave passes through the medium without any attenuation, it is termed transparent, while a body with partial attenuation is called semi-transparent. An opaque surface that does not reflect any radiation is called a perfect absorber or a black surface. When we "see" an object, our eyes absorb electromagnetic waves from the visible part of the spectrum, which have been emitted by a light source and have been reflected by the object towards our eyes. We cannot see a surface that does not reflect radiation; therefore, it appears "black" to our eyes. Since black surfaces absorb the maximum possible amount of radiative energy, they serve as a standard for the classification of all other surfaces.

It is easy to show that a black surface also emits a maximum amount of radiative energy, i.e., more than any other body at the same temperature. To show this, the second Kirchhoff law [31] is used: Consider two identical black-walled enclosures, thermally insulated on the outside, with each containing a small object, one black and the other one not, as shown in Figure 2.2.

After a long time, in accordance with the Second Law of Thermodynamics, both entire enclosures and the objects within are at the same uniform temperature. This characteristic implies that every

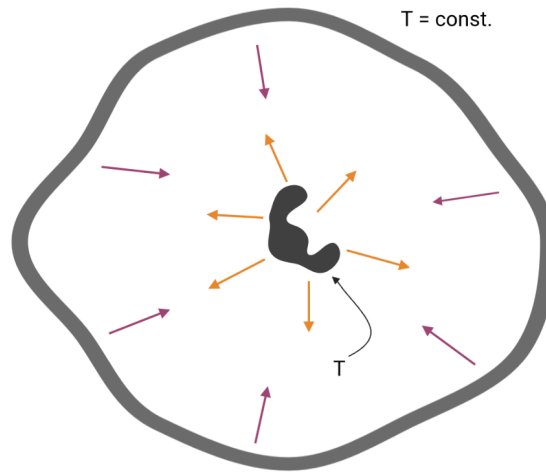


Figure 2.2: Kirchhoff Law presentation.

part of the surface emits precisely as much energy as it absorbs and that both objects in the different enclosures receive exactly the same amount of radiative energy. However, since the black object absorbs more energy (i.e., the maximum possible), it must also emit more energy than the non-black object. By the same reasoning, it is easy to show that a black surface is a perfect absorber and emitter at every wavelength for any direction (of incoming or outgoing electromagnetic waves) and that the radiation field within an isothermal black enclosure is isotropic and homogeneous (i.e., the radiative energy density is the same at any point and in any direction within the enclosure). Before going further in the description of IR, it is important to introduce some physical quantities that describe radiation.

## 2.4 Useful radiometry quantities

Figure 2.3 illustrates the notation of the International System of Units (SI) dedicated to radiometric quantities [32].

In this manuscript, the notations of Michael F. Modest [33] are used to describe radiometric quantities as described in Figure 2.3. The **radiant flux (or emissive power)** corresponds to the amount of energy emitted by a source. The emissive power can be described as the **total power** while working on the whole spectrum ( $q : W$ ) or the **spectral emissive power** ( $q(\lambda) : W \cdot \mu m^{-1}$ ) at a given frequency (or range). The **radiant flux density** corresponds to the amount of energy emitted per unit of time from a given surface. The radiant flux density can be described as **total** while working

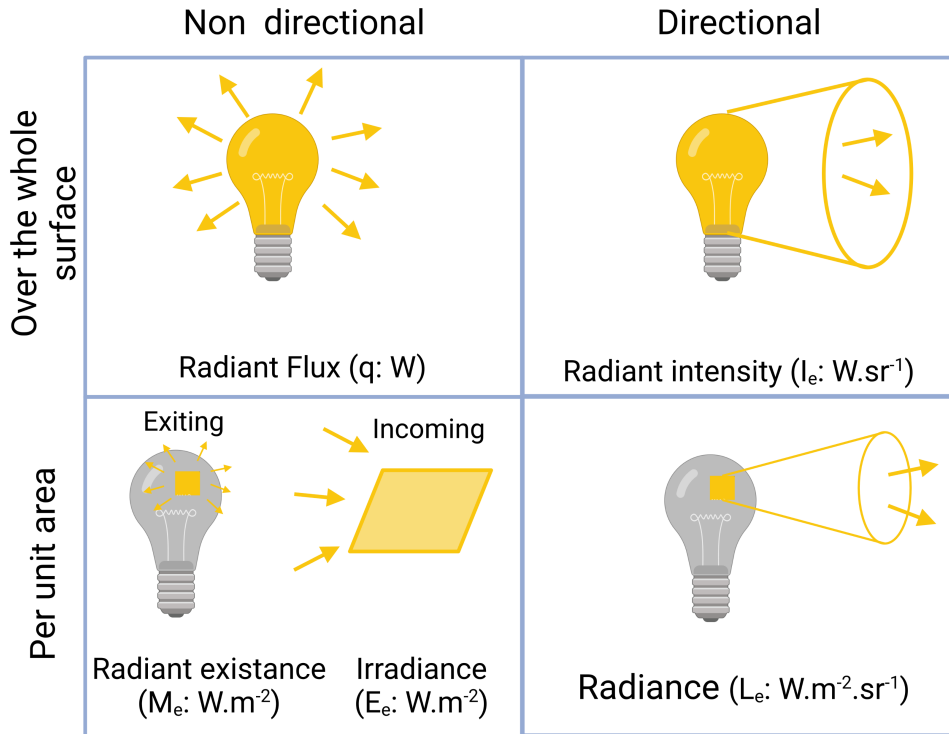


Figure 2.3: Introduction to hemispherical/directional radiative quantities.

on the whole spectrum ( $\dot{q} : W \cdot m^{-2}$ ) or by the **spectral radiant flux density** ( $\dot{q}(\lambda) : W \cdot m^2 \cdot \mu m^{-1}$ ) at a given frequency (or range). Even though the radiant flux density appears to be the natural choice to describe radiative heat flux leaving a surface, it is inadequate for describing the directional dependency of electromagnetic waves that leave a surface. Therefore, very similar to the emissive power, one defines the **radiative intensity** ( $I : W \cdot m^2 \cdot sr^{-1} \mu m^{-1}$ ) as the radiative energy flow per unit solid angle, wavelength and unit area normal to the rays. This quantity can also be used for reflection ( $I_r$ ), transmission ( $I_t$ ) and emission ( $I_e$ ).

## 2.5 Planck's law

Now that the fundamental quantities have been introduced, one can express the amount of energy radiated from a surface in a given direction for a given wavelength from a black body ( $I_b(\lambda, T) : W \cdot m^2 \cdot sr^{-1} \mu m^{-1}$ ) by Planck's law as described in Eq. 2.2.

## 2.5. PLANCK'S LAW

$$I_b(\lambda, T) = \frac{2hc^2}{\lambda^5} \frac{1}{e^{\frac{hc}{\lambda k_B}} - 1} \quad (2.2)$$

where  $h$  is the Planck constant ( $h \approx 6.626 \times 10^{-34} \text{ m}^2 \cdot \text{kg} \cdot \text{s}^{-1}$ ),  $k_B$  is the Boltzmann constant ( $k_B = 1.380649 \times 10^{-25} \text{ J} \cdot \text{K}^{-1}$ ),  $c$  is the speed of light ( $\text{m} \cdot \text{s}^{-1}$ ) in air and  $\lambda$  is the wavelength ( $\text{m}$ ).

Figure 2.4 shows the black body radiative intensity function of wavelength for representative temperatures upon laser interaction with a material. The maximum intensity is observed to shift towards lower wavelengths for each higher-temperature condition.

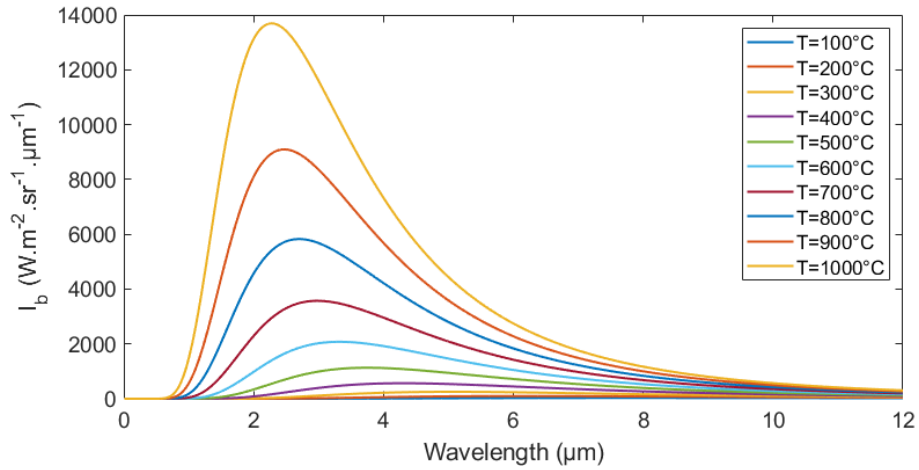


Figure 2.4: Black body radiative intensity function of the wavelength for different temperatures.

In this work, two cameras with two spectral ranges, InSb (1-5  $\mu\text{m}$ ) and MCT (7-13  $\mu\text{m}$ ), are used. To choose the best kind of sensor, one can study the sensitivity of Planck's law to the temperature shift over two different wavelengths that are representative of the sensor (i.e., 4  $\mu\text{m}$  and 10  $\mu\text{m}$ ). To choose the best wavelength, the sensitivity of the Planck's law as a function of temperature is presented in Figure 2.5.a, illustrating that the sensitivity in both spectral ranges increases with increasing temperature. For a wavelength of 10  $\mu\text{m}$ , the sensitivity follows a logarithmic curve starting from 0.1 to 0.7  $\text{W} \cdot \text{m}^2 \cdot \text{sr}^{-1} \mu\text{m}^{-1} \cdot \text{K}^{-1}$ , and for a wavelength of 4  $\mu\text{m}$ , the observed curves have the same logarithmic shape but a larger amplitude (from 0.01 to 25  $\text{W} \cdot \text{m}^2 \cdot \text{sr}^{-1} \mu\text{m}^{-1} \cdot \text{K}^{-1}$ ). The intercept between both curves is at 130  $^{\circ}\text{C}$ . Based on this observation, one chooses a far-infrared camera while working near ambient temperature and a mid-infrared camera while working with temperatures greater than 250  $^{\circ}\text{C}$ .

## 2.5. PLANCK'S LAW

In this study, the high power of the laser imposes a large thermal shift. Measuring large thermal gradients is a challenging situation because one wishes to simultaneously measure low and high temperatures in the same frame. This often leads to image saturation for high-temperature areas and insufficient signal for measurement in other areas. A way to overcome this issue is to choose an instrument (camera) with an adequate spectral range where Planck's law does not vary much with temperature. This is illustrated in Figure 2.5.b for both wavelengths of  $4\ \mu\text{m}$  and  $10\ \mu\text{m}$ , where the temperature is plotted as a function of Planck's law. Both curves have an exponential shape; however, the range of radiative intensity required to observe a thermal dynamic of  $1500\ ^\circ\text{C}$  extends over four decades to  $4\ \mu\text{m}$ , and only two decades are needed at  $10\ \mu\text{m}$ . Based on this observation, one chooses the MCT sensor to study dynamic thermal changes.

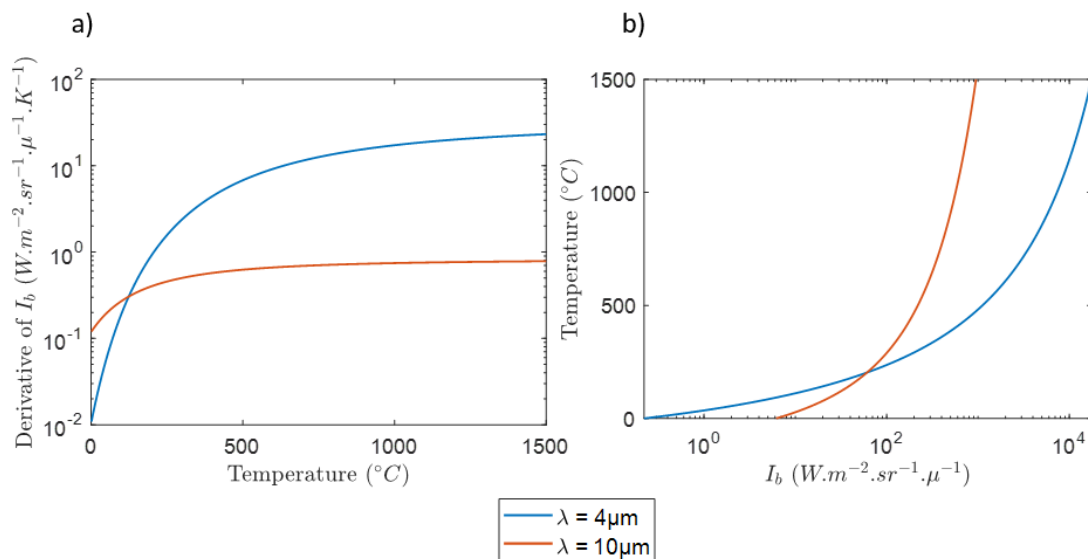


Figure 2.5: Study of Planck's law as a function of the temperature for two wavelengths (4 and  $10\ \mu\text{m}$ ): (a) temperature function of black body radiative intensity and (b) derivative of the black body radiative function of the temperature intensity.

The major drawback of this choice appears while working with noisy data. Considering a 10% error in the radiometric measurement, the error in the temperature measurements is higher at  $10\ \mu\text{m}$  than at  $4\ \mu\text{m}$  due to the slope of the curve. This is illustrated in Figure 2.6, where the error generated is 2 to 3 times larger at  $10\ \mu\text{m}$  than at  $4\ \mu\text{m}$ .



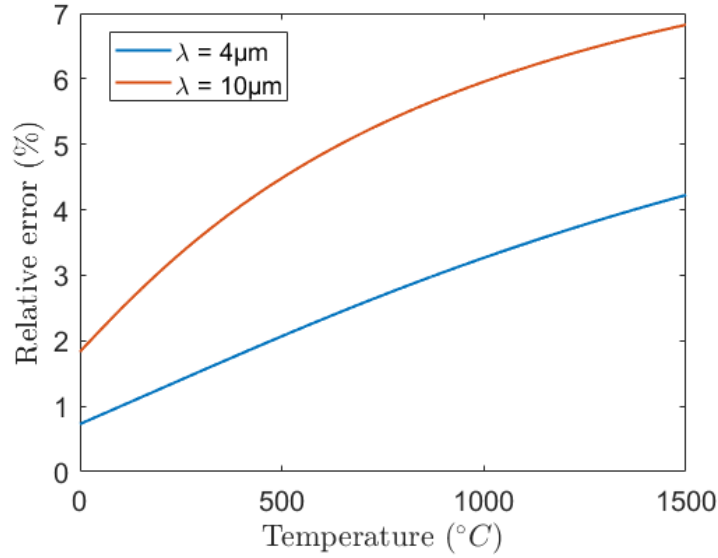


Figure 2.6: Theoretical relative error in temperature measurement with a 10% underestimation of Planck's law for 2 wavelengths (4  $\mu m$  and 10  $\mu m$ ).

## 2.6 Wien's displacement law

Wien's displacement law states that the peak of the black body radiation curve ( $\lambda_{peak} : m$ ) depends on the black body's temperature. The shift in wavelength is inversely proportional to the temperature. Eq. 2.3 describes the shift of that peak and is a direct consequence of Planck's radiation law, as shown in Figure 2.7.

$$\lambda_{peak} = \frac{b}{T} \quad (2.3)$$

where  $b$  is Wien's displacement constant ( $b \approx 2.89 \times 10^{-3}, m \cdot K$ ) and  $\lambda_{peak}$  is the wavelength ( $m$ ).

## 2.7 Stefan-Boltzmann law

By integrating Planck's law over the upper hemisphere and on the entire spectrum, one can compute the total radiative flux density emitted ( $\dot{q}(T) : W \cdot m^{-2}$ ) by a surface with the Stefan-Boltzmann law described in Eq. 2.4.

$$\dot{q}(T) = \sigma T^4 \quad (2.4)$$

## 2.7. STEFAN–BOLTZMANN LAW

---

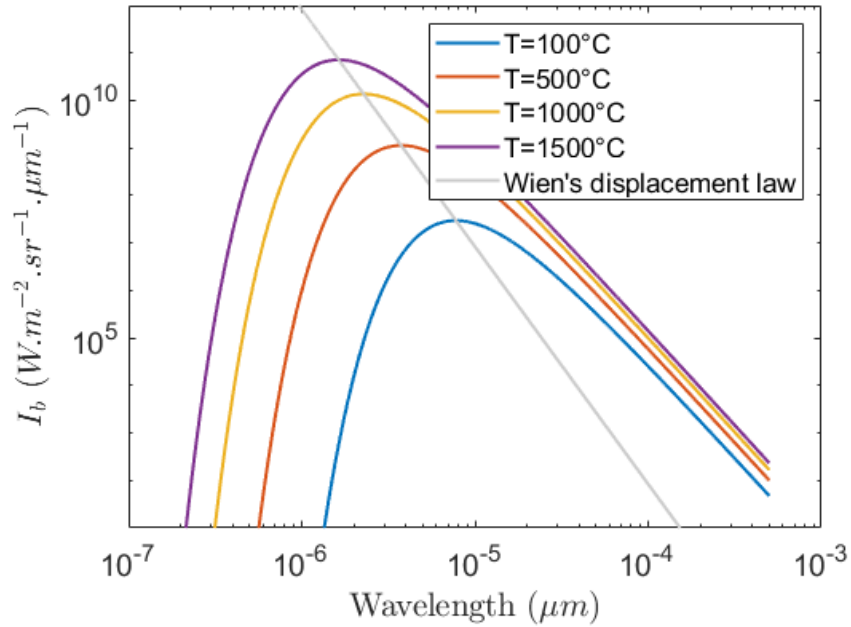


Figure 2.7: Relation between Planck's and Wien's laws.

where  $\sigma$  is the Stefan–Boltzmann constant ( $\sigma \approx 5.670 \times 10^{-8} W \cdot m^{-2} \cdot K^{-4}$ ) and  $T$  is the surface's temperature ( $K$ ).

All the laws described before (Planck's law, Wien's law and Stefan–Boltzmann's law) characterise the emission of electromagnetic waves for a perfect emitter. Nevertheless, these laws are not directly applicable for non-black-body objects. The following section describes the radiative properties and factors that influence them.

## 2.8 Black bodies and real bodies: radiative properties and Kirchhoff's law

When the surface of a material receive is illuminated by a beam, the incident energy is distributed in three ways [31, 34, 35], as shown in Figure 2.8:

- A part is reflected (without penetrating the material). It is referred to as the reflection coefficient (or reflectance):

$$\text{Reflectance: } \mathcal{R} = \frac{\text{reflected energy}}{\text{incident energy}} = \frac{Q_r}{Q_i}$$

- A part is transmitted through the sample:

$$\text{Transmittance: } \mathcal{T} = \frac{\text{transmitted energy}}{\text{incident energy}} = \frac{Q_t}{Q_i}$$

- A part is degraded as heat within the material and is referred to as the energy absorption factor (or absorbance):

$$\text{* Absorbance: } \mathcal{A} = \frac{\text{absorbed energy}}{\text{incident energy}} = \frac{Q_a}{Q_i}$$

The three quantities of absorbance, reflectance and transmittance are linked together by the law of conservation of energy and described by Kirchhoff's first law as written in Eq. 2.5:

$$\mathcal{A} + \mathcal{T} + \mathcal{R} = 1 \tag{2.5}$$

Inconveniently, these quantities depend on surface conditions (roughness, oxidation, temperature) [36] and therefore must be studied dynamically during laser interaction with the surface.

When applied to opaque bodies, the transmittance of the body is null ( $\mathcal{T} = 0$ ); thus, the terms used are as follows:

- Absorptivity for absorbance:  $\alpha$  for the energy absorbed by the body
- Reflectivity for reflectance:  $\rho$  for the energy reflected by the body

## 2.8. BLACK BODIES AND REAL BODIES: RADIATIVE PROPERTIES AND KIRCHHOFF'S LAW

---

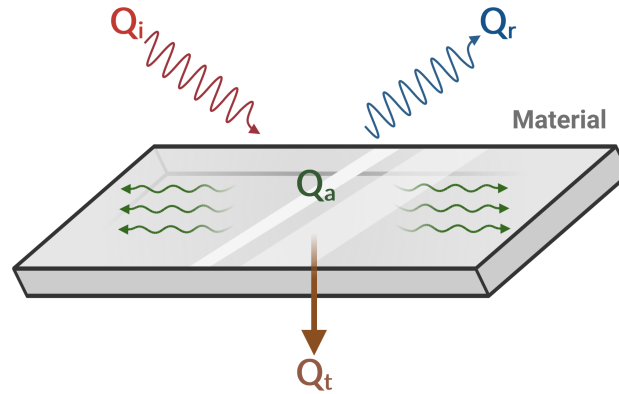


Figure 2.8: Schematic of the optical balance on semi-transparent media illuminated by an incident electromagnetic wave.

As this study is dedicated to opaque bodies, these terms are used later. To describe the reflectivity, two prefixes are generally added. The first one refers to the incident illumination, which can be described as hemispherical ( $\cap$ ) or directional (denoted by an apostrophe, where the incident direction is noted as  $\vec{\omega}_i$ ). The second one refers to the reflections and can be described as hemispherical ( $\cap$ ) or directional (denoted with an apostrophe, where the reflected direction is noted as  $\vec{\omega}_r$ ). This leads to four different quantities:

- The **hemispherical reflectivity** ( $\rho^\cap$ : unitless) describes the effectiveness of the surface in reflecting radiant energy regardless of the incident and reflected direction.
- The **directional hemispherical reflectivity** ( $\rho'^\cap$ : unitless) describes the effectiveness of the surface in reflecting radiant energy from an incident direction  $\vec{\omega}_i$  and reflected in all directions.
- The **hemispherical directional reflectivity** ( $\rho'^\cap$ : unitless) describes the effectiveness of the surface in reflecting radiant energy regardless of the incident direction and reflected direction  $\vec{\omega}_r$ . By an extension of Fermat's principle, it can be shown that  $\rho'^\cap(\lambda) = \rho'^\cap(\lambda)$ .
- The **bidirectional reflectance distribution function (BRDF)**: ( $\rho''(\vec{\omega}_r|\vec{\omega}_i)$ :  $sr^{-1}$ ) is defined as the ratio of radiance to irradiance (2.3). It describes the effectiveness of the surface in reflecting radiant energy coming from  $\vec{\omega}_i$  and reflected in  $\vec{\omega}_r$ .

## 2.8. BLACK BODIES AND REAL BODIES: RADIATIVE PROPERTIES AND KIRCHHOFF'S LAW

---

The relationship between  $\rho'^{\wedge}$  and the BRDF ( $\rho''$ ) is given in Eq. 2.6:

$$\rho'^{\wedge}(T(\vec{x}), \vec{\omega}_i, \lambda) = \int_{2\pi} \rho''(T(\vec{x}), \vec{\omega}_r | \vec{\omega}_i, \lambda) |\vec{n} \cdot \vec{\omega}_r| d\Omega(\vec{\omega}_r) \quad (2.6)$$

where  $\Omega$  is the solid angle ( $sr$ ),  $T(\vec{x})$  is the temperature at point  $\vec{x}$  and  $\vec{n}$  is normal to the surface. Finally, the prefix “spectral” is added for monochromatic quantities ( $\rho(\lambda)$ ).

One can also define a quantity that corresponds to the radiative emitted flux of a body at a given temperature compared to the radiative emitted flux of the black body at a given temperature:

- Emittance:  $\mathcal{E}$  for a semi-transparent body (unitless)
- Emissivity:  $\varepsilon$  for an opaque body (unitless)

The emissivity can be described as **total** while working over the entire spectrum or **spectral emissivity** ( $\varepsilon(\lambda)$ ) for a given frequency (or spectral range). A distinction can also be made between the **hemispherical emissivity** ( $\varepsilon^{\wedge}$ ) and the **directional emissivity** ( $\varepsilon'$ ) depending on the spatial distribution of the emissivity. By definition, for an opaque body, the spectral directional emissivity is equal to the ratio between the emitted radiative intensity of the surface ( $I_e$ ) and the emitted radiative intensity of the black body at the same temperature.

$$\varepsilon'(\lambda, T(\vec{x}), \vec{\omega}_r) = \frac{I_e(\lambda, T(\vec{x}), \vec{\omega}_r)}{I_b(\lambda, T)} \quad (2.7)$$

where  $T(\vec{x})$  is the temperature (K) at point  $\vec{x}$ ,  $\vec{\omega}_r$  is the direction of interest,  $I_e$  is the radiative intensity ( $W \cdot m^2 \cdot sr^{-1} \mu m^{-1}$ ) emitted by the body of interest and  $I_b$  is the radiative intensity emitted by the black body. As most infrared sensors are directional and have a narrow spectral range, this is the most commonly used quantity for temperature measurements.

By taking into account the fact that an opaque body at thermal equilibrium must radiate as much flux that it absorbs, Kirchhoff showed that the absorptivity is equal to the hemispherical emissivity [35].

$$\mathcal{A}(\lambda) = \varepsilon^{\wedge}(\lambda) \quad (2.8)$$

## 2.8. BLACK BODIES AND REAL BODIES: RADIATIVE PROPERTIES AND KIRCHHOFF'S LAW

---

These quantities depend on multiple parameters, such as temperature, wavelength, surface roughness, orientation, oxidation, and crystallography.

### 2.8.1 Link between emissivity and reflectivity for opaque media

The factors of absorbance, transmittance and reflectance are selective and dependent on the wavelength. Based on Kirchhoff's first law (Eq. 2.5), one can describe an opaque body with Eq. 2.9.

$$\mathcal{A}(\lambda) + \mathcal{R}(\lambda) = 1 \quad (2.9)$$

Considering Kirchhoff's first and second laws, the directional emissivity is expressed in Eq. 2.10 for an opaque body. To obtain this equation, only the radiant flux ( $W$ ) is used for both the emitted part that occurs in the entire upper hemisphere ( $\varepsilon^\Omega$ ) and the reflected part from the entire upper hemisphere of the surface, which is reflected in all directions ( $\rho^\Omega$ ).

$$\varepsilon^\Omega = 1 - \rho^\Omega \quad (2.10)$$

This equation can be customised for a given direction and wavelength. The directional emissivity ( $\varepsilon'$ ) in the direction ( $\vec{\omega}_r$ ) of an opaque body surface is expressed as a function of the directional-hemispherical reflectivity ( $\rho'^\Omega$ ).

$$\varepsilon'(\lambda, \vec{\omega}_r) = 1 - \rho'^\Omega(\lambda, -\vec{\omega}_r) \quad (2.11)$$

Based on the two Kirchhoff laws, the directional emissivity based on the measurement of directional hemispherical reflectivity can be expressed. From the knowledge of these two physical parameters, it becomes possible to deduce the absolute temperature of an opaque surface. Therefore, in the specific case of an IR camera, the absolute temperature fields can be retrieved.

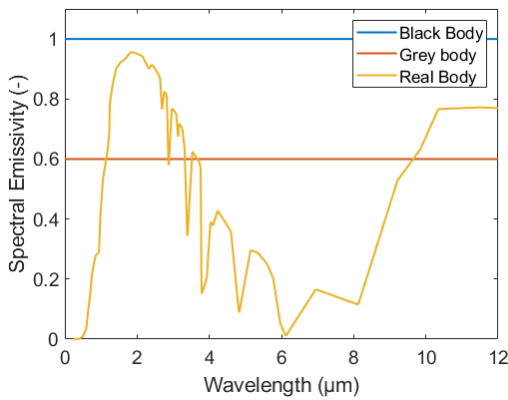
### 2.8.2 Different kinds of opaque materials

Following introduction of Eqs. 2.10 and 2.11, two characteristic cases are notable. The first one is the **black body** ( $\mathcal{A} = \varepsilon^\Omega = \varepsilon' = 1$ ), and the second one is the **white body** ( $\mathcal{R}(\lambda) = \rho^\Omega = \rho'^\Omega = 1$ ), also known as a perfect mirror. Depending on the wavelength, any real body can transition from the

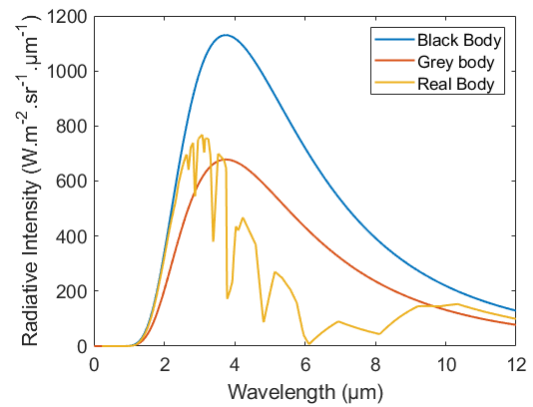
## 2.9. CONCLUSION

---

first to the second case. A real body is a characteristic case where the value of emissivity depends on the spectral range. Because an opaque body is not a perfect emitter or a white body, it is considered a grey body when the emissivity does not exhibit spectral variation. These bodies are illustrated in Figure 2.9a, and their respective radiative intensities are given in Figure 2.9b. As shown, the presented grey body has a constant emissivity of 0.6 (-). In contrast, the signal produced by the real body is more disordered; nevertheless, there are two interesting areas. Between  $1\ \mu\text{m}$  and  $2\ \mu\text{m}$ , the real body is black, and between  $10\ \mu\text{m}$  and  $12\ \mu\text{m}$ , the real body is a grey body with an emissivity of 0.8 (-).



(a) Spectral distribution of emissivity for a black body, a grey body and a real body.



(b) Spectral distribution for different bodies at the same temperature.

Figure 2.9: Description of a real body.

## 2.9 Conclusion

In this section, an overview of the basic laws and quantities governing radiative heat transfer are provided. These fundamental equations are important for describing the complex nature of light-matter interactions for opaque materials. In this study, we seek to determine this complete radiation balance by determining **where, when and how** the laser energy spreads. This identification relies on thermal aspects for absorption and on optical means for reflection. These aspects are studied in the following chapter.

## Chapter 3

# Optical characterisation of a opaque metallic material over infrared wavelengths

### Table of Contents

---

<b>3.1</b>	<b>Context</b> . . . . .	<b>50</b>
<b>3.2</b>	<b>Introduction to BRDF measurement</b> . . . . .	<b>51</b>
<b>3.3</b>	<b>BRDFs in the IR spectral range</b> . . . . .	<b>52</b>
3.3.1	Devices for measuring BRDFs . . . . .	53
<b>3.4</b>	<b>Methods for characterising BRDFs</b> . . . . .	<b>54</b>
3.4.1	Experimental set-up . . . . .	54
3.4.2	Presentation of the studied samples and wavelength . . . . .	56
3.4.3	Qualitative BRDF acquisition and data processing . . . . .	57
3.4.4	Presentation of the collimation part of the set-up . . . . .	61
3.4.5	Optical path of the incident beam . . . . .	61
3.4.6	Optical path of the reflected beam . . . . .	65
<b>3.5</b>	<b>Set-up and method validation</b> . . . . .	<b>70</b>
<b>3.6</b>	<b>Analysis of the set-up, method capacities and limits</b> . . . . .	<b>73</b>
<b>3.7</b>	<b>Implementation of the multi-spectral BRDF measurement system</b> . . . . .	<b>74</b>
<b>3.8</b>	<b>Conclusions regarding infrared multi-spectral data based on qualitative BRDFs</b> . . . . .	<b>79</b>

---



### 3.1 Context

As seen in the preceding chapter and illustrated in Figure 3.1, when a continuous laser beam illuminates an opaque material, a part of the incident light is absorbed and turned into heat, and the remaining part is reflected. As both reflection and absorption are directly proportional to the incident light intensity or power, when high-power, lasers are used, the consequences for the sample can be extreme. The Bidirectional Reflectance Distribution Function (BRDF) is an essential measurement from an industrial point of view, as the dimensions of a laser weapon system and ocular safety during engagement can be predetermined. To ensure ocular safety, it is better to avoid specular reflections during laser engagement. This industry-related subject is one of the main motivations of the work presented in this chapter.

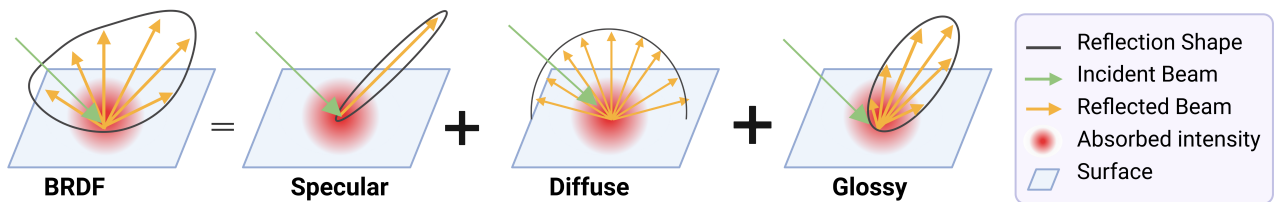


Figure 3.1: Schematic of specular, diffuse and glossy reflections.

When the wavelengths are greater than the surface roughness, the reflections are mainly specular [37]. As it is best to avoid specular reflections during laser engagement, this work is focused on pairing the roughness/wavelength transition of BRDF shapes from specular to non-specular reflections. According to the literature, this transition is expected when the wavelength is 5 to 10 times higher than the roughness. Measuring BRDFs requires the realisation of an experimental set-up for acquiring **multi-spectral BRDFs**. This **experimental set-up** utilises multi-spectral infrared sources, an infrared camera, an off-axis parabolic mirror (OAPM) and a monochromator. To observe this behaviour, the wavelength range of interest is  $2.5 \mu m$  to  $5.5 \mu m$ , and the sample surface roughness ranges from  $0.05 \mu m$  to  $1.6 \mu m$ .

Here, the dynamic behaviour for BRDFs in the mid-infrared range is measured through two different studies. The first is an attempt to measure the BRDF on static samples with multiple standard roughnesses at different wavelengths. Towards this goal, the complete set-up is introduced, as well as the development method, and then the results are shown. The second is an attempt to

measure the dynamic BRDF on an industrial sample when illuminated with a continuous laser on the kW scale. This topic is developed in Chapter 6.

## 3.2 Introduction to BRDF measurement

Identifying the BRDFs of opaque materials in IR is a subject that has attracted the interest of the scientific community for seventy years. For example, nearly 600 publications with both keywords "BRDF" and "infrared" since 1950 can be counted on Google Scholar, and 209 publications can be counted when the third keyword "roughness" is added. Among all the publications on BRDF in IR, none are available in open-access databases, in stark contrast to BRDF databases in the visible light domain that are very common and accessible (i.e., the MERL BRDF or UTIA BTF database). One possible explanation is that a portion of BRDF studies have been conducted by military research laboratories [38, 39, 40, 41].

BRDFs illustrate the probability that light from an incident direction ( $\vec{\omega}_i$ ) is reflected to another given direction ( $\vec{\omega}_r$ ). Defined by Nicodemus [42], the BRDF noted  $\rho''$  ( $sr^{-1}$ ) is given for a specific wavelength as the ratio between the reflected radiance  $L_r$  ( $W \cdot m^{-2} \cdot sr^{-1}$ ) in a given direction  $\vec{\omega}_r$  to the incident irradiance  $E_i$  ( $W \cdot m^{-2}$ ) in another direction  $\vec{\omega}_i$  (see Eq. 3.1) and is expressed in steradian<sup>-1</sup>.

$$\rho''(\vec{\omega}_r|\vec{\omega}_i, \lambda) = \frac{dL_r}{dE_i} \quad (3.1)$$

Both directions are unitary vectors defined by polar ( $\theta$ ) and azimuthal ( $\phi$ ) angles, as illustrated in Figure 3.2, where  $d\omega$  represents the solid angle. Additionally, the indices  $i$  and  $r$  specify the incident and reflected directions, respectively. Finally,  $dS$  is the elementary surface.

The radiance ( $L_r$ ) is the radiant flux (or power)  $P$  emitted by the surface per unit of solid angle  $\Omega$  and per unit of the projected area  $dA$  and is expressed in  $W^{-1} \cdot sr^{-1} \cdot m^{-2}$ .

$$L = \frac{d^2P}{\cos\theta \cdot dA \cdot d\Omega_r} \quad (3.2)$$

where  $\Omega_r$  is the solid angle expressed in steradians ( $sr$ ). The solid angle corresponds to a tridimensional angle. One standard SI measure is defined as the solid angle of a sphere subtended by a portion of the surface ( $dA$ ) whose area is equal to the square of the sphere's radius ( $r$ , Britannica definition); see

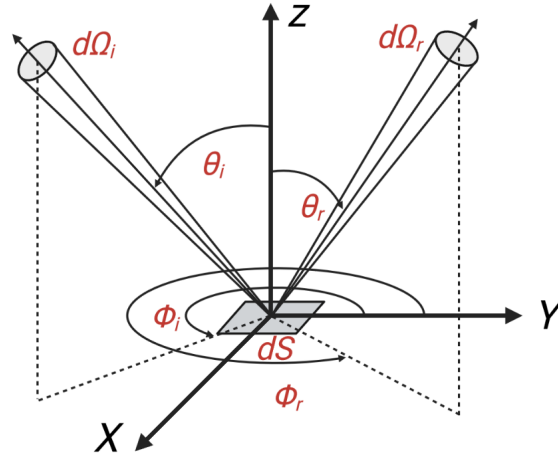


Figure 3.2: Geometrical definition of a BRDF angle and its associated coordinates.

Eq. 3.3.

$$d\Omega_r = \frac{dA}{r^2} \quad (3.3)$$

The irradiance ( $E_i$ ) is the radiant flux received by a surface per unit area, expressed in  $W^{-1} \cdot m^{-2}$ .

$$E = \frac{dP}{dA} \quad (3.4)$$

### 3.3 BRDFs in the IR spectral range

In 1981, S. Smith [38] studied BRDFs of two black coatings in the far-infrared [10-350  $\mu m$ ], concluding that the amplitude and specularity of the BRDF increases with increasing wavelength. Ten years later, R. Young and B. Wood provided IR BRDF data (2.25-5.25  $\mu m$ ) of NASA space shuttle tiles [43]. U. Oppenheim et al. [44] developed BRDF reference standards in the IR spectrum and characterised diffuse materials such as sulphur, gold-coated sandpaper and gold surfaces at  $\lambda=10.6 \mu m$ . That study shed light on the back-scattering behaviour of a surface and its impact on BRDFs. In 1998, D. White et al. [45] explored BRDFs in the near infrared domain (NIR) at 0.84  $\mu m$  on reformer catalyst tubes. The associated opaque material is a complex alloy of metals (chromium, nickel, carbon, silicon, etc.) for specific industrial applications. That study revealed the interesting fact that when the light source is a laser beam, the laser speckle patterns make the BRDF's signal-to-noise ratio (SNR) increase. S.

### 3.3. BRDFS IN THE IR SPECTRAL RANGE

---

Sandmeier conducted a hyper-spectral study in both visible and broad IR domains for soils and grass [46]. The thesis of M. Proctor [40] (USAF Institute of Technology) described device optimisation for multi-spectral BRDFs measurements to create an IR BRDF database for target recognition on battlefields. This very ambitious project was the first to promote the creation of such a database; however, the data were never publicly published. Z. Zhao et al. proposed a multi-spectral BRDF measurement system design that could be used from the visible range to  $10.5 \mu m$  [47]. In 2009, B. Balling realised a comparative study of BRDFs in the MWIR domain on Spectralon standards [48]. The results are helpful to validate measurements of a BRDF acquisition set-up, but the author investigated only those reference cases and unfortunately did not publish any BRDF characterisation results with the developed test bench.

This literature review highlights that despite the existing knowledge, there is a lack of BRDF characterisation in the IR range for opaque materials. The literature on measurement designs is quite rich and provides many methods for measuring BRDFs as well as possible avenues for innovation. Some studies have provided valuable BRDF data for common opaque materials. To conclude, the field of BRDFs in the IR range still has many opportunities for expansion, which is one of the main motivations for this chapter.

#### 3.3.1 Devices for measuring BRDFs

The common device for measuring BRDFs is the gonireflectometer, which has the ability to move the light source and the detector over the hemisphere. Gonireflectometers are a convenient tool used in the majority of publications on experimental BRDFs, whether for laboratory use [45, 49, 50, 51, 52] or outdoor field applications [39, 46].

A gonireflectometer is characterised by a high angular resolution and large angle range that allow the production of accurate and complete BRDF measurements. One major drawback of gonireflectometers is the tedious method of data acquisition, as the whole hemisphere must be scanned step by step. The gonireflectometer size can reach 2-3 m, making laboratory implementation complex. More innovative designs for BRDF measurements have been realised, such as the kaleidoscopic imaging system developed by J. Han [5], which has the capacity to image the whole hemisphere at once. The acquisition time is then faster than it would be for a gonireflectometer device. The implementation is also simpler, as it requires no moving parts. However, the extraction and data processing from a

### 3.4. METHODS FOR CHARACTERISING BRDFS

---

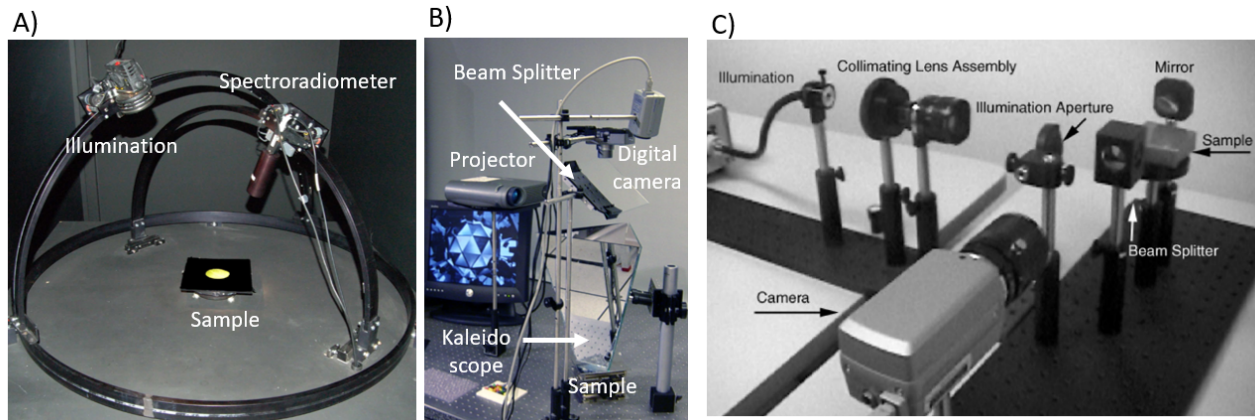


Figure 3.3: Illustration of the bases for BRDF experimental measurement: (a) goniometer [4], (b) kaleidoscope [5] and (c) off-axis parabolic mirror [6].

single image is complex, and the spatial resolution is lower than that of gonioreflectometers. Another way to measure the BRDF was proposed by K. Dana [6], who used an Off-Axis Parabolic Mirror (OAPM) to image the reflections originating from a single point of the sample's surface. The mirror captures rays over polar angles that depend on its dimensions. This method permits the acquisition of reflections in all directions over the mirror's polar angle for a single image. A drawback of this technique is that the original creator did not show clear BRDF measurement results aside from the spatial exploration of textured samples. Thus, BRDF measurement is still an open research topic, motivating the current project.

## 3.4 Methods for characterising BRDFs

### 3.4.1 Experimental set-up

The laboratory is equipped with an IR camera; therefore, the set-up proposed by K. Dana [6] is adopted. The wavelength spectral range searched is from  $2.5 \mu\text{m}$  to  $12 \mu\text{m}$ , and the angle range of reflected light captured is half of the hemisphere.

The importance of OAPMs in the field of surface BRDF measurement has been demonstrated by K. Dana et al. As illustrated in Figure 3.4, a collimated beam passes through the focal point of the OAPM. On the other hand, any ray produced from a point source at the focal point of the OAPM is collimated by the mirror

### 3.4. METHODS FOR CHARACTERISING BRDFS

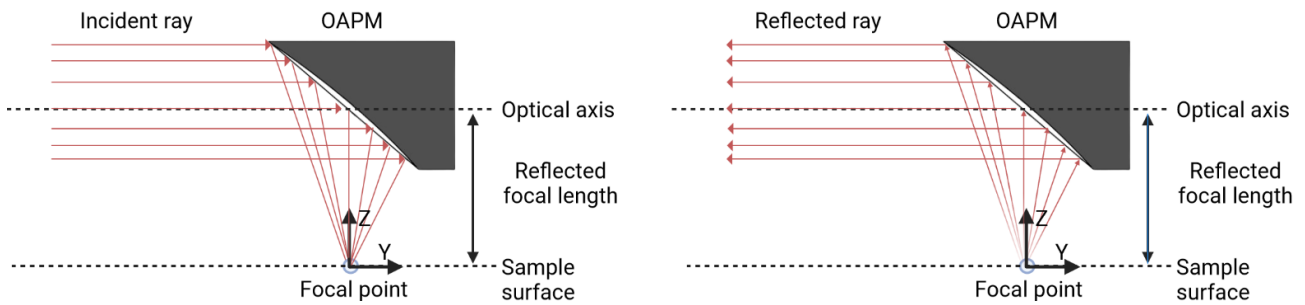


Figure 3.4: Schematic showing the OAPM's focusing property.

By aligning the sample's surface to the focal point of the OAPM, the reflection measured from each point of the OAPM's surface can theoretically be associated with the reflected direction. By doing so, the BRDF measurement can be acquired.

As illustrated in Figure 3.5, the OAPM concept is included in the complete set-up developed by C. Pradere & al. [17]. The set-up is composed of the following:

- (1) a single monochromator (TMc300 Bentham) that offers a large spectral range with precise scanning possibilities coupled with a halogen-SiN (ILD-QH-IR Bentham) light source equipped with an IR emitter that radiates from over the entire spectrum of interest,
- (2) a beam shutter,
- (3) multiple OAPMs for the collimation stage and for the BRDF measurement. For the BRDFs, the mirror used to fulfil this role is a  $90^\circ$  silver-coated OAPM from Edmunds Optics with an effective focal length of 50.8 mm and a diameter of 76.2 mm,
- (4) multiple optical apertures,
- (5) a silicon wafer (where both reflectance and transmittance are nearly 50%) of 10.54 mm diameter and 0.985 mm thickness,
- (7) an optical lens (focal length: 100 mm, diameter: 100 mm) to image the OAPM, and
- (8) a camera (model SC7000) with an InSb sensor ( $2.5 \mu\text{m} - 5.5 \mu\text{m}$ ) with a pixel area of  $320 \times 256$ , a pitch of  $30 \mu\text{m}$ , a frame rate of 100 Hz and an integration time of 1900  $\mu\text{s}$ .

### 3.4. METHODS FOR CHARACTERISING BRDFS

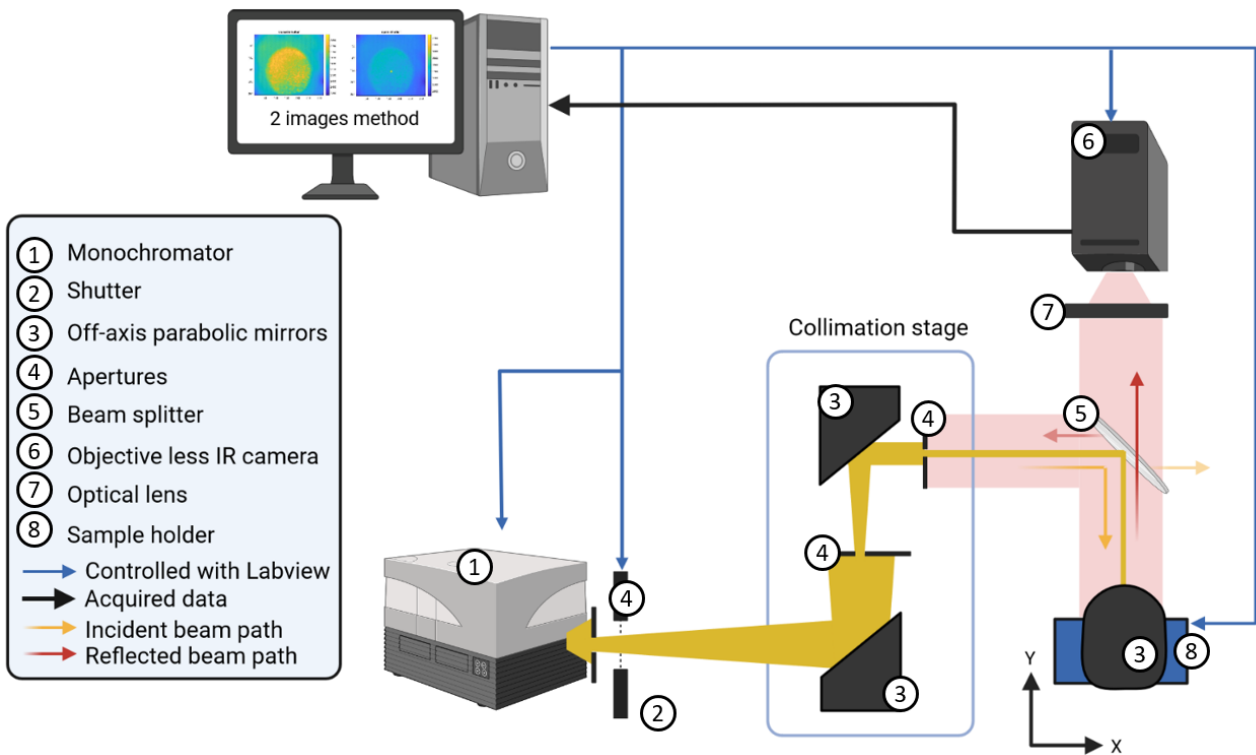


Figure 3.5: Schematic of the experimental set-up - XY view.

During the measurements with the set-up (Figure 3.5), there are three key points to consider to ensure good results. First, the sample's surface must be on the same geometrical plane as the OAPM's focal plane. Second, the incident beam must be collimated. Finally, one has to image the reflected collimated beam with the same diameter as the OAPM.

#### 3.4.2 Presentation of the studied samples and wavelength

To choose the sample of interest, it is important to examine the surface conditions. In this study, a common material used in industry and a manufacturing process are chosen. To describe the surface condition, multiple surface roughnesses are obtained with the same process. A common parameter used to describe the surface condition is the average profile height deviation from the mean line, denoted by  $Ra$  (Figure 3.6.a). Industrial grinding is used to obtain the necessary surface roughness by removing material from a workpiece with a grinding wheel (Figure 3.6.b)

The samples studied to explore the dependence of surface roughness towards the acquired BRDF are a set of roughness standard specimens - No. 130 by Rubert & Co. Ltd. In this study, 6 aluminium



### 3.4. METHODS FOR CHARACTERISING BRDFS

---

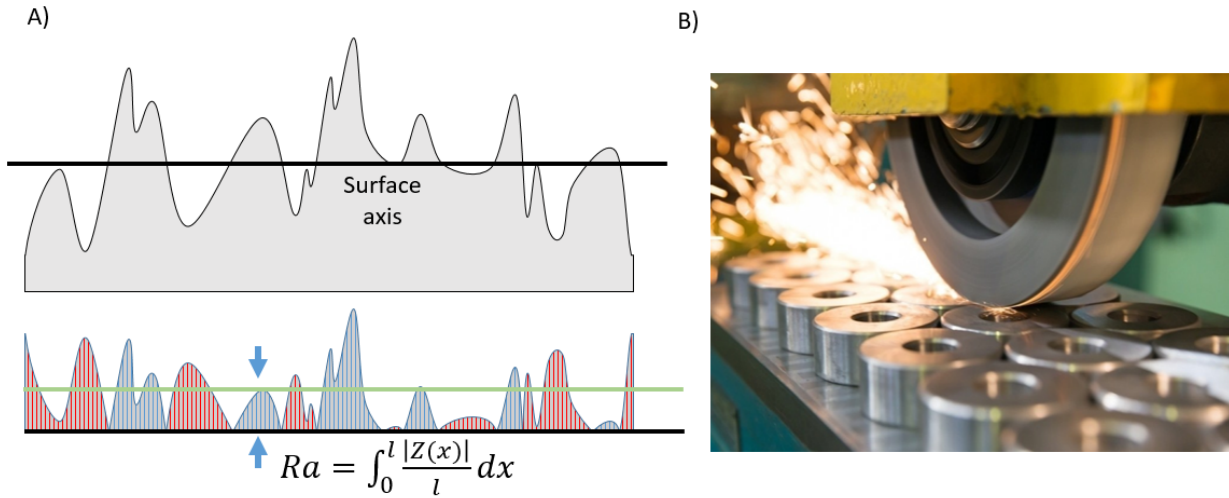


Figure 3.6: Description of the surface condition: (a) definition of the surface roughness and (b) illustration of the grinding process (image from the company Luxalp).

samples with different surface roughnesses are studied:  $[0.05, 0.1, 0.2, 0.4, 0.8, 1.6] \mu m$ . Each sample is studied at wavelengths between  $3 \mu m$  and  $5.5 \mu m$ . The specimens are numbered from 1 to 6, corresponding to low to high roughness.

The surface topography for each sample is measured with a ZEISS laser scanning confocal microscope LSM 900 (made available by ALPhANOV) on a surface of  $550\mu m \times 475\mu m$ .

This chapter presents the results for sample 4 (Figure 3.7), and the rest can be found in Appendix A. The surface topography is orthotropic with a preferred direction of peaks and valleys along the x-axis, whereas there is little variation along the y-axis. This is attributed to the orientation of the grinding wheel during the machining process. Due to the repetitive surface pattern, the area surveyed can be considered representative of the surface. Based on this measurement, one can assume that the BRDFs of these samples has a preferred direction of reflection.

#### 3.4.3 Qualitative BRDF acquisition and data processing

Figure 3.8 shows the data acquisition process. First, the sample, wavelength and camera settings are chosen. Then, the sample is placed on the holder at the OAPM focal plane; to do so, the holder is placed on a micrometric translation plate. MATLAB is used to drive the camera acquisition and settings, and LabView is used in parallel to control the monochromator.

In this study, the incident beam is fixed normal to the sample. The camera has an integration



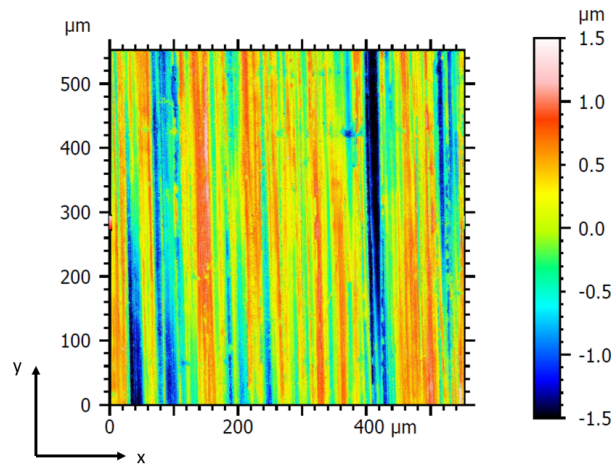


Figure 3.7: Measured sample 4 surface topography.

times of  $2000 \mu\text{s}$ . Then, the captured images are averaged over 500 frames to remove noise from the measurements. The acquisition and averaging take approximately 6 s. The resulting image contains more than 57000 useful pixels corresponding to the same number of reflected directions for each wavelength. Once images are captured over the entire wavelength range, the chopper is closed to acquire a background image.

Fundamentally, the BRDF is the ratio between the reflected intensity and incident beam (see Eq. 3.1). This ratio changes for each reflected direction. However, it is challenging to capture the incident beam; therefore, it is ignored in this study, and the acquired BRDFs are normalised by the maximum to obtain this ratio. By doing so, the resulting BRDFs can be considered only **relative or qualitative**.

The data processing is presented in Figure 3.9. First, all of the data are loaded and then averaged. Then, the background is subtracted for all measurements. Concurrent with the data processing, the user determines the centre of the OAPM, enabling computation of the pixel size, the coordinates of each pixel in the real space, the pixel position on the polar coordinate system and the corresponding solid angle of each pixel. Next, the background is subtracted from the image, and the outcome is then divided by the solid angle field. The resulting image is normalised by the maximum value. Finally, the qualitatively measured BRDF can be visualised.

### 3.4. METHODS FOR CHARACTERISING BRDFS

---

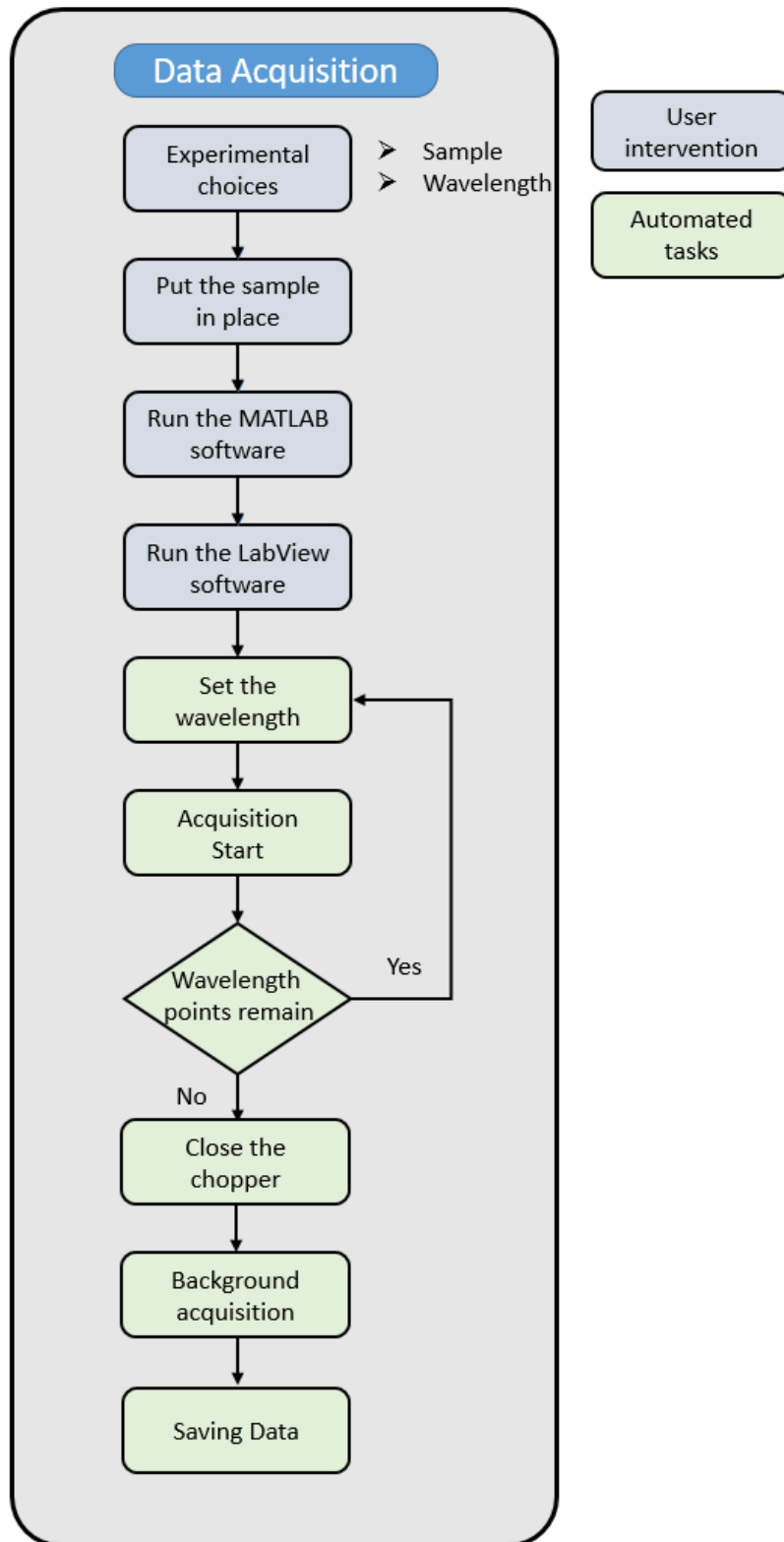


Figure 3.8: Representation of BRDF acquisition.

### 3.4. METHODS FOR CHARACTERISING BRDFS

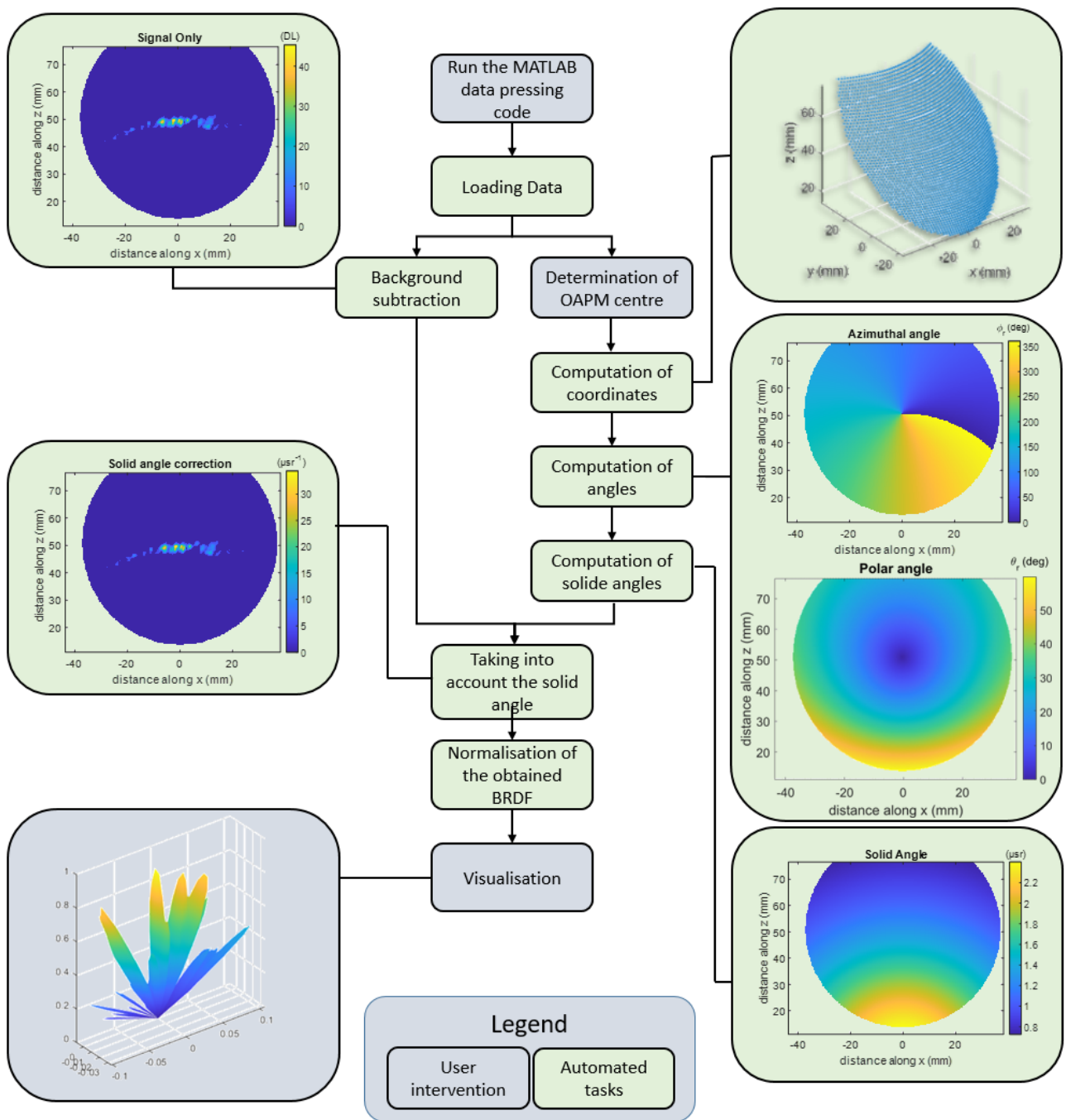


Figure 3.9: BRDF acquisition flowchart with images captured at their corresponding steps.

### 3.4.4 Presentation of the collimation part of the set-up

The light beam coming from the monochromator is divergent; therefore, a collimation stage has to be implemented (see Figure 3.5). This stage is composed of two OAPMs (50329AU and 50331AU from Newport) and two apertures to optimise the beam shape. The first OAPM is implemented to image the beam on an optical plane. A keyhole optical aperture is placed on this optical plane to attenuate a portion of the beam that does not pass through the keyhole. The second OAPM has its focal plane superimposed on the centre of the first aperture. This combination collimates the incident beam. Finally, another optical aperture is used to adjust the beam diameter (see Figure 3.10). This optical assembly creates a circular beam with low divergence (no visible divergence over 5 *m*). The diameter of the beam leaving the collimation stage is 3 *mm*.

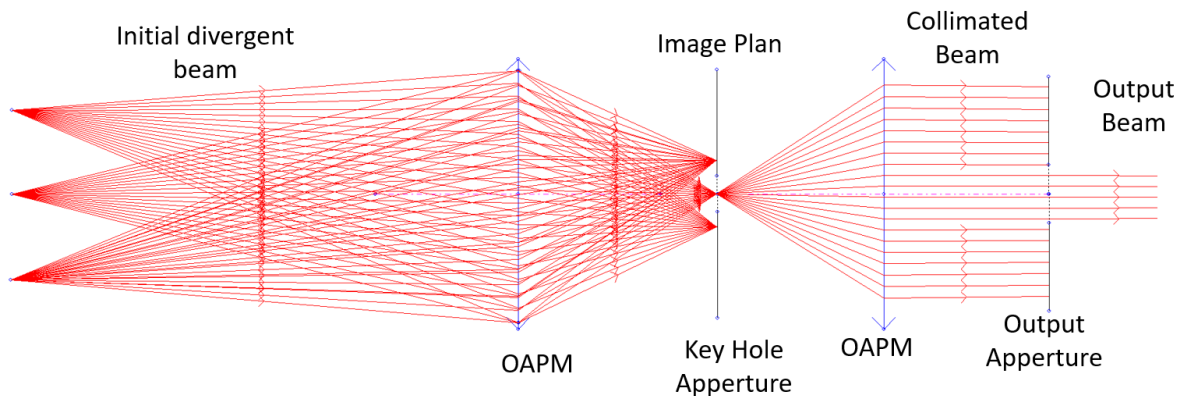


Figure 3.10: Optical schema of the collimation optical assembly.

One must note that the collimation stage is composed only of mirrors. Thus, no chromatic aberration occurs during the wavelength scan. Moreover, the presence of the two apertures used induces a loss in the signal intensity. Although this loss can be problematic over some wavelengths, the described configuration is the best solution available.

### 3.4.5 Optical path of the incident beam

The OAPM constitutes a portion of a parent parabolic mirror. It is defined by two focal lengths: the parent focal length ( $F_p$ ) pertaining to the parent parabola and the effective focal length  $F_e$  pertaining to the OAPM itself. OAPMs are also defined by the off-axis angle, meaning the angle between the incident beam that passes through the optical axis and the reflected beam. For 90° OAPMs (36 - 595

### 3.4. METHODS FOR CHARACTERISING BRDFS

from Edmund Optics), such as the one used in this study,  $F_p$  is equal to half  $F_e$  ( $F_p = \frac{F_e}{2} = 25.4 \text{ mm}$ ). The silver coating of the surface allows near-perfect reflection (96-97%) over the  $0.45 \mu\text{m}$  to  $20 \mu\text{m}$  wavelength range. Figure 3.11 illustrates the incident beam path and its properties.

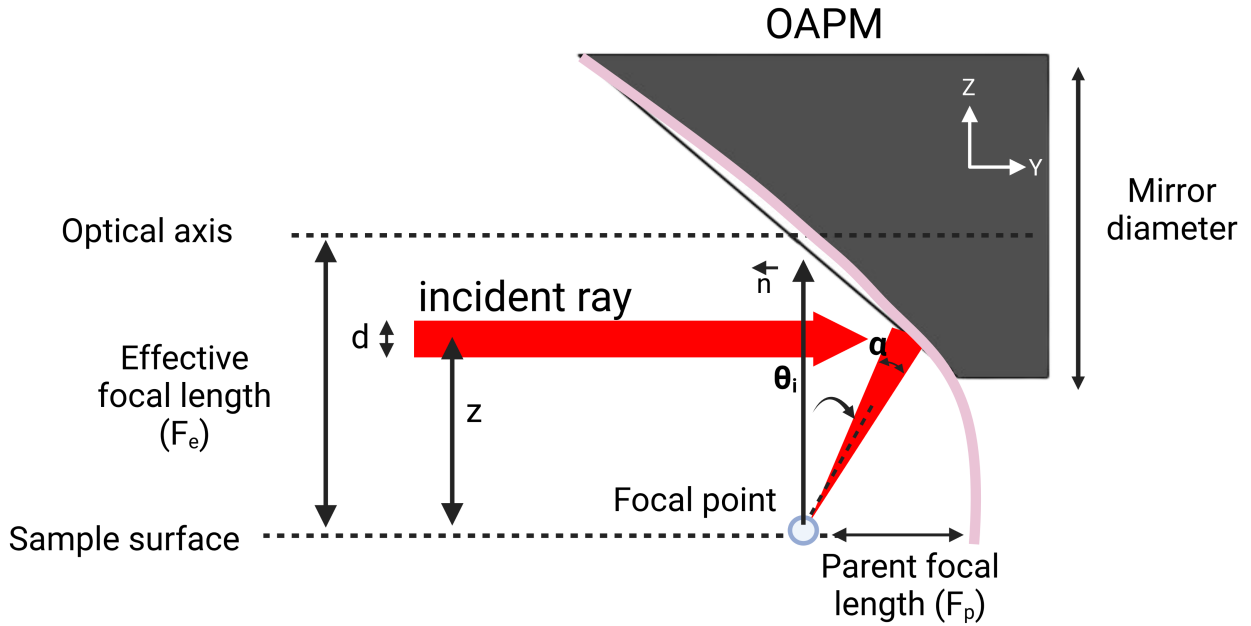


Figure 3.11: Scheme of the OAPM:  $F_e = 50.8 \text{ mm}$ ,  $F_p = 25.4 \text{ mm}$ , and the mirror diameter is  $76.2 \text{ mm}$ .

The equation of the mirror surface is given in Eq. 3.5.

$$y + F_p = \frac{z^2 + x^2}{4F_p} \quad (3.5)$$

where  $x$ ,  $y$  and  $z$  are the spatial coordinates (m). Based on this equation, the OAPM diameter (Figure 3.11),  $F_e$  and  $F_p$ , it is possible to compute the surface point of the mirror as described in Figure 3.12

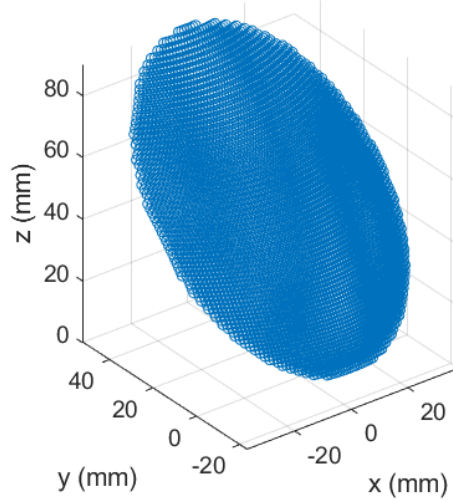


Figure 3.12: Description of the mirror surface points.

The effective focal length and the diameter of the OAPM are the two parameters that define the range of reflectance angles that can be redirected by the mirror itself. Based on the beam position on the mirror, Eqs. 3.6 and 3.7 respectively give the polar and azimuthal angles of the incident direction (Figure 3.2).

$$\theta = \cos^{-1} \left( \frac{z}{\sqrt{x^2 + y^2 + z^2}} \right) \quad (3.6)$$

$$\phi = \cos^{-1} \left( \frac{x}{\sqrt{x^2 + y^2}} \right) \quad (3.7)$$

Based on those equations,  $\theta$  and  $\phi$  can be computed for every point of the mirror's surface, as shown in Figure 3.13.

The beam diameter is approximately 3 mm ( $d = 3 \text{ mm}$  in Figure 3.11) and impinges on the centre of the mirror to ensure normal illumination. Thus, one can compute the aperture angle (denoted by  $\alpha$  in Figure 3.11) as described in Eq. 3.8.

$$\alpha(z, d) = \arctan \left[ \frac{z - d/2}{\frac{(z-d/2)^2}{4F_p} - F_p} \right] - \arctan \left[ \frac{z + d/2}{\frac{(z+d/2)^2}{4F_p} - F_p} \right] \quad (3.8)$$

Figure 3.14 shows the aperture angle as a function of the  $z$  coordinate for a beam diameter of 3

### 3.4. METHODS FOR CHARACTERISING BRDFS

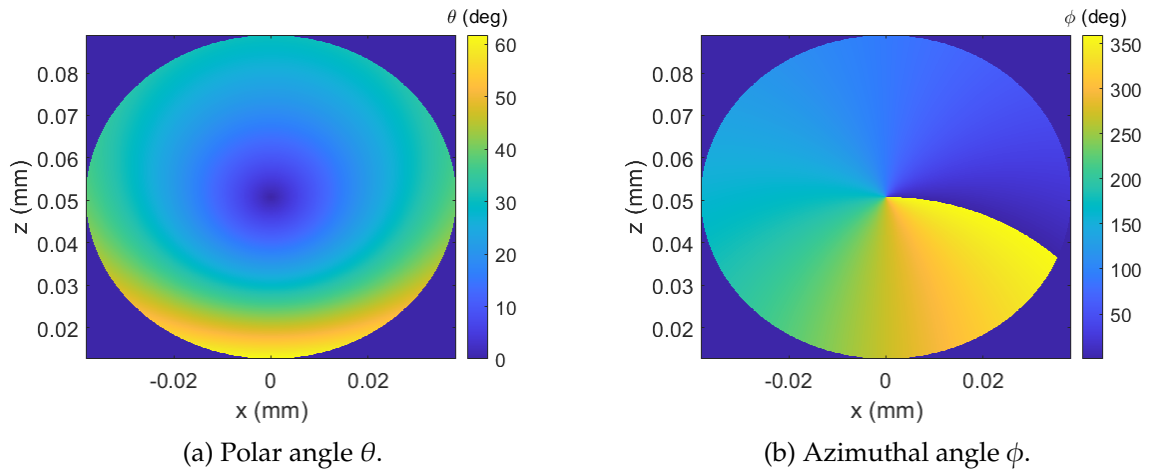


Figure 3.13: Theoretical OAPM corresponding angle.

mm. Note that for the specific case of **normal incidence** ( $z = F_e$ ) used in this study, the aperture angle is  $\alpha(z = F_e, d = 3) = 3.4^\circ$ .

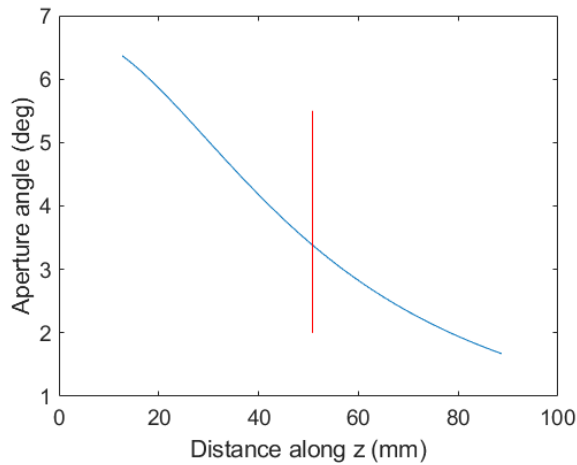


Figure 3.14: Schematic of the OAPM's ( $F_e=50.8$  mm and  $d=76.2$  mm) cross section and the maximum angle.

To conclude, based on this section and the location  $(x,y,z)$  of the incident beam on the OAPM, one can compute the polar and azimuthal angles of the incident direction as well as the aperture angle of the incident beam.

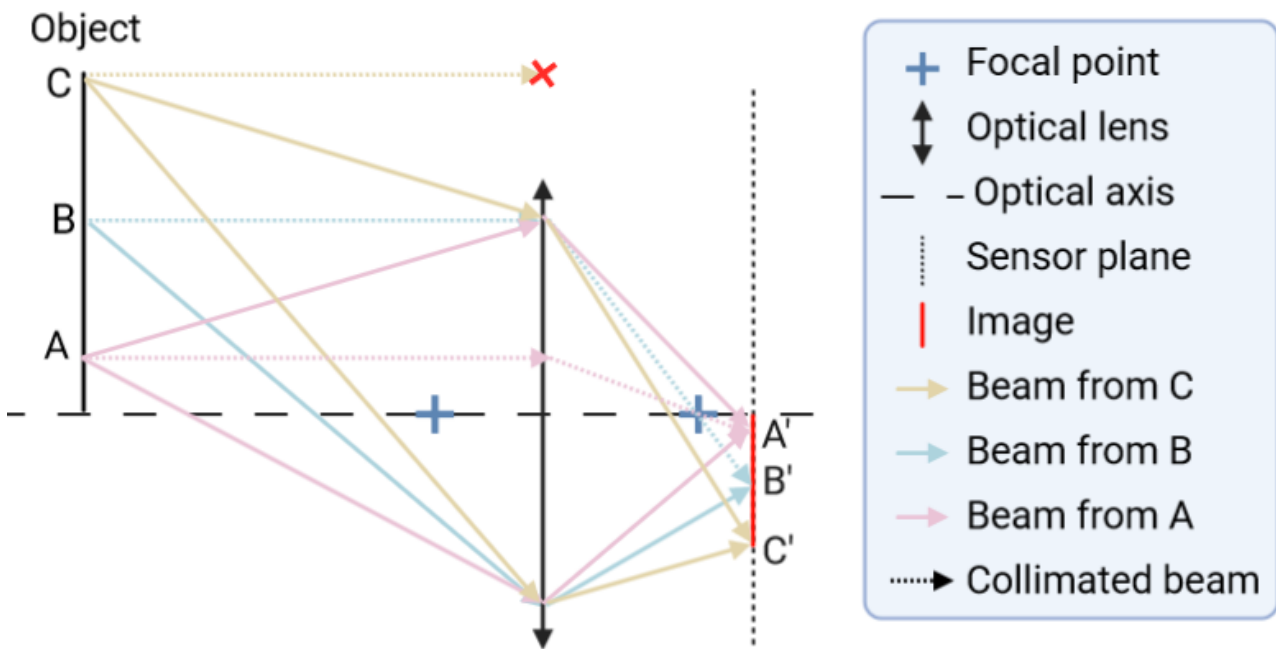


Figure 3.15: Schematic of the imaging system.

### 3.4.6 Optical path of the reflected beam

#### 3.4.6.1 Imaging system

To image the reflected collimated beam with the same diameter as the OAPM, K. Dana et al. used a telecentric objective (orthographic lens). Unfortunately, this kind of objective is not available in the IR domain, so another solution must be found. A classic camera objective can be assimilated to a lens with a given diameter and focal length, as described in Figure 3.15. Here, points A, B and C of the object are imaged by the sensor. Nevertheless, this allows imaging of the collimated beam of points A and B only. To image the entire collimated beam leaving the OAPM, the commercial objective of the camera is replaced by a 100 mm lens, which is larger than the OAPM's diameter.

#### 3.4.6.2 From pixel-based images to BRDF images

##### Calculating pixel coordinates in real space

Now that all of the collimated beam leaving the OAPM is imaged, all pixels must be associated with their respective polar and azimuthal angles. First, the centre of the OAPM must be identified. A simple way to do this is to fit an inscribed rectangle to the boundary of the OAPM circle. The point



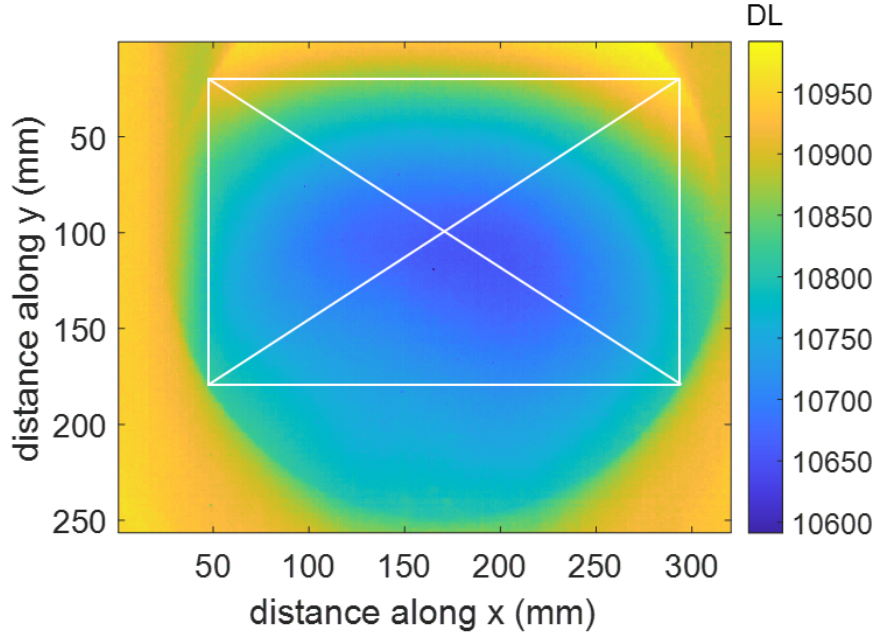


Figure 3.16: Identifying the position of the OAPM centre. The centre of the white box corresponds to the centre of the OAPM.

where the diagonals of the rectangle are coincident is taken as the centre of the mirror ( $C_x, C_y$ ). This step also allows the size of each pixel (denoted  $p$ ) to be identified by dividing the length in pixels of both diagonals by the mirror's diameter.

The focus is aligned to the centre of the OAPM ( $y=0$ ), where the depth of focus seems sufficient for imaging the entire OAPM. Figure 3.16 shows an experimental image taken with the set-up, illustrating that the top of the OAPM extends past the limits of the image.

From our calculations, this yields a pixel size of  $p \approx 0.23 \text{ mm}$ , and the centre is located at the following coordinates:  $C_x = 102$  pixels and  $C_y = 170$  pixels.

Based on the extracted mirror centre and pixel size, the image coordinates ( $x_p$  and  $y_p$ ) can be converted to real 3D coordinates ( $x$ ,  $y$  and  $z$ ):  $x_p$  is first matched to its  $x$  coordinate through Eq. 3.9, and then Eq. 3.10 is used to match  $y_p$  to  $z$ . Finally, based on  $x$ ,  $z$  and Eq. 3.5, the corresponding  $y$  is computed. In this way, the 3D coordinates are determined.

$$x = (x_p - C_x) \times p \quad (3.9)$$

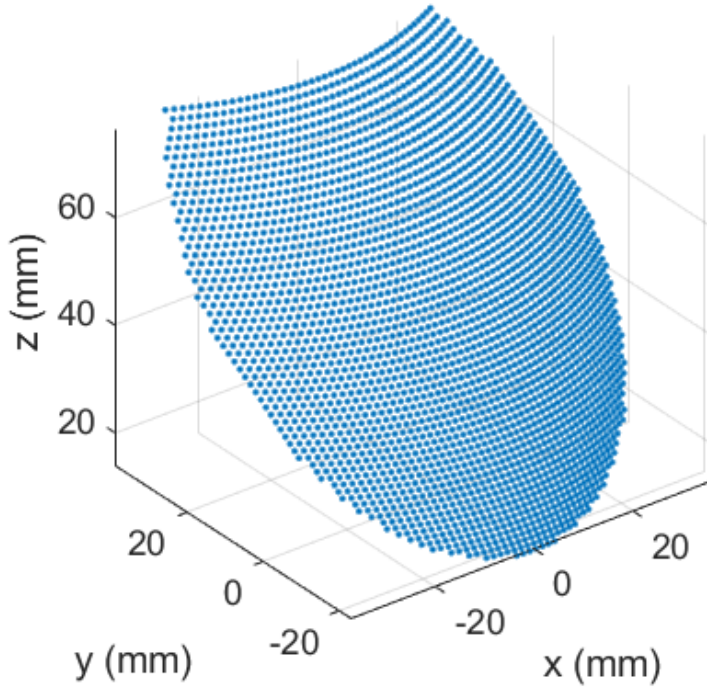


Figure 3.17: Computed pixel coordinates  $\theta$ .

$$z = (y_p - C_y) \times p + F_e \quad (3.10)$$

Figure 3.17 illustrates the coordinates of each pixel in the 3D spatial coordinates ( $x$ ,  $y$  and  $z$ ).

**Calculating the corresponding polar and azimuthal angles of reflection ( $\theta_r$  and  $\phi_r$ )**

Once the coordinates of each pixel have been computed, it is possible to match each pixel to the reflected beam's polar ( $\theta_r$ ) and azimuthal ( $\phi_r$ ) angles (Eqs. 3.6 and 3.7, respectively), illustrated as follows.

**Calculating the corresponding solid angle**

In contrast to goniometer measurements, where the reflected solid angle is constant for all measurements regardless of the sensor's position, the solid angle is not constant for our dedicated set-up. The solid angle definition defined in Eq. 3.3 is revisited in Eq. 3.11. Thus, one has to determine the surface area ( $dA : m^2$ ) of each pixel onto the OAPM and the radius ( $r : m$ ) between the focal point of the OAPM and its 3D pixel location. This is expressed in Eq. 3.12.

### 3.4. METHODS FOR CHARACTERISING BRDFS

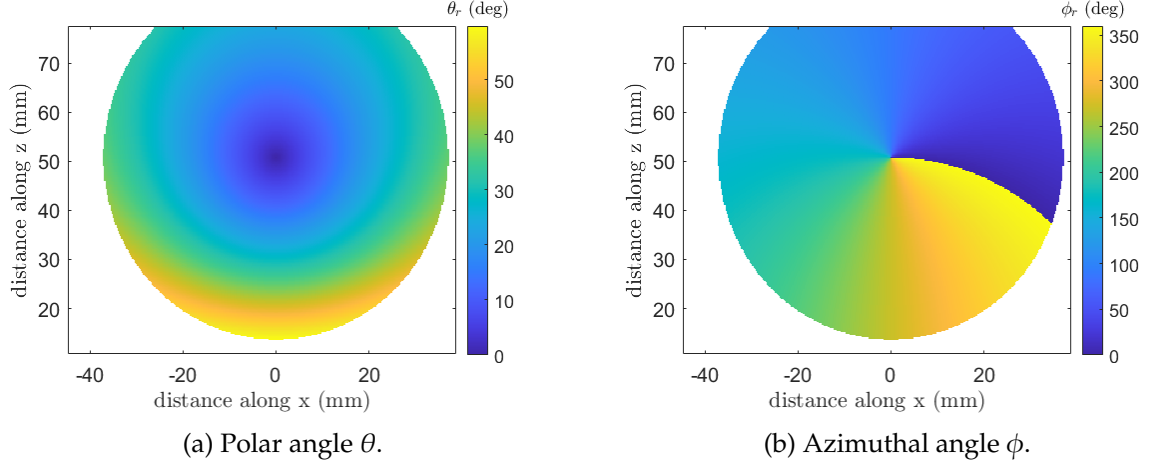


Figure 3.18: Reconstruction of the mirror in real space from the images.

$$d\Omega_r = \frac{dA}{r^2} \quad (3.11)$$

$$r = \sqrt{x^2 + y^2 + z^2} \quad (3.12)$$

The area is slightly more cumbersome to compute. The coordinates of each pixel vertex ( $x_1, x_2, x_3$  and  $x_4$ ) are computed based on their centre coordinates ( $x_i$ ) and the pixel size. Then, the area is computed by dividing this 4-sided polygon into 2 triangles (Figure 3.19), for which the area is the determinant of the matrix coordinates described in the following equation.

$$A_i = \frac{1}{2} \det \begin{Bmatrix} x_1 & y_1 & z_1 \\ x_2 & y_2 & z_2 \\ x_3 & y_3 & z_3 \end{Bmatrix} + \frac{1}{2} \det \begin{Bmatrix} x_2 & y_2 & z_2 \\ x_3 & y_3 & z_3 \\ x_4 & y_4 & z_4 \end{Bmatrix} \quad (3.13)$$

where:

$$\begin{array}{l|l|l} x_1 = x_i + p/2 & z_1 = z_i + p/2 & y_1 = f(x_1, z_1) \\ x_2 = x_i + p/2 & z_2 = z_i - p/2 & y_2 = f(x_2, z_2) \\ x_3 = x_i - p/2 & z_3 = z_i + p/2 & y_3 = f(x_3, z_3) \\ x_4 = x_i - p/2 & z_4 = z_i - p/2 & y_4 = f(x_4, z_4) \end{array}$$

Figure 3.20 shows the result of the computed solid angle for the entire mirror.

### 3.4. METHODS FOR CHARACTERISING BRDFS

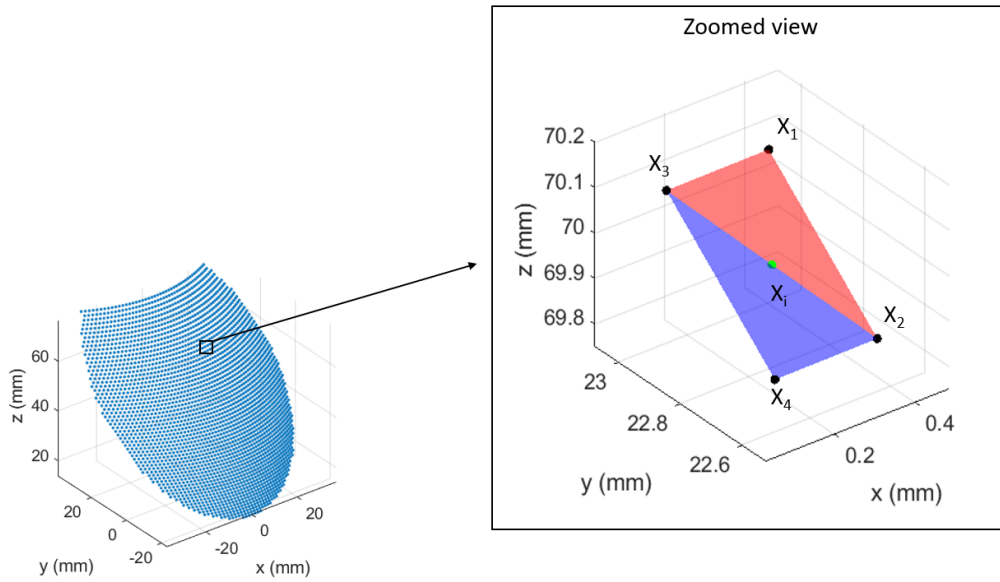


Figure 3.19: Computation of the pixel vertex and pixel area.

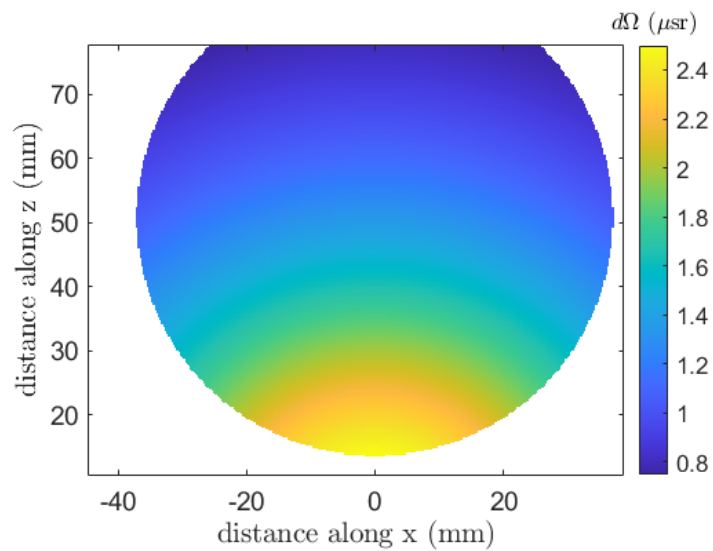


Figure 3.20: Evolution of the solid angle along the OAPM.

### 3.5 Set-up and method validation

To validate the set-up, two samples are used. The first is a mirror whose spatially reflected energy repartition must be perfectly specular. The second is an Infragold-LF® manufactured by Labsphere with reflections close to those of a Lambertian body at 10  $\mu\text{m}$ . The measurements are acquired at 4500 nm. Both theoretical BRDFs are represented in Figure 3.21.

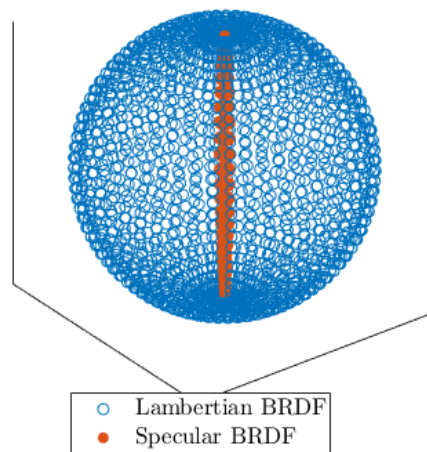


Figure 3.21: Theoretical Lambertian and specular BRDFs.

Figure 3.22a shows the normalised image obtained with the mirror after background subtraction. Two important points can be highlighted:

- The reflected beam is at the centre of the mirror, meaning that the alignment of the optical illumination is correct. Therefore, the illumination and the reflection are considered normal to the surface.
- By considering the specular reflection of the mirror, the correct optical alignment of the set-up and the reversibility of the optical path (Figure 3.4), one can conclude that the obtained image represents a direct observation of the illumination beam.

Based on this measurement, the polar angle ( $\theta_r$ ), the azimuthal angle ( $\phi_r$ ) and the computation of the solid angle, it is possible to compute the normalised BRDF. Figure 3.22b shows the projection

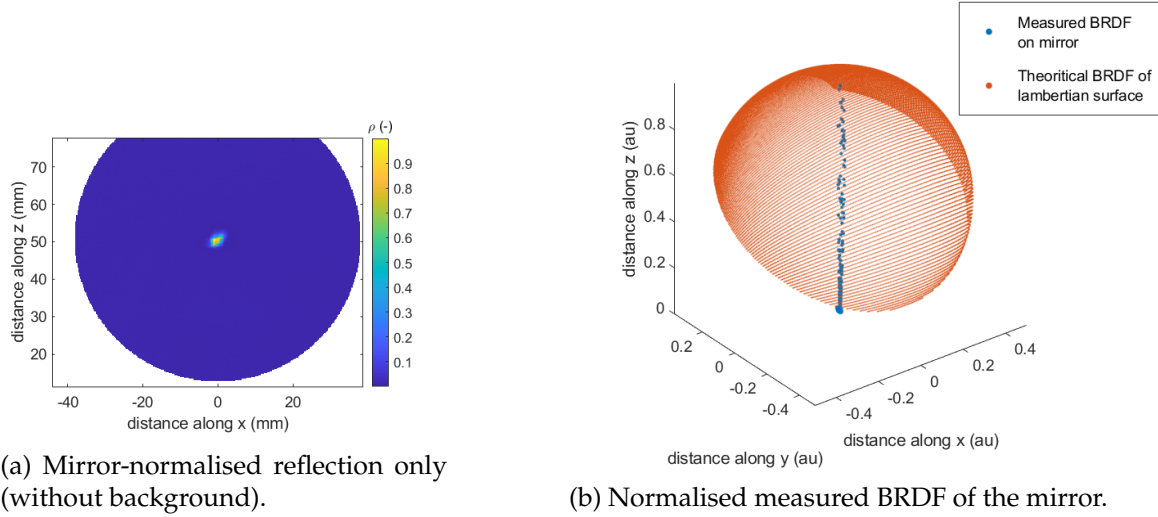


Figure 3.22: Validation on the mirror.

of the measured mirror’s normalised BRDF in comparison to the theoretical BRDF of a Lambertian surface over the same azimuthal and polar angles. The repartition of the measured bidirectional reflectance can be seen as similar to a spatial Dirac distribution, as expected.

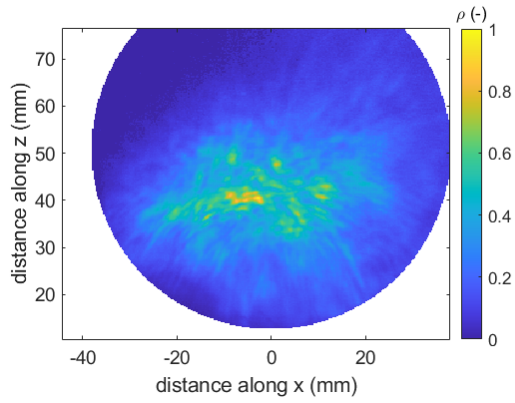
Figure 3.23a shows the normalised image obtained for the Infragold after background subtraction; the reflections are more complicated than those of the mirror. K. Dana et al. showed that the intensity measured on the OAPM is proportional to the solid angle (see Figure 3.23b). Comparing Figures 3.23a and 3.23b, the Infragold case is clearly different from Dana et al.’s sample (which is made of chalk). This is attributed to Infragold’s Lambertian aspect being measured at a wavelength of  $10 \mu\text{m}$ , which deviates from the measurement acquired here ( $4.5 \mu\text{m}$ ).

Projections of the normalised BRDFs compared to the theoretical BRDFs of a Lambertian surface over the same azimuthal and polar angles are presented in Figure 3.24.

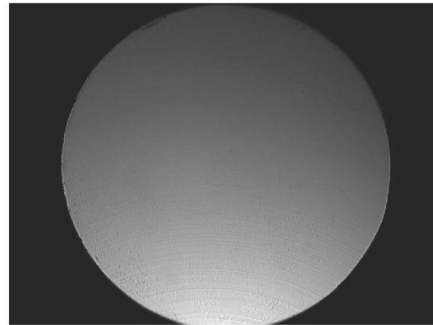
While the validation at this stage is not performed with a perfect Lambertian body, preliminary evaluation of the set-up shows good results for both cases, enabling the study to proceed.

### 3.5. SET-UP AND METHOD VALIDATION

---



(a) Infragold normalised reflection only.



(b) Camera image of the Lambertian body as reported by [6].

Figure 3.23: Partial validation on the Infragold.

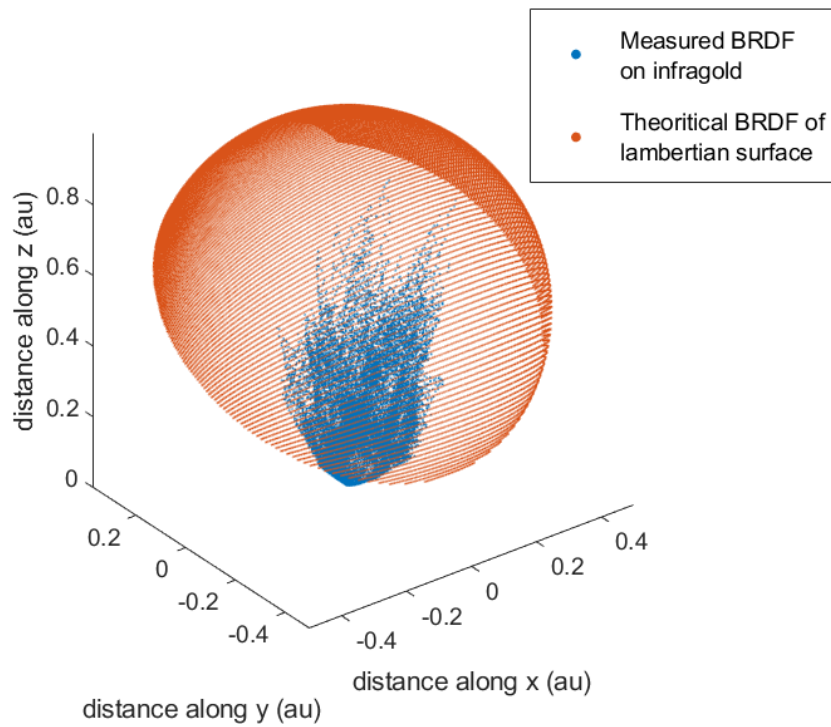


Figure 3.24: Normalised measured BRDFs of the mirror.



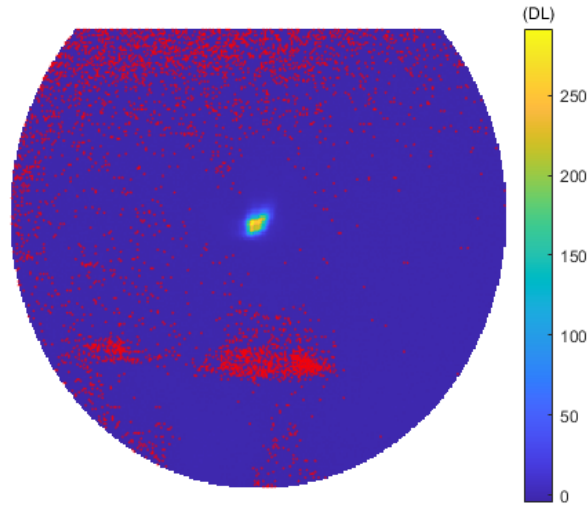


Figure 3.25: Illustration of pixels below the threshold of 1 DL after image subtraction.

### 3.6 Analysis of the set-up, method capacities and limits

The main issue of this set-up is the Signal to Noise Ratio (SNR). A sufficient signal for the OAPM requires the camera to have high integration times, for which we use  $2000 \mu s$ . However, this makes acquisitions highly sensitive to extraneous reflections, temperature shifts of the sample and camera sensor drift.

This noise includes negative pixel values after background subtraction. Figure 3.25 shows the background subtraction, where negative pixels are highlighted in red. This negative value does not have physical meaning; therefore, a threshold is set in place, and all pixels inferior to 1 DL (digital level) are arbitrarily set to 0.

Additionally, the spectral sensitivity of the set-up is not constant for three main reasons. First, the Bentham IR source is a hot wire that follows Planck's law (Eq. 2.2) and thus irradiates irregularly over the IR spectrum. Second, the air present along the optical path absorbs a fraction of the light in the studied wavelength range. Third, the sensor spectral sensitivity is also spectrally dependent. It is challenging to experimentally distinguish the contribution of each factor. Nevertheless, one can estimate a global spectral sensitivity using a mirror with a homogeneous spectral response instead of the sample. To do so, images are taken at different wavelengths, and the background is subtracted.



### 3.7. IMPLEMENTATION OF THE MULTI-SPECTRAL BRDF MEASUREMENT SYSTEM

---

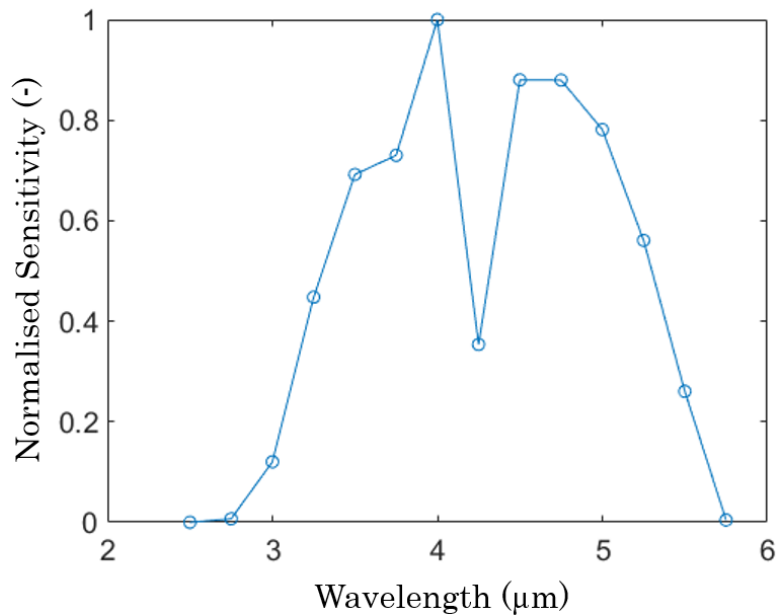


Figure 3.26: IR spectrum normalised sensitivity of a monochromator associated with an IR InSb camera.

A discrete integral is then performed on the resulting image to obtain a single scalar as a function of the incident beam wavelength. Figure 3.26 shows the measured normalised spectral sensitivity of the set-up. There is hardly any captured signal for wavelengths lower than 3 µm. The sensitivity of the set-up then increases up to 4 µm, where it reaches its maximum. A gap is observed between 4 and 4.5 µm; this gap corresponds to the absorption ray of carbon dioxide. Finally, the sensitivity decreases from 4.5 to 5.5 µm until no more signal is captured in this spectral range.

### 3.7 Implementation of the multi-spectral BRDF measurement system

As a reminder, the sample surface roughness ( $R_a$ ) used in this study ranges from 0.05 µm to 1.6 µm, and the camera spectral range is 3.5 to 5.5 µm with a spectral step of 0.250 µm. This provides nine measurements for each of 6 different samples. The total size of the raw data is approximately 10 GB.

Regarding the selected wavelength range and roughnesses, the transition of the BRDF shape is not specular at low wavelengths and is expected to trend towards a specular reflection or a Dirac repartition of reflected energy at higher wavelengths.

Generally, one can observe three different cases: (i) a specular case, (ii) a preferred direction of

### 3.7. IMPLEMENTATION OF THE MULTI-SPECTRAL BRDF MEASUREMENT SYSTEM

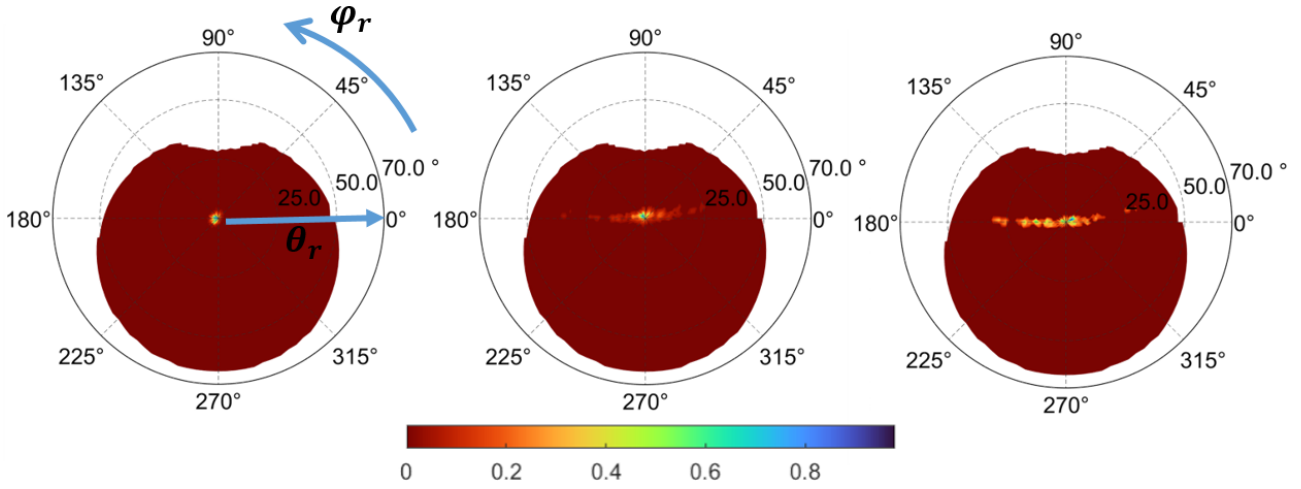


Figure 3.27: Normalised BRDFs with highlighted polar and azimuthal angles for samples 1, 4 and 5 ( $Ra = 0.05 \mu m, Ra = 0.4 \mu m$  and  $Ra = 0.8 \mu m$ ) at 4000 nm.

reflection for an azimuthal angle of  $\phi \approx 0$  degrees, and (iii) an intermediate case between the first two. These cases are presented in Figure 3.27. The preferred direction of reflection for case (ii) is attributed to the surface roughness topography presented in Figure 3.7 and in Appendix A.

In this section, the data obtained from sample 4 (surface roughness:  $0.4 \mu m$ ) is discussed; the results for the remaining samples can be found in Appendix A.

Figure 3.28 illustrates the BRDFs measured on sample 4 for different wavelengths. At  $5.25 \mu m$ , reflections are mainly specular normal to the sample ( $\theta = \phi = 0$ ), with some rebounding observed along the azimuthal angle  $\phi = 0$  and polar angle  $\theta < 25$  degrees. At lower wavelengths, the orientation of the preferred azimuthal reflections does not change. The rebounding in this direction gradually becomes a continuous signal. This behaviour is accompanied by the polar angle opening to  $\theta = 0^{+25}_{-35}$  degrees for a wavelength  $\lambda = 3.75 \mu m$ .

At  $\lambda = 3.25 \mu m$ , the only peak is observed at approximately  $\theta = \phi = 0$ , and no other signal is observed for other  $\theta$ . In the same manner, the change in signal across the azimuthal line is notably inconsistent, attributed to the low sensitivity of the set-up.

### 3.7. IMPLEMENTATION OF THE MULTI-SPECTRAL BRDF MEASUREMENT SYSTEM

---

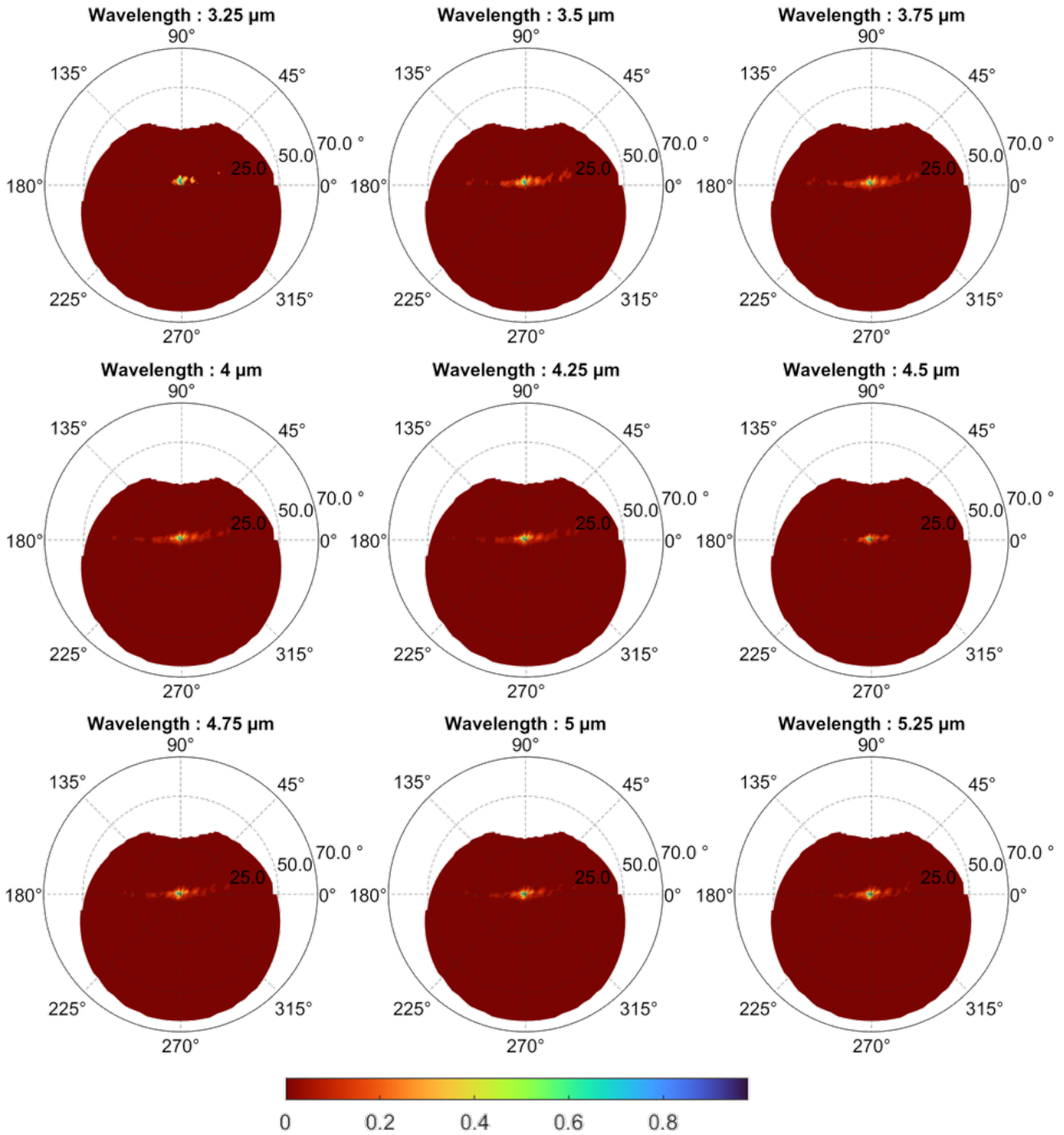


Figure 3.28: Sample 4 ( $R_a = 0.4 \mu\text{m}$ ) normalised BRDFs at different wavelengths.

### 3.7. IMPLEMENTATION OF THE MULTI-SPECTRAL BRDF MEASUREMENT SYSTEM

---

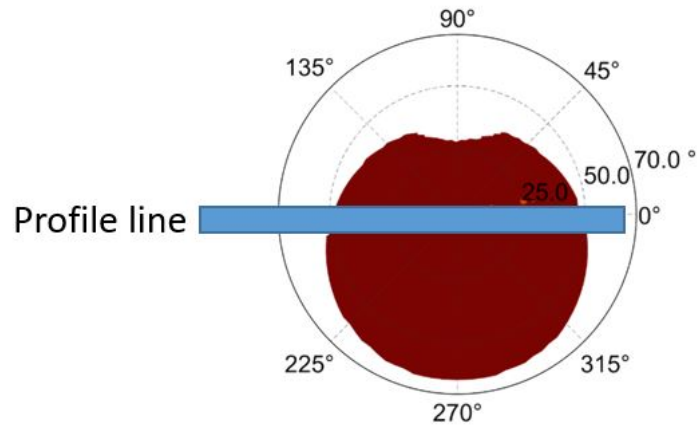


Figure 3.29: Illustration of the used profile line.

To examine the expansion of light along the polar angle, the reflection profile is plotted along the azimuthal angle  $\phi = 0$ . To obtain the complete reflection profile, lines parallel to the profile line shown in Figure 3.29 are added with the polar angle  $\theta = 5^\circ$  for multiple wavelengths.

Figure 3.30 shows the normalised BRDFs along the presented profile line for different wavelengths (3, 3.5, 4, 4.5 and 5  $\mu\text{m}$ ). Generally, two peaks at  $\theta \approx \pm 0^\circ$  can be observed, and they are quasi-symmetrical. Moreover, at 3  $\mu\text{m}$ , a non-specular reflection is observed. The peaks are composed of a continuous non-null signal with local peaks. The signal continuously decreases until the polar angle  $\theta \approx \pm 20^\circ$  is reached. For higher wavelengths, the curves decrease faster up to a polar angle as high as  $\theta \approx \pm 35^\circ$ . The local peaks and valleys are still present, and a shift is observed along the polar angle as a function of the wavelength. Finally, the larger the wavelength is, the smaller the non-specular reflections are.

### 3.7. IMPLEMENTATION OF THE MULTI-SPECTRAL BRDF MEASUREMENT SYSTEM

---

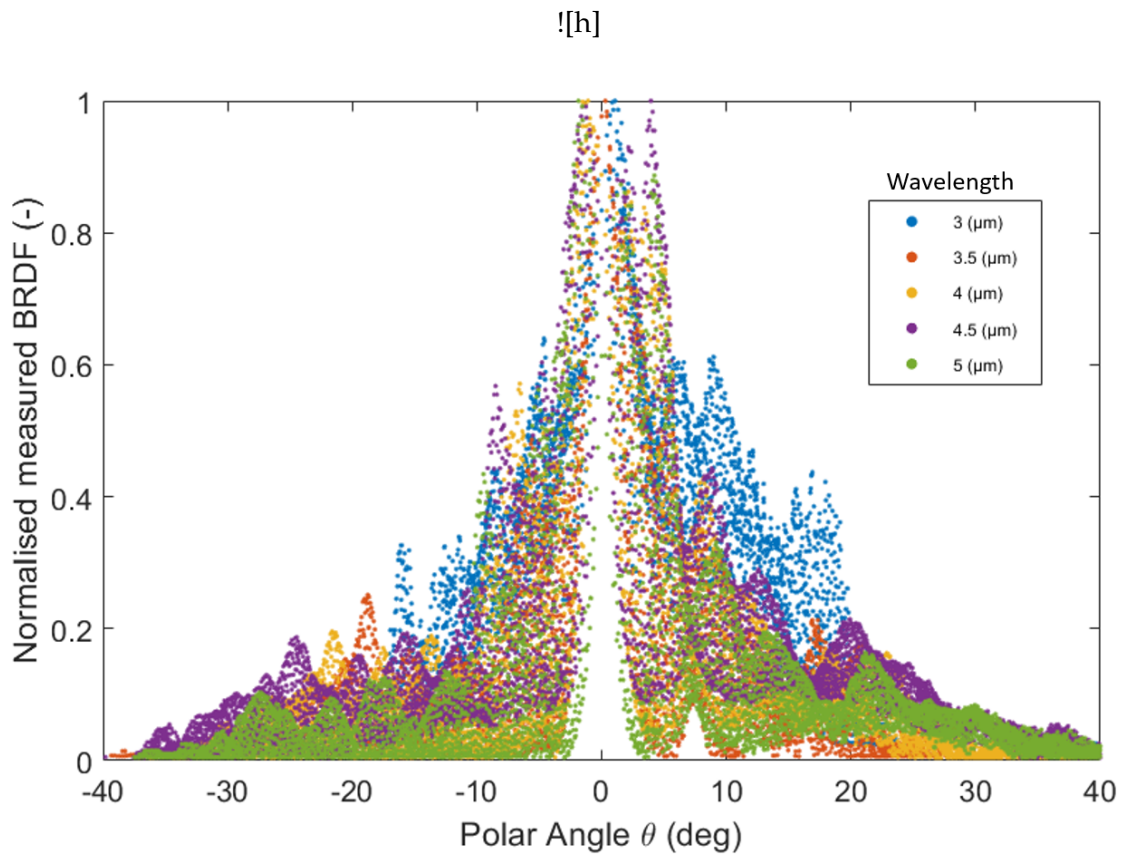


Figure 3.30: Sample 4 normalised BRDFs for several wavelengths.

To elucidate the transition of the BRDFs, more wavelengths are measured in the wavelength range of 3  $\mu\text{m}$  to 5  $\mu\text{m}$  but with spectral steps of 0.05  $\mu\text{m}$ . The same processing is applied as for the other acquired wavelengths. The obtained refined discretisation allows the surface of normalised BRDFs along the presented profile line to be obtained. This is illustrated in Figure 3.31. The local peaks and valleys along the polar angle depend linearly on the wavelength. Similar patterns are observed when light passes through a circular aperture, known as Airy diffraction [53]. Moreover, reflection around the normal becomes more important with regard to the other directions for higher wavelengths. In this figure, all results are normalised. It can be assumed that this shape metamorphosis is accompanied by a difference in amplitude that cannot be observed.

### 3.8. CONCLUSIONS REGARDING INFRARED MULTI-SPECTRAL DATA BASED ON QUALITATIVE BRDFS

---

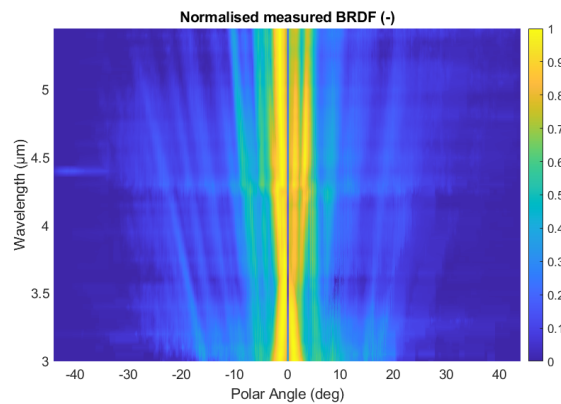


Figure 3.31: Sample 4 normalised BRDFs for different wavelengths.

### 3.8 Conclusions regarding infrared multi-spectral data based on qualitative BRDFs

To conclude this chapter, quantification of the reflected component is imperative for characterising the radiative balance between the reflected and absorbed radiative energy.

The laser sources used in this study have a wavelength of  $1.07\ \mu\text{m}$ . Consequently, infrared BRDF measurements are key to deepening the knowledge of laser–material interactions.

Currently, there is a lack of data accessible to the scientific community on the study of reflectance distribution in IR. To fill this gap, the complete bench capability presented in this chapter has been developed from scratch. This set-up is capable of capturing qualitative spectral measurements of BRDF images between the  $3\ \mu\text{m}$  and  $5.5\ \mu\text{m}$  wavelength ranges. Prior to this work, the spectral limitation was mainly dependent on the camera sensor and the beam splitter. By changing these, one can easily transition from the visible range to far-infrared. Additionally, the data processing method allows us to treat high quantities of data generated during the experiments (e.g., 8 GB for a sample and 60 wavelengths) in a few minutes. The imaging-based measurement of BRDFs allows the acquisition of approximately 60,000 simultaneous acquisition points.

The set-up is partially validated on a specular model, although the lack of a Lambertian body in the laboratory does not allow us to validate the set-up for this last case. The results are shown for 6 samples, including a complete description of the sample surface through topography measurement. This work can be considered a starting point for the elucidation of the BRDF of materials in IR

### 3.8. CONCLUSIONS REGARDING INFRARED MULTI-SPECTRAL DATA BASED ON QUALITATIVE BRDFS

---

wavelengths.

Several perspectives can be gained from the work presented in this chapter and should be considered in future work. First, due to the lack of time, this work introduces the measurement of data points, but no BRDF models are fitted to those points. Second, a major drawback of this method is the sensitivity of the set-up, which may not detect weak reflections. A solution to this problem should be implemented. Finally, identification of the incident beam would provide further information towards making quantitative measurements.

## Chapter 4

# Absolute temperature measurement with an IR camera by active thermo-reflectometry (ATR)

### Table of Contents

---

<b>4.1</b>	<b>Introduction</b>	<b>83</b>
<b>4.2</b>	<b>Contactless temperature measurements with an IR camera</b>	<b>83</b>
<b>4.3</b>	<b>Introduction to the IR sensor</b>	<b>85</b>
4.3.1	Difference sensors	85
4.3.2	Sensor characteristics	86
4.3.3	Sensor and wavelength sensitivity	87
4.3.4	Conclusions regarding IR sensors	87
<b>4.4</b>	<b>State of the art of the radiative measurement of temperature</b>	<b>89</b>
4.4.1	Radiative measurement of temperature: emission	89
4.4.2	Radiative measurement of temperature: reflection	94
4.4.3	Conclusions regarding the analysis of the state of the art of temperature measurement by IR technology	94
<b>4.5</b>	<b>Experimental set-up of ATR</b>	<b>95</b>
<b>4.6</b>	<b>From images to temperature fields: black body calibration</b>	<b>98</b>
4.6.1	Experimental set-up for black body calibration	99
4.6.2	Black body calibration model	102
4.6.3	InSb high-temperature calibration	105
4.6.4	InSb low-temperature calibration	107
4.6.5	Sensitivity to camera noise	109
4.6.6	Conclusions regarding the black body calibration	111
<b>4.7</b>	<b>Presentation of ATR</b>	<b>112</b>
4.7.1	Radiative balance	112
4.7.2	Introducing the Fresnel model	114



---

4.7.3	Illustration of the model for numerical cases . . . . .	115
4.7.4	Presentation of ATR . . . . .	119
4.7.5	Numerical validation of ATR . . . . .	121
<b>4.8</b>	<b>Validation of ATR on heterogeneous samples at ambient temperatures . . . . .</b>	<b>124</b>
4.8.1	Stainless steel sample . . . . .	124
4.8.2	Three-layer aluminium sample . . . . .	129
4.8.3	Conclusions regarding static measurement . . . . .	132
<b>4.9</b>	<b>Conclusions regarding temperature measurement with infrared thermography . . .</b>	<b>133</b>

---

### 4.1 Introduction

On the basis of the work presented in Chapter 3, a specular reflection model can be used to describe the image processing of infrared images. Absolute temperature measurements of a thermal camera are relevant to this thesis, as the effects of an HEL are primarily thermal. Specifically, measuring absolute temperature fields is essential for quantifying the thermodynamic behaviours of their laser effects on the material. The simple but representative BRDF model allows **in situ measurements of emissivity fields**, the **estimation of reflections** present in thermal images, and consequently the **absolute measurement of temperature** fields with an infrared camera.

In this chapter, a **new approach** for capturing **the absolute temperature** by ATR is developed[54]. This development is based on the **complete radiative modelling** of a thermal camera capturing images of an **opaque object** within a **thermal scene**. Highly accurate images and replications via the model are imperative for understanding the **emissive properties** of the material and **the reflective properties of the infrared scene**.

### 4.2 Contactless temperature measurements with an IR camera

Radiative temperature measurements made with a camera or any kind of radiometer involve capturing the emitted radiation of the sample and determining the real-time temperature through calibration. The major issue behind this concept is that the emitted radiation depends not only on the temperature but also on the material's capacity to radiate light in the same wavelength range of the sensor. The surface spectral and directional radiative properties depend on the emissivity of the material, its surface roughness and any variations due to temperature changes. In addition to these properties, the radiant flux density in the scene depends on the temperature field, the scene geometry and the ambient atmosphere (which can be considered transparent). Thus, when considering opaque surfaces, the radiative flux measured by any IR sensor is dependent on the emission, absorption, reflections and scattering of light. Figure 4.1 illustrates the radiative balance that pertains during thermal imaging.

First, an introduction to the different types of infrared sensors available will be given. Then, a state of the art describing different methods allowing an absolute temperature measurement despite emissivity or reflection problems will be presented. Next, the experimental set-up required for

## 4.2. CONTACTLESS TEMPERATURE MEASUREMENTS WITH AN IR CAMERA

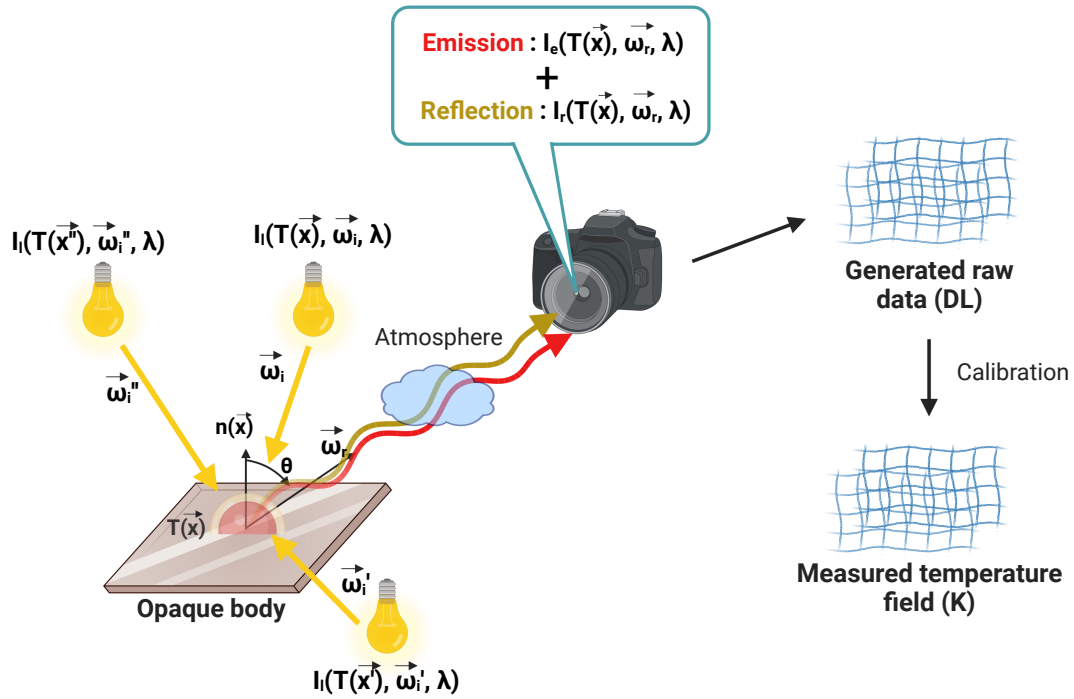


Figure 4.1: Schematic representation of contactless temperature measurements on an opaque surface.

ATR will be presented. Then, a description of the calibration to relate the camera response (DL) to temperature will be given. Finally, the ATR method will be presented through a description, a validation on numerical and experimental cases.

### 4.3 Introduction to the IR sensor

To introduce the contactless temperature measurement, it is necessary to understand the different parts of an infrared scene. First, one must understand the sensor as illustrated in Figure 4.2. The following section describes the IR sensors and their characteristics.

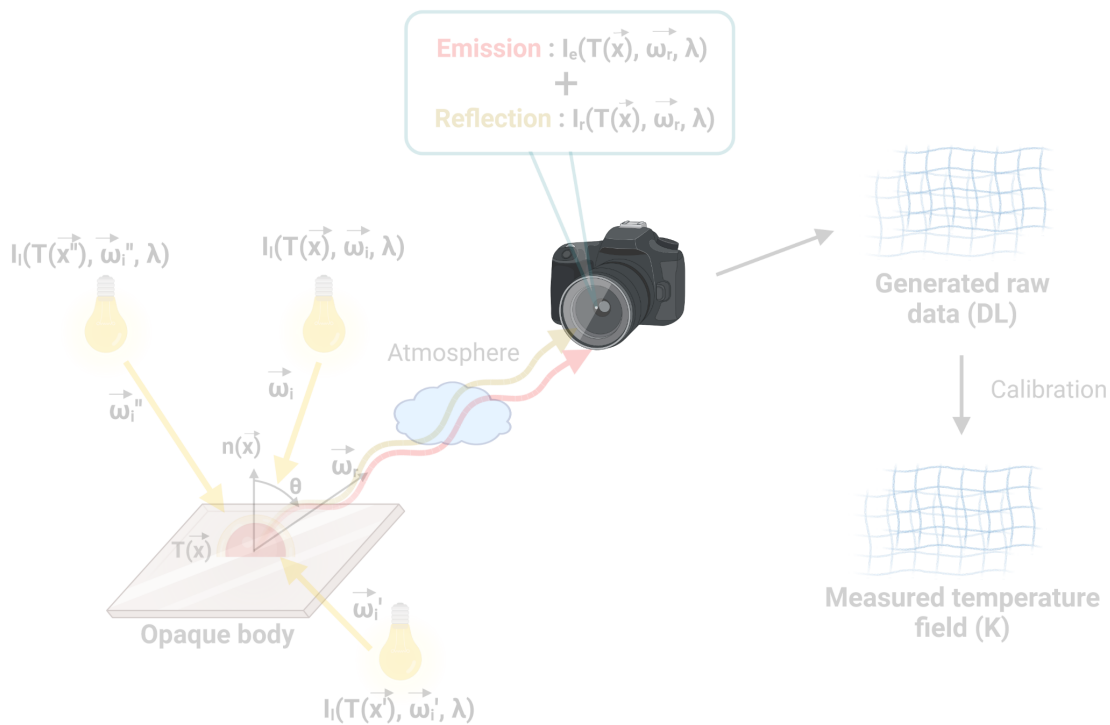


Figure 4.2: Schematic representation of any infrared scene on opaque media, focusing on the sensor.

#### 4.3.1 Difference sensors

An infrared camera is an optical device that captures a scene over an infrared wavelength range. Multiple sensors exist:

##### Thermal sensors

These sensors send a signal that is a function of their own temperature. The sensor is exposed to the IR of the observed scene and radiatively heats up. This phenomenon implies a variation in its properties. There are two main technologies: pyroelectric sensors and micro-bolometric sensors [81, 82].

### 4.3. INTRODUCTION TO THE IR SENSOR

---

A material is said to be **pyroelectric** when a temperature variation leads to a variation in its electrical polarisation. The potential created is temporary and has a characteristic response time before returning to its initial state. This type of sensor can be used over the entire infrared wavelength range.

**Bolometers** are thermometers whose output resistance varies with temperature. These sensors have the advantage of being coupled with silicon technology, which allows high resolution. This type of sensor is now widely used in industry [83].

Quantum sensors Quantum or photonic detectors have an output signal directly proportional to the number of photons received by the sensor surface. Some materials emit electrons under the effect of light radiation. To do this, the incident photon must have sufficient energy to excite the medium. Based directly on the interaction of radiation and matter, quantum detection is faster than thermal detection [84]. However, this technology requires the sensor to be cooled to cryogenic temperatures. There are three different types of sensors:

- **Photovoltaic (PV)**: PV cells convert electromagnetic radiation into electric current.
- **Photoconductor (PC)**: Electromagnetic radiation changes the conductivity of the photosensor.
- **Photoemissive (PE)**: The output signal of the sensor is proportional to the number of electrons that are stripped off by the electromagnetic radiation.

#### 4.3.2 Sensor characteristics

There are different types of sensors for thermal imaging. Before identifying the sensor architectures, we review some useful parameters when choosing a sensor:

- **Sensitivity**: the variation in the output signal as a function of the variation in the input signal.
- **Incident photon-to-electron conversion efficiency**: the ratio of the number of electronic charges collected by the sensor to the number of photons incident on the photoreactive surface. This parameter depends on the radiation wavelength.
- **Rising time**: the time lag between an electronic input and the output signal.
- **Frame rate**: the number of images taken per second.

### 4.3. INTRODUCTION TO THE IR SENSOR

---

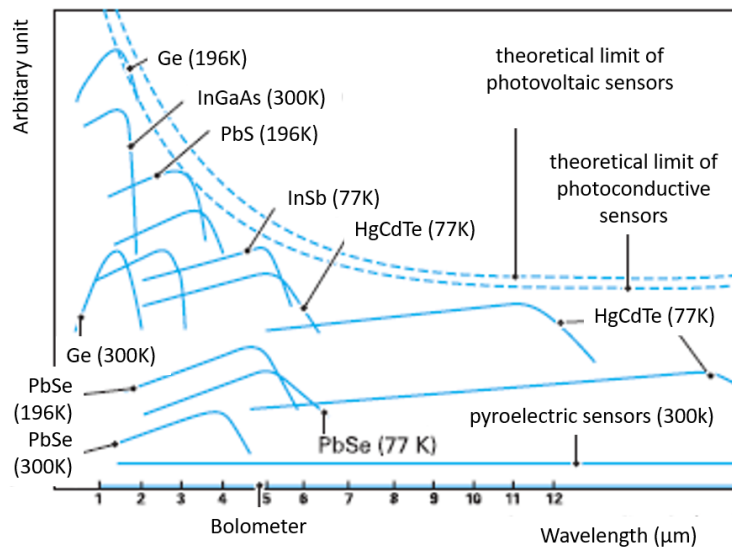


Figure 4.3: Sensitivity of different sensors as a function of wavelength (translated from [7]).

- Noise equivalent power: the smallest luminous flux detectable by the sensor.
- Noise equivalence temperature difference: the thermal difference such that the SNR is equal to 1.
- Minimum resolvable temperature difference: the smallest temperature difference that can be detected.

#### 4.3.3 Sensor and wavelength sensitivity

Choosing a sensor is a key point for thermography measurement, with each sensor having advantages and drawbacks. Figure 4.3 summarises different sensors and their sensitivities.

As one can observe, there are many different sensors with different spectral ranges and sensitivities. Thus, finding or choosing a good value of emissivity that also considers the sensor spectral sensitivity is quite complicated. Considering both the apparent luminance field and the emissivity simultaneously with the same sensor tends to simplify this process.

#### 4.3.4 Conclusions regarding IR sensors

In conclusion, this section includes the following:

### 4.3. INTRODUCTION TO THE IR SENSOR

---

- a presentation of different sensors,
- the main characteristics of each for choosing a sensor, and
- a focus on the sensor wavelength dependency - a link with the emissivity - to remind the readers that the specific value used for emissivity depends on the wavelength used.

## 4.4 State of the art of the radiative measurement of temperature

As demonstrated previously, the complete scheme for contactless temperature measurements includes a sensor, calibration, reflections, and emissions. Behind this complexity, we seek to identify the emission solely at the surface, which is dependent on the temperature and emissivity. This section introduces methods that allow the estimation of temperature considering emissions even when the emissivity is unknown. Next, we introduce methods considering the reflection of the thermal scene. Figure 4.4 highlights the considered aspect of temperature measurement in this section.

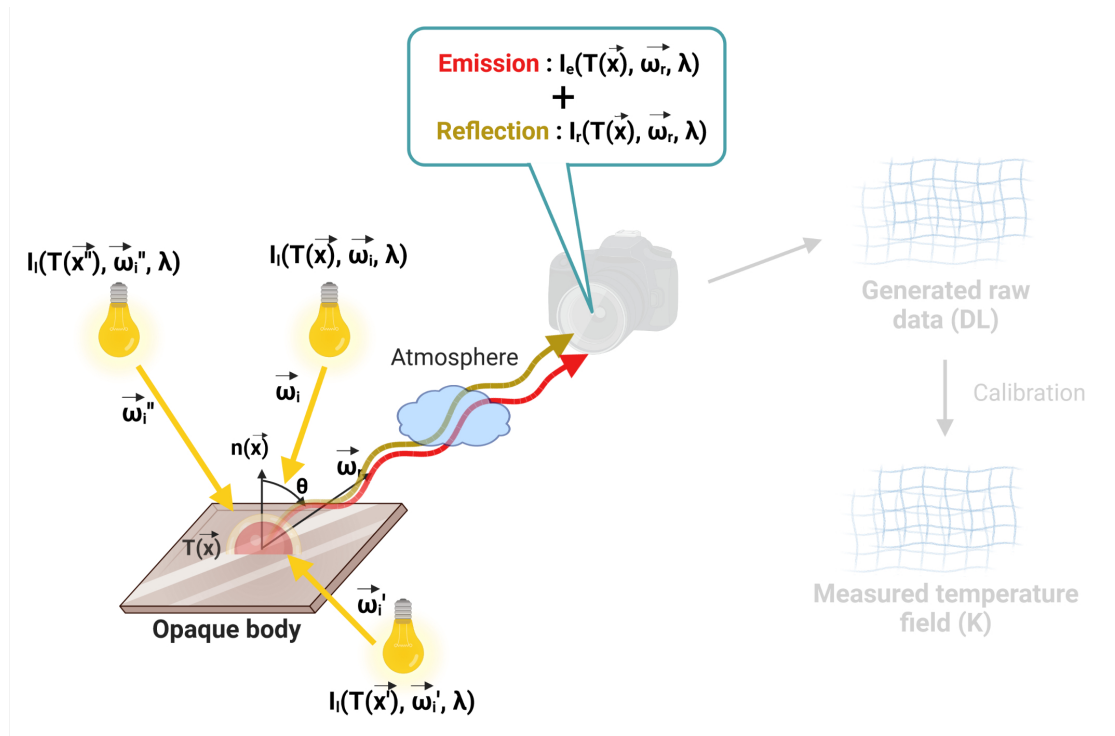


Figure 4.4: Schematic representation of contactless temperature measurements on an opaque surface with a focus on the radiative balance.

### 4.4.1 Radiative measurement of temperature: emission

The radiative measurement of temperature is based on the conversion of a signal captured with a photodetector into temperature. For a black body, this conversion is given by Planck's law (Eq. 2.2), which is then integrated over the sensor's spectral range. The conversion is dependent on the experimental set up (i.e., optics, working distance...) and can be done through calibration.



#### 4.4. STATE OF THE ART OF THE RADIATIVE MEASUREMENT OF TEMPERATURE

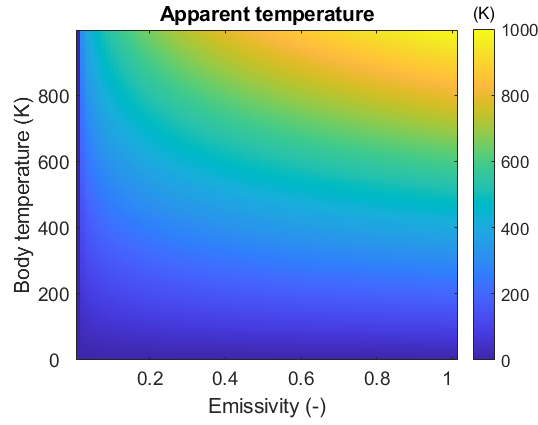


Figure 4.5: Illustration of the apparent temperature for a real body as a function of emissivity and temperature.

For a real body, the measured radiation depends on the emissivity and reflections. The temperature captured with raw images is called the "**apparent temperature**" and is denoted by " $T_a$ ", whereas the temperature interpreted from the image after processing for emissivity corrections is called the "**absolute temperature**".

The radiative intensity emitted ( $I_e$ ) from an opaque body is expressed as:

$$I_e(\lambda, T(\vec{x}), \vec{\omega}_r) = \varepsilon'(\lambda, T(\vec{x}), \vec{\omega}_r) I_b(\lambda, T(\vec{x})) = I_b(\lambda, T_a) \quad (4.1)$$

with  $I_b$  defined as the black body luminance in Eq. 2.2.

Given that the emissivity ranges between 0 and 1, the apparent temperature is inferior or equal to the absolute temperature. Figure 4.5 illustrates the apparent temperature for different temperatures and emissivities obtained from the Stefan–Boltzmann law. It is clear that without knowledge of emissivity, the apparent temperature cannot be used for quantitative estimation of the absolute temperature.

The emissivity of a material depends on many parameters, such as its temperature and surface roughness and the direction of the emitted light. For example, Keller et al. [55] studied the total hemispherical emissivity of Inconel 78 and showed that this parameter drifts between 0.2 and 0.51 depending on the sandblasting grit size used for the material's finish. This variation represents nearly 30% of the change in emissivity. Therefore, the emissivity is highly dependent on the surface condition of the sample or material of interest. As a result, there is no database for the emissivity of

#### 4.4. STATE OF THE ART OF THE RADIATIVE MEASUREMENT OF TEMPERATURE

materials with various surface states; however, in-depth studies are presented in works such as by Bakali et al. [56]. Here, we focus solely on the joint estimation of temperature and emissivity. To this end, two kinds of methods are presented. The first method, called the "passive method", is based on the measurement and processing of emitted radiation. The second method, called the "active method", introduces a local perturbation source to add information on thermal or optical excitation. Both methods assume that reflections are negligible.

##### 4.4.1.1 Presentation of the passive method

The passive method is used to measure the absolute temperature and emissivity of a surface based on the measurement of its emitted radiative flux.

First, we focus on the **monochromatic method**. This method does not allow joint identification of temperature and emissivity. However, one can often find a wavelength of interest where the emissivity does not depend on temperature. For dielectric materials, Christiansen showed that specific wavelengths are related to the vibrational frequencies of a material's crystal lattice, where the emissivity trends towards 1 [57, 58, 59].

Another approach of this method is to find a wavelength where the effect of emissivity is negligible for the temperature measurement. Ohji et al. [60] showed that this is the case for ultraviolet wavelengths. However, the main disadvantage of this spectral range is that the signal is weak and the studied body must have a high temperature.

We now focus on the **ratio pyrometer or multi-spectral pyrometer** method. The ratio pyrometer depends on two wavelengths, whereas the multi-spectral pyrometer uses more than two wavelengths. The goal behind this method is to add information to identify both temperature and emissivity. This method is based on the measurement of emitted radiative intensity at two (or more) wavelengths and introduces two assumptions. The first assumption is related to the spectral behaviour of emissivity at the wavelengths of interest, and the second assumption assumes that the thermal dynamics do not affect the first assumption.

For the ratio pyrometer, an assumption is made on the ratio of emissivity considering two wavelengths. By doing so, one can write a system of two equations with two unknowns (emissivity:  $\varepsilon'_1(\lambda_1)$ )

#### 4.4. STATE OF THE ART OF THE RADIATIVE MEASUREMENT OF TEMPERATURE

and temperature  $T$ ) written as follows.

$$\begin{cases} I_e(\lambda_1, T) &= \varepsilon'_1(\lambda_1)I_b(\lambda_1, T) \\ I_e(\lambda_2, T) &= K\varepsilon'_1(\lambda_1)I_b(\lambda_2, T) \end{cases} \quad (4.2)$$

where  $K$  is the ratio of emissivity between two wavelengths. When not measured, it is generally considered equal to one.

$$K = \frac{\varepsilon'_2(\lambda_2)}{\varepsilon'_1(\lambda_1)} \quad (4.3)$$

The multi-spectral pyrometer method is based on the same idea. In this case, there are  $N$  wavelengths, and the ratio  $K$  is replaced by an interpolation function  $f_\varepsilon$  having at most  $N - 1$  parameters. The system of equations can be written as follows:

$$\begin{cases} I_e(\lambda_1, T) &= f_\varepsilon(P_1, P_2, \dots, P_j, \lambda_1)I_b(\lambda_1, T) \\ I_e(\lambda_2, T) &= f_\varepsilon(P_1, P_2, \dots, P_j, \lambda_2)I_b(\lambda_2, T) \\ &\dots \\ I_e(\lambda_N, T) &= f_\varepsilon(P_1, P_2, \dots, P_j, \lambda_N)I_b(\lambda_N, T) \end{cases} \quad (4.4)$$

Two kinds of interpolation functions exist ( $f_\varepsilon$ ). The first is based on mathematical interpolation functions such as polynomial functions, and the second is based on a physical model that describes the transport properties of electrons in materials such as the Drude or Maxwell model [61, 62].

Regardless of how many wavelengths are used, the passive method always relies on two hypotheses: an assumption on the emissivity spectral dependency for one, two or  $N$  wavelengths and temperature independence.

##### 4.4.1.2 Presentation of the active method

In contrast to the passive method, which simply collects radiative measurements, the active method introduces a local perturbation to determine the absolute temperature. Two kinds of perturbations are used.

The first perturbation is a precise thermal stimulation on the material. The excitation is often a sinusoidal function, and the relaxation provides information on the temperature [63].

#### 4.4. STATE OF THE ART OF THE RADIATIVE MEASUREMENT OF TEMPERATURE

The second perturbation is based on Kirchhoff's laws (Eqs. 2.5, 2.8) and gives an estimation of emissivity based on the measurement of directional hemispherical reflectivity [42, 64]. In this case, the perturbation is a radiative perturbation. The main methods are listed below.

- **Directional hemispherical reflectivity measurement.** This method is performed with an integrating sphere (or hemisphere) that contains a high-reflectivity coating that averages reflections in all directions. Generally, one or two pinholes are added to the integrating sphere: one for illumination of the sample and one to collect the mean reflection inside the sphere. This set-up is coupled with an FTIR spectrometer to study spectral dependency and is often used at high temperatures [65, 66, 67]. Unfortunately, this method is usable only for fields measurements where the emissivity can spatially changes.
- **Transient thermo-reflectance (TTR) or time domain thermo-reflectometry (TDTR)** is a method developed in the late 1980s for temperature measurement at the micro- or nano-scale [68, 69]. This method, especially useful for temperature measurements on semi-transparent materials, is based on calibrating the thermo-reflectance coefficient, which then allows the temperature to be measured by measuring the sample reflectance.
- **Pyroreflectometry or thermo-reflectometry** involves measuring the bidirectional reflectivity and deducing a joint identification of temperature and emissivity by introducing another unknown: the scattering factor. This parameter is considered constant between close wavelengths, or its wavelength behaviour is assumed to be known by an interpolation model. This approach was first implemented for punctuate measurement [70, 71, 72]; subsequently, a matrix-based approach using the same method was developed [73, 74]. The latest developments linked to this method concern the scattering model based on surface modelling [75, 76].

The directional hemispherical reflectivity measurement is not considered here because of its lack of adaptability for matrix-based sensors. The TTR is not considered either because the applications involved are outside of the scope presented here. Thermo-reflectometry depends on two hypotheses: an assumed interpolation function and its temperature independence. As a final note, none of the presented methods considers the reflected flux.

## 4.4. STATE OF THE ART OF THE RADIATIVE MEASUREMENT OF TEMPERATURE

### 4.4.2 Radiative measurement of temperature: reflection

The methods presented in the previous section are based on the assumption that there is no reflection in the thermal scene. This assumption may be true while working at high temperatures or at specific wavelengths but reduces the range of application. Moreover, this assumption is not applicable while working at or near ambient temperatures. To overcome this issue, multiple approaches have been developed.

The first solution is to work under a dome with a uniform temperature that has been surface-treated to suppress radiative emission [77]. Other studies mix data obtained for visible and IR wavelengths to suppress reflected radiation [78]. Furthermore, multiple studies have shown that by simulating the thermal scene and the radiative heat transfer, it is possible to determine the reflected flux. This is possible for controlled experimental settings, such as the international nuclear fusion research centre Tokamak [79] or reflected atmospheric plasma spraying torch radiation [80], unfortunately, this greatly reduces the possible applications.

### 4.4.3 Conclusions regarding the analysis of the state of the art of temperature measurement by IR technology

Although the full implementation of this technology is offered by IR cameras today, the state-of-the-art presented earlier highlight the difficulty of obtaining robust real-time measurements for the absolute temperature of thermal scenes acquired with IR cameras.

In this thesis, a method referred to as ATR is developed to answer this issue and is available on **any specular material in infrared wavelengths**. This reflection model, which is widely applicable in industry with regard to the roughness and flatness of the surface, allows both emissivity and reflections to be determined without any assumptions. The set-up and implementation ease makes this method easy and versatile to transfer to industry.

This work is based on a new measurement system for an active optical approach that involves illuminating objects by expanding the beam from the black body to the surface of the material. This is performed normal to the surface being measured. This source is coupled with the 2 images methods [16, 17] and allows the simultaneous measurement of the surface's normal reflectivity, as well as its own proper emission.

This approach, coupled with a specific calibration to estimate the reflection of the environment, allows emissivity fields to be obtained in real time. Knowledge of these fields, associated with the measurement of the radiative intensity and a black body calibration, allows contactless absolute temperature fields to be determined.

### 4.5 Experimental set-up of ATR

The complete set-up used for the ATR method is presented in Figure 4.6. The experimental bench is composed of (1), a multi-spectral black body source (1: CN-MT described in Section 4.6.2) whose temperature range extends from 20 °C to 500 °C. In this study, the temperature set point is 200 °C. A chopper (2) is used to modulate the intensity of the beam in lock-in mode. Typically, the frequency modulation ( $f_{BB}$ ) is set to 60 Hz, whereas the camera frequency acquisition ( $f_{acq}$ ) is set to double this value. A pair of parabolic mirrors (3 and 4) is used as an optical doublet to image a plane of the black body cavity onto the sample plane. The object plane (black body cavity) of the doublet is imaged on the image plane (sample) with a theoretical magnification of 2. As the diameter of the black body cavity is approximately 25.4 mm, the beam that illuminates the sample surface reaches a theoretical diameter of 50 mm. Mirror (3) is a 15° gold-coated off-axis mirror with a focal length of 645,92 mm, whereas mirror (4) is a 15° off-axis mirror with a focal length of 542,92 mm and has a silver coating.

A beam splitter (6) (with 50% transmissivity, 50% reflectivity) is used to both normally illuminate the sample and record the normal radiative intensity, leaving the sample then directed to and captured by an IR camera. A motorised rail (8) allows linear motion of the reference mirror (9) and the sample (10). Both are mounted with particular attention to coplanar alignments that are normal to the camera and beam axis. Due to the beam splitter, the camera field of view is the superposition of the sample plane (transmitted by the beam splitter) and the beam dump plane (reflected by the beam splitter). To minimise the beam dump participation, this component is positioned far from the camera focal plane and painted with absorbing black paint to avoid any reflection. The specimen is placed 1300 mm from the camera.

Two experimental cases are studied in this chapter. They are both static cases at ambient temperature. For these cases, the laser source presented in 4.6 is inaccurate. The IR camera (5), model SC7000 (synchronised with the optical chopper:  $f_{acq} = 2 f_{BB}$ ), has an InSb sensor (2,5 – 5,5  $\mu m$ ), a pixel area

#### 4.5. EXPERIMENTAL SET-UP OF ATR

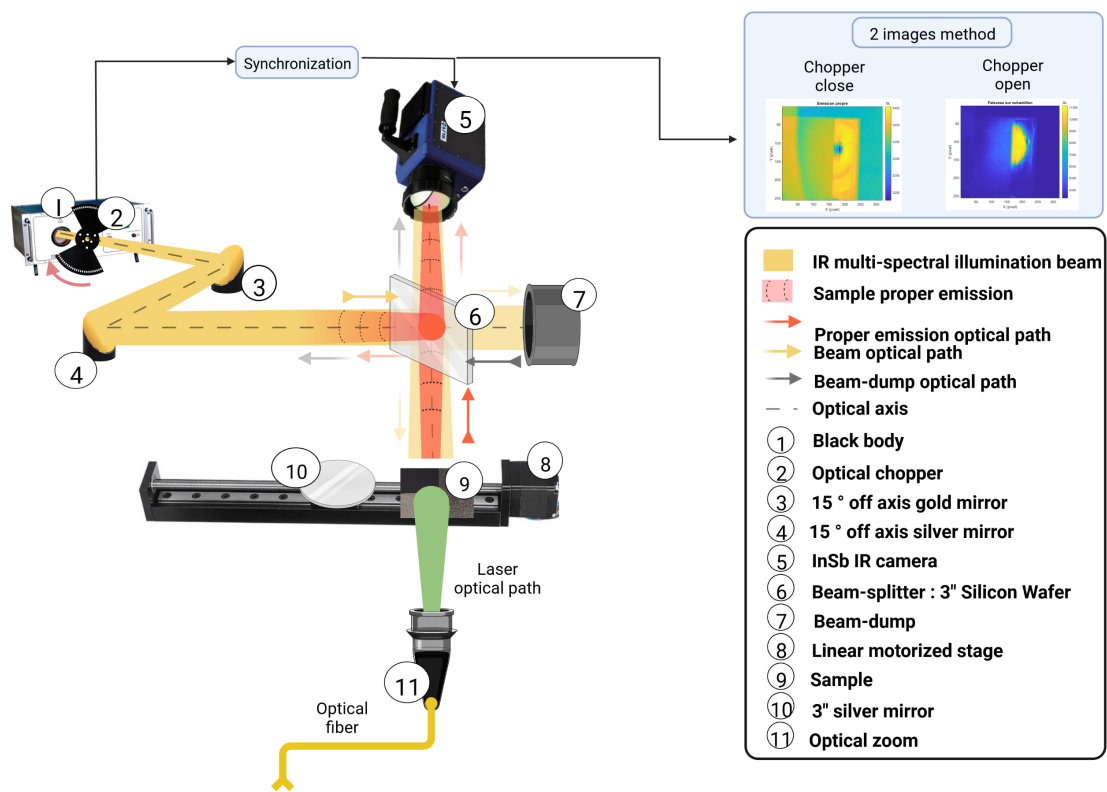


Figure 4.6: Schematic representation of the experimental set-up.

#### 4.5. EXPERIMENTAL SET-UP OF ATR

---

of  $320 \times 256$ , and a pitch of  $30 \mu m$  and is equipped with a  $50 mm$  focal lens.



## 4.6 From images to temperature fields: black body calibration

Now that the IR sensor has been introduced, one can focus on how to measure the temperature based on infrared images under certain circumstances. Since the detector delivers an analogue pulse proportional to the number of incident photons, the output is expressed in terms of the DL. This unit is arbitrary and proportional to the radiative intensity of the black body ( $I_b$ ) under certain temperature conditions ( $T_b$ : K), integration times ( $IT$ :  $\mu s$ ), optics, etc.  $I_b$  and  $T_b$  are both linked by Planck's law (Eq. 2.2). Thus, a calibration must first be performed to establish a relationship between the scene temperature and the electrical signals. This step is important to obtain quality results. This calibration is carried out experimentally by establishing relationships between the temperature of a black body placed in front of the sensor and the signals from the sensor. Figure 4.7 illustrates the aspects of interest of this section.

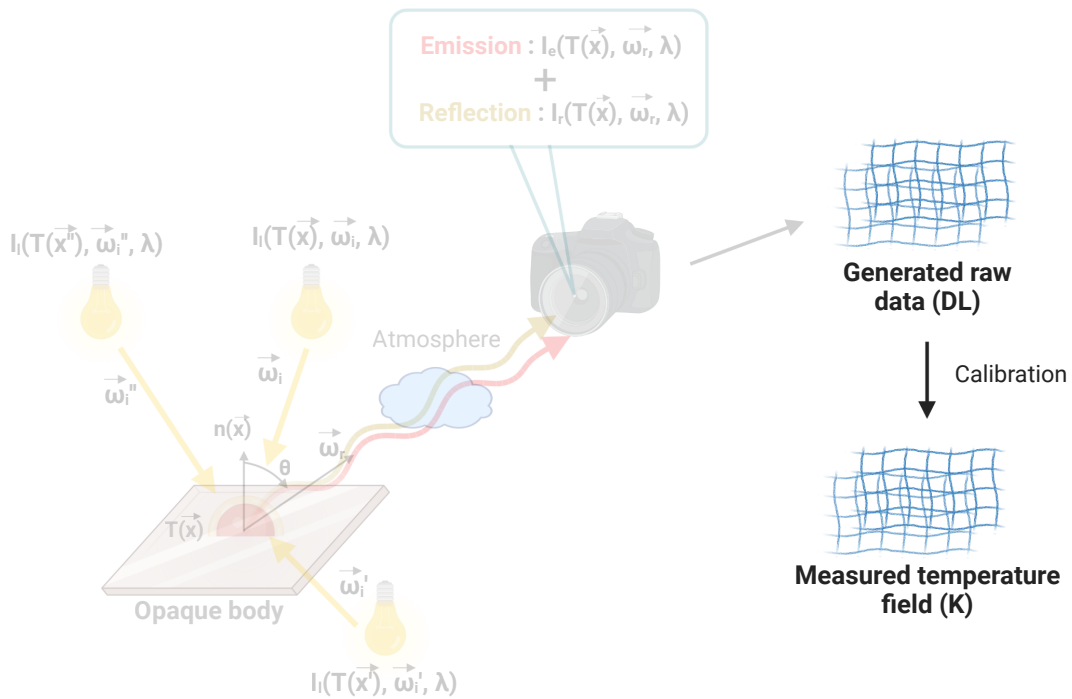


Figure 4.7: Schematic representation of any infrared scene on opaque media, with a focus on the calibration.

The signal generally evolves linearly with the radiant flux. However, the function linking the actual temperature to the measured temperature is not linear because the evolution of the radiation

## 4.6. FROM IMAGES TO TEMPERATURE FIELDS: BLACK BODY CALIBRATION

emitted by a surface is not proportional to its temperature.

The calibration is performed before the experiment and is considered valid for months. The literature regarding IR camera calibration is abundant [85, 86, 87, 88, 89, 90, 91]. Multiple parameters influence the calibration, such as the object-to-camera distance [92], object orientation [93], detector type [85, 94] and magnification [95].

In this section, a description of the complete set-up used for the camera calibration is presented. Then, multiple calibration models are compared.

### 4.6.1 Experimental set-up for black body calibration

Each calibration is specific to the measurement conditions (optics, filters, exposure time, distance between object and camera, etc.), so it is necessary to implement calibration corresponding to user conditions. To consider the optical window present between the sample and the camera and the distance between the camera and the sample, the whole measurement chain is calibrated (see section 4.5).

As described in Figure 4.8, the experimental set-up used for the calibration phase is a part of a more complete set-up needed for the ATR method (presented in Figure 6.16). The calibration set-up takes into account the transmissivity of the beam splitter (element number 3 in Figure 4.8, denoted by  $\tau_{bs}$ ) and the background reflected by the beam splitter ( $I_{bs}$  is considered negligible because it is far from the sharp field of view for the camera). In this set-up, the camera-to-object distance is fixed at 1300 mm.

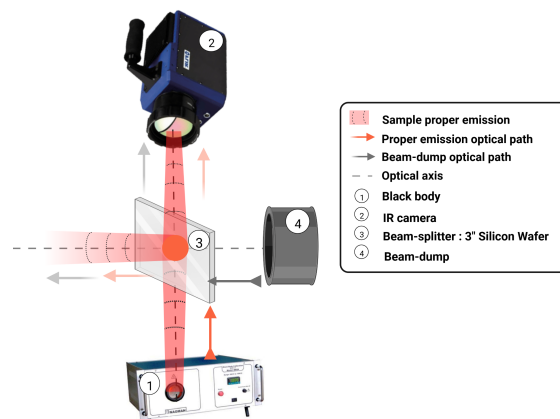


Figure 4.8: Schematic representation of black body calibration.

#### 4.6. FROM IMAGES TO TEMPERATURE FIELDS: BLACK BODY CALIBRATION

---

The experimental set-up is presented in Figure 4.8. In this set-up, two cameras and two black bodies are used:

- Camera 1:

Flir model SC7500BB InSb

Spectral range 2,5–5,5  $\mu m$

Pixel area of 320  $\times$  256

Pitch 30  $\mu m$

Encoding number 14 bits

- Camera 2:

Flir model A6753sc SLS

Spectral range: 7,5-11  $\mu m$

Pixel area of 640  $\times$  512

Pitch 15  $\mu m$

Encoding number 14 bits

- Black body 1:

Prisma instrument: model CM-MT

Emissivity 0.98

Temperature range 50 - 600  $^{\circ}C$

Accuracy: 0.5% (min. 2  $^{\circ}C$ )

Time period 40 s

- Black body 2:

Prisma instrument: model CM-HT

Emissivity 0.98

Temperature range 500 - 1200  $^{\circ}C$

Accuracy: 0.5% (min. 3  $^{\circ}C$ )

Time period 4 s

The method is the same for the two cameras. The following paragraph addresses only the calibration of the InSb camera for the prescribed temperature ranges. The first range is referred to as the low-temperature range (37 - 150  $^{\circ}C$ ) and the second as the high-temperature range (300-1200  $^{\circ}C$ ). For the latter, an infrared filter is used.

The black bodies used cannot be remotely controlled; thus, the temperature points are obtained manually. A pause of at least one hour is included at each temperature to obtain thermal equilibrium inside the black body cavity. The black body temperature is driven by a PID controller such that the temperature of the body oscillates around the command temperature with the previous time period. To eliminate those oscillations, a film of 50 images is acquired for multiple oscillation periods and for each measurement.

The camera can be remotely controlled through GiGe internet communication. MATLAB code is developed to automatically sweep the range of integration times. The best way to calibrate a sensor is

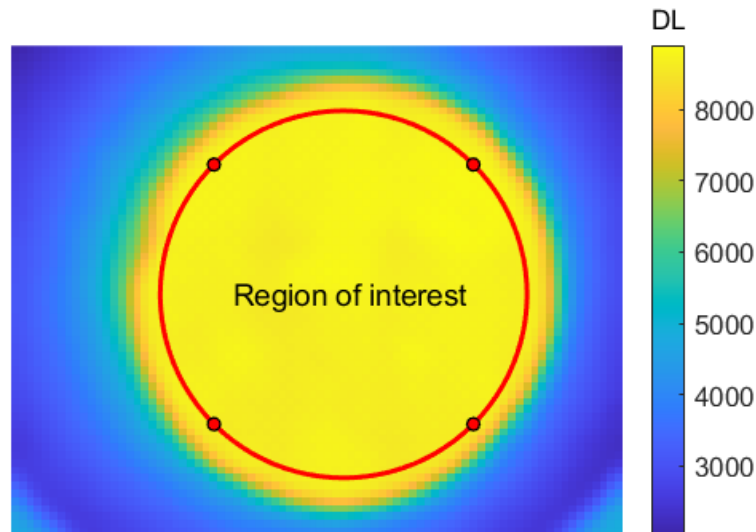


Figure 4.9: Typical black body calibration image.

to conduct a pixel-based calibration. This includes a black body source that is larger than the camera field of view. As this is not the case in this specific experimental set-up (see Figure 4.9 for a typical black body calibration image), we use the mean value over the region of interest, that is, 1125 pixels.

Both camera images are coded on 14 bits, so the camera has a range up to 16,000 DL. However, neither camera is reliable below 2000 DL and above 12000 DL. Temperature and integration time combinations where the camera response is not within this DL range are not considered.

Figure 4.10 illustrates the acquisition process of camera calibration.

It is important to highlight the limitations of such an experimental set-up. The thermal equilibrium of the thermal cavity is an essential element of the experimentation but takes time to set up. Moreover, focusing the camera, which is common for camera users, is ultimately not an easy task to perform while working with a cavity. The delivered signal changes from tens to hundreds of DL depending on the sharpness of the image or "where" in the cavity the focus is obtained. This is not a large variation, but it is quite crucial, as all the results depend on this step. Focusing the camera involves placing an object at the desired distance and adjusting the output of the cavity on this plane.

Figures 4.11a and 4.11b show the measured DL for different pairs of temperature and IT.

The obtained discrete values are not usable as such, and one must identify a law to interpolate data between different points. To do so, different models from the literature are presented as follows.

#### 4.6.2 Black body calibration model

As the camera is placed normal to the sample and the distance between the object and the camera is fixed, there is no need to consider the camera positioning in the calibration model. Thus, the calibration model can be written as:

$$S(T) = \left[ \int_0^{\infty} \tau_{bs}(\lambda) R(\lambda) I_b(\lambda, T) d\lambda \right] IT + \text{offset} \quad (4.5)$$

where  $R(\lambda)$  is the sensor spectral sensitivity,  $\tau_{bs}$  is the beam splitter transmissivity (see Figure 4.8) and  $I_b$  is Planck's law (Eq. 2.2). Interpolation methods approximate this integral equation with a calibration equation containing a small number of adjustable parameters that are determined from a set of multiple measured temperature–signal pairs [96] (see Figure 4.11).

In this study, four interpolation models are used and compared. The first comes from the Sakuma–Hattori [97, 98] equation, the second is a simplification of the Flir model equation, and the last is a simple polynomial interpolation. The polynomial order is chosen depending on the dataset to obtain the best results without over-fitting.

The first two models are reversible ( $S = f(T)$  and  $T = f^{-1}(S)$ ). The last model includes a polynomial of 4th order, and two fits are made.

- Sakuma–Hattori Planck III:

4.6. FROM IMAGES TO TEMPERATURE FIELDS: BLACK BODY CALIBRATION

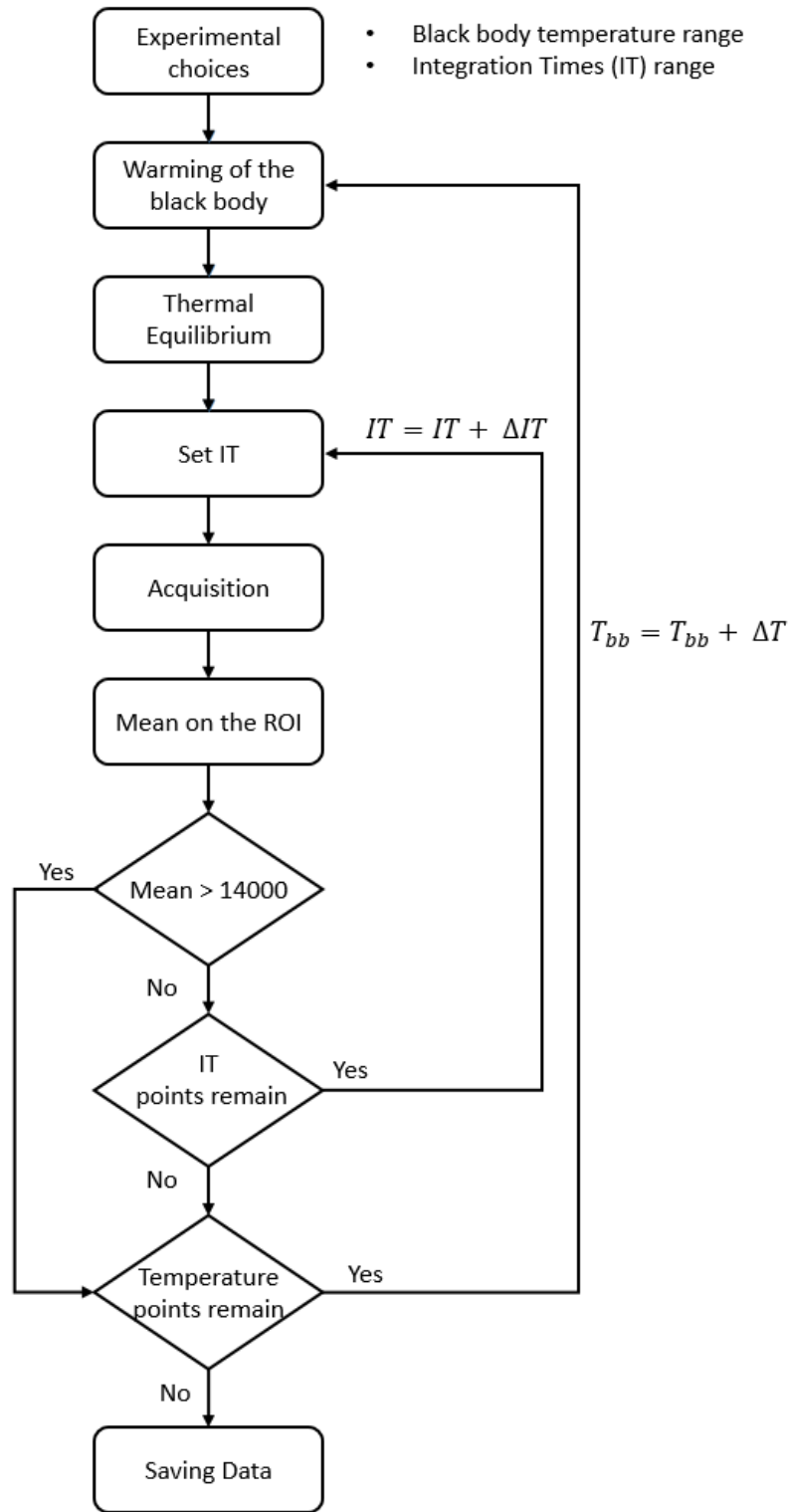


Figure 4.10: Schematic representation of the data acquisition.

#### 4.6. FROM IMAGES TO TEMPERATURE FIELDS: BLACK BODY CALIBRATION

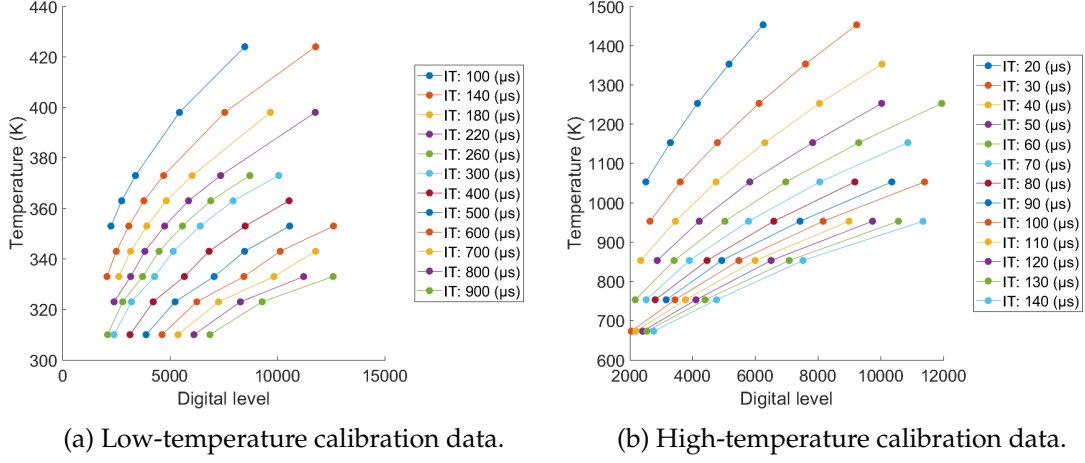


Figure 4.11: Presentation of calibration data.

$$S(T) = \left[ \frac{C}{\exp\left(\frac{c_2}{AT+B}\right) - 1} \right] IT + \text{offset} \quad (4.6)$$

$$T = \frac{1}{A} \left[ c_2 / \ln\left( \frac{C \times IT}{S(T) - \text{offset}} + 1 \right) - B \right] \quad (4.7)$$

with  $c_2$  being the second radiation constant ( $c_2 \approx 1.43 \times 10^{-2} \text{ mK}$ ).

- Flir:

$$S(T) = \left[ \frac{A}{\exp\left(\frac{B}{T}\right) - 1} + C \right] IT + \text{offset} \quad (4.8)$$

$$T = B / \ln\left( \frac{A \times IT}{S(T) - \text{offset} - C \times IT} + 1 \right) \quad (4.9)$$

- Polynomial function:

$$S(T) = \left[ AT^4 + BT^3 + CT^2 + DT + E \right] IT + \text{offset} \quad (4.10)$$

As the reverse function of the polynomial is not easily available, another polynomial of order 4 is assumed to express the temperature as a function of the camera response. This is described in Eq. 4.11.

$$T = A \left[ \frac{S(T) - \text{offset}}{IT} \right]^4 + B \left[ \frac{S(T) - \text{offset}}{IT} \right]^3 + C \left[ \frac{S(T) - \text{offset}}{IT} \right]^2 + D \left[ \frac{S(T) - \text{offset}}{IT} \right] + E \quad (4.11)$$

where coefficients A, B, C, D and E need to be identified for each model, camera and experimental set-up.

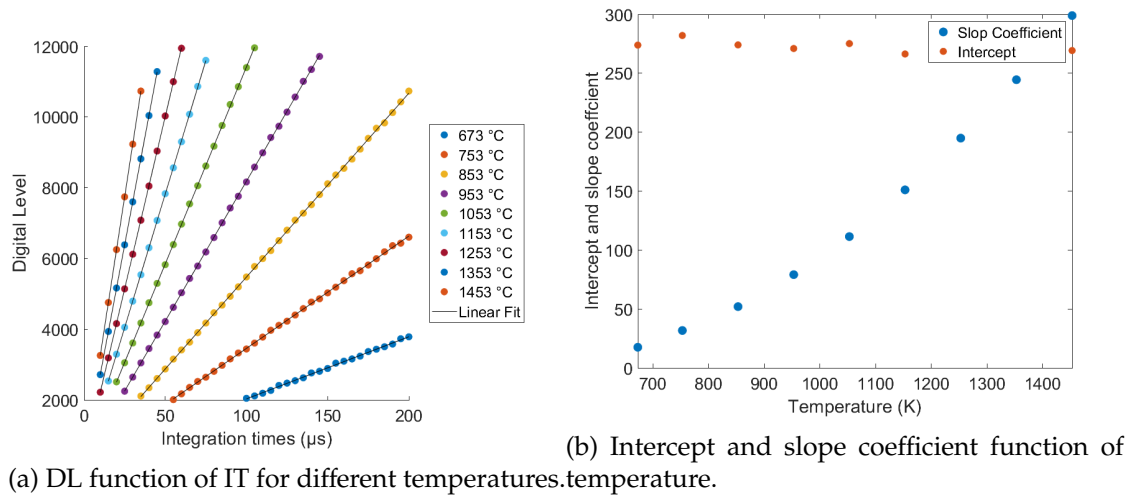


Figure 4.12: Linear fit description of the InSb high-temperature calibration.

### 4.6.3 InSb high-temperature calibration

The first step of the calibration is to compute the linear dependency between the camera response ( $S(T)$ ) and the integration times, as shown in Figure 4.12a. The coefficients of different linear fits are presented in Figure 4.12b. The intercept is constant for each fit, whereas the slope coefficient depends on the temperature.

The slope coefficient is then fitted with the different models presented in Section 4.6.2. Parameters A, B and C are first found in Figure 4.13a and then used to identify the temperature as a function of the slope coefficient (Figure 4.13b). For the Sakuma Planck case the Flir model and two different fits are implemented for the polynomial function. Nonlinear regression is used to identify different parameters with the Levenberg–Marquardt algorithm [99, 100, 101].

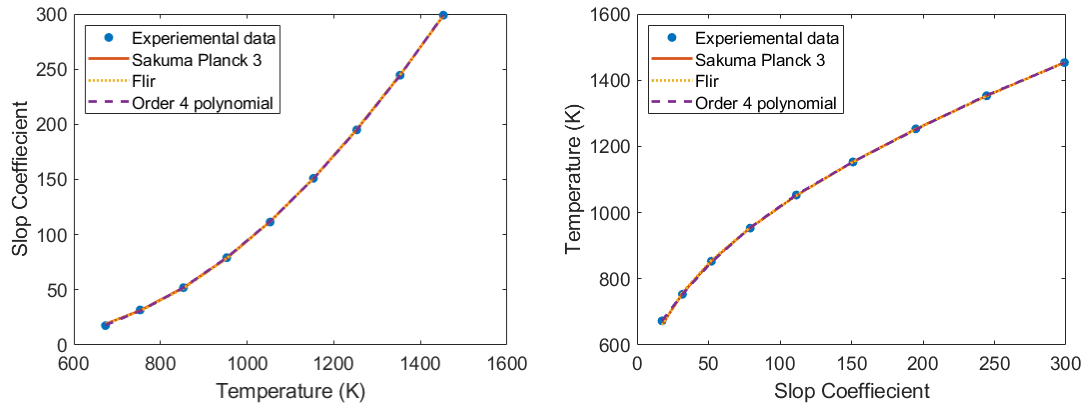
Each model verifiably matches the data, and it is not possible to choose one at this step.

Finally, the fits are used to express the temperature as a function of DL for different ITs, as described in Figure 4.14. The lower mean squared error (MSE) is computed for each fit.

Comparison of the MSE obtained from each model to the accuracy of the black body indicates that the only model that does not introduce bias is the polynomial fit.



#### 4.6. FROM IMAGES TO TEMPERATURE FIELDS: BLACK BODY CALIBRATION



(a) Slope coefficient function of temperature. (b) Temperature function of the slope coefficient.

Figure 4.13: Slope coefficient fitting for InSb high-temperature calibration.

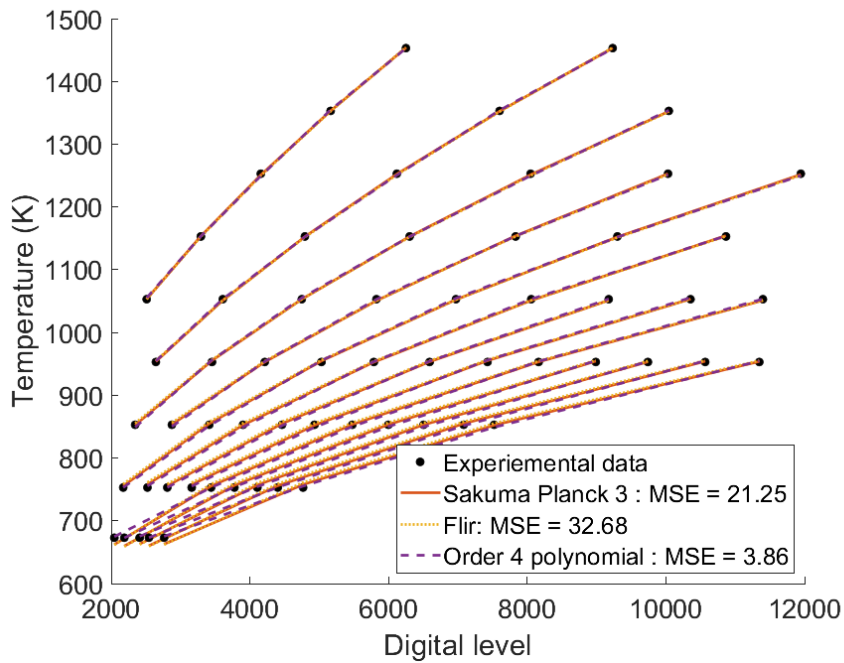


Figure 4.14: Projection of the fit atop the data.

#### 4.6. FROM IMAGES TO TEMPERATURE FIELDS: BLACK BODY CALIBRATION

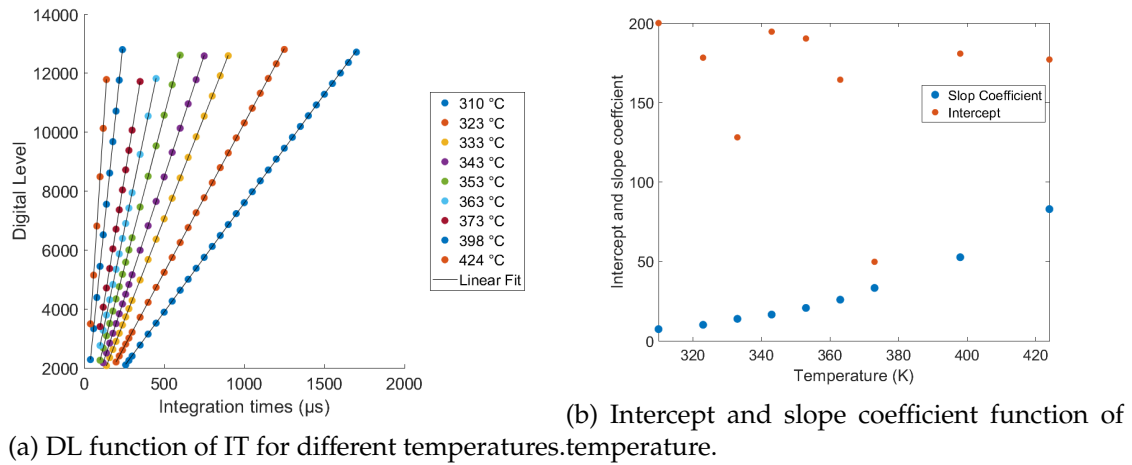


Figure 4.15: Linear fit description.

#### 4.6.4 InSb low-temperature calibration

The first step of the calibration is to compute the linear dependency between the camera response ( $S(T)$ ) and the integration times, as shown in Figure 4.15a. The coefficients of different linear fits are presented in Figure 4.15b. Once again, the intercept is constant for each fit, whereas the slope coefficient is dependent on the temperature.

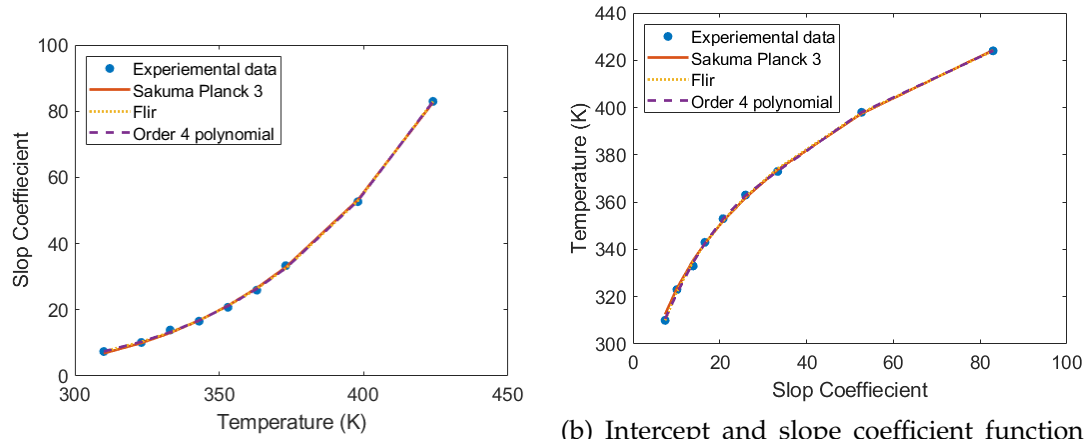
The slope coefficient is now fitted with the different models presented in Section 4.6.2. For the Sakuma Planck case and the Flir model, the parameters identified in Figure 4.16a are also used in Figure 4.16b, based on Eqs. 4.6, 4.7, 4.8 and 4.9.

For the polynomial fit, two sets of parameters are identified.

Finally, those fits are used to express the temperature as a function of DL for different ITs, as described in Figure 4.17. All the used models have an MSE lower than the accuracy of the black body used for the calibration. Thus, they do not introduce error. The lowest MSE is obtained with the Flir fit; nevertheless, for consistency with the previous calibration, the polynomial fit is used.

Using a model that tends to physically represent the integer of Planck's law weighted by the camera's spectral sensitivity would be ideal. Nevertheless, those fits are hard to implement because of the inverse method used, and the multiple local maxima found during minimisation are not always the global maxima. Even if the polynomial fit is less sophisticated, it shows good results and is easier to implement due to the uniqueness of the solution. Moreover, the 4th-order polynomial can be seen as a Stefan–Boltzmann law (Eq. 2.4), and deviations is attributed to the lower-order components of Eq. 4.11.

4.6. FROM IMAGES TO TEMPERATURE FIELDS: BLACK BODY CALIBRATION



(a) DL function of IT for different temperatures. temperature.

(b) Intercept and slope coefficient function of

Figure 4.16: Slope coefficient fitting for InSb low-temperature calibration.

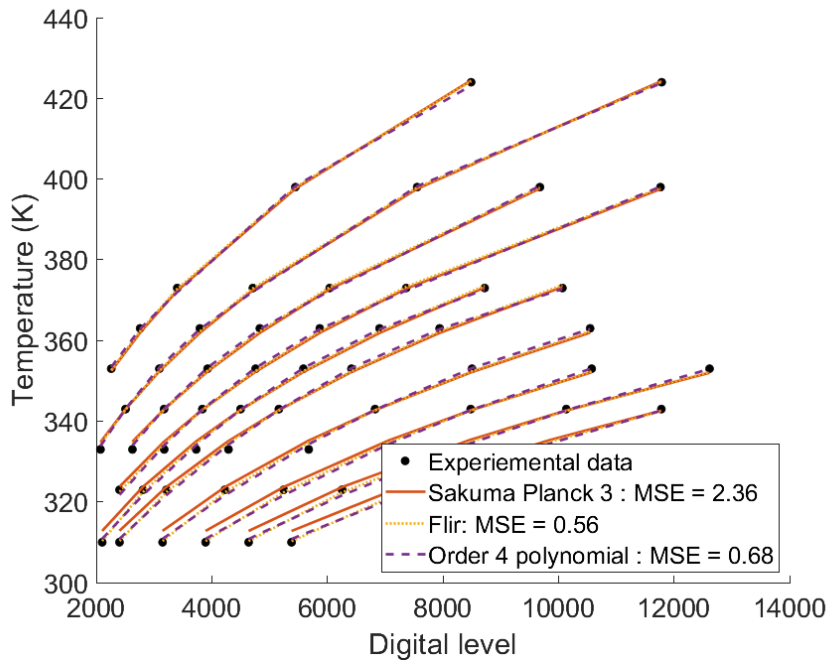


Figure 4.17: Projection of the fit atop the data.

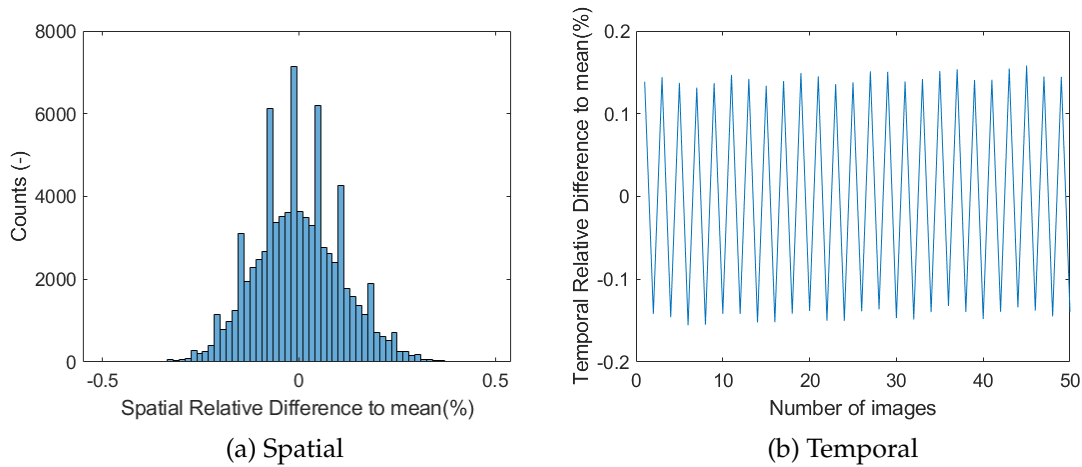


Figure 4.18: Relative difference.

#### 4.6.5 Sensitivity to camera noise

By placing a black body at a constant temperature in front of the camera lens, the sensor noise can be quantified.

Figure 4.18 shows a histogram of the spatial (Figure 4.18.a) and temporal (Figure 4.18.b) relative differences to the mean value observed on the black body. The spatial noise follows a Gaussian law, whereas the temporal noise oscillates around a mean value.

While here the noise is studied for short time periods, the effect of the sensor’s inherent deviations over the course of a day must be considered. To do so, the preceding operation is repeated every 30 minutes over 6 hours, with the corresponding results shown in Figure 4.19. The maximum variation observed rises 3% after 5 hours. One can suppose that this variation is principally dependent on the sensor temperature, which is 76 K at the beginning of the day and 76.6 K at the end of the experiment.

By comparing variation over short and long time scales, the difference in sensitivity is observed to be one order of magnitude. Specifically, the long-term variation ranges from approximately 0% to 3%, and the short-term variation range is  $\pm 0.5\%$ . This is problematic because experiments are often performed over short time intervals (minute scale), whereas calibrations take days. By introducing 3% noise into the calibration function described earlier, one can estimate the error obtained during temperature measurements. Figure 4.20 shows the computed error based on noise for both low-temperature (Figure 4.20a) and high-temperature (Figure 4.20b) calibration.

4.6. FROM IMAGES TO TEMPERATURE FIELDS: BLACK BODY CALIBRATION

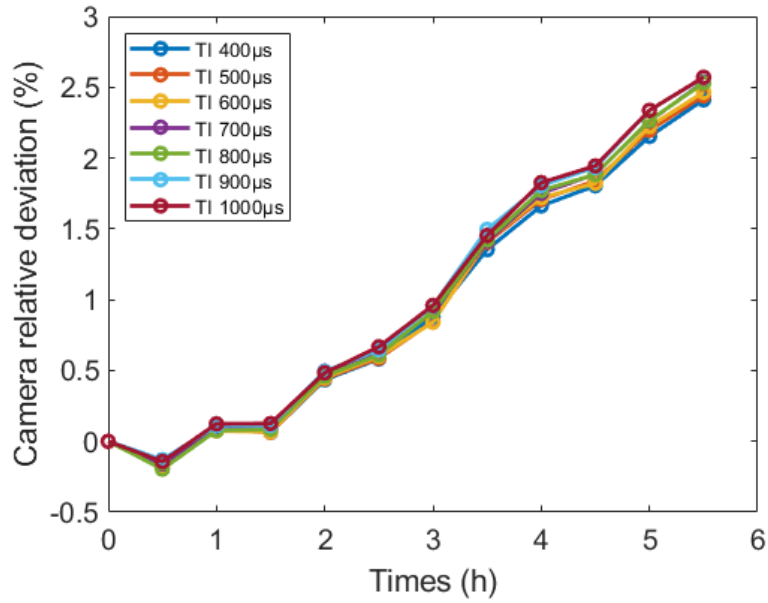
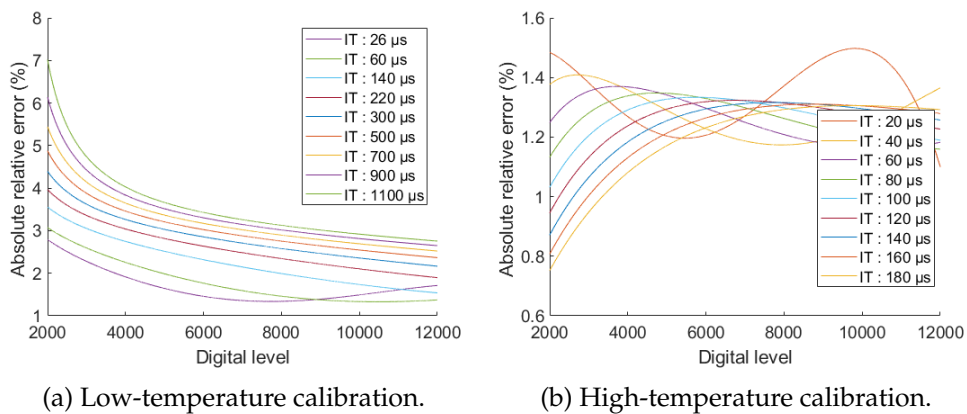


Figure 4.19: Relative measured camera deviation.



(a) Low-temperature calibration.

(b) High-temperature calibration.

Figure 4.20: Computed error from temperature measurements due to camera noise.

#### 4.6. FROM IMAGES TO TEMPERATURE FIELDS: BLACK BODY CALIBRATION

---

Considering the black body accuracy, the error of the fit and the long-term camera deviation, one can conclude that the DL-temperature precision range is between  $\pm 2\%$  and  $\pm 5\%$

##### 4.6.6 Conclusions regarding the black body calibration

- Black body calibration is a key step in temperature measurements with infrared sensors.
- In this presentation, the aspect of distance between object to camera is not considered, but this aspect introduces high variations with working distances under one metre.
- A complete set-up is developed for both the acquisition and data processing to match the experimental set-up used for the ATR method.
- The camera deviation is quantified to estimate the measurement precision.
- Based on the calibration, one can measure the temperature, but only if the observed scene is black.

## 4.7 Presentation of ATR

Parts of the following sections are taken from two scientific publications composed over the course of this thesis program. The first is already published [54], and the second is a conference paper submitted to the 16<sup>th</sup> Quantitative Infrared Thermography Conference and is currently being peer-reviewed.

### 4.7.1 Radiative balance

To describe the radiative balance that occurs during temperature measurements, one must introduce the experimental set-up used.

Considering a **transparent** atmosphere and **opaque** surfaces, the radiative intensity leaving a surface ( $I_l$ :  $W \cdot m^{-2} \cdot sr^{-1} \cdot \mu m^{-1}$ ) at  $\vec{x}$  (with outwards normal  $\vec{n}$ ) and incident to the camera in direction  $\vec{\omega}_r$  (Figure 4.1) is the sum of emitted ( $I_e$ :  $W \cdot m^{-2} \cdot sr^{-1} \cdot \mu m^{-1}$ ) and reflected ( $I_r$ :  $W \cdot m^{-2} \cdot sr^{-1} \cdot \mu m^{-1}$ ) radiative intensities (see Eq. 4.12). Both quantities depend on the local temperature since the emissivity, the reflectivity or Planck's law depends on it.

$$I_l(T(\vec{x}), \vec{\omega}_r, \lambda) = I_e(T(\vec{x}), \vec{\omega}_r, \lambda) + I_r(T(\vec{x}), \vec{\omega}_r, \lambda) \quad (4.12)$$

Due to the beam splitter (Figure 4.6) in the optical path from the sample to the IR camera, the monochromatic radiative intensity arriving at the camera ( $I_l$ ) results in the superposition of the radiative intensity leaving the sample surface at  $\vec{x}$  towards the camera (Eq. 4.12, which is transmitted by the beam splitter,  $\tau_{bs}$ ) and the background radiative intensity reflected by the beam splitter. This background intensity,  $I_{bd}$ , comes from the beam dump emission and reflections.

$$I_l(T(\vec{x}), \vec{\omega}_r, \lambda) = \tau_{bs} \left[ I_e(T(\vec{x}), \vec{\omega}_r, \lambda) + I_r(T(\vec{x}), \vec{\omega}_r, \lambda) \right] + I_{bd} \quad (4.13)$$

Because the beam dump is positioned far from the camera's sharp field of view, one can consider that  $I_{bd}$  is **negligible** ( $I_{bd} \approx 0$ ). The radiative intensity emitted by any kind of opaque body in a direction  $\vec{\omega}_r$  is the product of the black body radiative intensity (Eq. 2.2) and the directional emissivity ( $\varepsilon'$ ) (Eq. 4.14):

$$I_e(T(\vec{x}), \vec{\omega}_r, \lambda) = \varepsilon'(T(\vec{x}), \vec{\omega}_r, \lambda) I_b(T(\vec{x}), \lambda) \quad (4.14)$$

The directional emissivity  $\varepsilon'$  of an opaque surface is related to the directional-hemispherical reflectivity  $\rho'^{\wedge}$  [31, 102] by Kirchhoff's law (described earlier in Eq. 4.15), whereas the relationship between  $\rho'^{\wedge}$  and the BRDF ( $\rho''$ ) is given in Eq. 4.16:

$$\varepsilon'(T(\vec{x}), \vec{\omega}_r, \lambda) = 1 - \rho'^{\wedge}(T(\vec{x}), -\vec{\omega}_r, \lambda) \quad (4.15)$$

$$\rho'^{\wedge}(T(\vec{x}), \vec{\omega}_i, \lambda) = \int_{2\pi} \rho''(T(\vec{x}), \vec{\omega}_r | \vec{\omega}_i, \lambda) |\vec{n} \cdot \vec{\omega}_r| d\Omega(\vec{\omega}_r) \quad (4.16)$$

where  $\Omega$  is the solid angle (*sr*). As identified in the literature [103, 33],  $I_r$  is the reflected radiative intensity at  $\vec{x}$  in the direction  $\vec{\omega}_r$  and coming from incident directions  $\vec{\omega}_i$  as described in Eq. 4.17:

$$I_r(T(\vec{x}), \vec{\omega}_r, \lambda) = \int_{2\pi} \rho''(T(\vec{x}), \vec{\omega}_r | \vec{\omega}_i, \lambda) I_l(T(\vec{x}'), \vec{\omega}_i, \lambda) |\vec{n} \cdot \vec{\omega}_i| d\Omega(\vec{\omega}_i) \quad (4.17)$$

where  $I_l(T(\vec{x}'), \vec{\omega}_i, \lambda)$  is the radiative intensity coming from the surroundings towards the sample, which originates from  $\vec{x}'$  due to the multiple reflections and emissions in the thermal scene. This quantity is named  $I_{scn} = I_l(T(\vec{x}'), \vec{\omega}_i, \lambda)$ .

Based on Eqs. 4.14 and 4.17 and considering that the camera is perpendicular to the sample ( $\vec{\omega}_r = \perp$ ), Eq. 4.13 can be written as Eq. 4.18 ( $I_{bs} = 0$ ).

$$I_l(T(\vec{x}), \perp, \lambda) = \tau_{bs} \left[ (1 - \rho^{\perp \wedge}) I_b(T(\vec{x}), \lambda) + \int_{2\pi} \rho''(T(\vec{x}), \perp | \vec{\omega}_i, \lambda) I_{scn}(T(\vec{x}'), \vec{\omega}_i, \lambda) |\vec{n} \cdot \vec{\omega}_i| d\Omega(\vec{\omega}_i) \right] \quad (4.18)$$

From the general equation of mixed emission reflection presented in Eq. 4.18, the encountered problem is strongly linked to the directional aspect of the reflected luminous beam. To access  $\rho^{\perp \wedge}$  and  $I_r$ , one must determine all of the BRDFs. As this value depends on many parameters (temperature, surface condition, etc.), the measurement of BRDFs should be conducted as soon as those parameters vary, which is not suited to experiments. Thus, one must find a way to simplify the problem. An easy and versatile approach is to **consider only specular reflection**. As seen in Chapter 3, this hypothesis is valid if the studied wavelengths are larger than the surface roughness [104]. Fortunately, this assumption is applicable in many cases because IR cameras work with long wavelengths.

To ensure that this condition is met, the difference between the wavelength of the camera and the surface roughness must be further studied. To do so, a camera with an MCT or SLS sensor that works at longer wavelengths (8 – 14  $\mu m$ ) can be used towards this goal.



### 4.7.2 Introducing the Fresnel model

The Fresnel model describes the reflection cone of a perfect mirror[105]. It is expressed in Eq. 4.19, where  $Fr(\perp)$  is the normal Fresnel reflectivity that depends on the incident angle;  $\vec{R}(\vec{\omega}_i, \vec{n}(\vec{x}))$  is the specular direction from the incident direction  $\vec{\omega}_i$ , and the surface normal  $\vec{n}(\vec{x})$  and  $\rho_F''$  are the Fresnel BRDFs.

$$\rho_F''(\vec{x}, \perp | \vec{\omega}_i, \lambda) = \frac{Fr(\vec{x}, \perp, \lambda) \delta(\perp - \vec{R}(\vec{\omega}_i, \vec{n}(\vec{x})))}{|\vec{n}(\vec{x}) \cdot \perp|} \quad (4.19)$$

Considering the sample as an optical mirror with unknown reflectivity implies that for a given  $\vec{\omega}_r$ , there is only one direction  $\vec{\omega}_i$  for which  $\rho_F''(\vec{x}, \vec{\omega}_r | \vec{\omega}_i, \lambda) \neq 0$ . In the specific case of a normal reflection ( $\vec{\omega}_r = \perp$ ), the only incident direction ( $\vec{\omega}_i$ ) for which  $\rho_F''(\perp | \vec{\omega}_i, \vec{x}, \lambda) \neq 0$  is the normal incident direction ( $\vec{\omega}_r = \vec{\omega}_i = \perp$ ). Thus, the specular BRDF expression (Eq. 4.19) is replaced in Eqs. 4.16 and 4.17 to lead to Eqs. 4.20 and 4.21, respectively. To simplify the notation,  $\rho_F''(\vec{x}, \perp | \perp, \lambda)$  is denoted by  $\rho_F^\perp(\vec{x}, \lambda)$ :

$$\rho^{\perp \cap}(T(\vec{x}), \lambda) = \rho_F^\perp(T(\vec{x}), \lambda) \quad (4.20)$$

$$I_r(T(\vec{x}), \perp, \lambda) = \rho_F^\perp(T(\vec{x}), \lambda) I_{scn}^\perp \quad (4.21)$$

Based on Eqs. 4.20 and 4.21, Eq. 4.18 can be written as:

$$I_l(T(\vec{x}), \perp, \lambda) = \tau_{bs} \left[ \left( 1 - \rho_F^\perp(T(\vec{x}), \lambda) \right) I_b(T(\vec{x}), \lambda) + \rho_F^\perp(T(\vec{x}), \lambda) I_{scn}^\perp \right] \quad (4.22)$$

As the camera integrates the radiative intensity field on its wavelength range  $[\lambda_1, \lambda_2]$  and a minuscule opening angle  $\Delta\Omega^\perp$  around the sample's surface normal, one can introduce the radiant flux density measured by a camera pixel  $\dot{q}^l$  as follows:

$$\dot{q}^l(T(\vec{x}), \perp) = \int_{\Delta\Omega^\perp} d\vec{\omega}_r \int_{\lambda_1}^{\lambda_2} \tau_{bs} \left[ \left( 1 - \rho_F^\perp(T(\vec{x}), \lambda) \right) I_b(T(\vec{x}), \lambda) + \rho_F^\perp(T(\vec{x}), \lambda) I_{scn}^\perp \right] d\lambda \quad (4.23)$$

Following the introduction of this model for the camera response to a specular sample, the model is evaluated for a numerical case and validated experimentally at ambient temperatures.

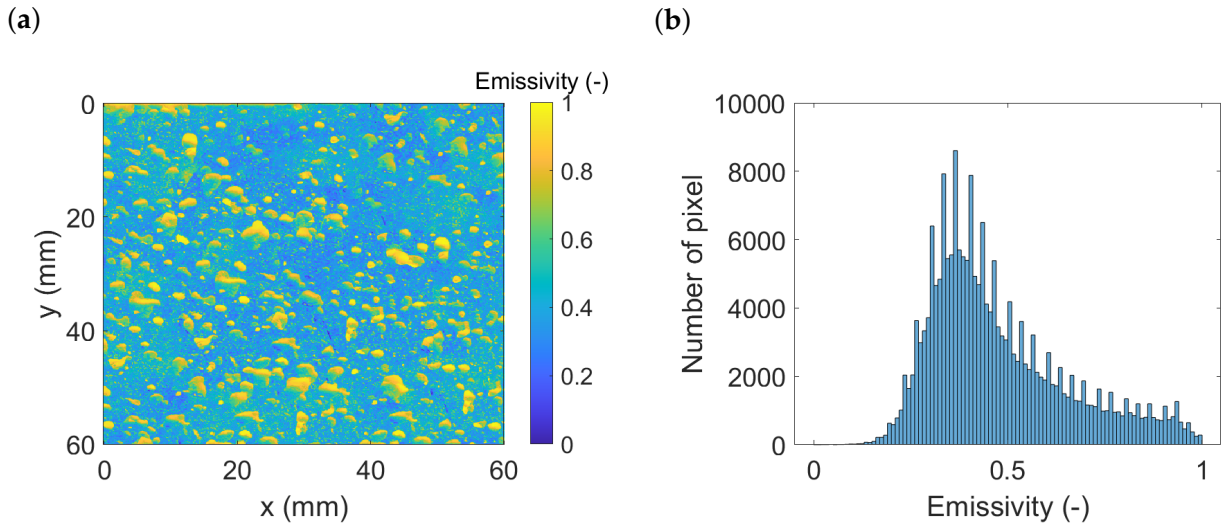


Figure 4.21: Presentation of the numerical study: (a) emissivity field, (b) histogram of emissivity.

### 4.7.3 Illustration of the model for numerical cases

Four numerical examples of thermography measurements are presented. These examples implement the radiometric model described above and illustrate the difficulties that can arise from variations in optical properties and the effects of surrounding irradiation. To represent cases of interest, a metal object at 300 K with a specular surface is considered. The emissivity field is extracted from [106]. Figure 4.21.a shows the emissivity field, and Figure 4.21.b shows the histogram of emissivity values. The emissivity distribution is heterogeneous, extending from 0 (-) to 1 (-), with a maximum distribution at 0.4 (-).

The surrounding radiation coming from the scene is assumed to follow Planck's law at a constant temperature, which can lead to the following three cases.

- The first occurs when the environment is at a lower temperature than the studied sample:  $I_e(T(\vec{x})) > I_{scn}(T(\vec{x}'))$ . To illustrate this situation, one can simulate a surrounding field at a homogeneous temperature (290 K), which carries a radiative intensity field  $1.28 \text{ W} \cdot \text{m}^{-2} \cdot \text{sr}^{-1}$ . This case can also represent an environment at the same temperature as the studied sample but with a low uniform emissivity.
- The second configuration occurs when the surroundings have a temperature similar to that of the sample:  $I_e(T(\vec{x})) \approx I_{scn}(T(\vec{x}'))$ . To illustrate this situation, one can simulate a surrounding field at

a homogeneous temperature (300 K), which carries a radiative intensity field  $1,87 \text{ W} \cdot \text{m}^{-2} \cdot \text{sr}^{-1}$ .

- The third configuration occurs when the sample is at a lower temperature than the surrounding sample:  $I_e(T(\vec{x})) < I_{scn}(T(\vec{x}'))$ . To illustrate this situation, one can simulate a surrounding field at a homogeneous temperature (350 K), which carries a radiative intensity field  $9,1 \text{ W} \cdot \text{m}^{-2} \cdot \text{sr}^{-1}$ .

Finally, a fourth configuration with a more realistic simulation of the surrounding environment is considered. It involves multiple sources with a high variability of optical properties.

For each configuration, the radiant flux density is obtained by integrating the radiative intensity between  $\lambda_1 = 2,5 \mu\text{m}$  and  $\lambda_2 = 5 \mu\text{m}$  to simulate an IR camera sensor.

The surrounding radiant flux density detected by the camera through a perfect mirror is presented in Figure 4.22.a for the first case and Figure 4.22.b for the fourth case. The density corresponds to the second term of Eq. 4.23 and is referred to as  $\dot{q}_m^r$ . The density detected by the camera through the heterogeneous specular sample ( $\dot{q}_s^r$ ) is shown in Figure 4.22.c for the first case and Figure 4.22.d for the fourth case.

Based on the emitted ( $I_e$ ) and reflected ( $I_r$ ) intensities, the radiant flux density leaving the sample ( $\dot{q}_s^l = \dot{q}_l / \Delta\Omega^\perp$ ) is computed for the four different (see Eq. 4.20) cases, as depicted in Figure 4.23.

At this step, there is an unlikely conclusion. If the surrounding irradiation is at the same temperature as the studied sample, the signal of the camera is uniform and correct over the whole image (case 2, Figure 4.23). However, the measurement is totally invalid because of the emissivity and reflections. This phenomenon can be explained with Eq. 4.23. By considering  $I_b \approx I_{scn}^\perp$ , Eq. 4.23 can be written as Eq. 4.24.

$$\dot{q}_s^l(T(\vec{x}), \perp) \approx \int_{\Delta\Omega^\perp} d\vec{\omega}_r \int_{\lambda_1}^{\lambda_2} d\lambda \tau_{bs} \left[ I_b(T(\vec{x}), \lambda) \right] \quad (4.24)$$

Thus, the reflected flux compensates for the emitted flux variation (due to emissivity), and the signal given by the camera is uniform. Although this case is numerical and the field obtained is perfectly homogeneous, it is representative of many experimental cases at room temperature, with camera images being almost homogeneous despite emissivity field heterogeneity. In this specific case, the measured field temperature seems almost constant and correct, whereas the measurement is biased by reflection.

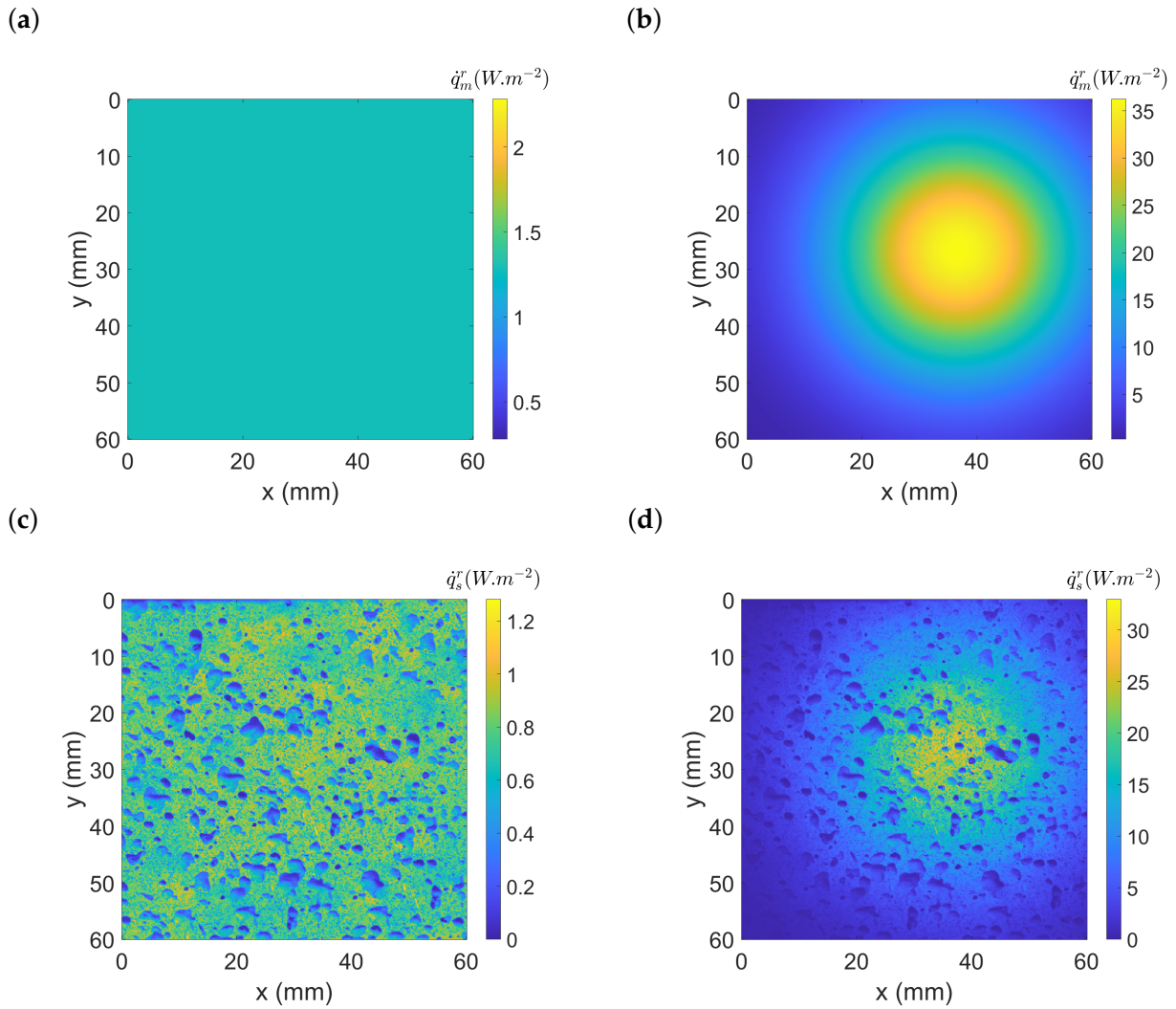


Figure 4.22: The surrounding radiant flux density is detected by the camera through a perfect mirror, (a) and (b), or through the heterogeneous sample, (c) and (d), in a homogeneous irradiation configuration (290 K), (a) and (c), and in a heterogeneous irradiation case, (b) and (d).

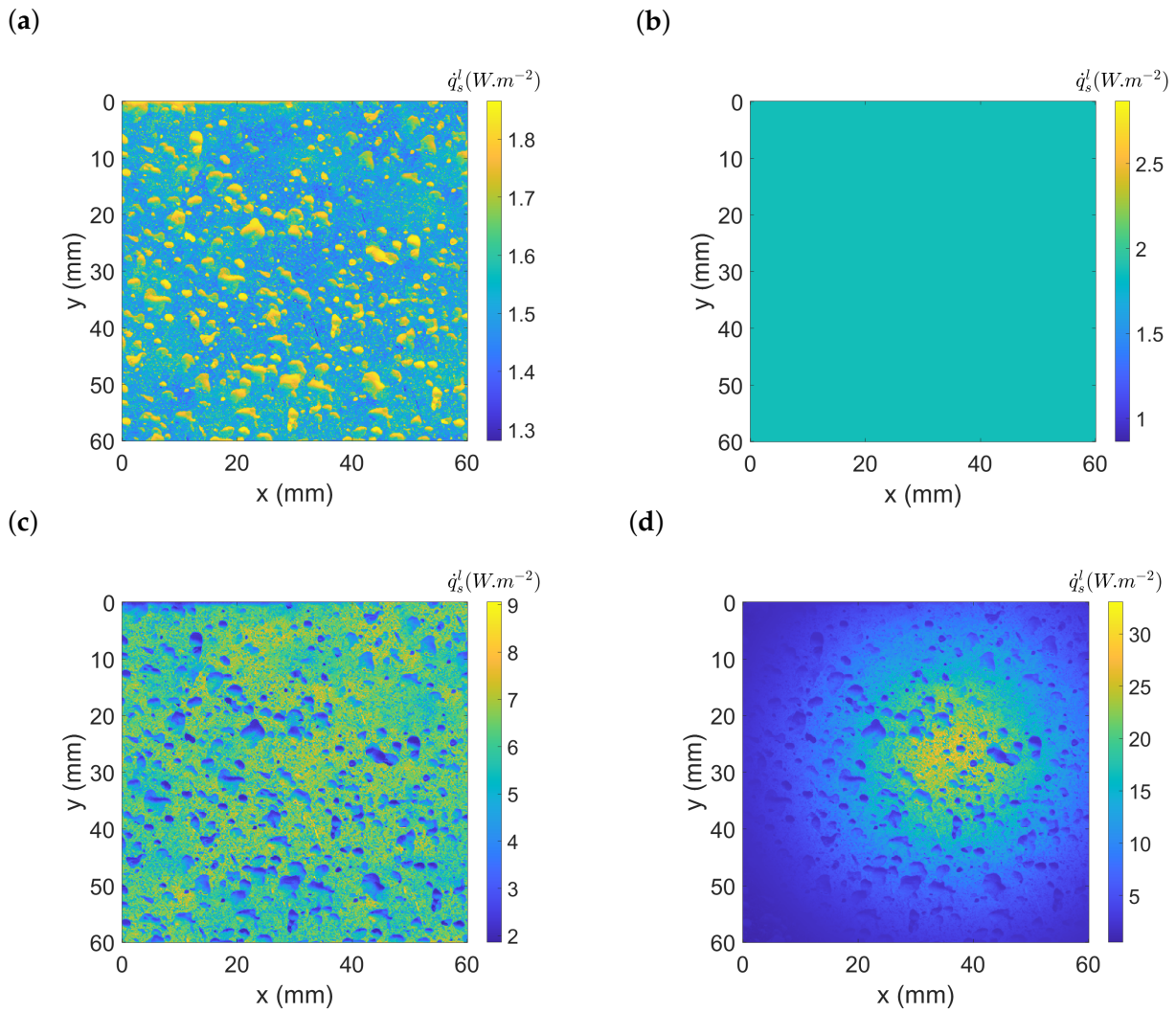


Figure 4.23: Radiative flux leaving ( $\dot{q}_s^l$ ) the sample (300 K) with different black body equivalent temperatures of the surrounding scene: (a) uniform at 290 K; (b) uniform at 300 K; (c) uniform at 350 K; (d) heterogeneous case.

In contrast, for the other cases, the radiative intensity leaving the sample is insufficient for measuring the temperature. For those reasons, we have developed a new method called ATR, which is presented in the following section.

#### 4.7.4 Presentation of ATR

The ATR method seeks to identify  $T(\vec{x})$  from the radiometric model of Eq. 4.23. To achieve this goal, the proposed method includes 7 steps:

1. determine a black body calibration relationship to link  $\int d\lambda \tau_{bs} I_b(T(\vec{x}), \perp, \lambda)$  to  $T(\vec{x})$ ,
2. acquire a raw image of the sample:  $\dot{q}_s^l(T(\vec{x}), \perp)$ ,
3. estimate the scene's reflection on the sample:  $\int d\lambda \tau_{bs} I_{scn}$ ,
4. estimate the sample's normal-normal reflectivity:  $\rho_{F,s}^\perp$ ,
5. compute the sample's transmitted emittance:  $\dot{q}_s^e$ ,
6. compute the sample's transmitted black body emittance  $\dot{q}_s^b$ , and
7. infer the sample's true temperature with its emissivity and black body calibration.

The **first** and **second** steps have been described previously (Sections 4.6 and 4.7.3). The camera calibration is introduced in Section 4.6, and the acquisition of  $\dot{q}_l$  corresponds to the raw image produced by the IR camera. In the **third** step, the radiative contribution ( $I_{scn}$ ) of the surroundings must be determined. Towards this aim, we introduce  $\dot{q}_{m,1}$  since the sample is assumed to be specular. This corresponds to the pixel-based camera response during the closed chopper position when imaging the reference mirror.

$$\dot{q}_{m,1}(T(\vec{x}), \perp) = \Delta\Omega^\perp \int_{\lambda_1}^{\lambda_2} d\lambda \tau_{bs} \left[ \left(1 - \rho_{F,m}^\perp(T(\vec{x}), \lambda)\right) I_b(T(\vec{x}), \lambda) + \rho_{F,m}^\perp(T(\vec{x}), \lambda) I_{scn}^\perp \right] \quad (4.25)$$

where  $\lambda_1$  and  $\lambda_2$  are the bounds of the camera spectral window,  $\Delta\Omega^\perp$  corresponds to a pixel solid angle and  $\rho_{F,m}^\perp$  is the mirror's specular reflectivity. The thermal emission of the reference mirror with  $\rho_{F,m}^\perp \approx 1$  may be neglected, and Eq. 4.25 can be simplified to:



$$\dot{q}_{m,1}(T(\vec{x}), \perp) = \Delta\Omega^\perp \int_{\lambda_1}^{\lambda_2} d\lambda \tau_{bs} I_{scn}^\perp \quad (4.26)$$

To estimate  $\dot{q}_{m,1}$ , the reference mirror must be placed in the exact same position and orientation as the sample. The **fourth** step is particularly important. To determine the sample's specular reflectivity, we introduce  $\dot{q}_{s,1}$  and  $\dot{q}_{s,2}$  to represent the pixel-based camera response with the chopper in closed and open positions, respectively. To express  $\dot{q}_{s,2}$ , we introduce the nearly collimated radiation  $I_{BB}^\perp$  coming from the black body at a normal incident angle. Under these conditions,  $\dot{q}_{s,1}$  and  $\dot{q}_{s,2}$  are expressed as in Eqs. 4.27 and 4.28, respectively.

$$\begin{aligned} \dot{q}_{s,1}(T(\vec{x}), \perp) = \Delta\Omega^\perp \int_{\lambda_1}^{\lambda_2} d\lambda \tau_{bs} \left[ (1 - \rho_{E,s}^\perp(T(\vec{x}), \lambda)) I_b(T(\vec{x}), \lambda) + \right. \\ \left. \rho_{E,s}^\perp(T(\vec{x}), \lambda) I_{scn}^\perp \right] \end{aligned} \quad (4.27)$$

$$\begin{aligned} \dot{q}_{s,2}(T(\vec{x}), \perp) = \Delta\Omega^\perp \int_{\lambda_1}^{\lambda_2} d\lambda \tau_{bs} \left[ (1 - \rho_{E,s}^\perp(T(\vec{x}), \lambda)) I_b(T(\vec{x}), \lambda) + \right. \\ \left. \rho_{E,s}^\perp(T(\vec{x}), \lambda) (I_{scn}^\perp + I_{BB}^\perp) \right] \end{aligned} \quad (4.28)$$

Then, the image of the sample in the absence of the reflection of the black body ( $\dot{q}_{s,1}$ ) is subtracted from the image with the source reflection ( $\dot{q}_{s,2}$ ). This eliminates the reflection from the surroundings and the sample's thermal emission:

$$\dot{q}_{s,2} - \dot{q}_{s,1} = \Delta\Omega^\perp \int_{\lambda_1}^{\lambda_2} d\lambda \tau_{bs} \rho_{E,s}^\perp(T(\vec{x}), \lambda) I_{BB} \quad (4.29)$$

To evaluate  $I_{BB}$ , an additional measurement is performed on a reference mirror with a known reflectivity  $\rho_{E,m}^\perp$  considered equal to one:

$$\dot{q}_{m,2} - \dot{q}_{m,1} = \Delta\Omega^\perp \int_{\lambda_1}^{\lambda_2} d\lambda \tau_{bs} I_{BB} \quad (4.30)$$

The ratio of these differences (Eqs. 4.29-4.30) is used to evaluate the specular normal-normal reflectivity of the sample ( $\rho_{E,s}^\perp$ ).

$$\frac{\dot{q}_{s,2} - \dot{q}_{s,1}}{\dot{q}_{m,2} - \dot{q}_{m,1}} = \frac{\int_{\lambda_1}^{\lambda_2} d\lambda \tau_{bs} \rho_{E,s}^\perp(T(\vec{x}), \lambda) I_{BB}}{\int_{\lambda_1}^{\lambda_2} \tau_{bs} I_{BB} d\lambda} = \tilde{\rho}_{E,s}^\perp(T(\vec{x})) \quad (4.31)$$

This ratio corresponds to the averaged sample reflectivity weighted by the radiative intensity of the black body source and is denoted by  $\tilde{\rho}_{F_s}^\perp$ .

To achieve the **fifth** step, the radiometric equation (Eq. 4.23) needs to be solved to obtain the black body radiative intensity of the sample. This requires knowledge of  $\rho_{F_s}^\perp$  (Eq. 4.31) and  $I_{scn}^\perp$  (Eq. 4.26) and the assumption that  $\rho_{F_s}^\perp$  is constant inside the wavelength range  $[\lambda_1, \lambda_2]$ , leading to  $\rho_{F_s}^\perp = \tilde{\rho}_{F_s}^\perp$ . Thus, an expression of the sample's emittance  $\dot{q}_s^e$  transmitted to the camera in its spectral window may be written as:

$$\dot{q}_s^e = \Delta\Omega^\perp \left( 1 - \tilde{\rho}_{F_s}^\perp(T(\vec{x})) \right) \int_{\lambda_1}^{\lambda_2} d\lambda \tau_{bs} I_b(T(\vec{x}), \lambda) \quad (4.32)$$

and computed with Eq. 4.27, where the reflected surrounding radiative flux is removed using the reflectivity and Eq. 4.26:

$$\dot{q}_s^e = \dot{q}_{s,1}(T(\vec{x}), \perp) - \tilde{\rho}_{F_s}^\perp(T(\vec{x})) \dot{q}_{m,1}(T(\vec{x}), \perp) \quad (4.33)$$

The **sixth** step involves dividing the sample transmitted emittance ( $\dot{q}_s^e$ ) by the constant sample emissivity ( $1 - \tilde{\rho}_{F_s}^\perp$ ) to compute the transmitted black body emittance ( $\dot{q}_s^b$ ), expressed in Eq. 4.34.

$$\dot{q}_s^b = \frac{\dot{q}_s^e}{1 - \tilde{\rho}_{F_s}^\perp(T(\vec{x}))} \quad (4.34)$$

The **last** step makes use of the measured reflectivity and the previously recorded calibration relationship, Eq. 4.10, and links the sample's true temperature to the sample's black body equivalent emittance ( $\dot{q}_s^b$ ), which is then transmitted to the camera (Eq. 4.11).

$$T(\vec{x}) = g \left[ S(\dot{q}_s^b) \right] \quad (4.35)$$

#### 4.7.5 Numerical validation of ATR

The example studied in Section 4.7.3 is used to numerically validate the ATR method. The illumination beam ( $I_{BB}$ ) is simulated with normally collimated black body radiation at 400 K. The illumination is chosen to be circular to match the experimental set-up. Figure 4.24 shows the experi-



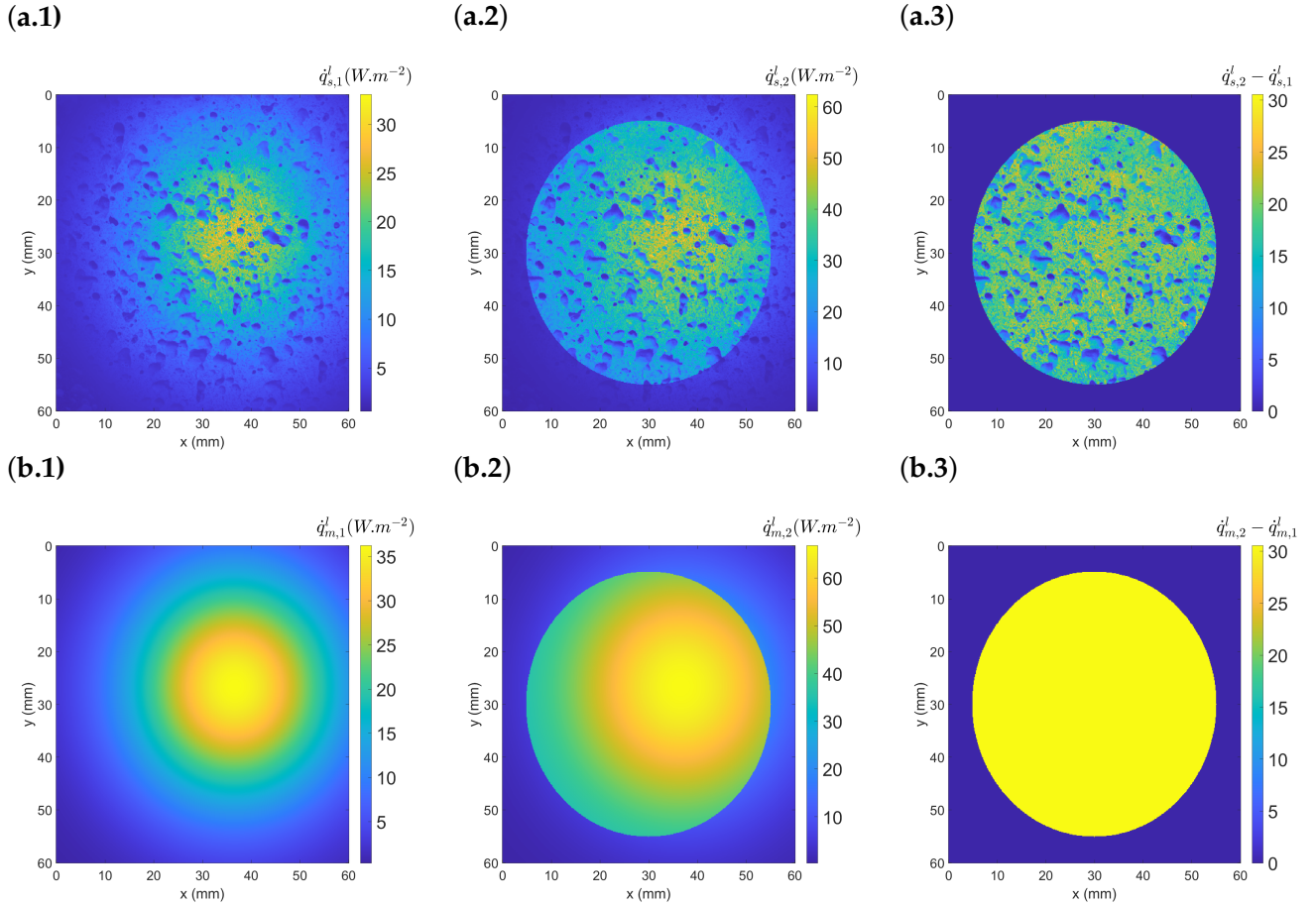


Figure 4.24: Simulated camera response (step 2 of ATR) for a heterogeneous sample (a) and a reference mirror (b): (a.1) radiative image from the sample  $\dot{q}_{s,1}$ ; (a.2) radiative image from the illuminated sample  $\dot{q}_{s,2}$ ; (a.3) difference between both images  $\dot{q}_{s,2} - \dot{q}_{s,1}$ ; (b.1) radiative image from the mirror  $\dot{q}_{m,1}$ ; (b.2) radiative image from the illuminated mirror  $\dot{q}_{m,2}$ ; (b.3) difference between both images  $\dot{q}_{m,2} - \dot{q}_{m,1}$ .

mental part of the ATR method with simulated infrared images of a heterogeneous specular sample and a reference mirror (steps 2, 3 and 4).

Figure 4.25 corresponds to the data processing method. Figure 4.25.a corresponds to the measurement of  $\tilde{\rho}_{F,s}$  described in step 4, where the division of  $\dot{q}_{s,2} - \dot{q}_{s,1}$  (Figure 4.24.a.3) by  $\dot{q}_{m,2} - \dot{q}_{m,1}$  (Figure 4.24.b.3) is performed. Figure 4.25.b illustrates the measured emissivity maps obtained with Eq. 4.15. The determination of  $\dot{q}_s^e$  (fifth step) is realised with  $\dot{q}_{s,1}$  (Figure 4.24.a.1),  $\dot{q}_{m,1}$  (Figure 4.24.b.1) and  $\tilde{\rho}_{F,s}$  (Figure 4.25.a) and shown in Figure 4.25.c. Then, the black body equivalent emittance ( $\dot{q}_s^b$ ) is determined using  $\dot{q}_s^e$  and the emissivity maps  $(1 - \tilde{\rho}_{F,s}^\perp)$  described in Figure 4.25.d.

#### 4.7. PRESENTATION OF ATR

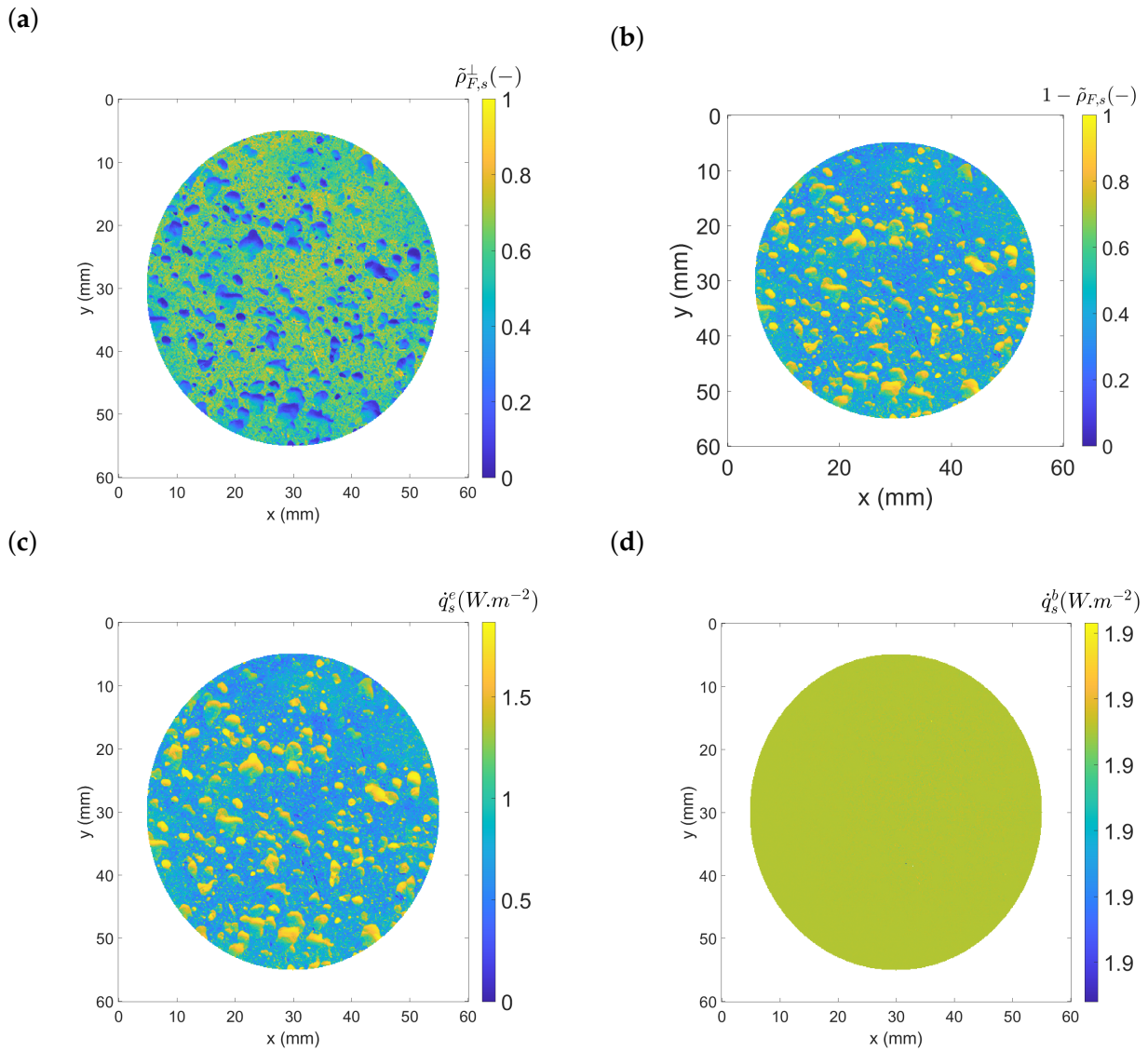


Figure 4.25: Illustration of the ATR method (a) normal reflectivity  $\tilde{\rho}_{F,s}^{\perp}$ ; (b) emissivity  $(1 - \tilde{\rho}_{F,s}^{\perp})$ ; (c) sample emittance  $\dot{q}_s^e$ ; (d) sample black body emittance  $\dot{q}_s^b$ .

## 4.8. VALIDATION OF ATR ON HETEROGENEOUS SAMPLES AT AMBIENT TEMPERATURES

---

The obtained emittance is constant along all specimens. Then, with the calibration curves, one can identify the temperature from  $\dot{q}_s^b$  (Figure 4.25.d). In this section, the steps of the ATR method are introduced in a theoretical study, whereas in the next section, they are applied to experimental images of actual samples.

### 4.8 Validation of ATR on heterogeneous samples at ambient temperatures

#### 4.8.1 Stainless steel sample

Figure 4.26 shows the first sample, which is a stainless steel cubic sample with two different surface treatments: (i) rough (untreated) (Figure 4.26.1) and (ii) laser polished (Figure 4.26.2). A detailed description of the samples is given in [107].

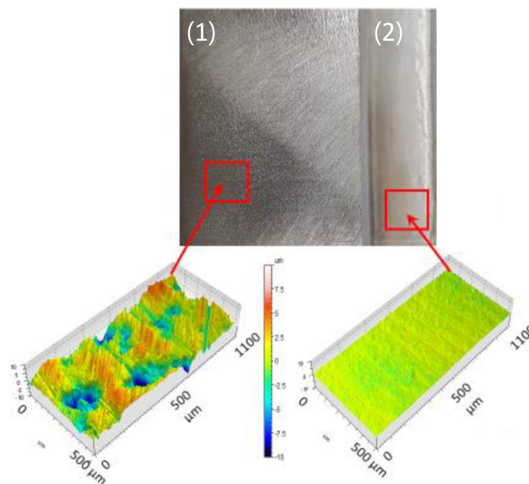


Figure 4.26: Presentation of the stainless steel sample with two surface treatments: (1) rough (untreated) and (2) laser polished.

Figure 4.27 shows the results of step 2 in the ATR method with the recorded thermographic images for both the sample and the reference mirror.

Figure 4.27.a.1 shows the raw DL (proportional to  $\dot{q}_{s,1}$ ) of the sample. There are two parts in Figure 4.27.a.3, corresponding to the rough (untreated, left) and laser-polished (right) surfaces. Figure 4.27.b.1 shows  $\dot{q}_{m,1}$ , where a cold spot is visible due to the cooled camera narcissus, which is also present in Figure 4.27.a.1 [108]. Figure 4.27.a.3 and 4.27.b.3 show the reflections of the black body source on the sample and on the mirror.

#### 4.8. VALIDATION OF ATR ON HETEROGENEOUS SAMPLES AT AMBIENT TEMPERATURES

---

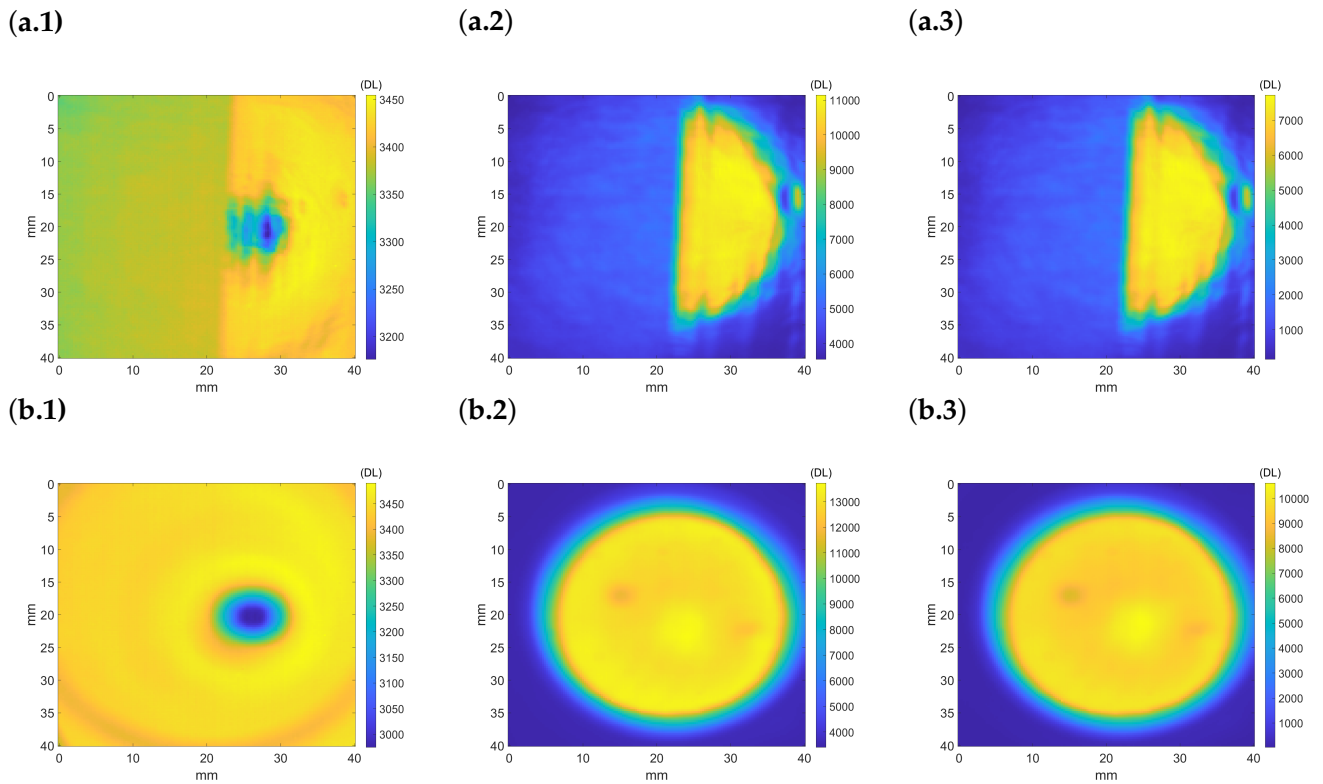


Figure 4.27: Camera measurements (step 2 of ATR) on the (a) stainless steel sample, where the left side is the rough surface and the right is the laser-polished surface, and (b) for the reference mirror. (a.1) raw sample measurement  $\dot{q}_{s,1}$ ; (a.2) illuminated sample  $\dot{q}_{s,2}$ ; (a.3) difference  $\dot{q}_{s,2} - \dot{q}_{s,1}$ ; (b.1) raw mirror measurement  $\dot{q}_{m,1}$ ; (b.2) illuminated mirror  $\dot{q}_{m,2}$ ; (b.3) difference  $\dot{q}_{m,2} - \dot{q}_{m,1}$ .

#### 4.8. VALIDATION OF ATR ON HETEROGENEOUS SAMPLES AT AMBIENT TEMPERATURES

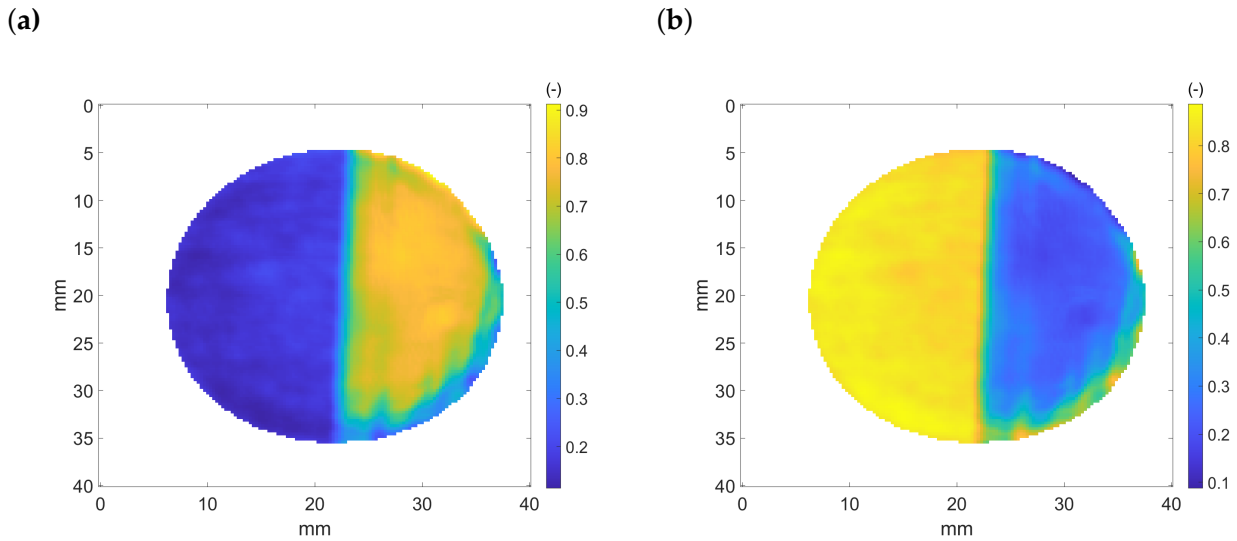


Figure 4.28: Measured sample radiative properties (step 4): (a) reflectivity  $\tilde{\rho}_{F_s}^\perp$ ; (b) emissivity  $(1 - \tilde{\rho}_{F_s}^\perp)$ .

Small heterogeneities of the source illumination are detected in Figure 4.27.b.3, which are attributed to black body cavity heterogeneity. When the beam is reflected by the sample (Figure 4.27.a.3), the two surface treatments can be clearly distinguished. Based on the results of Figures 4.27.a.3 and 4.27.b.3, the sample's reflectivity and emissivity may be computed (step 4 of ATR), resulting in the radiative properties presented in Figure 4.28.a and 4.28.b, respectively.

Figure 4.28.a indicates that the polished part (right) of the sample is more reflective than the rough part (left). With reference to Figure 4.28.a, the average total reflectivity and its standard deviation are computed and presented in Table 4.1. From Figure 4.27.a.1, the polished part (right) of the sample appears warmer than the rough part (left), whereas the sample is isothermal.

This case illustrates the difficulty of temperature measurements with thermography, which requires modelling and experimental separation of all the contributions (emission and reflection) captured by the sensor.

	Rough part	Polished part
$\tilde{\rho}_{F_s}^\perp$	0.16	0.68
Standard deviation	0.02	0.12

Table 4.1: Measured effective reflectivity of the stainless steel sample.

#### 4.8. VALIDATION OF ATR ON HETEROGENEOUS SAMPLES AT AMBIENT TEMPERATURES

---

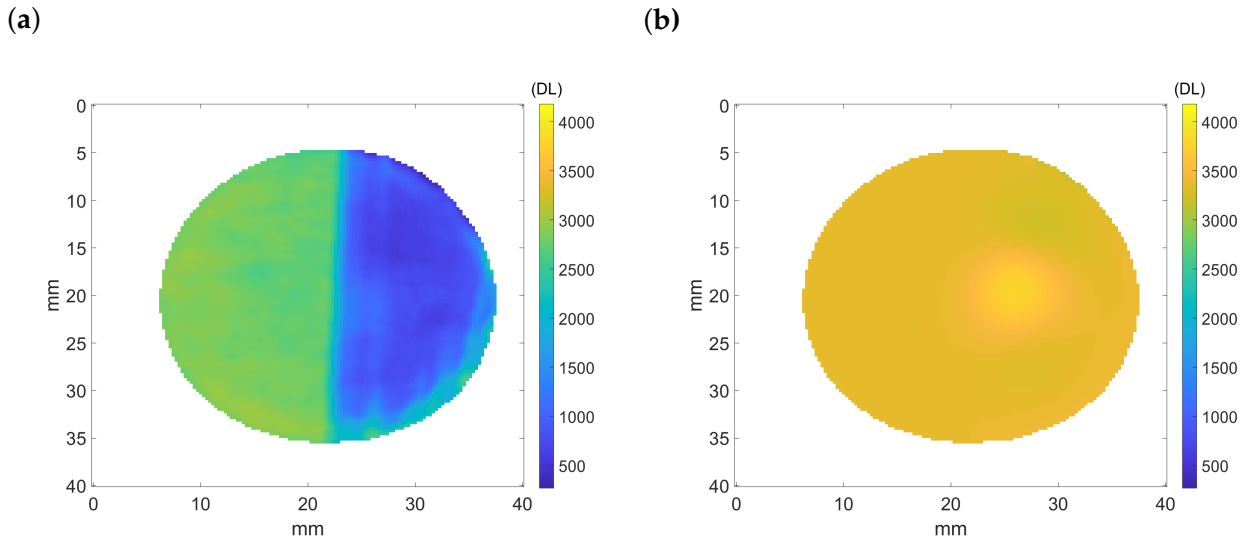


Figure 4.29: Measured stainless steel sample emittance: (a)  $\dot{q}_s^e$  (b)  $\dot{q}_s^b$ .

Figure 4.29.a presents the results of the ATR fifth step,  $\dot{q}_s^e$ , and the black body sample emittance is shown in Figure 4.29.b (sixth step). The rough part in Figure 4.29.a corresponds to the region at 2500 DL, and the laser polished part is at 1000 DL. This is particularly interesting as opposed to the raw DL (Figure 4.27.a.1), where the reflection is dominant compared to the emission.

As expected,  $\dot{q}_s^b$  appears to be quasi-isothermal after correction by the sample's emissivity (Eq. 4.34), and there is continuity between the rough and polished parts. Additionally, in Figure 4.29.a, one can observe bright vertical streaks on the polished part. The vertical lines are due to the laser path of the polishing process described in Figure 4.26, which induces error in the reflectivity measurements. The error is amplified for highly reflective materials. In Figure 4.29.b, the bright spot of the sample is attributed to the camera's narcissus attenuation. The persistence of the narcissus artefact is attributed to several factors, such as the sample's surface waviness, camera misalignment, beam, sample and reference mirror.

Figure 4.30.a presents a map of the measured true temperatures computed with ATR, and Figure 4.30.b shows a histogram of the measured temperature distribution obtained with ATR (blue) or exclusively by emissivity correction ( $\dot{q}_s^e/(1 - \tilde{\rho}_{F,s}^\perp)$  red). This latter does not account for the surrounding reflection. With ATR, it is difficult to distinguish the temperature differences between the polished and rough parts. In addition, the error due to the narcissus artefact has a negligible effect on the



#### 4.8. VALIDATION OF ATR ON HETEROGENEOUS SAMPLES AT AMBIENT TEMPERATURES

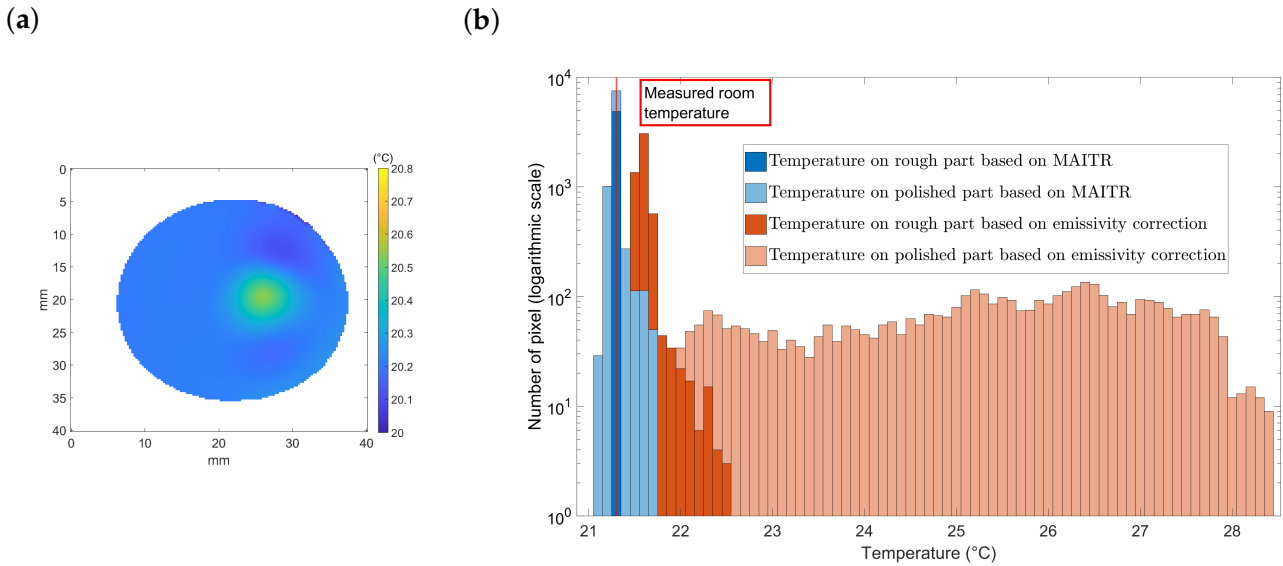


Figure 4.30: Sample temperature distribution ( $^{\circ}\text{C}$ ): (a) temperature map; (b) histogram of temperatures for ATR and emissivity correction methods. The room temperature is measured to be  $21.3^{\circ}\text{C}$ .

temperature evaluation. However, when applying only the emissivity correction, even if the emissivity is known, the two parts are distinct. The measured temperature on the rough part fluctuates between  $21.5^{\circ}\text{C}$  and  $22.5^{\circ}\text{C}$ , whereas the measured temperature on the polished part is completely heterogeneous. The ATR method is considered to be superior to the standard emissivity correction approach for specular materials at ambient temperature.

*Remark:* In this specific case, the assumption that the sample's surface roughness is smaller than the wavelength is not satisfied for the rough part. Nevertheless, the results show that the reflections are mostly specular. If this were not the case, one would underestimate  $\tilde{\rho}_{F,s}^{\perp}$  for this surface. Consequently, the corrected temperature would be higher, and the interface between each surface finish would be clearly distinguishable.

### 4.8.2 Three-layer aluminium sample

The second sample (see Figure 4.31) is a custom-made heterogeneous aluminium sample divided into three parts: (i) a raw surface (Figure 4.31.1); (ii) a raw surface painted uniformly in black (Figure 4.31.2); and (iii) a raw surface speckled with the same paint (Figure 4.31.3). The paint used is matte black (RAL 9005) and has an emissivity estimated to be approximately 0.92, as depicted in Ref. [109].

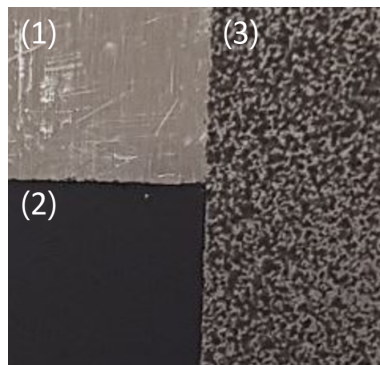


Figure 4.31: Presentation of the three-layer aluminium sample: (1) raw surface, (2) painted black, and (3) speckled.

Figure 4.32 shows the results of step 2 from the ATR method with the recorded thermographic images for both the (a) sample and the (b) reference mirror. Figures 4.32.a.1 and 4.32.b.1 show images of the sample ( $\dot{q}_{s,1}$ ) and the mirror ( $\dot{q}_{m,1}$ ) with the chopper closed, respectively. Figures 4.32.a.2 and 4.32.b.2 are with the chopper open for ( $\dot{q}_{s,2}$ ) and ( $\dot{q}_{m,2}$ ), respectively. Figures 4.32.a.3 and 4.32.b.3 show the difference for the sample and the reference mirror, respectively.

Based on these measurements, one can proceed with the fourth step of the ATR method and compute the normal reflectivity (Figure 4.33.a) and the normal emissivity (Figure 4.33.b) of the sample. Figure 4.33.a indicates that the raw part is reflective ( $\rho_{F_s}^\perp \approx 0.8$ ) and that the painted part has an emissivity of approximately 0,96, which is close to that found in [109]. Surprisingly, the speckled area does not have such sharp reflectivity fields. This is due to the spatial resolution of the IR camera, which has a lower resolution than the speckled pattern. Such problems are addressed in digital image correlation approaches [110].

Based on these results, the average effective reflectivity and associated standard deviation for each section of the sample are computed and presented in Table 4.2.



#### 4.8. VALIDATION OF ATR ON HETEROGENEOUS SAMPLES AT AMBIENT TEMPERATURES

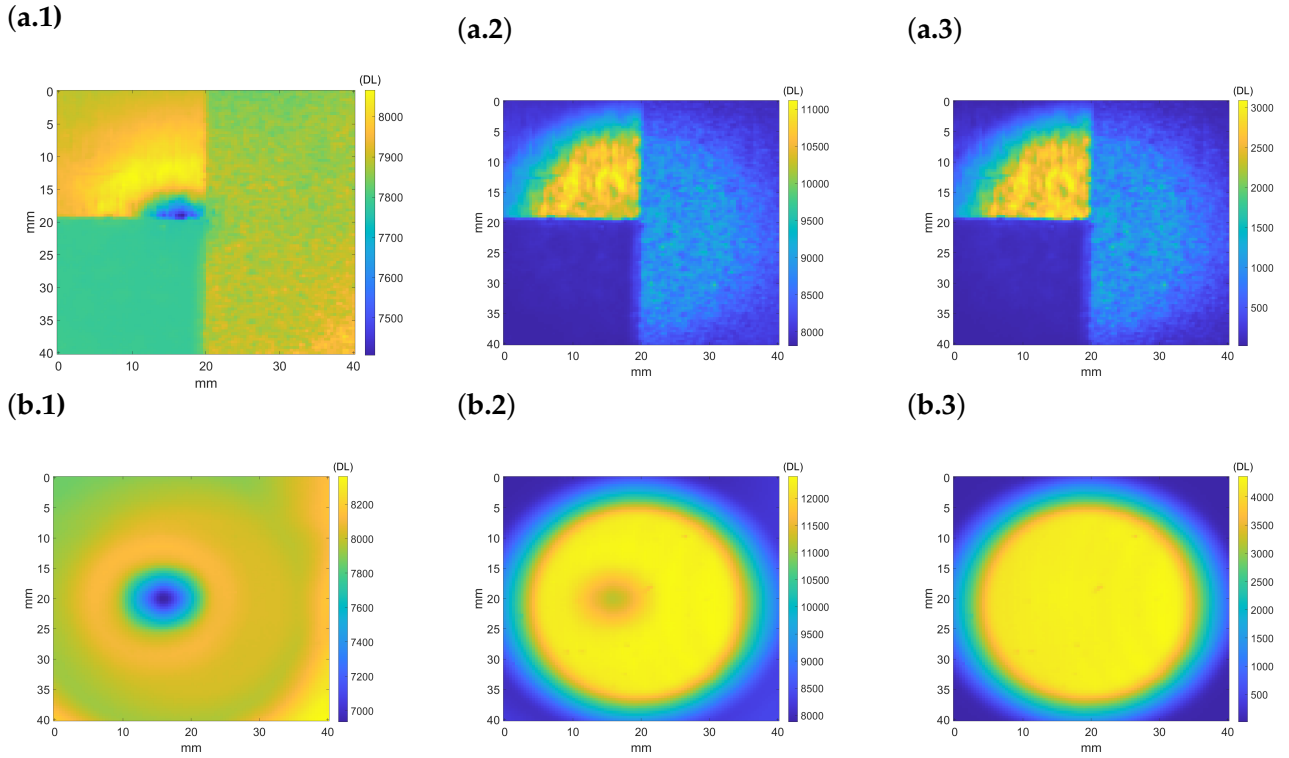


Figure 4.32: Camera measurements (step 2 of ATR) (a) on the three-layer aluminium and (b) for the reference mirror. (a.1) Raw sample measurement  $\dot{q}_{s,1}$ ; (a.2) illuminated sample  $\dot{q}_{s,2}$ ; (a.3) difference  $\dot{q}_{s,2} - \dot{q}_{s,1}$ ; (b.1) raw mirror measurement  $\dot{q}_{m,1}$ ; (b.2) illuminated mirror  $\dot{q}_{m,2}$ ; (b.3) difference  $\dot{q}_{m,2} - \dot{q}_{m,1}$ .

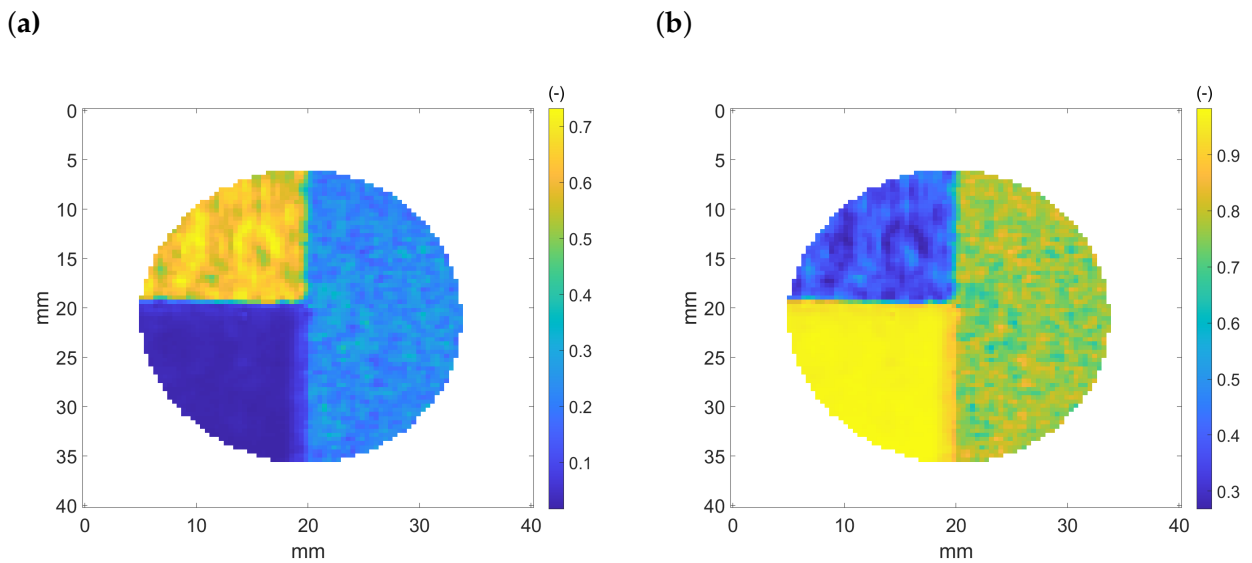


Figure 4.33: Measured sample radiative properties (step 4): (a) reflectivity  $\tilde{\rho}_{F_s}^\perp$ ; (b) emissivity  $(1 - \tilde{\rho}_{F_s}^\perp)$ .

#### 4.8. VALIDATION OF ATR ON HETEROGENEOUS SAMPLES AT AMBIENT TEMPERATURES

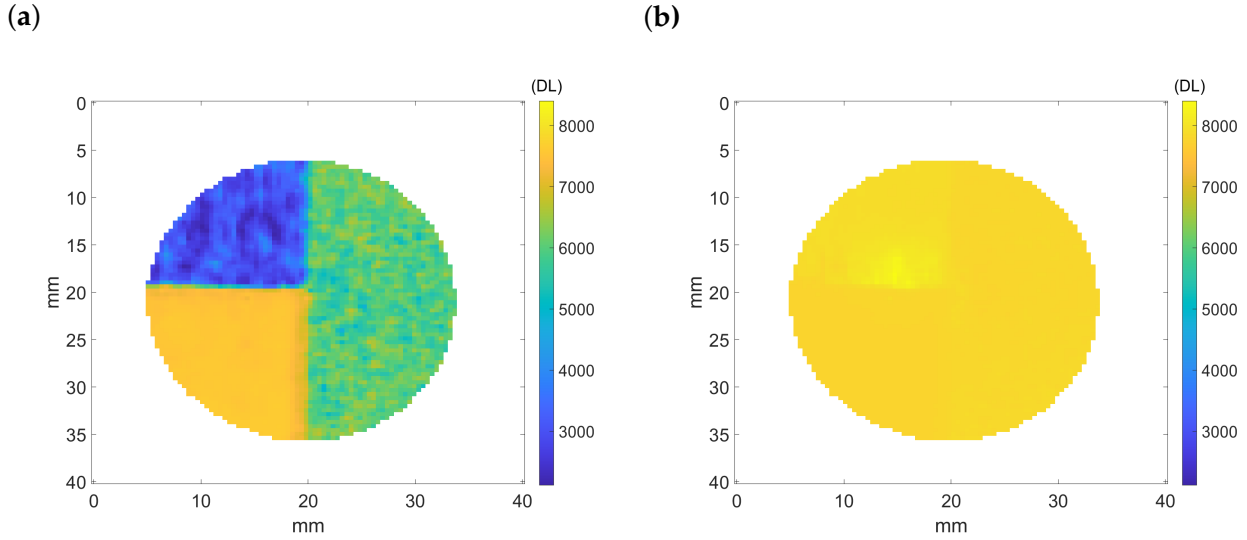


Figure 4.34: Measured emittance of the three-layer aluminium sample: (a) sample's emittance  $\dot{q}_s^e$  (b) sample's black body emittance  $\dot{q}_s^b$ .

Table 4.2: Measured effective reflectivity of the aluminium three-part sample.

	Rough	Speckled	Painted
$\tilde{\rho}_{F,s}^\perp$	0.62	0.23	0.04
Standard deviation	0.0546	0.0421	0.0227

The rough part is observed to have a higher total reflectivity than the speckled and uniformly painted parts. The standard deviation of the total reflectivity follows the same trend. In comparison to the stainless steel sample, the standard deviation is also lower. This reinforces the hypothesis that the method is sensitive to the surface topography and noise measurements on highly reflective samples. From these measurements, we can apply the fifth step of the ATR method and plot  $\dot{q}_s^e$  and  $\dot{q}_s^b$  in Figure 4.34.a and 4.34.b, respectively. Unlike the previous measurement, we do not use an average reflectivity for each surface condition because of the high variability of the speckled surface. Consequently, the black body emittance is computed on a per-pixel basis and appears quasi-constant on the sample, where only a small area of the narcissus is still visible.

After converting the black body emittance with the last step of ATR, the temperature map is obtained and displayed in Figure 4.35.a, and its histogram distribution is plotted in Figure 4.35.b.

#### 4.8. VALIDATION OF ATR ON HETEROGENEOUS SAMPLES AT AMBIENT TEMPERATURES

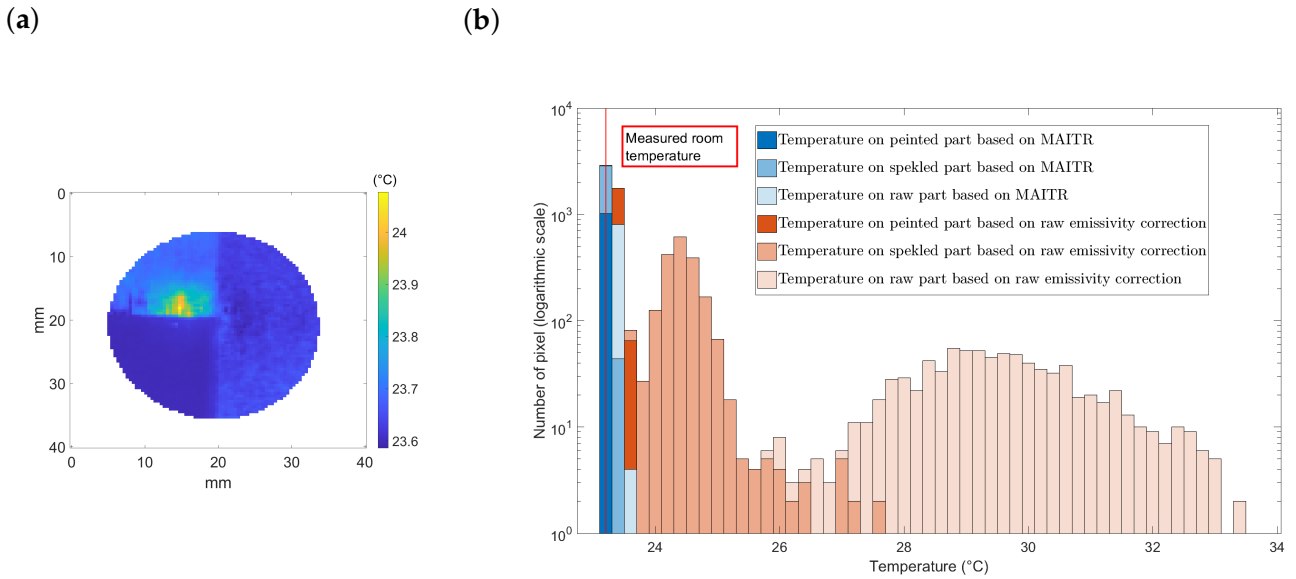


Figure 4.35: Sample temperature distribution ( $^{\circ}\text{C}$ ): (a) temperature map; (b) histogram of temperatures for the ATR and emissivity correction methods. The room temperature is measured as  $23.2^{\circ}\text{C}$ .

The uniformity of the sample temperature is almost recovered by the ATR method, and the measured temperature corresponds to room temperature ( $\approx 23.2^{\circ}\text{C}$ ). The error due to the narcissus artefact on the reflective raw part leads to local overestimation of the sample's true temperature. In the black-painted part, however, this error is negligible since the reflection of the narcissus is negligible.

#### 4.8.3 Conclusions regarding static measurement

In conclusion, the raw images captured by IR cameras are insufficient for easy absolute and remote measurements of the temperature for observed thermal scenes. The lack of local knowledge about the emissivity fields and the influence of reflections from the environment preclude accurate radiometric assessment.

A rapid and versatile ATR method is proposed to characterise the normal emissivity of a specular opaque body with any type of IR camera. The detailed protocol of the ATR method allows simultaneous acquisition of the emissivity and temperature fields through an analytical radiation model and an experimental methodology. This method is validated on opaque material surfaces such as treated metallic surfaces, black bodies, and raw samples, which can be assumed to be mirrors ( $\tilde{\rho}^{\perp} \approx 0.9 -$ ).

For each case, the application of radiometric balances allows us to highlight the contribution and interest of the ATR method for the absolute and contactless measurement of temperature fields by IR thermography.

### 4.9 Conclusions regarding temperature measurement with infrared thermography

As seen in this chapter, temperature measurements are essential to understanding and characterising HEL interactions with matter.

The conventional method often relies on a hypothesis of the spectral behaviour for emissivity (or reflectivity) and does not consider reflections. In this study, another assumption is proposed. This relies on the BRDF shape itself assuming specular reflections. The **ATR** method allows **in situ measurements of emissivity fields**, an **estimation of the reflections** present in the thermal scene and consequently **absolute measurement of temperature** fields by infrared cameras on **specular materials**.

The proposed method is first validated on a **radiative numerical study**. Then, a **complete set-up is developed** and fully described. To finish, **results are shown on samples at ambient temperature**.

From a personal point of view, there is no ideal solution for infrared temperature measurement. The experimenter must know all relevant behaviours that occur in the infrared scene and make well-founded assumptions. The ATR method has the advantage of considering thermal reflections that most methods do not consider. Finally, by tilting the sample during illumination, it is easy to check that the sample is specular. This is a major advantage of the method, as it eliminates the need for assumptions.

#### 4.9. CONCLUSIONS REGARDING TEMPERATURE MEASUREMENT WITH INFRARED THERMOGRAPHY

---

## Chapter 5

# From quantitative thermal imaging to spatio-temporal heat flux estimation

### Table of Contents

---

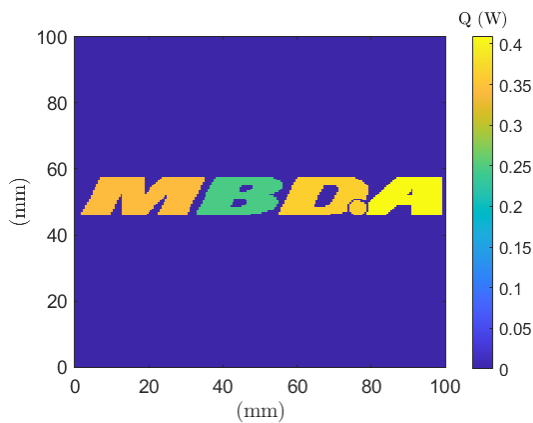
<b>5.1</b>	<b>Introduction</b>	<b>136</b>
<b>5.2</b>	<b>Direct and inverse problems</b>	<b>137</b>
<b>5.3</b>	<b>Generation of numerical direct problems</b>	<b>139</b>
5.3.1	Analytical approach	139
5.3.2	Introduction to the finite volume method (FVM) applied to thermal diffusion in 2D	146
<b>5.4</b>	<b>Inverse method for a quantitative spatio-temporal estimation of the heat flux - FVM-based approach</b>	<b>148</b>
5.4.1	Estimation of the 2D heat source based on the FVM	148
5.4.2	Towards a 3D estimation	157
5.4.3	Conclusions regarding the FVM-based spatio-temporal heat flux estimation	159
<b>5.5</b>	<b>Description of the inverse method for the quantitative spatial and temporal estimation of an excitation flux - an analytical approach</b>	<b>160</b>
5.5.1	Mathematical description of the inverse method for the time and space estimation of heat flux	160
5.5.2	Spatio-temporal heat flux estimation for 3D thermal conduction	163
<b>5.6</b>	<b>General conclusions regarding heat flux estimation</b>	<b>168</b>

---

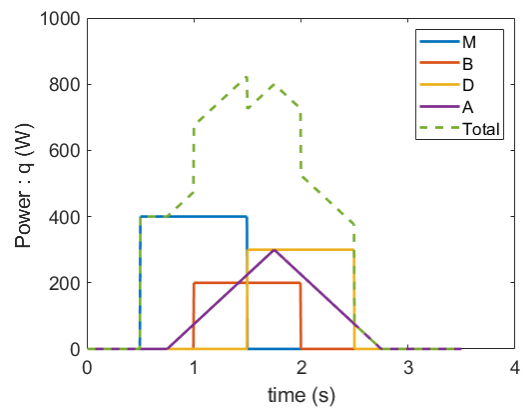
## 5.1 Introduction

The aim of this chapter is to implement tools for evaluating the behaviour of materials that are illuminated by a continuous multi-kW laser source. Even if the spatial and temporal characteristics of the incident beam are known, the **major issue** lies in quantifying the **power absorbed by the sample**, which is dependent on its surface conditions. Information from both **spatial and temporal heat flux profiles** can be used as a starting point for this quantification. As the data from the laser impacting the sample are difficult to collect, we propose to study the target sample's behaviour far from the contact interface, where the evolution of properties is linear. From these data, we use **analytical and numerical methods** to track the kinetics of the impact.

Here, one considers numerical studies in 2D and 3D. The aim is to develop a method for estimating heat flux boundary conditions in any spatial and temporal form. Consequently, the MBDA logo shown in Figure 5.1a is used as a heat source. Each letter of the logo has a different power and appears at different times in the simulation (see Figure 5.1b).



(a) Maximum deposited power (W).



(b) Temporal shape of the imposed power on each letter of MBDA.

Figure 5.1: Heat flux description.

### 5.2 Direct and inverse problems

Direct problems calculate a final solution (or a time evolution) as a function of known values and boundary conditions. Direct problems are common and are widely used for system design. To compute the response of a system, one must know the following:

- the geometry of the system,
- the involved materials and their properties,
- the transport mode of energy present in the system (conduction, convection, radiation),
- the initial conditions of the system,
- the exchange between the system and the surrounding boundary conditions, and
- the spatial and temporal discretisation needed to solve the problem.

Inverse problems are defined as the set of methods that allow us to monitor the cause of an event from the observation of its effects, as opposed to direct problems, which make it possible to determine the effects from a set of known causes. Computational methods for **solving inverse problems** have been widely developed and have now become essential tools in industry and research [111, 112, 113, 114, 115, 116, 117, 118]. The **relations between experimental observations and numerical simulations** that are identified through inverse techniques make it possible to identify physical quantities that are not directly accessible through direct methods [119].

In the specific case of thermal problems, this requires calculating the temperature response of a medium, object or system based on the knowledge of heat sources, heat losses and thermophysical properties. The inverse problem in thermics makes it possible to estimate the "input" quantities of the direct problem (i.e., thermophysical properties, flux, etc.), starting from the temperature measurement. There are multiple parameters to be sought during the inversion [120, 121]. In the case of laser-material interactions, one seeks to identify the imposed heat flux (boundary condition), as illustrated in Figure 5.2.

The cause of direct problems is known, and the effects are searched for. This intuitively implies that the same causes lead to the same consequences. However, it is more difficult to determine all the



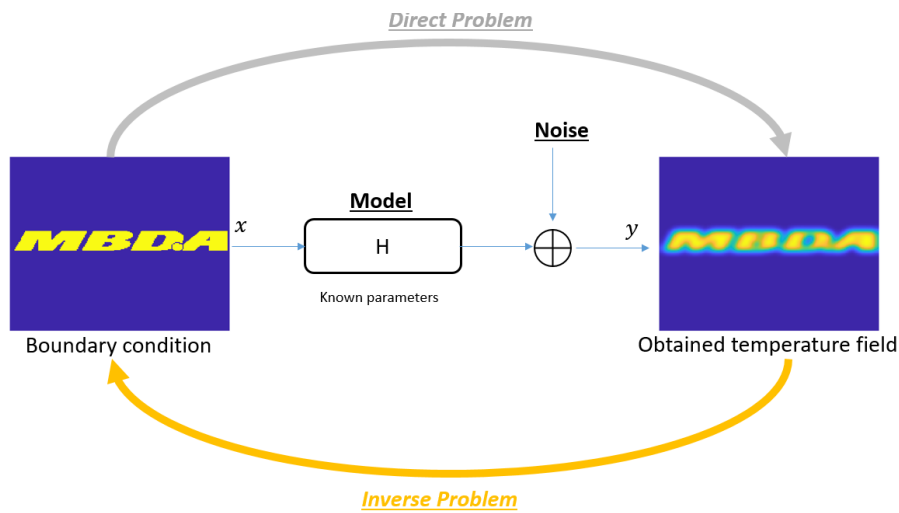


Figure 5.2: Elementary schematic of direct and inverse problems.

possible causes of a certain consequences. This illustrates the difficulty in studying inverse problems, as they may have several solutions. Therefore, it is necessary to have additional information to differentiate between them. It then becomes clear that the very nature of an inverse problem poses real difficulties in its implementation. To solve this, J. Hadamard [122, 123] introduced the notion of a "well-posed" problem and defined the three associated necessary conditions:

- A solution exists,
- the solution is unique, and
- the solution is stable according to the data.

The first two criteria can be handled more easily than the third. If a solution to the direct problem exists, it is natural to think that it also exists for inverse problems. If the second criterion is not met, then there are methods to impose additional restrictions, thus isolating a unique solution. In this field, we can cite the work of A. Benabdallah et al. [124], who showed the existence and uniqueness of a solution for a 1D von Karman model. Bryan Kurt and L. Caudill [125] conducted a study of the uniqueness and stability of results for inverse thermal problems. In particular, considering an object subjected to a heat flux, the unknown boundary conditions can be studied by measuring the temperature of its surfaces. The third criterion is much more complicated for inverse problems. This is usually the reason for the "ill-posed" character of thermal inverse problems. A part of the input

### 5.3. GENERATION OF NUMERICAL DIRECT PROBLEMS

data is experimental and is therefore subject to measurement and calibration noise. The solution of inverse problems must therefore be stable despite variable input noise.

## 5.3 Generation of numerical direct problems

For the implementation of direct problems, we consider an industrial grade of aluminium (AL2024), for which the thermal properties are presented in Table 5.1.

Density ( $\rho_v$ $kg \cdot m^{-3}$ )	Specific heat capacity ( $C_p$ $J \cdot kg^{-1} \cdot K^{-1}$ )	Thermal conductivity ( $k$ $W \cdot m^{-1} \cdot K^{-1}$ )	Thermal diffusivity ( $mm^2 \cdot s^{-1}$ )
2700	897	239	98.5

Table 5.1: Thermal properties of AL2024.

The geometry used for the simulation also corresponds to industrial samples. We consider two kinds of direct 2D and 3D problems. The corresponding dimensions are presented in Table 5.2.

	2D problem	3D problem
Length (m)	0.1	0.1
Width (m)	0.1	0.1
Thickness (m)	0.002	0.005

Table 5.2: Geometry for the 2D and 3D direct problems.

### 5.3.1 Analytical approach

#### 5.3.1.1 Direct thermal diffusion problem in 2D

By considering the boundary conditions presented in Figures ?? and 5.1 and by neglecting the heat transfer through the thickness, the temperature field can be described with the following system of equations:

$$\begin{cases}
 \rho_m C_p \frac{\partial T(x, y, t)}{\partial t} = k \left[ \frac{\partial^2 T(x, y, t)}{\partial x^2} + \frac{\partial^2 T(x, y, t)}{\partial y^2} \right] + Q_v \\
 k \frac{\partial T(x, y, t)}{\partial x} \Big|_{x=0, L_x} = 0 \\
 k \frac{\partial T(x, y, t)}{\partial y} \Big|_{y=0, L_y} = 0 \\
 T(x, y, t = 0) = 0
 \end{cases} \quad (5.1)$$

### 5.3. GENERATION OF NUMERICAL DIRECT PROBLEMS

---

where  $\rho_m$  is the volumetric mass,  $C_p$  is the specific heat,  $T(x, y, t)$  is the temperature (K) and  $Q_v$  is the heat source ( $W \cdot m^{-3}$ )

The thermal load  $Q_v$  can be described as follows:

$$Q_v = \sum_{i=1}^4 Q_v(x, y, i) \times F_i(t) \quad (5.2)$$

where  $Q_v(x, y, i)$  represents the spatial profile of each letter in MBDA and  $F_i(t)$  represents their temporal variations (see Figures 5.1a and 5.1b).

One manner of solving Eq. 5.1 is to project the problem onto the Laplace (temporal) and Fourier (spatial  $x$  and  $y$ ) domain [126]. Those projections are presented in Eqs. 5.3, 5.4 and 5.5.

$$\tilde{\Theta}(x, y, p) = \int_{t=0}^{+\infty} T(x, y, t) e^{-pt} dt \quad (5.3)$$

$$\hat{\Theta}(\alpha_n, y, p) = \int_{x=0}^{L_x} \tilde{\Theta} \cos(\alpha_n x) dx \quad (5.4)$$

$$\Theta(\alpha_n, \beta_m, p) = \int_{y=0}^{L_y} \hat{\Theta} \cos(\beta_m y) dy \quad (5.5)$$

where  $\alpha_n$  and  $\beta_m$  represent the spatial Fourier frequencies considering the adiabatic boundary conditions. These frequencies are expressed in Eqs. 5.6 and 5.7.

$$\alpha_n = \frac{n\pi}{L_x}, n \in \mathbb{N} \quad (5.6)$$

$$\beta_m = \frac{m\pi}{L_y}, m \in \mathbb{N} \quad (5.7)$$

This leads to a temperature expression in the transformed space (Eq. 5.8):

$$\Theta(\alpha_n, \beta_m, p) = \int_{y=0}^{L_y} \int_{x=0}^{L_x} \int_{t=0}^{+\infty} T(x, y, t) e^{-pt} \cos(\alpha_n x) \cos(\beta_m y) dx dy dt \quad (5.8)$$

The transition into the transformed domain simplifies the spatial and temporal derivative in Eq. 5.1:

**Temporal Laplace transition:**

$$\int_{t=0}^{+\infty} \frac{\partial T(x, y, p)}{\partial t} e^{-pt} dt = p \int_{t=0}^{+\infty} T(x, y, p) e^{-pt} dt \quad (5.9)$$

**First Fourier transition:**

$$\int_{x=0}^{L_x} \frac{\partial^2 T(x, y, t)}{\partial x^2} \cos(\alpha_n x) dx = -\alpha_n^2 \int_{x=0}^{L_x} T(x, y, t) \cos(\alpha_n x) dx \quad (5.10)$$

**Second Fourier transition:**

$$\int_{y=0}^{L_y} \frac{\partial^2 T(x, y, t)}{\partial y^2} \cos(\beta_m y) dy = -\beta_m^2 \int_{y=0}^{L_y} T(x, y, t) \cos(\beta_m y) dy \quad (5.11)$$

Considering Eqs. 5.9, 5.10, and 5.11, Eq. 5.1 can be rewritten in the transformed domain.

$$p\Theta(\alpha_n, \beta_m, p) = -d\alpha_n^2\Theta(\alpha_n, \beta_m, p) - d\beta_m^2\Theta(\alpha_n, \beta_m, p) + \frac{\tilde{Q}_v(\alpha_n, \beta_m, p)}{\rho_m C_p} \quad (5.12)$$

where  $d$  is the thermal diffusivity and  $\tilde{Q}_v(\alpha_n, \beta_m, p)$  is the volumetric source into the transformed domain defined in Eq. 5.13.

$$\tilde{Q}_v(\alpha_n, \beta_m, p) = \int_{y=0}^{L_y} \int_{x=0}^{L_x} \int_{t=0}^{+\infty} \sum_{i=1}^4 Q_v(x, y, i) \times F_i(t) e^{-pt} \cos(\alpha_n x) \cos(\beta_m y) dx dy dt \quad (5.13)$$

Finally, one can express the temperature in the transformed domain as:

$$\Theta(\alpha_n, \beta_m, p) = \frac{\tilde{Q}_v(\alpha_n, \beta_m, p)}{\rho_m C_p \times (p + d\alpha_n^2 + d\beta_m^2)} \quad (5.14)$$

The return to real space is achieved with two inverse Fourier transforms and one inverse Laplace transform and is not described here (readers can refer to [126, 127]).

Figure 5.3 illustrates different temperature fields obtained with this equation and the boundary conditions presented in Figures 5.1a and 5.1b.

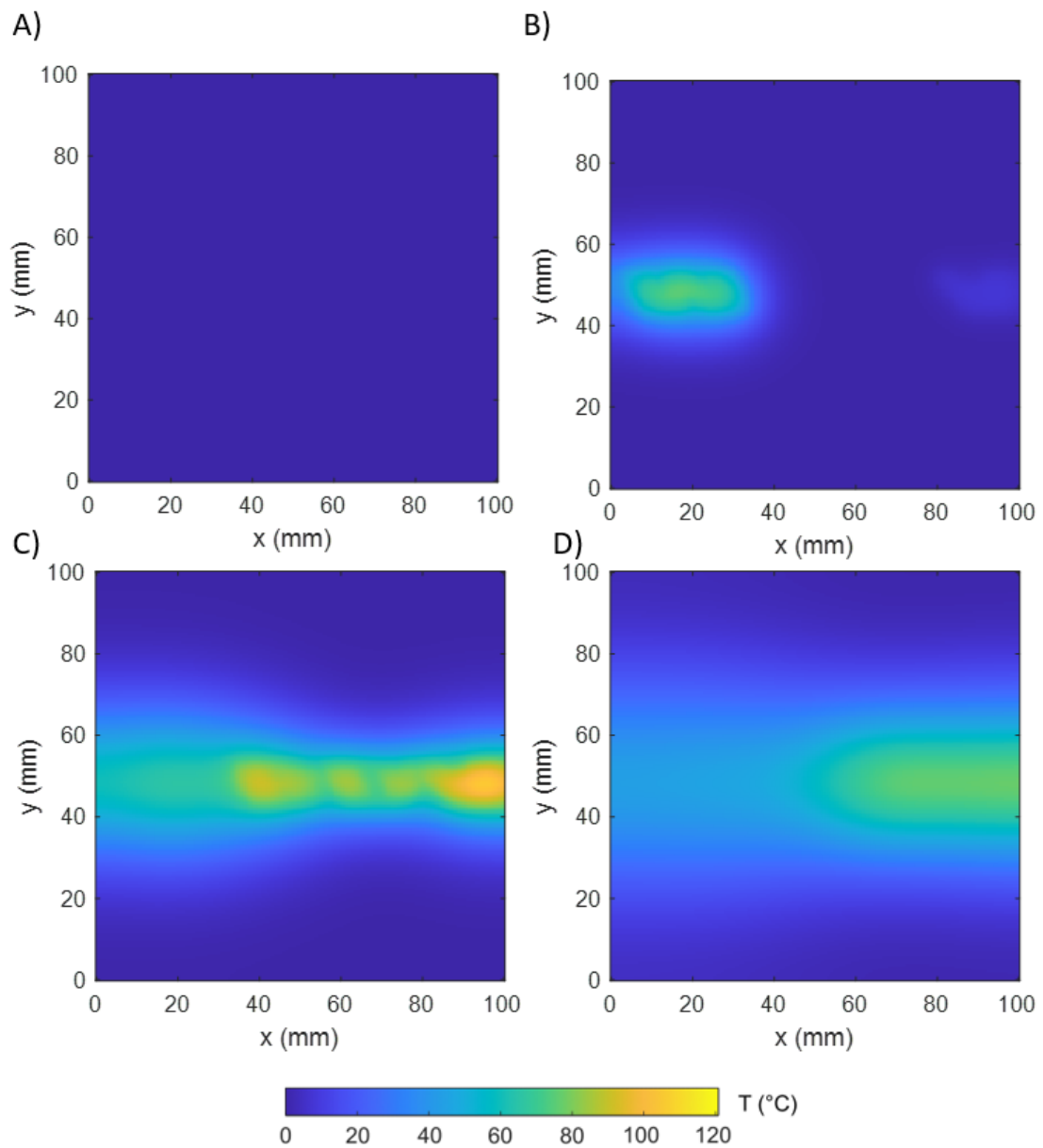


Figure 5.3: Obtained temperature fields on the rear face at different time steps: (a)  $t=0.5$  s, (b)  $t=1$  s, (c)  $t=2$  s and (d)  $t=3$  s.

### 5.3.1.2 Direct thermal diffusion problem in 3D

By considering the same boundary conditions, the temperature field can be described with the following system of equations:

$$\left\{ \begin{array}{l} \rho_m C_p \frac{\partial T(x, y, z, t)}{\partial t} = k \left[ \frac{\partial^2 T(x, y, z, t)}{\partial x^2} + \frac{\partial^2 T(x, y, z, t)}{\partial y^2} + \frac{\partial^2 T(x, y, z, t)}{\partial z^2} \right] \\ k \frac{\partial T(x, y, z, t)}{\partial x} \Big|_{x=0, L_x} = 0 \\ k \frac{\partial T(x, y, z, t)}{\partial y} \Big|_{y=0, L_y} = 0 \\ -k \frac{\partial T(x, y, z, t)}{\partial z} \Big|_{z=0} = \dot{q}(x, y, t) \\ k \frac{\partial T(x, y, z, t)}{\partial z} \Big|_{z=L_z} = 0 \\ T(x, y, z, t=0) = 0 \end{array} \right. \quad (5.15)$$

where  $\rho_m$  is the volumetric mass,  $C_p$  is the specific heat,  $T(x, y, z, t)$  is the temperature (K) and  $\dot{q}$  is the surface heat flux ( $W \cdot m^{-2}$ )

Here,  $\dot{q}(x, y, i)$  represents the spatial profile of each letter of MBDA, and  $F_i(t)$  represents their respective temporal variations (see 5.1a and 5.1b) and is expressed as follows:

$$\dot{q} = \sum_{i=1}^4 \dot{q}(x, y, i) \times F_i(t) \quad (5.16)$$

where  $\dot{q}(x, y, i)$

Once again, a double spatial (x,y) Fourier transform and a Laplace transform (t) are performed. Consequently, the temperature in the transformed space ( $\Theta(\alpha_n, \beta_m, z, p)$ ) is described in Eq. 5.17.

$$\Theta(\alpha_n, \beta_m, z, p) = \int_{y=0}^{L_y} \int_{x=0}^{L_x} \int_{t=0}^{+\infty} T(x, y, z, t) e^{-pt} \cos(\alpha_n x) \cos(\beta_m y) dx dy dt \quad (5.17)$$

where  $\alpha_n$  and  $\beta_m$ , which represent the spatial Fourier frequencies considering the adiabatic boundary conditions, are respectively given in Eqs. 5.18 and 5.19.

$$\alpha_n = \frac{n\pi}{L_x}, n \in \mathbb{N} \quad (5.18)$$

### 5.3. GENERATION OF NUMERICAL DIRECT PROBLEMS

---

$$\beta_m = \frac{m\pi}{L_y}, m \in \mathbb{N} \quad (5.19)$$

After simplification, Eq. 5.15 can be rewritten in the transformed domain (Eq. 5.20):

$$\begin{cases} \frac{\partial^2 \Theta(\alpha_n, \beta_m, z, p)}{\partial z^2} - \Theta(\alpha_n, \beta_m, z, p) \left[ \frac{p}{d} + \alpha_n^2 + \beta_m^2 \right] = 0 \\ k \frac{\partial \Theta(\alpha_n, \beta_m, z, p)}{\partial z} \Big|_{z=0} = \tilde{q}(\alpha_n, \beta_m, p) \\ \frac{\partial \Theta(\alpha_n, \beta_m, z, p)}{\partial z} \Big|_{z=L_z} = 0 \end{cases} \quad (5.20)$$

where  $d$  is the thermal diffusivity ( $m^2 \cdot s^{-1}$ ) and  $\tilde{q}(\alpha_n, \beta_m, p)$  is the heat flux into the transformed domain.

The solution of the characteristic equation of the partial differential equation (5.20) is given in Eq. 5.21.

$$\Lambda = \pm \sqrt{k} \quad (5.21)$$

where  $k = \frac{p}{d} + \alpha_n^2 + \beta_m^2$

The solution to Eq. 5.20 is rewritten as:

$$\begin{cases} \Theta(\alpha_n, \beta_m, z, p) = Ae^{\sqrt{k}z} + Be^{-\sqrt{k}z} \\ \sqrt{k}A - \sqrt{k}B = \tilde{q}(\alpha_n, \beta_m, p) \\ \sqrt{k}Ae^{\sqrt{k}L_z} - \sqrt{k}Be^{-\sqrt{k}L_z} = 0 \end{cases} \quad (5.22)$$

Finally, one can express the temperature in the transformed domain as:

$$\begin{cases} \Theta(\alpha_n, \beta_m, z, p) = Ae^{\sqrt{k}z} + Be^{-\sqrt{k}z} \\ A = \tilde{q}(\alpha_n, \beta_m, p) \frac{e^{-2\sqrt{k}L_z}}{\sqrt{k}(e^{-2\sqrt{k}L_z} - 1)} \\ B = \tilde{q}(\alpha_n, \beta_m, p) \frac{1}{\sqrt{k}(e^{-2\sqrt{k}L_z} - 1)} \end{cases} \quad (5.23)$$

The return to real space is achieved with two inverse Fourier transforms and one inverse Laplace transform and is not described here [126].

Figure 5.4 illustrates different temperature fields on the rear face obtained with Eq. 5.23 considering the boundary conditions presented in Figures 5.1a and 5.1b.

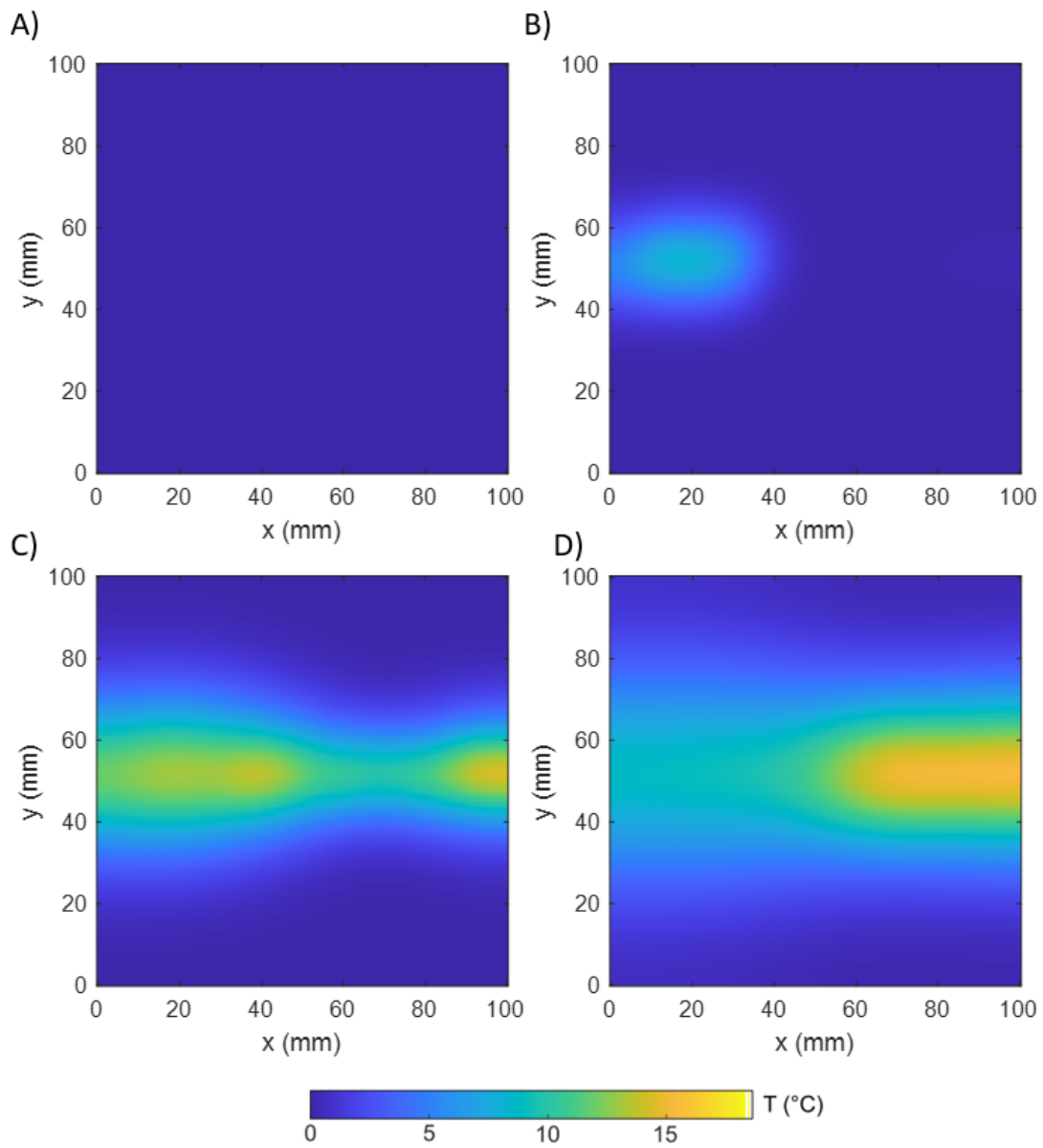


Figure 5.4: Illustration of the obtained temperature fields on the rear face at different time steps: (a)  $t=0.5$  s, (b)  $t=1$  s, (c)  $t=2$  s and (d)  $t=3$  s.



5.3.2 Introduction to the finite volume method (FVM) applied to thermal diffusion in 2D

Rewriting Eq. 5.1 as Eq. 5.24,

$$\begin{cases} \rho_m C_p \frac{\partial T(x, y, t)}{\partial t} = k \left[ \frac{\partial^2 T(x, y, t)}{\partial x^2} + \frac{\partial^2 T(x, y, t)}{\partial y^2} \right] + Q_v \\ k \frac{\partial T(x, y, t)}{\partial x} \Big|_{x=0, L_x} = 0 \\ k \frac{\partial T(x, y, t)}{\partial y} \Big|_{y=0, L_y} = 0 \\ T(x, y, t = 0) \end{cases} \quad (5.24)$$

The first step of the FVM is to define the discretized volume domain illustrated in Figure 5.5.

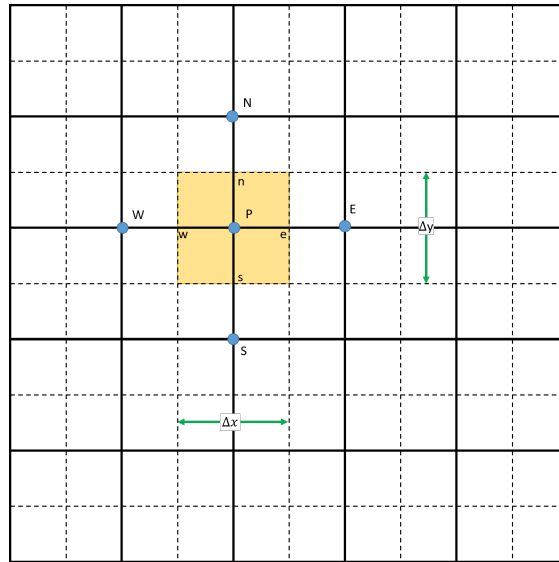


Figure 5.5: Illustration of a portion of the 2D grid used for discretisation.

The key step of the FVM is to integrate Fourier’s law over a controlled volume  $\Delta V$  and time step  $\Delta t$ . Eq. 5.25 shows the obtained equation on any coordinate P of the grid at a given time step t, for which the temperature is given as  $T_{coordinate}^{time\ step}$

$$\int_{\Delta V} \int_t^{t+\Delta t} \rho_m C_p \frac{\partial T}{\partial t} dV dt = k \int_{\Delta V} \int_t^{t+\Delta t} \left( \frac{\partial^2 T}{\partial x^2} + \frac{\partial^2 T}{\partial y^2} \right) dV dt + \int_{\Delta V} \int_t^{t+\Delta t} Q_v dV dt \quad (5.25)$$

The first term leads to:

### 5.3. GENERATION OF NUMERICAL DIRECT PROBLEMS

---

$$\begin{aligned}
\int_{\Delta V} \int_t^{t+\Delta t} \rho_m C_p \frac{\partial T}{\partial t} dV dt &= \int_{X_{p-\Delta x/2}}^{X_{p+\Delta x/2}} \int_{Y_{p-\Delta y/2}}^{Y_{p+\Delta y/2}} \int_0^{L_z} \int_t^{t+\Delta t} \rho_m C_p \frac{\partial T}{\partial t} dx dy dz dt \\
&= \Delta x \times \Delta y \times L_z \times \rho_m \times C_p \times \int_t^{t+\Delta t} \frac{\partial T}{\partial t} dt \\
&= \Delta x \times \Delta y \times L_z \times \rho_m \times C_p \times \left[ T_p \right]_t^{t+\Delta t} \\
&= \Delta x \times \Delta y \times L_z \times \rho_m \times C_p \times \left[ T_p^{t+\Delta t} - T_p^t \right]
\end{aligned} \tag{5.26}$$

The  $x$  component of the second term leads to:

$$\begin{aligned}
k \int_{\Delta V} \int_t^{t+\Delta t} \frac{\partial^2 T}{\partial x^2} dV dt &= k \int_{X_{p-\Delta x/2}}^{X_{p+\Delta x/2}} \int_{Y_{p-\Delta y/2}}^{Y_{p+\Delta y/2}} \int_0^{L_z} \int_t^{t+\Delta t} \frac{\partial^2 T}{\partial x^2} dx dy dz dt \\
&= k \times \Delta y \times L_z \times \Delta t \times \int_{X_E}^{X_W} \frac{\partial^2 T}{\partial x^2} dx \\
&= k \times \Delta y \times L_z \times \Delta t \times \left[ \frac{\partial T}{\partial x} \right]_E^W \\
&= k \times \Delta y \times L_z \times \Delta t \times \left[ \frac{T_E^t - T_p^t}{\Delta x} - \frac{T_p^t - T_W^t}{\Delta x} \right] \\
&= k \times \Delta y \times L_z \times \Delta t \times \frac{T_E^t + T_W^t - 2T_p^t}{\Delta x}
\end{aligned} \tag{5.27}$$

The  $y$  component of the second term leads to:

$$k \int_{\Delta V} \int_t^{t+\Delta t} \frac{\partial^2 T}{\partial y^2} dV dt = k \times \Delta x \times L_z \times \Delta t \times \frac{T_N^t + T_S^t - 2T_p^t}{\Delta y} \tag{5.28}$$

The last term leads to:

$$\begin{aligned}
\int_{\Delta V} \int_t^{t+\Delta t} Q_v dV dt &= \int_{X_{p-\Delta x/2}}^{X_{p+\Delta x/2}} \int_{Y_{p-\Delta y/2}}^{Y_{p+\Delta y/2}} \int_0^{L_z} \int_t^{t+\Delta t} Q_v dx dy dz dt \\
&= \Delta x \times \Delta y \times L_z \times \Delta t \times Q_v(p, t)
\end{aligned} \tag{5.29}$$

By combining Eqs. 5.26, 5.27, 5.28 and 5.29, Eq. 5.25 expresses the temperature  $T_p^{t+\Delta t}$ :

$$T_p^{t+\Delta t} = \Delta t \times d \left[ \frac{T_E^t + T_W^t - 2T_p^t}{\Delta x^2} + \frac{T_N^t + T_S^t - 2T_p^t}{\Delta y^2} \right] + T_p^t + \Delta t \times \frac{Q_v(p, t)}{\rho_m \times C_p} \tag{5.30}$$

## 5.4. INVERSE METHOD FOR A QUANTITATIVE SPATIO-TEMPORAL ESTIMATION OF THE HEAT FLUX - FVM-BASED APPROACH

---

This formula is valid for every point on the grid except corner and edge control volumes. The corners have two neighbouring volumes, and the edges have three neighbouring volumes. These points are not necessary for understanding the following section. The reader can refer to [128, 129] for more information.

In this demonstration, an explicit scheme is used. This scheme imposes restrictions on the maximum time step  $\Delta t$  described as follows: [129].

$$\Delta t < \frac{1}{2d} \left[ \frac{\Delta x^2 \Delta y^2}{\Delta x^2 + \Delta y^2} \right] \quad (5.31)$$

### 5.4 Inverse method for a quantitative spatio-temporal estimation of the heat flux - FVM-based approach

In 2008, C. Pradere et al. [130] developed a novel approach to make a joint estimation of the volumetric heat source and thermal diffusivity. In this work, a correlation-based criterion between the temporal derivative and the spatial Laplacian is introduced to determine where (or when) sources are turned on. This study is an extension of this work. Efforts were made to improve the correlation criterion to determine where (or when) the convective losses biased the estimation. Furthermore, an approach is proposed to generalise this method to 3D problems. The latter has not yet been tested.

#### 5.4.1 Estimation of the 2D heat source based on the FVM

##### 5.4.1.1 Description of the method

As we have just seen, the FVM allows the estimation of temperature fields based on an initial state, on boundary conditions and/or a volumetric heat source while considering the heat flux and convective heat losses. Consequently, Eq. 5.30 can be rewritten as

$$\Delta T_p^t = d \nabla^2 T_p^t + \frac{Q_v(p, t)}{\rho_m C_p} - \frac{h}{L_z \rho_m C_p} (T_p^t - T_0) \quad (5.32)$$

where  $\Delta T$  represents the discrete temporal derivative ( $K \cdot s^{-1}$ ),  $\nabla^2 T$  is the discrete Laplacian ( $K \cdot m^{-2}$ ),  $d$  is the thermal diffusivity ( $m^2 \cdot s^{-1}$ ),  $h$  is the convective heat transfer coefficient ( $W \cdot m^{-2} \cdot K^{-1}$ ),  $\rho_m$  is the density ( $kg \cdot m^{-3}$ ),  $C_p$  is the heat capacity ( $J \cdot K^{-1} \cdot kg^{-1}$ ),  $T_0$  is the temperature of the surrounding air (K)

#### 5.4. INVERSE METHOD FOR A QUANTITATIVE SPATIO-TEMPORAL ESTIMATION OF THE HEAT FLUX - FVM-BASED APPROACH

---

and  $Q_v(p, t)$  is the volumetric heat source ( $W \cdot m^{-3}$ ). The indices and the exponent of the temperature (denoted by  $T$  in  $K$ ) represent the spatial and temporal positions. Note that this equation is valid only in internal nodes of the 2D heat transfer problem solved by the FVM.

Based on the discrete temperature field measurement and in the absence of convective heat losses, Eq. 5.32 allows the estimation of the heat flux with the discrete temperature derivative ( $\Delta T$ ) and the discrete Laplacian ( $\nabla T$ ) (see Eq. 5.33). The absence of heat sources also leads to the estimation of the thermal diffusivity (Eq. 5.34).

$$Q_v(p, t) = \rho_m \times C_p \left[ \Delta T_p^t - d \nabla T_p^t \right] \quad (5.33)$$

$$d = \frac{\Delta T_p^t}{\nabla T_p^t} \quad (5.34)$$

To make a good estimation, one must be able to correctly detect the spatial and temporal positions where the source is active/pure diffusion/heat losses are no longer negligible.

To overcome this problem, a method initially studied by [131], based on the statistical approach of the linear correlation that links the temporal derivative and the Laplacian performed with singular value decomposition (SVD). The statistical linear correlation parameter between two variables ( $C_{xy}$ ) is defined in Eq. 5.35. The coefficient is a dimensionless quantity ranging from -1 to 1. When  $C_{xy}$  approaches 1, both parameters ( $x$  and  $y$ ) are positively correlated, meaning they either increase or decrease simultaneously. In contrast, when  $C_{xy}$  approaches -1, the parameters are negatively correlated, meaning that when one increases, the other decreases, and vice versa.

$$C_{xy} = \frac{\sum_{i=1}^n (x_i)(y_i)}{\sqrt{\sum_{i=1}^n (x_i)^2 \sum_{i=1}^n (y_i)^2}} \quad (5.35)$$

where  $n$  represents the number of images taken, i.e., the size of the temporal window.

By taking  $x_i = \Delta T_p^i$  and  $y_i = \nabla T_p^i$ , the correlation  $C_{\Delta T, \nabla T}$  can be calculated. When  $C_{\Delta T, \nabla T} \approx 1$ , the system is in pure diffusion, and when  $C_{\Delta T, \nabla T} \approx -1$ , the presence of heat flux is indicated.

Thus, this method can be used as a pointer to spatially and temporally indicate the diffusivity estimation of heat sources. Nevertheless, it is insufficient because this nodal approach is sensitive to

#### 5.4. INVERSE METHOD FOR A QUANTITATIVE SPATIO-TEMPORAL ESTIMATION OF THE HEAT FLUX - FVM-BASED APPROACH

---

heat losses. This approach can be made more robust by including a global parameter that considers heat losses.

To naturally introduce the global correlation parameter, one can write Eq. 5.32 with a matrix-based system as described in Eq. 5.36.

$$\underbrace{\begin{bmatrix} \Delta T_p^1 \\ \Delta T_p^2 \\ \vdots \\ \Delta T_p^n \end{bmatrix}}_y = \underbrace{\begin{bmatrix} \nabla T_p^1 & T_0 - T_p^1 \\ \nabla T_p^2 & T_0 - T_p^2 \\ \vdots & \vdots \\ \nabla T_p^n & T_0 - T_p^n \end{bmatrix}}_A \underbrace{\begin{bmatrix} d \\ \frac{h}{L_z \rho_m C_p} \end{bmatrix}}_x \quad (5.36)$$

where  $\nabla$  is the Laplacian,  $y$  is an  $n \times 1$  matrix,  $x$  is a  $2 \times 1$  matrix and  $A$  is an  $n \times 2$  matrix.

The system can be simplified as  $Y=Ax$ , where the ordinary mean square solution is given in Eq. 5.37

$$x = (A^t(a)^{-1}A^t)y \quad (5.37)$$

where  $^t$  denotes the transposed matrix.

This leads to the following system. To simplify the notation, the position  $p$  is not indicated.

$$\begin{bmatrix} d \\ \frac{h}{L_z \rho_m C_p} \end{bmatrix} = M \begin{bmatrix} \nabla T^1 \sum \tilde{T} \tilde{T} - \tilde{T}^1 \sum \nabla T \tilde{T} & \dots \\ \tilde{T}^1 \sum \nabla T \nabla T - \nabla T^1 \sum \nabla T \tilde{T} & \dots \end{bmatrix} \begin{bmatrix} \Delta T^1 \\ \Delta T^2 \\ \vdots \\ \Delta T^n \end{bmatrix} \quad (5.38)$$

where:

$$M = \frac{1}{\sum \nabla T \nabla T \sum \tilde{T} \tilde{T} - \sum \nabla T \tilde{T} \sum \nabla T \tilde{T}}$$

$$\tilde{T}^t = T_0 - T^t$$

This leads to Eq. 5.39.

$$d = \frac{\sum \Delta T \nabla T \sum \tilde{T} \tilde{T} - \sum \Delta T \tilde{T} \sum \nabla T \tilde{T}}{\sum \nabla T \nabla T \sum \tilde{T} \tilde{T} - \sum \nabla T \tilde{T} \sum \nabla T \tilde{T}} \quad (5.39)$$

$$\frac{h}{L_z \rho_m C_p} = \frac{\sum \Delta T \tilde{T} \sum \nabla T \nabla T - \sum \Delta T \nabla T \sum \nabla T \tilde{T}}{\sum \nabla T \nabla T \sum \tilde{T} \tilde{T} - \sum \nabla T \tilde{T} \sum \nabla T \tilde{T}} \quad (5.40)$$

#### 5.4. INVERSE METHOD FOR A QUANTITATIVE SPATIO-TEMPORAL ESTIMATION OF THE HEAT FLUX - FVM-BASED APPROACH

---

Note that the obtained equation is no longer dependent on time.

At this step, the correlations appear for different parameter pairs:

- Correlation between the Laplacian and the temporal derivative:  $C_{\nabla T, \Delta T} = \frac{\sum \nabla T \Delta T}{\sqrt{\sum \nabla T \nabla T \sum \Delta T \Delta T}}$
- Correlation between the Laplacian and convective losses:  $C_{\nabla T, h} = \frac{\sum \nabla T \tilde{T}}{\sqrt{\sum \nabla T \nabla T \sum \tilde{T} \tilde{T}}}$
- Correlation between the temporal derivative and convective losses:  $C_{\Delta T, h} = \frac{\sum \Delta T \tilde{T}}{\sqrt{\sum \Delta T \Delta T \sum \tilde{T} \tilde{T}}}$

Consequently, Eq. 5.39 can be expressed as a function of the temporal derivative, the Laplacian and three different correlation parameters, as expressed in Eq. 5.41.

$$d = \frac{\sqrt{\sum \Delta T \Delta T \sum \nabla T \nabla T} C_{\nabla T, \Delta T} \sum \tilde{T} \tilde{T}}{\sum \nabla T \nabla T \sum \tilde{T} \tilde{T} (1 - C_{\nabla T, h}^2)} - \frac{\sqrt{\sum \Delta T \Delta T \sum \tilde{T} \tilde{T}} C_{\Delta T, h} \sqrt{\sum \nabla T \nabla T \sum \tilde{T} \tilde{T}} C_{\nabla T, h}}{\sum \nabla T \nabla T \sum \tilde{T} \tilde{T} (1 - C_{\nabla T, h}^2)}$$

$$d = \sqrt{\frac{\sum \Delta T \Delta T}{\sum \nabla T \nabla T}} \times C_{global} \quad (5.41)$$

where

$$C_{global} = \frac{C_{\nabla T, \Delta T} - C_{\Delta T, h} C_{\nabla T, h}}{1 - C_{\nabla T, h}^2} \quad (5.42)$$

Eq. 5.41 is the product of two terms. The first term is the definition of the absolute mean thermal diffusivity over a specific time, and the second term is a global correlation criterion ( $C_{global}$  defined in Eq. 5.42).

In the same manner, one can express the heat losses as follows.

$$\frac{h}{L_z \rho_m C_p} = \sqrt{\frac{\sum \Delta T \Delta T}{\sum \tilde{T} \tilde{T}}} \times \frac{C_{\Delta T, h} - C_{\nabla T, \Delta T} C_{\nabla T, h}}{1 - C_{\nabla T, h}^2} \quad (5.43)$$

Finally, it is shown in the following section that when  $C_{global} \approx 1$ , only thermal diffusion occurs; thus, the thermal diffusivity can be estimated with Eq. 5.41. On the other hand, when  $C_{global} \approx -1$ , a heat source is active and can be estimated with Eq. 5.33. In this study, the development is performed on the time window  $[1, n]$ . Nevertheless, the demonstration could be performed between  $m$  and  $m+n$ . The sequence of this method is shown in Figure 5.6.

5.4. INVERSE METHOD FOR A QUANTITATIVE SPATIO-TEMPORAL ESTIMATION OF THE HEAT FLUX - FVM-BASED APPROACH

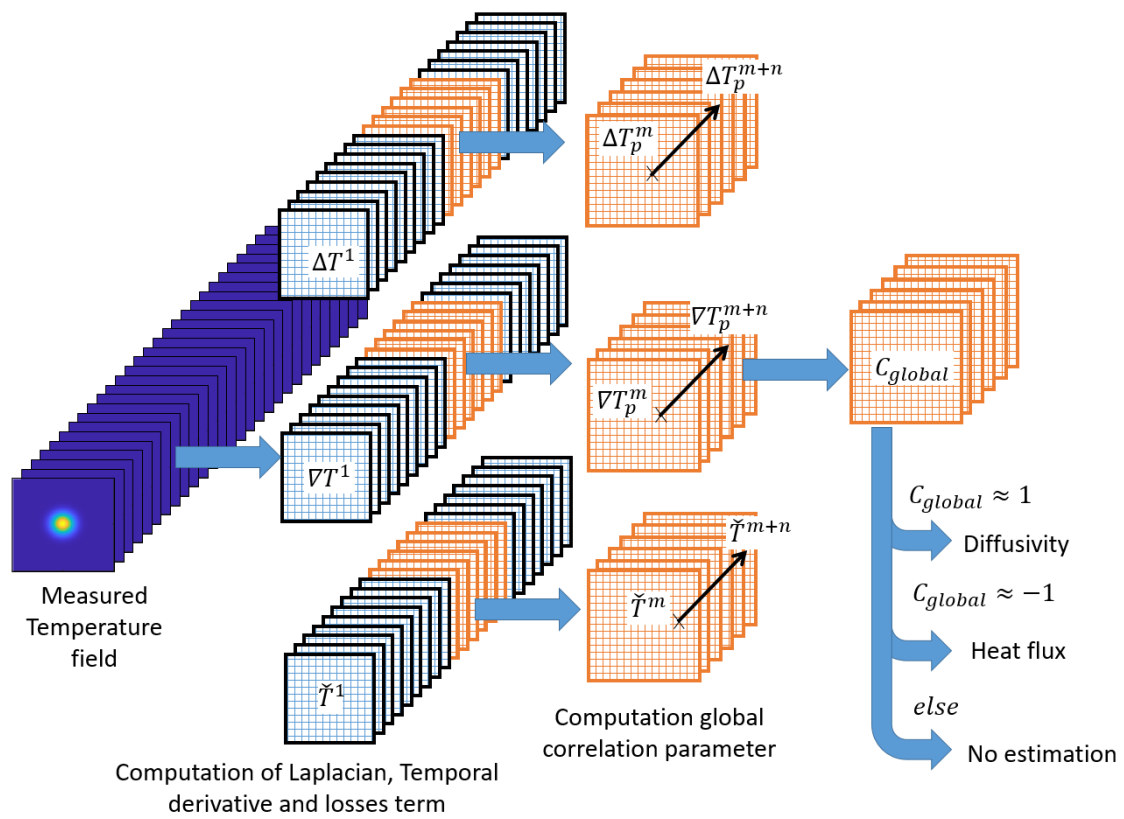


Figure 5.6: Description of the inverse method based on the finite volume approach in 2D cases.

## 5.4. INVERSE METHOD FOR A QUANTITATIVE SPATIO-TEMPORAL ESTIMATION OF THE HEAT FLUX - FVM-BASED APPROACH

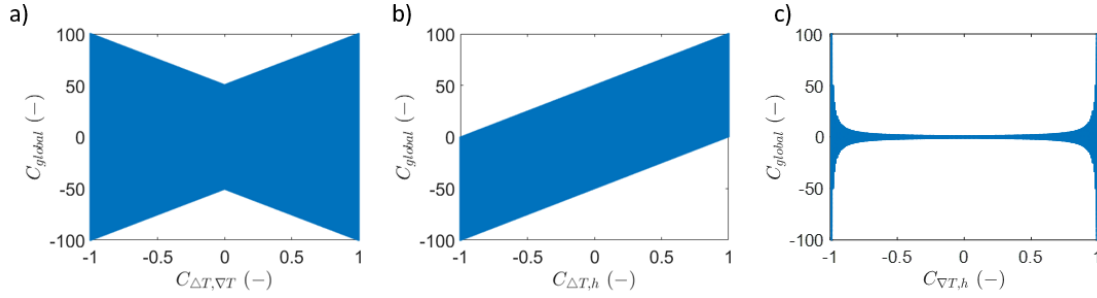


Figure 5.7: Behaviour of the  $C_{global}$  function of (a)  $C_{\nabla T, \Delta T}$ , (b)  $C_{\nabla T, h}$  and (c)  $C_{\nabla T, h}$ .

### 5.4.1.2 Global correlation parameter study

In this section,  $C_{global}$  is studied according to the different correlations  $C_{\nabla T, \Delta T}$ ,  $C_{\nabla T, h}$  and  $C_{\Delta T, h}$ . The following figure shows the evolution of  $C_{global}$  according to the different correlation parameters.

Analysis of these different graphs indicates that the global correlation parameter trends towards  $\pm\infty$  when the correlation between the Laplacian and the heat losses ( $C_{\nabla T, h}$ ) trends towards  $\pm 1$ . In a general manner, one can search for the spatio-temporal position where heat losses do not affect the heat transfer:  $C_{\nabla T, h} \approx C_{\nabla T, h} \approx 0$ . Under these conditions, two characteristic cases are interesting. The first is  $C_{global} \approx 1$ , which corresponds to pure diffusion (without convective heat loss). The second is  $C_{global} \approx -1$  with  $C_{\Delta T, h} \approx C_{\nabla T, h} \approx 0$ , which corresponds to active heat sources. This is illustrated in Figure 5.8.

This global correlation parameter integrates all aspects of heat transfer by including the correlation  $C_{\nabla T, \Delta T}$  but also  $C_{\nabla T, h}$  and  $C_{\Delta T, h}$ . By combining these different correlations,  $C_{global}$  is more reliable than the correlation between the Laplacian and the time derivative  $C_{\nabla T, \Delta T}$  because the latter correlation does not consider heat losses.

### 5.4.1.3 Application on numerical data

The data used to validate the method is extracted from Section 5.3.1.1. Random white noise with a standard deviation of  $0.75^\circ\text{C}$  is added to the data to simulate experimental noise. For the computation of  $C_{global}$ , a time window of 20 images is taken.

Based on the global correlation parameter ( $C_{global}$ ), one can determine the ideal moment for determining the thermal diffusivity of each pixel. Figure 5.9.a shows the mean thermal diffusivity estimated on each pixel. Figure 5.9.b shows how much time the thermal diffusivity has been estimated



#### 5.4. INVERSE METHOD FOR A QUANTITATIVE SPATIO-TEMPORAL ESTIMATION OF THE HEAT FLUX - FVM-BASED APPROACH

---

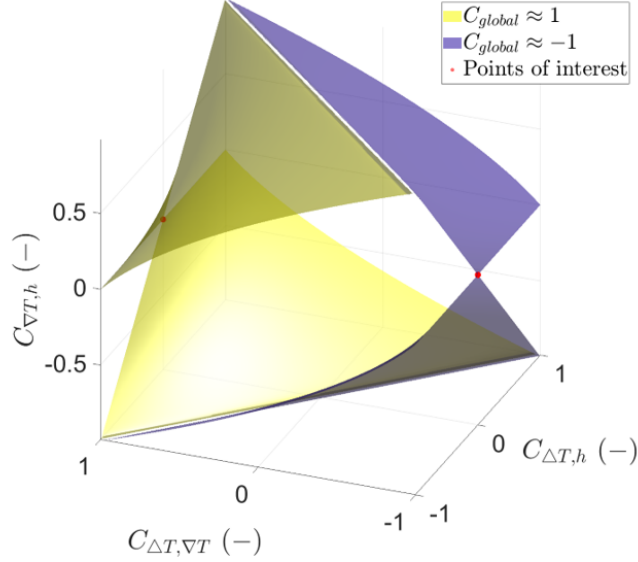


Figure 5.8: Behaviour of the  $C_{global}$  function of (a)  $C_{\nabla T, \Delta T}$ , (b)  $C_{\Delta T, h}$  and (c)  $C_{\nabla T, h}$ .

for each pixel. This estimation is made over 700 time windows of 20 frames each.

The following figures show the histogram of thermal diffusivity estimated over the course of the simulation with a time window of 8 frames. A Gaussian repartition of the estimated diffusivity is observed with a mean value of  $(9.7 \times 10^{-5} \text{ m}^2\text{s}^{-1})$ ,

which is considered close to the true value of  $(9.9 \times 10^{-5} \text{ m}^2\text{s}^{-1})$ . The observed standard deviation is  $1.7 \times 10^{-4} \text{ m}^2\text{s}^{-1}$ .

Figure 5.11.a illustrates the maximum estimated volumetric heat source over time, and Figure 5.11.b shows the estimated power of each letter from the MBDA logo and the total estimated power as a function of time. One can observe the presence of noise for both spatial and temporal estimations. The high sensitivity of the temporal derivative and the Laplacian to noise explains the noise observed on these curves.

Finally, Figure 5.12 shows the relative error of the estimated power along the entire surface over time. The relative error is quite low for the entire estimation, as some peaks are present when the sources are switched on or off due to the time window introducing a delay on the estimation.

#### 5.4. INVERSE METHOD FOR A QUANTITATIVE SPATIO-TEMPORAL ESTIMATION OF THE HEAT FLUX - FVM-BASED APPROACH

---

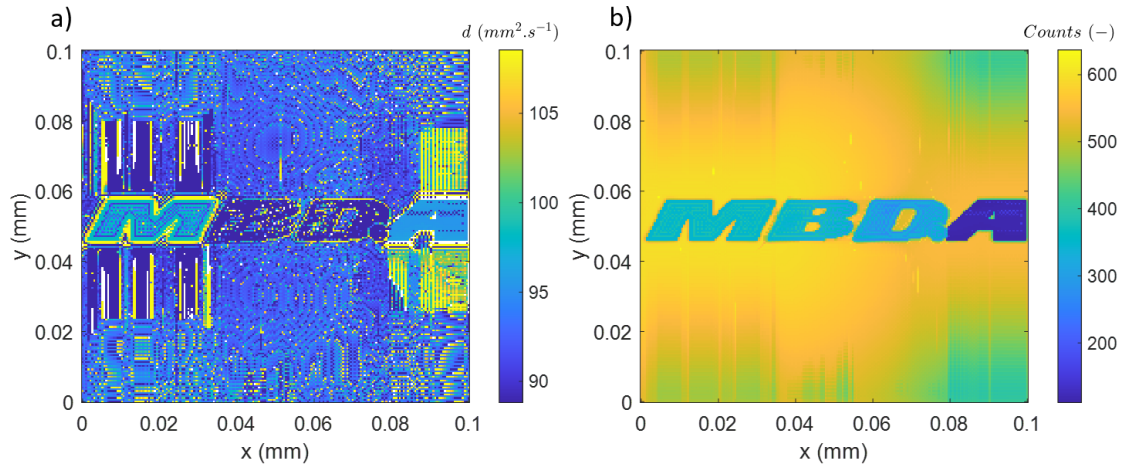


Figure 5.9: Diffusivity estimation: (a) mean estimated thermal diffusivity and (b) number of thermal diffusivity estimations.

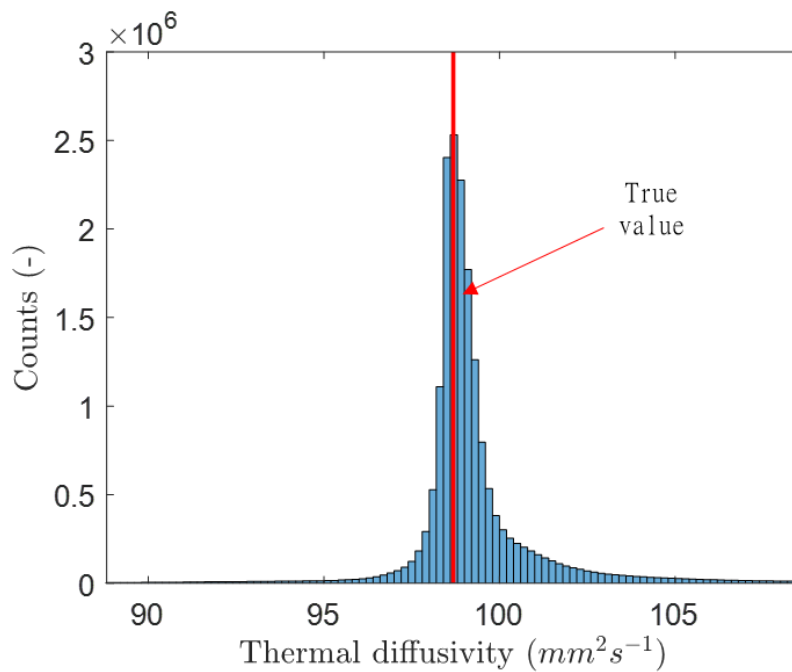


Figure 5.10: Histogram of thermal diffusivity estimation.

5.4. INVERSE METHOD FOR A QUANTITATIVE SPATIO-TEMPORAL ESTIMATION OF THE HEAT FLUX - FVM-BASED APPROACH

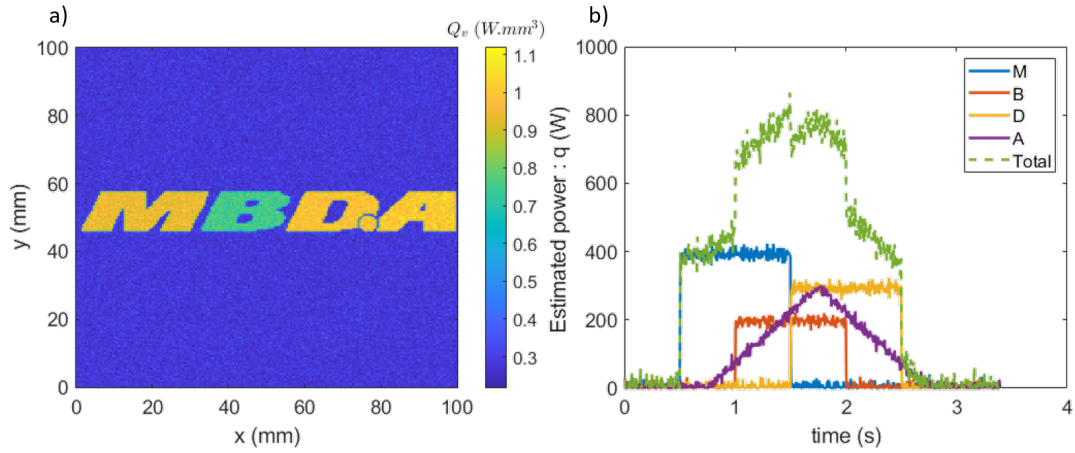


Figure 5.11: Volumetric heat source estimation: (a) maximum estimated volumetric heat source over time and (b) estimated power of each character as a function of time.

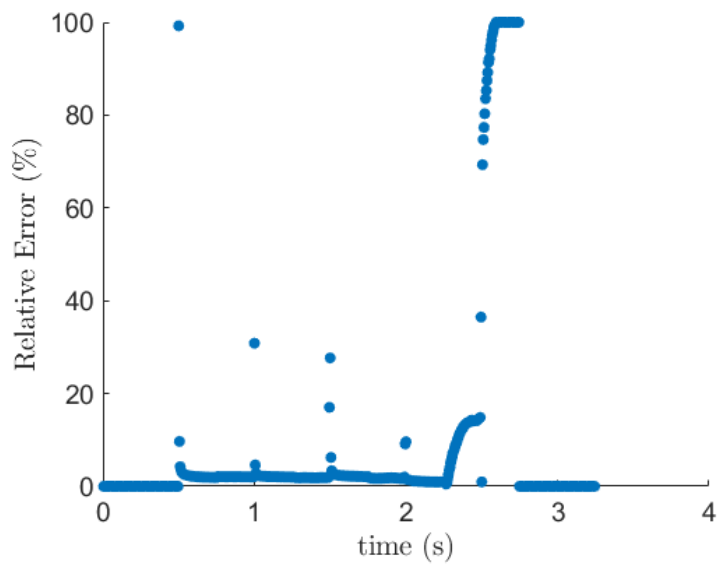


Figure 5.12: Relative error of heat flux estimation.

**5.4.1.4 Conclusions regarding heat source estimation in 2D heat diffusion based on the FVM**

In this section, a method previously developed by the I2M-TREFLE laboratory is implemented to estimate volumetric heat sources in a 2D heat diffusion problem based on the FVM. Implementing the global correlation parameter, which is derived from the inverse problem solution, improves the joint estimation of the thermal diffusivity and the volumetric sources. Despite this advancement, no criterion on the number of images used for calculating the correlation is found. This parameter is therefore based on the experimenter’s experience.

Finally, we validate these methods on 2D applications. The following section is an attempt to use the finite volume formalism for volumetric heat source estimation in 3D.

**5.4.2 Towards a 3D estimation**

Figure 5.13 shows the notation used for the spatial discretisation.

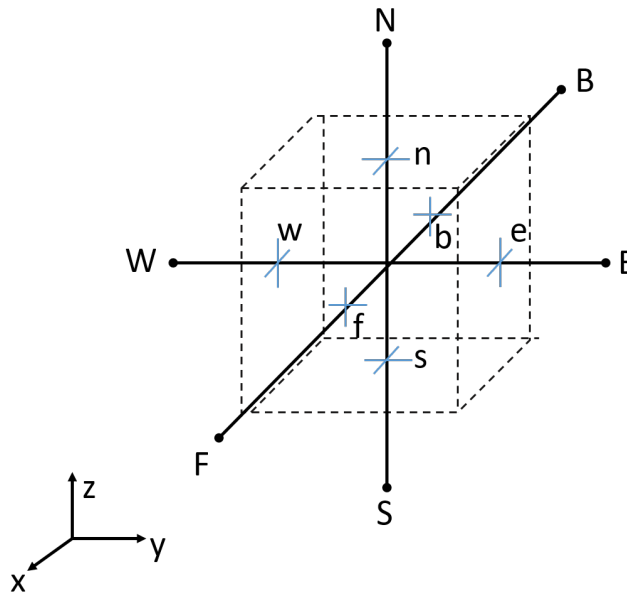


Figure 5.13: Illustration of a portion of the 3D grid used for discretisation.

Under these conditions, the resolution from Fourier’s law demonstrated in 2D with an explicit scheme is presented in Section 5.3.2 and leads to Eq. 5.44 for 3D.

#### 5.4. INVERSE METHOD FOR A QUANTITATIVE SPATIO-TEMPORAL ESTIMATION OF THE HEAT FLUX - FVM-BASED APPROACH

---

$$T_p^{t+\Delta t} = \Delta t \times d \left[ \frac{T_E^t + T_W^t - 2T_p^t}{\Delta x^2} + \text{frac} T_N^t + T_S^t - 2T_p^t \Delta y^2 + \frac{T_F^t + T_B^t - 2T_p^t}{\Delta z^2} \right] + T_p^t + \Delta t \times \frac{Q_v(p, t)}{\rho_m \times C_p} \quad (5.44)$$

Eq. 5.44 is valid for a given point of the mesh and can be generalised to determine all thermal fields through matrix form (Eq. 5.45).

$$\{T^{t+\Delta t}\} = [D]\{T\}^t + \frac{\Delta t}{\rho_m \times C_p} \times \{Q_v^t\} \quad (5.45)$$

where  $[D]$  represents diffusion in an  $nx \times ny \times nz$  square matrix ( $nx$ ,  $ny$  and  $nz$  represent the number of points in the grid along the  $x$ ,  $y$  and  $z$  directions, respectively),  $\{T\}$  is a vector ( $nx \times ny \times nz$ ) that contains the temperature and  $\{Q_v\}$  is a vector ( $nx \times ny \times nz$ ) that contains the volumetric sources of each point of the grid. The exponent expresses the time step.

If the temperature at the initial time step ( $t = 0$ ) is constant, one can express the temperature of the time step  $t = m\Delta t$  as described in Eq. 5.46.

$$\begin{aligned} \{\tilde{T}^{t=\Delta t}\} &= \frac{\Delta t}{\rho_m \times C_p} \times \{Q_v^{t=\Delta t}\} \\ \{\tilde{T}^{t=2\Delta t}\} &= [D]\{\tilde{T}^{t=\Delta t}\} + \frac{\Delta t}{\rho_m \times C_p} \times \{Q_v^{t=2\Delta t}\} = \frac{\Delta t}{\rho_m \times C_p} \times \left[ \{Q_v^{t=2\Delta t}\} + [D]\{Q_v^{t=\Delta t}\} \right] \\ &\vdots \\ \{\tilde{T}^{t=(m+1)\Delta t}\} &= \frac{\Delta t}{\rho_m \times C_p} \times \sum_{n=1}^{m+1} [D]^{m+1-n} \{Q_v^{t=n\Delta t}\} \end{aligned} \quad (5.46)$$

where  $[I]$  is the identity matrix.

The complete temperature field as a function of time can thus be described as:

$$\underbrace{\begin{Bmatrix} \{\tilde{T}^{t=\Delta t}\} \\ \{\tilde{T}^{t=2\Delta t}\} \\ \{\tilde{T}^{t=3\Delta t}\} \\ \vdots \\ \{\tilde{T}^{t=m\Delta t}\} \end{Bmatrix}}_{[T]} = \frac{\Delta t}{\rho_m \times C_p} \times \underbrace{\begin{bmatrix} [I] & & & & \\ [D] & [I] & & & \\ [D]^2 & [D] & [I] & & \\ \vdots & \ddots & \ddots & \ddots & \\ [D]^m & \dots & [D]^2 & [D] & [I] \end{bmatrix}}_{[M]} \cdot \underbrace{\begin{Bmatrix} \{\tilde{Q}_v^{t=\Delta t}\} \\ \{\tilde{Q}_v^{t=2\Delta t}\} \\ \{\tilde{Q}_v^{t=3\Delta t}\} \\ \vdots \\ \{\tilde{Q}_v^{t=m\Delta t}\} \end{Bmatrix}}_{[Q]} \quad (5.47)$$

## 5.4. INVERSE METHOD FOR A QUANTITATIVE SPATIO-TEMPORAL ESTIMATION OF THE HEAT FLUX - FVM-BASED APPROACH

---

By inverting the system, one can express the volumetric source as  $[Q] = [M]^{-1}[T]$ .

Multiple aspects should be highlighted:

- The system is an  $nx \times ny \times nz \times nt$  square. For the present example with a  $mm^3$  spatial discretisation and a time discretisation of 100 Hz, this leads to the square matrix  $[M]$  containing  $15,000,000^2$  elements.
- Accessing temperature measurements is not feasible for the whole sample, whereas the matrix  $[T]$  includes temperature for the whole discretisation. Thus, to solve this problem, gradient-based optimisation methods are not relevant.
- To solve this problem, the number of measurements must be greater than the number of sources. Thus, a hypothesis on the location of the sources must be made.
- The time discretisation needed for the FVM is not necessary for the same temporal discretisation of the experiment. A way to interpolate data must be identified.

Finally, considering the 3D problems presented in Section 5.3.1.2, by assuming a time discretisation of 0.1 s, a spatial discretisation of  $1 mm^3$  and heat sources only on the rear face, 300,000 unknowns arise. Suppose that a minimisation algorithm manages to converge to a solution (which is already complex and requires considerable time and computing resources). With such a large number of unknowns, how can the solution found by a minimisation algorithm be verified as a global minimum and not a local one?

All these difficulties and questions lead us to reconsider this method for determining the spatial and temporal boundary conditions of 3D problems. Therefore, another method using the convolution principle is described in the following section.

### 5.4.3 Conclusions regarding the FVM-based spatio-temporal heat flux estimation

In this section, the FVM coupled with the nodal approach is studied to estimate the heat sources in thermal diffusion problems. The work done on the 2D thermal diffusion problem enables further progress in the joint estimation of the heat sources and diffusivity. The global correlation criterion allows convective losses to be considered and estimated as well.

## 5.5. DESCRIPTION OF THE INVERSE METHOD FOR THE QUANTITATIVE SPATIAL AND TEMPORAL ESTIMATION OF AN EXCITATION FLUX - AN ANALYTICAL APPROACH

It is shown that these approaches are also applicable to 3D heat transfer cases. However, no validation is performed (even on numerical cases) due to the high computational cost.

### 5.5 Description of the inverse method for the quantitative spatial and temporal estimation of an excitation flux - an analytical approach

This work is a direct continuation of a previous thesis carried out within the I2M-TREFLE team by A. AOUALI [30] concerning 3D thermal-spectroscopic tomography for the study of a plasma torch and the work by M. GROZ concerning the 3D reconstruction of volumetric heat sources [132].

#### 5.5.1 Mathematical description of the inverse method for the time and space estimation of heat flux

In this section, a description of the inverse method is provided, allowing the estimation of the amplitude, the form and the temporal variation of surface heat flux.

The response of a thermal system can be described as the sum of the contributions from all heat sources. This is illustrated in Figure 5.14, where a rectangular excitation is discretised as a sum of Dirac excitation (Figure 5.14.a, and the thermal response of the system for both excitations is illustrated in Figure 5.14.b. As observed in Figure 5.14.b, the thermogram obtained with successive Dirac excitations corresponds to the thermogram obtained with rectangular excitations.

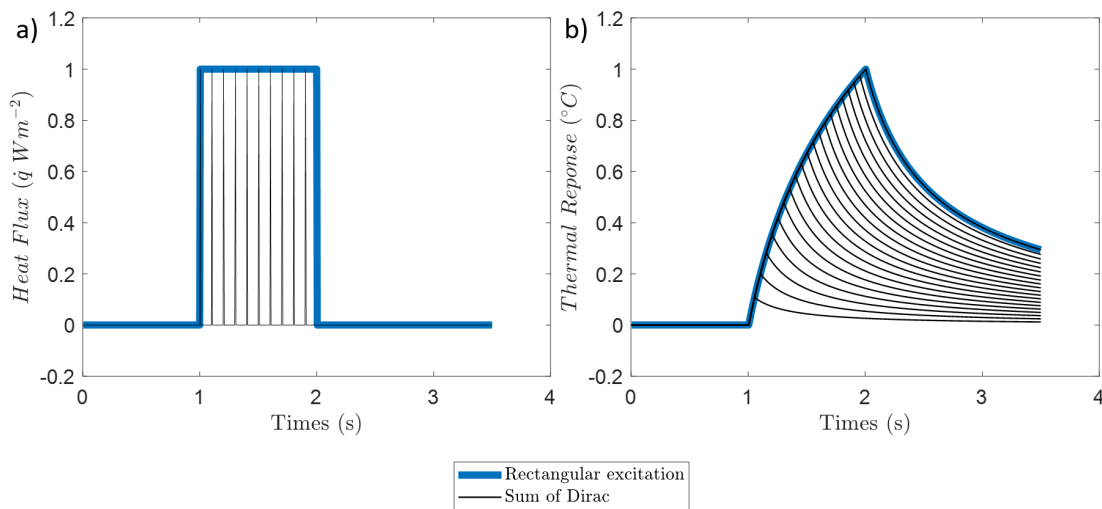


Figure 5.14: Decomposition of heat sources: (a) heat flux function of time and (b) thermal response of the system.

## 5.5. DESCRIPTION OF THE INVERSE METHOD FOR THE QUANTITATIVE SPATIAL AND TEMPORAL ESTIMATION OF AN EXCITATION FLUX - AN ANALYTICAL APPROACH

---

This illustration made on the temporal example also applies to spatial excitation. This reasoning leads to the expression of the thermal response of a system as the spatio-temporal convolution between the heat flux and the impulse response of the system (see Eq. 5.48).

$$T(x, y, z, t) = \dot{q}(x, y, z, t) \circledast_{s,t} \mathcal{H}(x, y, z, t) \quad (5.48)$$

where  $\dot{q}(x, y, z, t)$  is the surface heat flux,  $\circledast_{s,t}$  represents the spatio-temporal convolution (s,t) and  $\mathcal{H}(x, y, z, t)$  is the impulse response of the system.

In our case, the excitation is on the front surface ( $\dot{q}(x, y, z = 0, t)$ ), and the thermal measurement is on the back surface ( $\mathcal{H}(x, y, z = L_z, t)$ ). Thus, Eq. 5.48 can be written as follows.

$$T(x, y, z = L_z, t) = \dot{q}(x, y, z = 0, t) \circledast_{s,t} \mathcal{H}(x, y, z = L_z, t) \quad (5.49)$$

In this equation,  $\dot{q}(x, y, z, t)$  is searched for based on the temperature measurement ( $T(x, y, z = L_z, t)$ ). The difficulty is to change the convolution product into another mathematical operation so that the equation can be inverted, allowing us to obtain the flux as a function of impulse response and temperature.

The convolution of two functions can be written as the product of the Fourier transforms of the functions. Thus, two spatial Fourier transforms are performed along the x- and y-axes by applying the integral transform method [133, 126]. The temperature in Fourier space can therefore be written as described in Eq. 5.50.

$$T(\alpha_n, \beta_m, z = L_z, t) = \dot{q}(\alpha_n, \beta_m, z = 0, t) \circledast_t \mathcal{H}(\alpha_n, \beta_m, z = L_z, t) \quad (5.50)$$

where  $\alpha_n = \frac{n\pi}{L_x}$ ,  $n \in \mathbb{N}$  and  $\beta_m = \frac{M\pi}{L_y}$ ,  $M \in \mathbb{N}$  represent the spatial Fourier modes.

At this step, only the time convolution remains. A. AOUALI found an experimental solution where the temporal form of the heat flux was known [30]. Instead of deconvoluting through the impulse response, he deconvoluted through the step response, corresponding to the temporal form of the flux. By doing so, he was able to spatially deconvolute the source with a Wiener filter. Unfortunately, this assumption cannot be replicated in the present study because the absorbed flux depends on the time-dependent surface condition of the sample. To overcome the temporal convolution, O. Toeplitz



## 5.5. DESCRIPTION OF THE INVERSE METHOD FOR THE QUANTITATIVE SPATIAL AND TEMPORAL ESTIMATION OF AN EXCITATION FLUX - AN ANALYTICAL APPROACH

---

[134, 135] showed that the continuous temporal convolution can be approximated with the discrete Toeplitz matrix described in Eq. 5.51.

$$\left[ \tilde{\mathcal{H}}(\alpha_n, \beta_m, L_z) \right] = \begin{bmatrix} \mathcal{H}(\alpha_n, \beta_m, L_z, t(1)) & 0 & 0 & 0 \\ \mathcal{H}(\alpha_n, \beta_m, L_z, t(2)) & \mathcal{H}(\alpha_n, \beta_m, L_z, t(1)) & 0 & 0 \\ \vdots & \vdots & \ddots & 0 \\ \mathcal{H}(\alpha_n, \beta_m, L_z, t(n)) & \mathcal{H}(\alpha_n, \beta_m, L_z, t(n-1)) & \cdots & \mathcal{H}(\alpha_n, \beta_m, L_z, t(1)) \end{bmatrix} \{\Delta t\} \quad (5.51)$$

The matrix  $\left[ \tilde{\mathcal{H}}(\alpha_n, \beta_m, L_z) \right]$  is squared, and its size is given by the number of images acquired during the experimentation ( $nt$ ). The vector  $\{\Delta t\}$  contains the time steps during acquisition.

Based on Eqs. 5.50 and 5.51, the time variation of temperature for each of the modes as described in Eq. 5.52 becomes:

$$\{T(\alpha_n, \beta_m, z = L_z)\} = [\tilde{\mathcal{H}}(\alpha_n, \beta_m, L_z)]\{\dot{q}(\alpha_n, \beta_m, z = 0)\} \quad (5.52)$$

where  $\{T(\alpha_n, \beta_m, z = L_z)\}$  and  $\{\dot{q}(\alpha_n, \beta_m, z = 0)\}$  are vectors that contain discrete values with regard to temperature (K) and heat flux  $\dot{q}$  in Fourier space  $(\alpha_n, \beta_m, z = L_z)$  and  $(\alpha_n, \beta_m, z = 0)$  for every time step.

Finally, the temporal variation in heat flux can be estimated in the Fourier domain through the following equation:

$$\{\dot{q}(\alpha_n, \beta_m, z = 0)\} = [\tilde{\mathcal{H}}(\alpha_n, \beta_m, L_z)]^{-1}\{T(\alpha_n, \beta_m, z = L_z)\} \quad (5.53)$$

As described previously, inverse problems are known to be ill posed [136, 119, 114]. This is mainly due to the instability of solutions during the inversion. Therefore, many regularisation methods are used for improved system conditioning [137, 138, 139]. In the present study, Tikhonov regularisation is applied during the temporal inversion [140, 141]. The regularisations and inversions are performed in the Fourier space as described in Eq. 5.54.

$$\{\dot{q}(\alpha_n, \beta_m, z = 0)\} = [\tilde{\mathcal{H}}^t \tilde{\mathcal{H}} - \nu \Gamma]^{-1} [\tilde{\mathcal{H}}]^t \{T(\alpha_n, \beta_m, z = L_z)\} \quad (5.54)$$

where  $\Gamma$  is a temporal derivation matrix,  $\nu$  is the regularisation coefficient [142, 143] and  $^t$  is the transposed matrix.

## 5.5. DESCRIPTION OF THE INVERSE METHOD FOR THE QUANTITATIVE SPATIAL AND TEMPORAL ESTIMATION OF AN EXCITATION FLUX - AN ANALYTICAL APPROACH

---

Finally, once the spatio-temporal heat flux is completely identified in the Fourier space, two inverse transforms are performed to express it in real space. When the inverse transform is performed, the identified heat flux must be a real value. If not, the parameters used for the computation of the impulse response (boundary conditions/geometry/thermal properties) will not match the experimental conditions.

### 5.5.2 Spatio-temporal heat flux estimation for 3D thermal conduction

#### 5.5.2.1 Impulse response

The system of equations to be solved for calculating the impulse response is very similar to that presented in Section 5.3.1.2, but the heat flux expression changes, as shown in Eq. 5.55.

$$\left\{ \begin{array}{l} \rho_m C_p \frac{\partial T(x, y, z, t)}{\partial t} = k \left[ \frac{\partial^2 T(x, y, z, t)}{\partial x^2} + \frac{\partial^2 T(x, y, z, t)}{\partial y^2} + \frac{\partial^2 T(x, y, z, t)}{\partial z^2} \right] \\ -k \frac{\partial T(x, y, z, t)}{\partial x} \Big|_{x=0, L_x} = 0 \\ -k \frac{\partial T(x, y, z, t)}{\partial y} \Big|_{y=0, L_y} = 0 \\ -k \frac{\partial T(x, y, z, t)}{\partial z} \Big|_{z=0} = \partial(x) \partial(y) \partial(t) \\ -k \frac{\partial T(x, y, z, t)}{\partial z} \Big|_{z=L_z} = 0 \\ T(x, y, z, t = 0) = 0 \end{array} \right. \quad (5.55)$$

where  $\rho_m$  is the volumetric mass ( $kg \cdot m^{-3}$ ),  $C_p$  is the specific heat ( $J \cdot K^{-1} \cdot kg^{-1}$ ),  $T(x, y, t)$  is the temperature (K),  $k$  is the thermal conductivity ( $W \cdot m^{-1} \cdot K^{-1}$ ) and  $\partial$  is the Dirac function.

Once again, a double spatial (x,y) Fourier transform and a Laplace transform (t) are performed. The temperature of the transformed space ( $\Theta(\alpha_n, \beta_m, z, p)$ ) is described by Eq. 5.56

$$\left\{ \begin{array}{l} \Theta(\alpha_n, \beta_m, z, p) = Ae^{\sqrt{k}z} + Be^{-\sqrt{k}z} \\ A = \frac{e^{-2\sqrt{k}L_z}}{\sqrt{k}(e^{-2\sqrt{k}L_z} - 1)} \\ B = \frac{1}{\sqrt{k}(e^{-2\sqrt{k}L_z} - 1)} \end{array} \right. \quad (5.56)$$

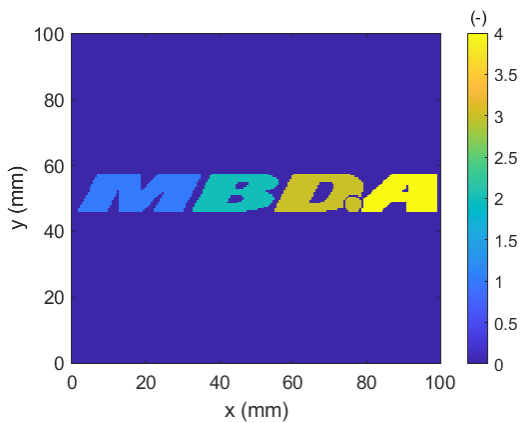
where  $k = \frac{p}{a} + \alpha_n^2 + \beta_m^2$  is the solution of the characteristic equation of Eq. 5.55.

## 5.5. DESCRIPTION OF THE INVERSE METHOD FOR THE QUANTITATIVE SPATIAL AND TEMPORAL ESTIMATION OF AN EXCITATION FLUX - AN ANALYTICAL APPROACH

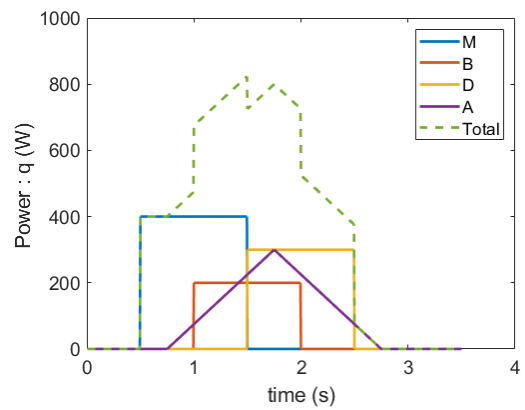
---

### 5.5.2.2 Application to the numerical 3D problem

As a reminder, the imposed heat flux follows the MBDA logo. Figure 5.15a shows the maximum power delivered during the simulation, and Figure 5.15b shows the power of each letter as a function of time. These are the shapes to be identified.



(a) Illustration of the heat flux spatial shape imposed on the front surface.



(b) Illustration of the heat flux temporal shape.

Figure 5.15: Imposed heat flux description.

## 5.5. DESCRIPTION OF THE INVERSE METHOD FOR THE QUANTITATIVE SPATIAL AND TEMPORAL ESTIMATION OF AN EXCITATION FLUX - AN ANALYTICAL APPROACH

Figure 5.16 shows the maximum power obtained during the inversion. For high regularisation factors ( $\nu = 10^{-4}$ ), the identified power is essentially zero. When decreasing the regularisation, the inversion becomes more accurate. For example, the blur of the logo becomes sharper, and the power sources are perfectly identified for  $\nu = 10^{-14}$ . After this step, the Fourier modes tend to diverge.

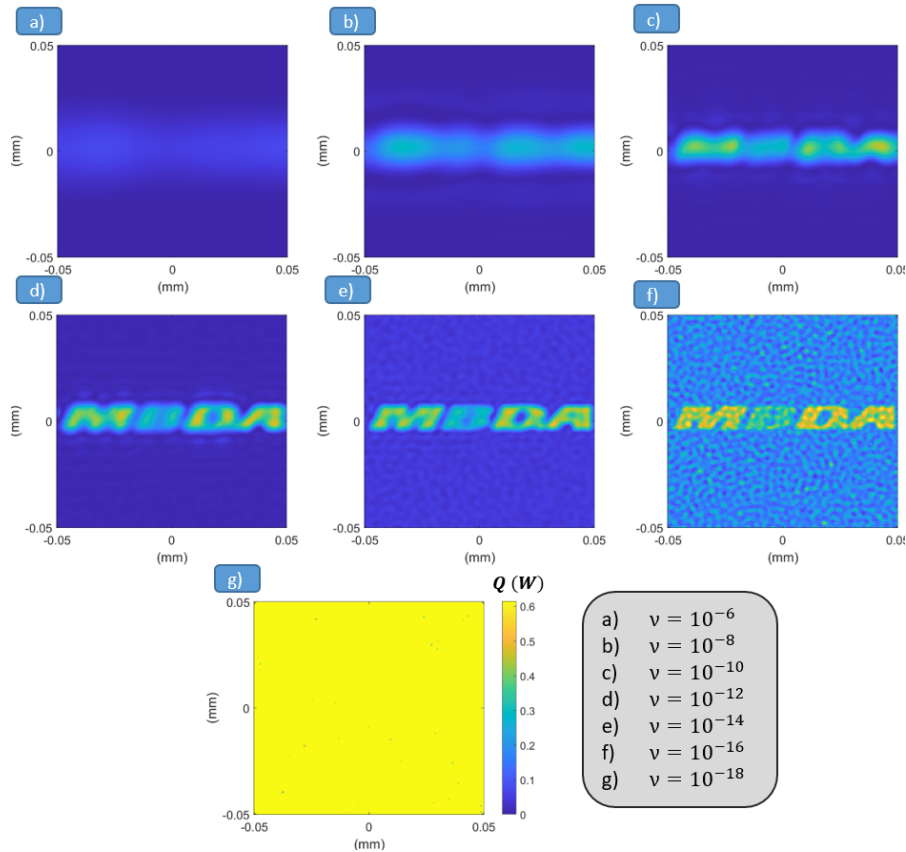


Figure 5.16: Maximum identified power for different regularisation factors ( $\nu$ ).

Figure 5.17 shows the identified power for each letter of the logo and on the whole surface. The temporal behaviour of the inversion is identical to the spatial behaviour. For high regularisation factors ( $\nu = 10^{-4}$ ), the identified power is essentially zero. As the regularisation coefficient decreases, the applied temporal profile can be identified. This behaviour is true up to regularisation coefficients of  $\nu = 10^{-14}$ , and further decreasing the coefficient causes the solution to diverge.

5.5. DESCRIPTION OF THE INVERSE METHOD FOR THE QUANTITATIVE SPATIAL AND TEMPORAL ESTIMATION OF AN EXCITATION FLUX - AN ANALYTICAL APPROACH

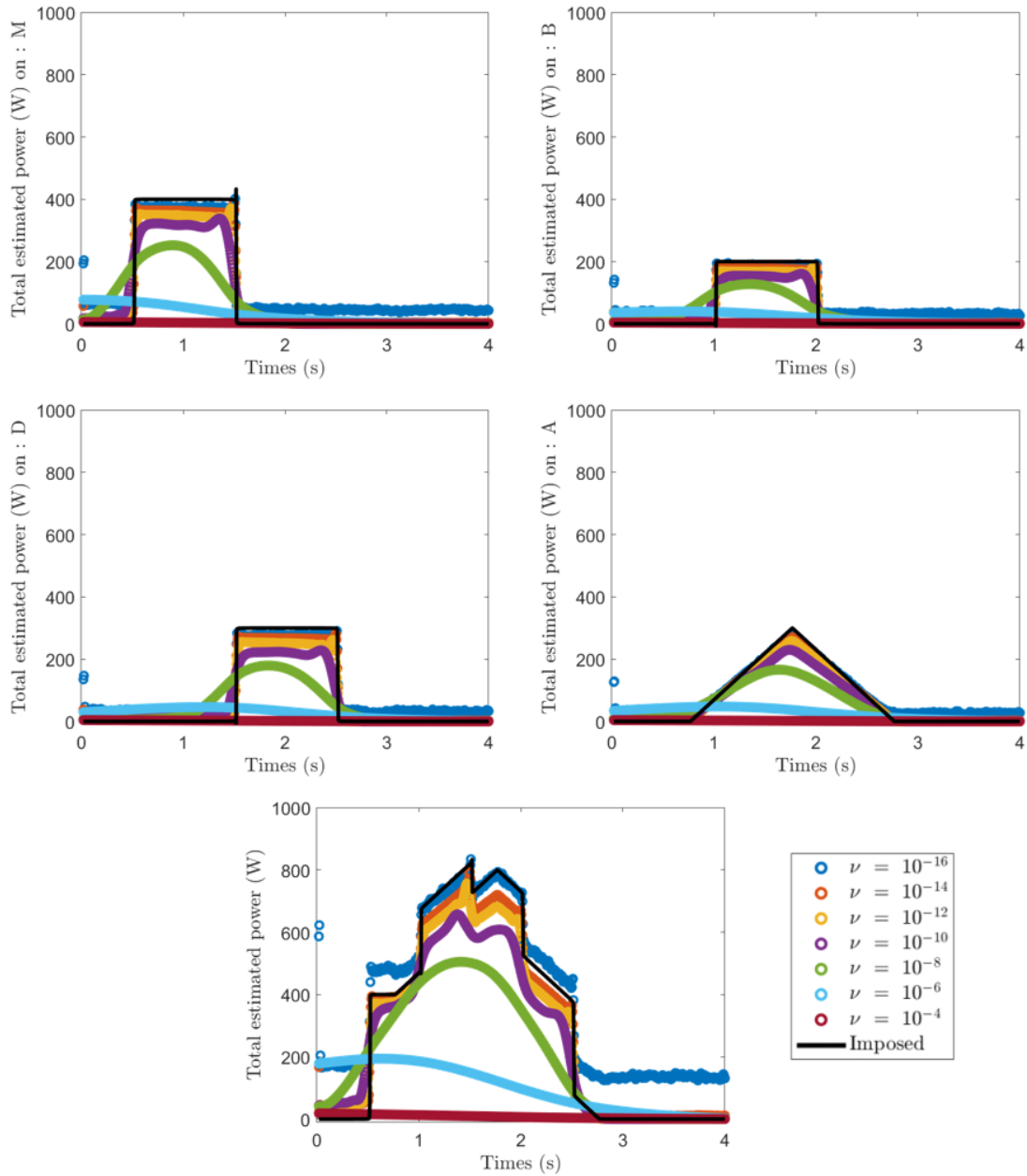


Figure 5.17: Estimated power on each letter and over the total surface as a function of time.

Finally, by considering the spatial and temporal behaviour, the heat flux of the sample's surface can be estimated for regularisation coefficients between  $10^{-8}$  and  $10^{-16}$  with the best results for  $\nu = 10^{-14}$ .

The tests reveal that the calculation time needed for the inversion varies with the applied regularisation coefficient, as illustrated in Figure 5.18. There are two criteria for choosing the  $\nu$  coefficient:

## 5.5. DESCRIPTION OF THE INVERSE METHOD FOR THE QUANTITATIVE SPATIAL AND TEMPORAL ESTIMATION OF AN EXCITATION FLUX - AN ANALYTICAL APPROACH

---

- The parameter  $\nu$  allows better matrix conditioning. Consequently, the best  $\nu$  corresponds to the lower computational times.
- The parameter  $\nu$  restricts the third Hadamard condition and causes the solution to converge to coherent results, despite data noise and measurement errors. In this case, proving that the coefficient used is valid requires a presumption about the solution.

In the various numerical and experimental studies carried out during this thesis work, the best regularisation coefficients often correspond to the shortest calculation times. In the current work, no criterion is found for determining this coefficient without preconceptions of the solution. However, the calculation time may be a clue for future work on this project.

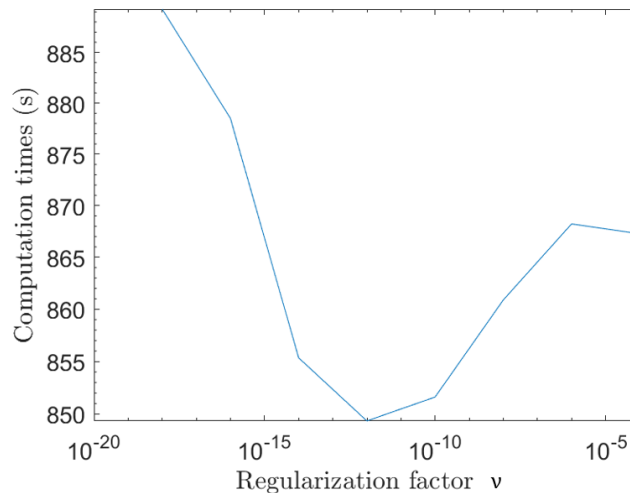


Figure 5.18: Measured computational times as a function of the regularisation factor ( $\nu$ ).

### 5.5.2.3 Conclusions regarding analytical spatio-temporal heat flux estimation

In this section, a deconvolution method is developed to identify the heat flux boundary condition of a 3D thermal diffusion problem. The method allows the estimation of the amplitude of the heat flux, as well as its temporal and spatial behaviours.

The results of this method depend on the regularisation factor, which can be tuned. However, there is often a preconception about the excitation form (spatial or temporal). Therefore, it is easier to determine the ideal coefficient.

The developed method is theoretically available for every 3D problem. However, some precautions must be considered for spatio-temporal discretisation. As the mesh is refined, the sensitivity obtained for each thermal source decreases. To overcome this issue, M. Groz [132] implemented a Fourier criterion while reconstructing 3D volumetric heat sources in semi-infinite media. Time constraints, which were strict for this project, precluded implementation of all the tools of interest.

### 5.6 General conclusions regarding heat flux estimation

In this chapter, numerical and analytical methods are developed to estimate the heat flux from temperature fields. This estimation is a key step for MBDA, enabling quantification of the energy absorbed by the sample during HEL illumination. This allows the energy efficiency of direct laser energy weapons to be determined.

The methods developed in this chapter are based on Fourier's law. **Two inverse methods are developed.** The first is based on an approximate solution of the heat equation by applying the **FVM**. This allows joint estimation of the thermal diffusivity and the absorbed flux. This method is based on the implementation of a **correlation criterion**, allowing us to determine **where and when the sources are present**. Although studies are carried out and validated for 2D diffusion cases, the computational costs and the cumbersome nature of the systems are still obstacles to applying these techniques to 3D cases. A second approach based on the **analytical resolution of Fourier's law and deconvolution** methods is developed to quantitatively determine the flux from temperature fields in 3D diffusion cases.

Regarding a comparison of these two methods, the numerical method is easier to implement, but the major drawback of this method lies in its sensitivity to noise. The global correlation criterion helps decrease sensitivity to noise, but it may not be sufficient for all cases. On the other hand, the analytical approach is more robust and allows 3D estimation. Nevertheless, the complexity of the implementation and the computational times are more cumbersome.

Both methods are validated in complex numerical cases where the **shape and amplitude of the sources vary with time**. This work provides the temperature fields used to find the heat flux of the sources, which constitutes the contribution of Chapter 4.

Here, we apply different methods to **quantify reflection (Chapter 3)** and absorption (Chapter 5) in

## 5.6. GENERAL CONCLUSIONS REGARDING HEAT FLUX ESTIMATION

---

laser-matter interactions. Through the development of the different tools, we encounter difficulties at each stage. It is now necessary to test these methods in specific cases of HEL-matter interaction.



## 5.6. GENERAL CONCLUSIONS REGARDING HEAT FLUX ESTIMATION

---

## Chapter 6

# Application to multi-KW laser–material interaction

### Table of Contents

---

<b>6.1</b>	<b>Introduction</b>	<b>172</b>
<b>6.2</b>	<b>Presentation of the VTF</b>	<b>172</b>
<b>6.3</b>	<b>Towards dynamic measurement of the BRDF</b>	<b>174</b>
6.3.1	Context	174
6.3.2	Presentation of the experimental set-up	176
6.3.3	Data acquired during the trials	176
6.3.4	Measurement of the incident beam	182
6.3.5	From pixel-based acquisition to dynamic BRDF-based images	186
6.3.6	Dynamic BRDF measurements	186
6.3.7	Summary of dynamic BRDF measurement	190
<b>6.4</b>	<b>Application of ATR for dynamic cases</b>	<b>191</b>
6.4.1	Introduction	191
6.4.2	Experimental set-up and sample description	191
6.4.3	Method reminders	193
6.4.4	Application of the ATR method during 4 kW continuous laser–material interaction	195
6.4.5	Summary of ATR temperature measurement during HEL illumination	201
<b>6.5</b>	<b>Heat flux measurement during HEL material interaction</b>	<b>203</b>
6.5.1	Reminders regarding the inverse method	203
6.5.2	Modelling the heat transfer	204
6.5.3	Estimation of the absorbed heat flux under HEL illumination	208
6.5.4	Summary of heat flux reconstruction	222
<b>6.6</b>	<b>Chapter summary</b>	<b>222</b>

---

## 6.1 Introduction

The methods developed in Chapters 3 and 5 allow complete characterisation of an HEL interaction with a sample material in terms of reflection and absorption. The methods studied in Chapter 5 are demonstrated on temperature fields extracted from numerical simulations. Prior to this work, the temperature fields had never been investigated, even if noise was artificially added. The challenge here is to further improve the experimental conditions of the set-up and to address the **extreme conditions** under **HEL illumination at the Vulnerability Test Facility (VTF)**.

In this chapter, 3 applied imaging methods are presented, including **visible optical imaging at different wavelengths, thermal imaging and thermo-reflectance**. The first experimental set-up utilising thermo-reflectance acquisitions is developed to study the **dynamic BRDF** behaviour of HEL-material interactions in the **visible - near-infrared** spectral range. A second experimental set-up based on **ATR** is used for **temperature measurements** in the **far-infrared** region during HEL illumination.

Finally, the skills acquired through **optical imaging methods, image processing, experimental set-ups, absolute temperature measurement and thermal inverse method** allow **quantitative spatio-temporal heat flux estimation** under HEL illumination.

## 6.2 Presentation of the VTF

The VTF is a laboratory shared between MBDA and ALPhANOV for studying laser-matter interactions for representative HEL engagements (Figure 6.1). The VTF targets defence and civil applications, such as welding and polishing on complex shapes [144].

It is a fully automatised experimental laboratory equipped with HEL sources manufactured by IPG whose output power ranges from 0 to 10 kW at a wavelength of  $1.07 \mu\text{m}$ .

The facility is equipped with four different laser heads:

- a scanner head (intelliWELD®), manufactured by Scanlab,
- an optical zoom, manufactured by Haas Laser Technologies,
- a top hat head, manufactured by Haas Laser Technologies, with a beam diameter of 10 mm, and
- a top hat head, manufactured by Haas Laser Technologies, with a beam diameter of 30 mm.

## 6.2. PRESENTATION OF THE VTF

The scanner head allows the laser beam to move at speeds up to  $10 \text{ m} \cdot \text{s}^{-1}$  and is used to simulate laser tracking of moving targets. The optical zoom enables spot sizes from 4 to 80 mm at a given working distance and is used to study the impact of the spot diameter during HEL engagement. The top hat heads are used to evaluate the HEL's spatial shape.

The selected laser head is mounted on a 6-axis robot. Both the robot and the head are remotely controlled to simulate representative engagement. The robot, the laser head and the instrumentation are placed in a laser safety cabinet, as presented in Figure 6.1.

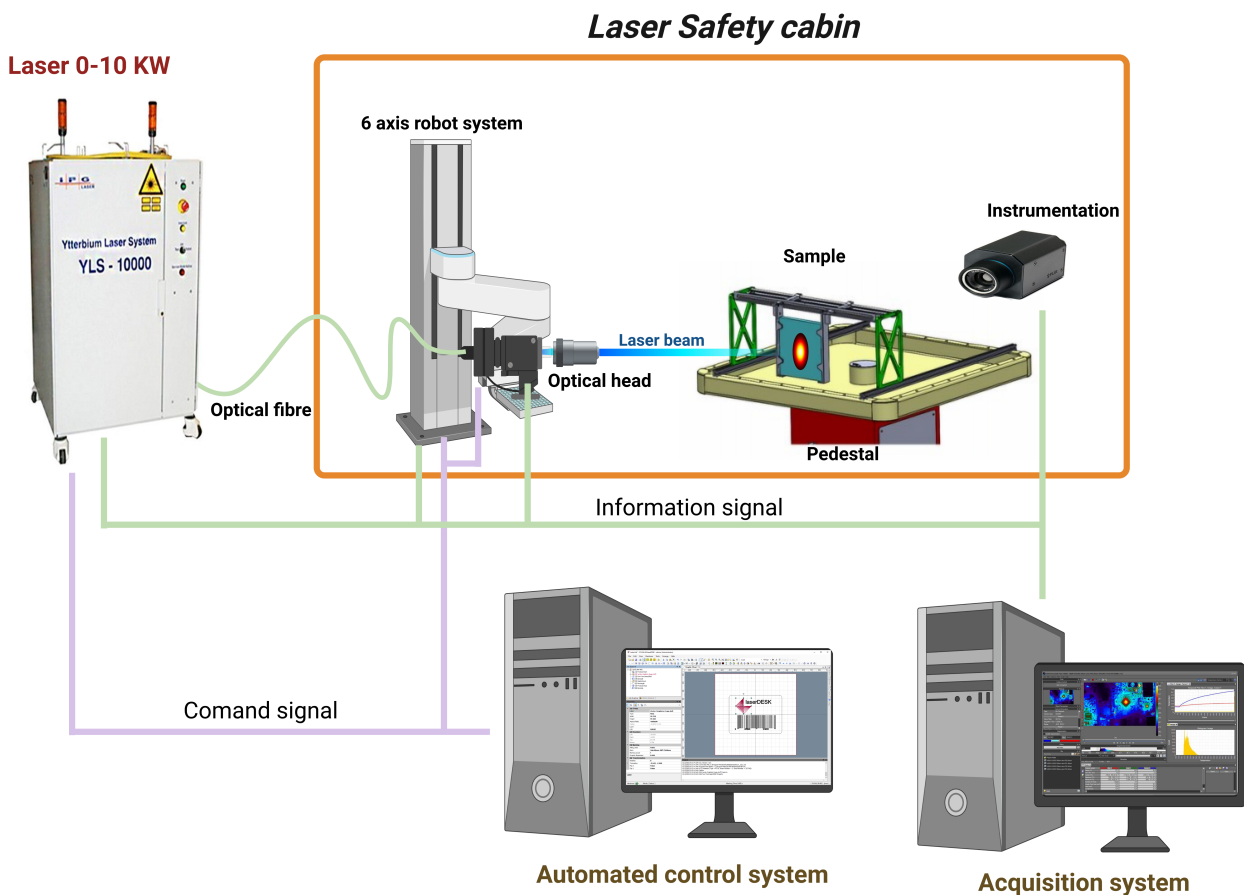


Figure 6.1: Experimental set-up for the characterisation of HEL radiation scattered from a solid surface.

The entire instrument and the processing part (robot, laser, etc.) are linked to two dedicated PCs that monitor the acquisition and control the laser process.

### 6.3 Towards dynamic measurement of the BRDF

The presented section is the result of close collaboration between the following:

- The Optics & Lasers Technology Centre - ALPhANOV (Talence, FRANCE): M. POMMIES, C. REGNAULT, E. CHALUMEAU
- The Materials, Processes and Surfaces Study and Research Laboratory team of the Carnot Interdisciplinary Laboratory of Bourgogne (ICB-LERMPS, UMR CNRS 6303: Sevenans, FRANCE): G. Darut and C. Verdy
- MBDA-France (Plessis-Robinsson, FRANCE): R. PEIFFER, M. TAILLANDIER, A. CARRARD-DRAGHI and T. LAFARGUE-TALLET
- The Fluid Energy Transfers team of the Institute of Mechanics and Engineering (I2M-TREFLE, UMR 5295 FRANCE): C. PRADERE, E. ABISSET-CHAVANNE and T. LAFARGUE-TALLET

In this collaboration, LERMPS oversaw realisation of Lambertian screens with high reflectivity and resistance to high temperatures. ALPhANOV oversaw the optical characterisation of the LERMPS Lambertian screens, as well as the implementation of the experimental set-up. MBDA-France, the project leader, provided the funding. I2M-TREFLE was involved in the implementation of the experimental set-up as well as the data processing.

#### 6.3.1 Context

As seen in Chapter 3, the acquisition of BRDFs is often performed through gonioreflectometers to collect reflected flux in all directions. This is not feasible for dynamic studies where the surface treatment changes quickly due to phase changes, oxidation of the sample, etc. Thus, the implementation of image-based BRDF measurement is once again adapted. Only a few reports on the measurement of BRDFs for HEL interaction with matter are present in the literature. Those specific studies are often focused on the computation of the nominal ocular hazard distance (NOHD), which is not the subject of the present study.

In a previously described set-up (Chapter 3), all reflected energy is directly projected onto the camera sensor by an off-axis parabolic mirror. Unfortunately, projecting the reflected beam directly

to the sensor cannot be applied for HELs because the camera sensor would be damaged. A method that captures the BRDF without damaging the sensor is needed. A way to resolve this issue is to image the scattered light onto a Lambertian screen to image the BRDF, thereby greatly diminishing the amplitude of the reflected energy.

This method is an extension of previous studies where the reflective panels used were Lambertian hemispheres imaged by a camera equipped with a fisheye objective [145, 49, 146]. Those studies were developed in the early nineties by pioneered allowing BRDF acquisition in laboratory conditions [14, 147, 148].

Then, researchers used this set-up to evaluate the ocular risks associated with HEL–matter interaction. Due to defence applications, this research is private, and few reports are available. However, in 2007, D. Huantes et al. [149] quantified the reflective properties of an HEL. Based on both the BRDF model and the experimental data, they developed a new approach that allows BRDF model parameters to be determined to compute the NOHD. In 2007, J-F. Daigle et al. [150] proposed a new approach to evaluate the NOHD based on experimental measurements. This novel approach is an innovative way of questioning the classic computation methods for NOHDs. In 2015, Sabatini et al. [151] realised a complete study of technologies enabling the design and operation of airborne laser sensors and introduced a detailed review of state-of-the-art avionic systems for civil and military applications. That manuscript has a dedicated part for NOHD computation including the consideration for factors of importance in ground-air engagements and Lambertian reflections.

Additionally, those studies were performed in ideal laboratory conditions where the incident beam diameter was on the scale of tens of micrometres, far from the representative beam diameter considered in the present study of 30 mm. Consequently, a study was conducted at the VTF to quantify the reflective behaviour of HEL–matter interaction.

The global architecture of the experimental set-up is described. Then, calibration is performed to identify the link between the optical flux and the camera response. Next, the link between image coordinates and the BRDF coordinates is shown. Finally, the results are presented for different laser head configurations.

#### 6.3.2 Presentation of the experimental set-up

Figure 6.2 shows the set-up used in this study. It is composed of a laser head, a reflective panel (considered Lambertian), a sample imaging system, a system to quantify the perforation time (drilling time) and two cameras that are used to image the laser reflection.

In this section, two laser heads are used: the first is an optical zoom with a Gaussian beam output of 30 mm, and the second is a top-hat beam with an output of 30 mm. Both laser heads are used separately but with the same orientation to the sample.

The sample imaging system is composed of an 810 nm pulsed laser (called Cavilux) and two cameras. Both cameras have a bandpass filter centred on the Cavilux wavelength to isolate the Cavilux for imaging. This allows undesired reflections from the HEL to be avoided.

Two other cameras are used to image the reflective panel. They are equipped with a bandpass filter to observe only the HEL. One camera (number 9 in Figure 6.2) is normal to the panel, and the other is set back to observe the whole panel (number 10 in Figure 6.2). A hole in the middle of the reflective panel allows the laser beam to pass through.

In this study, the laser output power is continuously set at **4000 W**. The samples used measure  $100\text{ mm} \times 100\text{ mm} \times 5\text{ mm}$  and are made of 304L steel. The surface finish is obtained by lapping, and the surface roughness obtained is  $0.8\text{ }\mu\text{m}$ .

#### 6.3.3 Data acquired during the trials

Before further describing the analysis of this first measurement, it is important to describe the mechanism occurring during HEL–matter interaction. A major parameter in this interaction is the irradiance (or power density, denoted by  $\dot{q}$ ,  $\text{W} \cdot \text{m}^{-2}$ ) that illuminates the sample surface. Comparison of different laser spot shapes indicates that the incident laser's spatial distribution varies, while its power is unchanged. Both top hat and Gaussian beams are illustrated in Figure 6.3.

Remark: The diameter measurement of a Gaussian beam is given by the norm  $D4\sigma$ . This norm defines the diameter of the beam (D) as 4 times the standard deviation of the Gaussian ( $D = 4\sigma$ ).

As shown in Figure 6.3, the local maximum of the Gaussian beam is 2 times that of the top hat when the diameter is held constant. This variation introduces temperature fields that are completely different for both cases. Consequently, the appearance and growth of the molten area also changes.

### 6.3. TOWARDS DYNAMIC MEASUREMENT OF THE BRDF

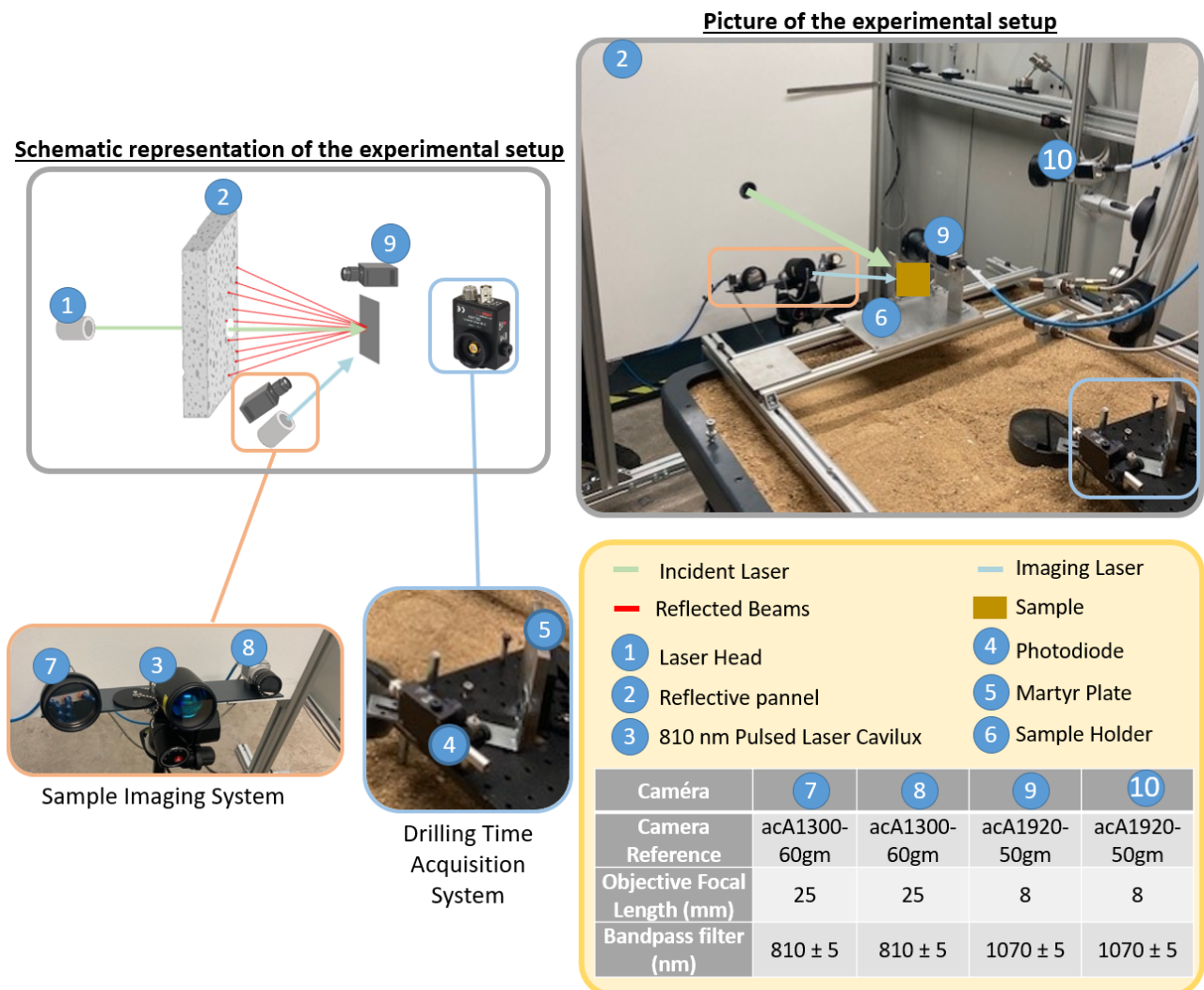


Figure 6.2: Experimental set-up for the characterisation of HEL radiation scattered from a solid surface.



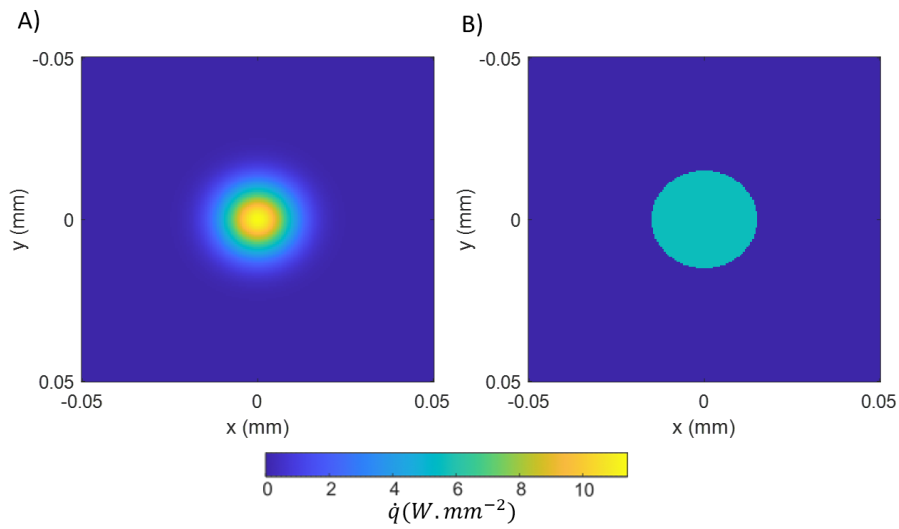


Figure 6.3: Numerical illustration of the incident power density for a laser power of 4 kW and a beam diameter of 30 mm (numerical data): (a) Gaussian beam and (b) top hat beam.

These variations are illustrated in Figure 6.4.

The molten area under Gaussian illumination appears shiny and smooth; in contrast, under top hat illumination, the surface condition of the molten area develops a crust, which may be due to oxidation.

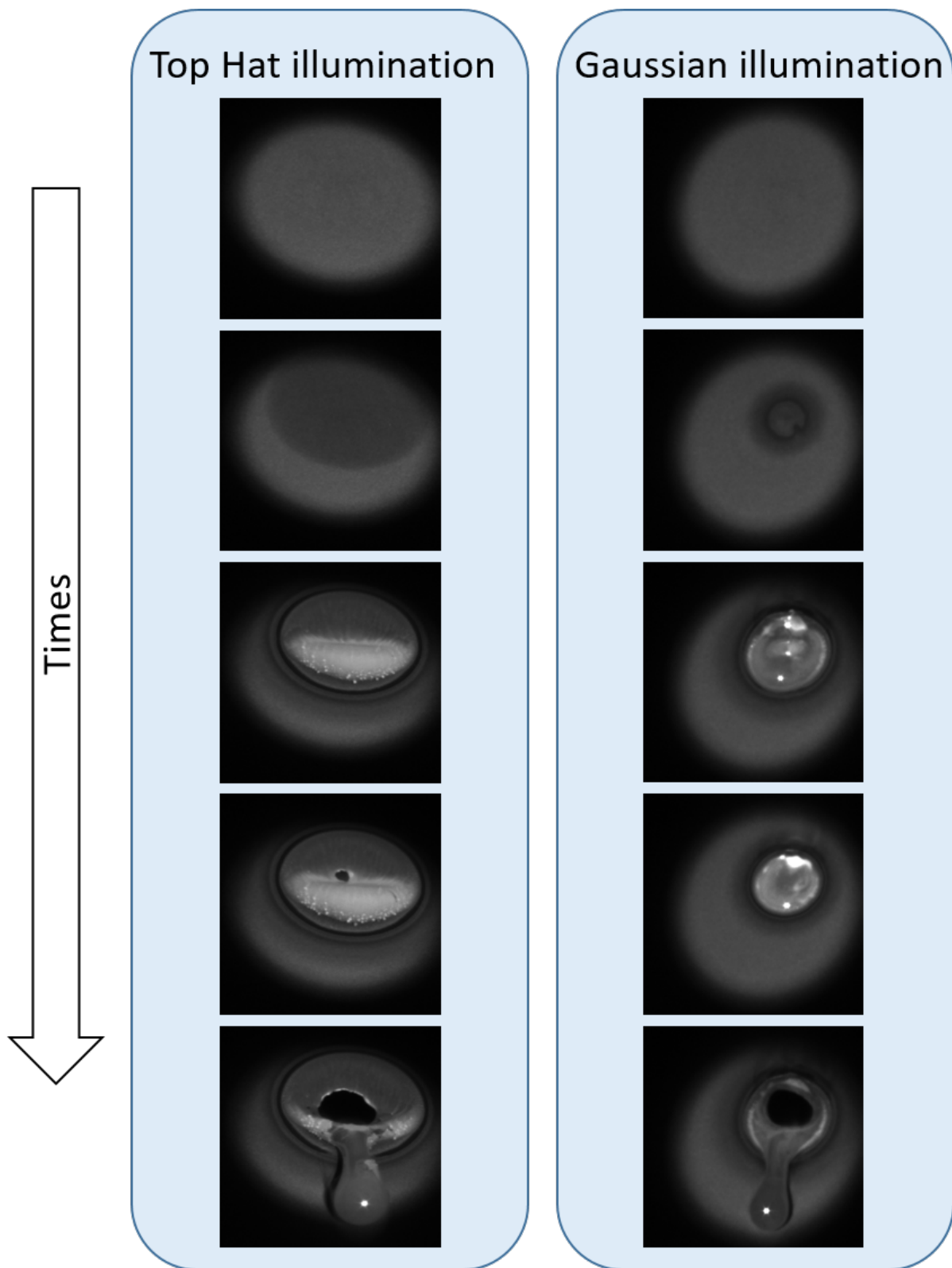


Figure 6.4: Sample behaviour at different time steps under top hat and Gaussian illumination.

From these images, one can already assume that the reflection shape is different between both laser heads. Figure 6.5 shows images of the Lambertian screen at different time steps of the experimentation for the Gaussian and top hat laser heads. When the laser beam is Gaussian, the reflections are mainly specular. The preferred direction moves vertically and is followed by a cone-shaped reflection. The specular aspect is attributed to the smoothness of the molten zone, and the vertical movement is likely due to the curvature of the droplet. On the other hand, the reflection of the top hat laser seems more diffused at the beginning of the experimentation and changes over the course of experimentation. Towards the end of the film, one can observe a bright spot appearing near the centre of the screen. The last picture reveals several aligned reflections, which are attributed to undesired reflection inside the camera objective.

It is important to use pixels located on the Lambertian panel. Consequently, pixels located outside this later as well as those corresponding to the hole inside are not considered, as illustrated in Figure 6.6, which shows the spatial filter used. The corresponding pixel size in this configuration is  $0.5 \text{ mm}^2$ .

Up to this point, the complete set-up including the acquisition steps and the raw generated data is presented. However, there are still multiple steps required to obtain a dynamic BRDF measurement from these data. The first step is to identify the camera response to the incident reference beam with a calibration. Then, each pixel in the image must be assigned to a reflection direction ( $\theta_r$  and  $\phi_r$ ) and an associated solid angle. These multiple steps finally allow us to obtain the dynamic BRDF. This process is explained in the following section.

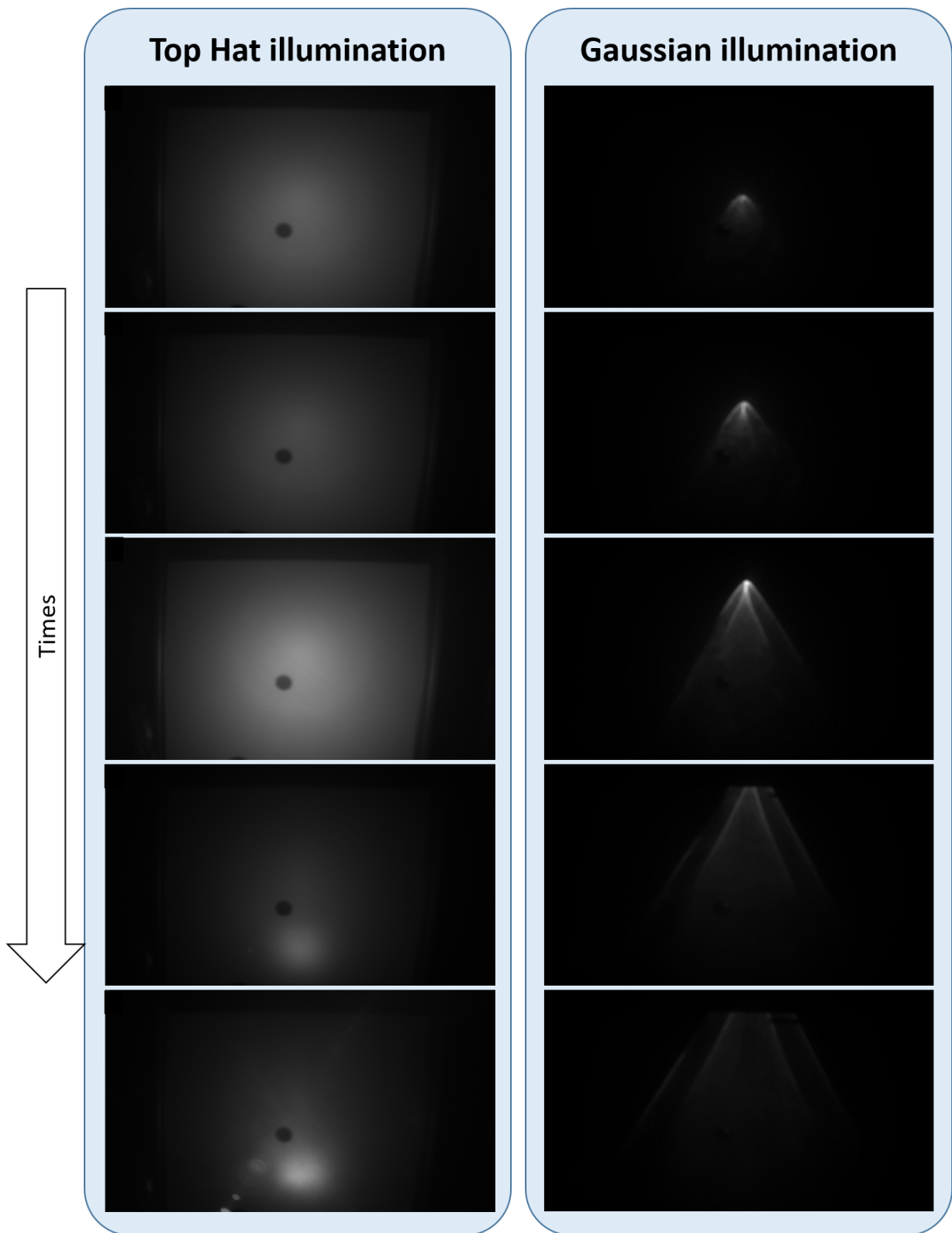


Figure 6.5: BRDF behaviour at different time steps under top hat and Gaussian illumination.

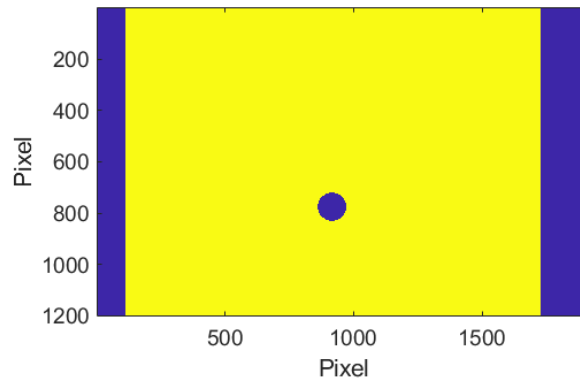


Figure 6.6: Spatial filter used during data processing: blue corresponds to pixels outside the panel, and yellow corresponds to pixels inside the panel.

#### 6.3.4 Measurement of the incident beam

To identify the camera's response to the incident beam, calibration is performed. To begin the calibration, the sample is replaced with a perfect mirror (Figure 6.7). This mirror has the same orientation and location as the sample's surface. This allows a link between the luminous flux ( $W$ ) and the camera response to be determined. However, delivering the same laser power as the trials is not ideal, as the Lambertian screen may be damaged. Thus, the power output is reduced, requiring the integration times (ITs) of the camera to be adjusted. The interpolation law of the camera transfer function must be identified to complete the calibration, as the luminous flux and the IT are both dependent on it.

The camera response is a linear function of the IT and a linear function of the luminous flux. Thus, those parameters must be identified, which requires a three-step process.

**First**, the camera response for multiple laser output powers must be measured. For each laser output power, multiple measurements are recorded for multiple ITs. Figure 6.8 shows a typical image acquired during this process. Pixels surrounding the Lambertian panel are not considered. The centre of the spot is considered normal to the sample. It is represented by a red dot in Figure 6.8.

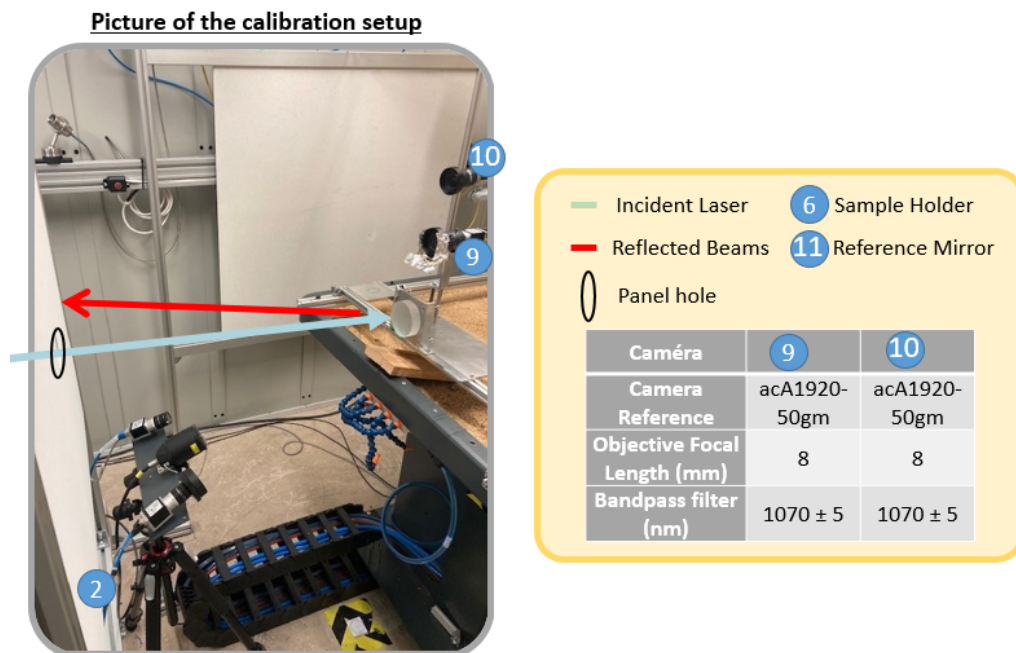


Figure 6.7: Experimental set-up developed to calibrate the incident beam.

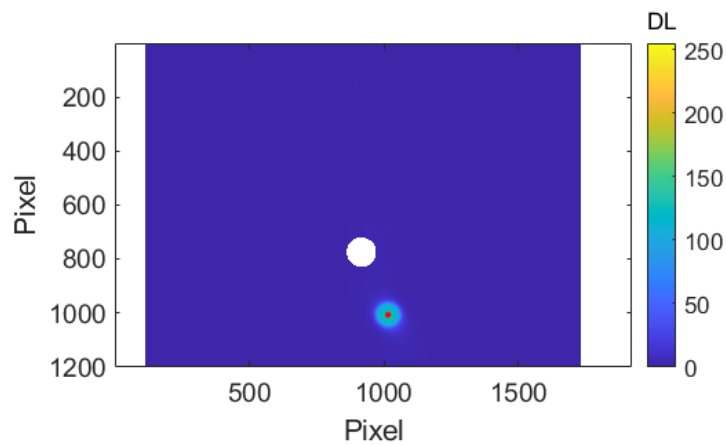


Figure 6.8: Typical image acquired during the calibration process.

**Second**, for each combination of IT and laser power, images are captured with and without illumination for background subtraction. Then, discrete integration of the DL is performed for the entire image. Figure 6.9 shows the integration results as a function of laser power for each acquired

IT with camera number 9 identified from Figure 6.7. The integrated image is linearly dependent on the laser output, allowing an IT-dependent slope coefficient to be determined.

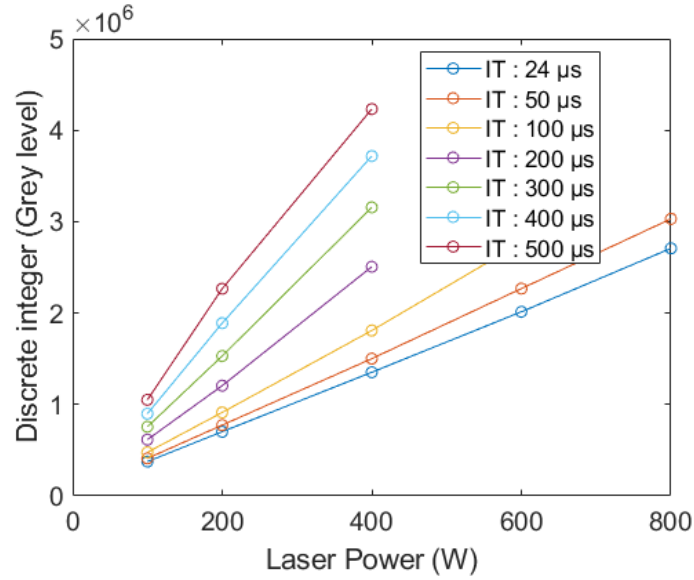


Figure 6.9: Experimental curves of image discrete integration as a function of laser power for multiple ITs.

Consequently, the camera transfer function can be written as:

$$S(q) = a(IT) \times q + b(IT) \tag{6.1}$$

where  $S$  is the camera output signal (DL),  $q$  is the laser power and parameters  $a$  and  $b$  describe the linear fit.

The following figure describes the slope coefficient (Figure 6.10a) and the intercept function (Figure 6.10b) of the IT. The intercept is always null ( $B = 0$ ), whereas the slope coefficient has a linear dependency on the IT:  $A(IT) = a \times IT + b$ . Consequently, one can fit parameters  $a$  and  $b$ .

Consequently, the camera transfer function can be written as:

$$S(q) = [a \times IT + b] \times q \tag{6.2}$$

where  $a \approx 15.6$  and  $b \approx 3000$ .

Figure 6.11 shows the projection of the identified parameter on the initial data.

### 6.3. TOWARDS DYNAMIC MEASUREMENT OF THE BRDF

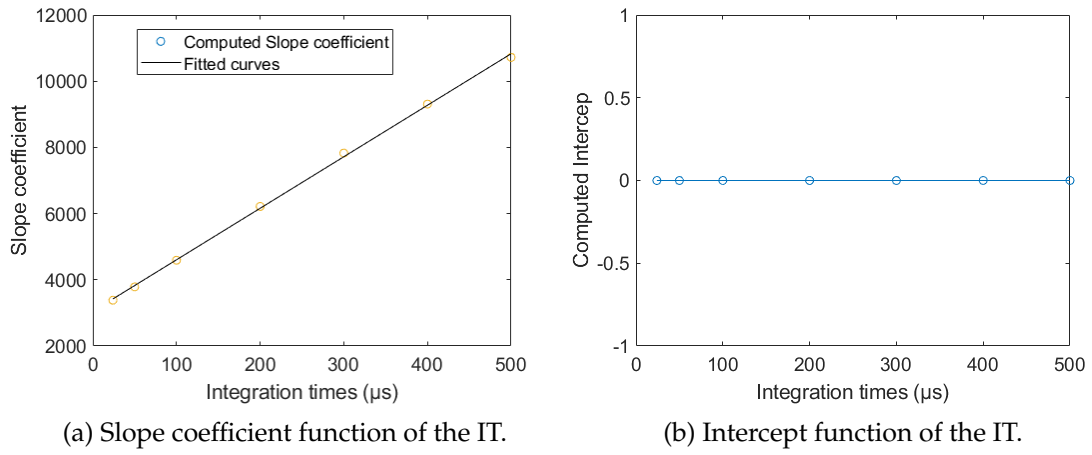


Figure 6.10: Fitting of the slope coefficient and intercept.

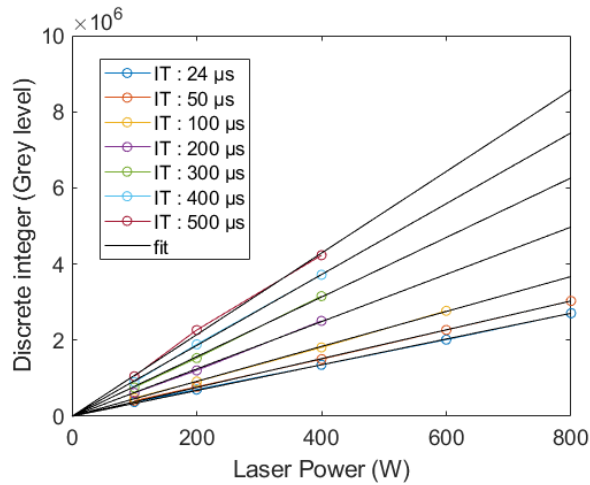


Figure 6.11: Projection of the identified fit atop the experimental data.

Finally, based on Eq. 6.2, the reflected flux on each pixel ( $p$ ) of the Lambertian screen can be expressed as follows:

$$q(p) = \frac{S(p)}{a \times IT + b} \quad (6.3)$$



In this process, the following hypotheses are proposed:

- The linear trend of the IT calibration is assumed to extend past the ITs used in the calibration process. The IT used during the calibration is lower than the IT used during the experimentation; therefore, it is necessary to extrapolate and assume that the linear trend remains ( $IT_{calibration} < 500 \mu s$  vs.  $IT_{experimentation} > 1000 \mu s$ ).
- The reflective panel is assumed to be a perfect Lambertian screen; the reflectance is the same in any given direction and for every point of the screen.

Note that only the laser output power, the ITs and the sample (replaced by the mirror) change from calibration to experimental settings. The camera aperture, location, etc., remain the same.

### 6.3.5 From pixel-based acquisition to dynamic BRDF-based images

In this section, the position of each pixel in the image is linked to its 3D position in the experiment ( $\theta$  and  $\phi$ ) and the corresponding solid angle.

At this step, the polar ( $\theta$ ) and azimuthal ( $\phi$ ) angles are searched for. They are normally defined in relation to the sample's normal surface, which is not easily accessible in this configuration. Instead of the normal direction, the centre of the beam during the calibration is used (Figure 6.8). The camera's location is assumed to correspond to the centre of the incident beam, illuminating the sample's surface, as illustrated in Figure 6.12. In reality, the camera is 155 mm higher (y direction in Figure 6.12).

Based on the screen location, the pixel size and the 3D coordinates of each pixel, one can compute the polar ( $\theta_r$ ) and azimuthal ( $\phi_r$ ) angles. Angles  $\theta_r$  and  $\phi_r$  are illustrated in Figure 6.13a and Figure 6.13b, respectively. Additionally, one can compute the solid angle of each pixel illustrated in Figure 6.14 (results are shown for camera number 9). The white pixels extend past the Lambertian screen.

### 6.3.6 Dynamic BRDF measurements

The dynamic BRDF can be calculated using the polar angle, azimuthal angle, computed solid angle, calibration and images. The results are shown for both top hat and Gaussian illumination (Figure 6.15). For the top hat illumination, the obtained BRDF is nearly homogeneous at the beginning of acquisition, and at the end of acquisition, a bright spot appears. On the other hand, under Gaussian illumination, the BRDFs are specular and exhibit a peak over the course of the experiment. Note that the measured BRDFs for the top hat illumination are approximately one twentieth of the BRDFs

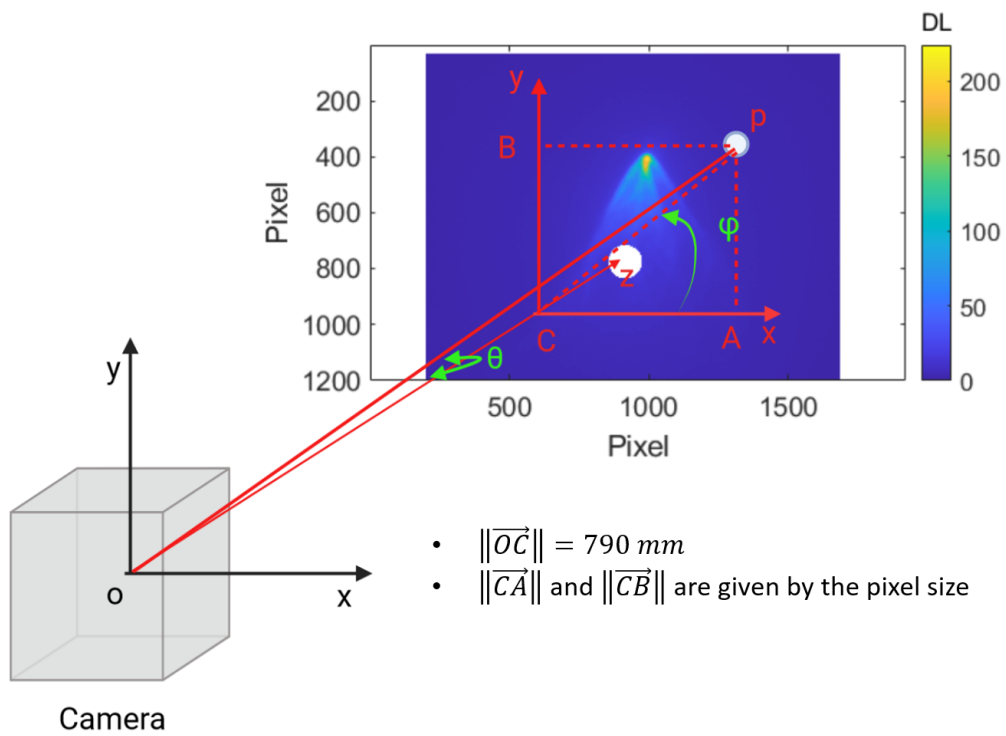


Figure 6.12: Considered geometry for identifying the pixel location and the corresponding to the solid angle

obtained with Gaussian illumination.

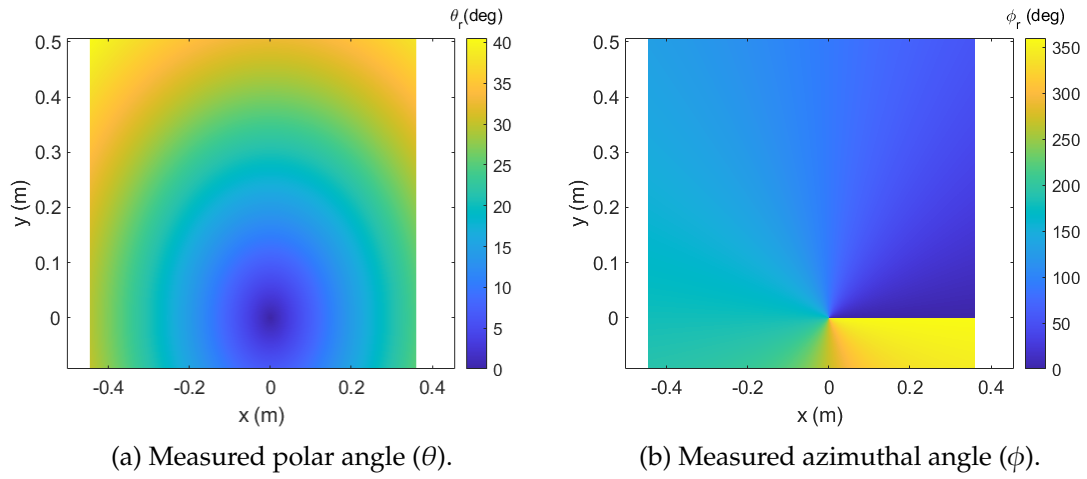


Figure 6.13: Illustration of measured polar coordinates.

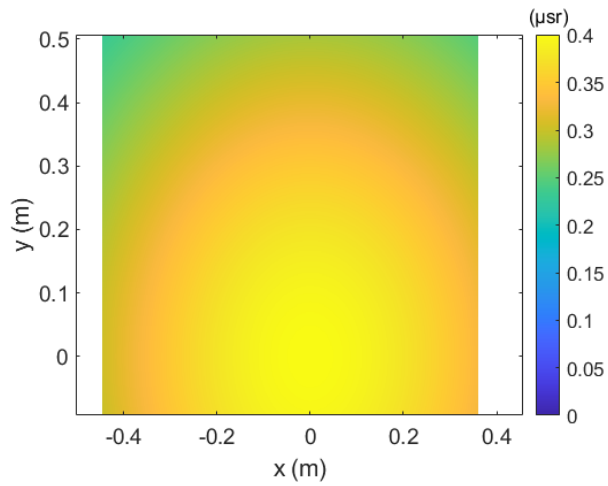


Figure 6.14: Measured solid angle cartography.

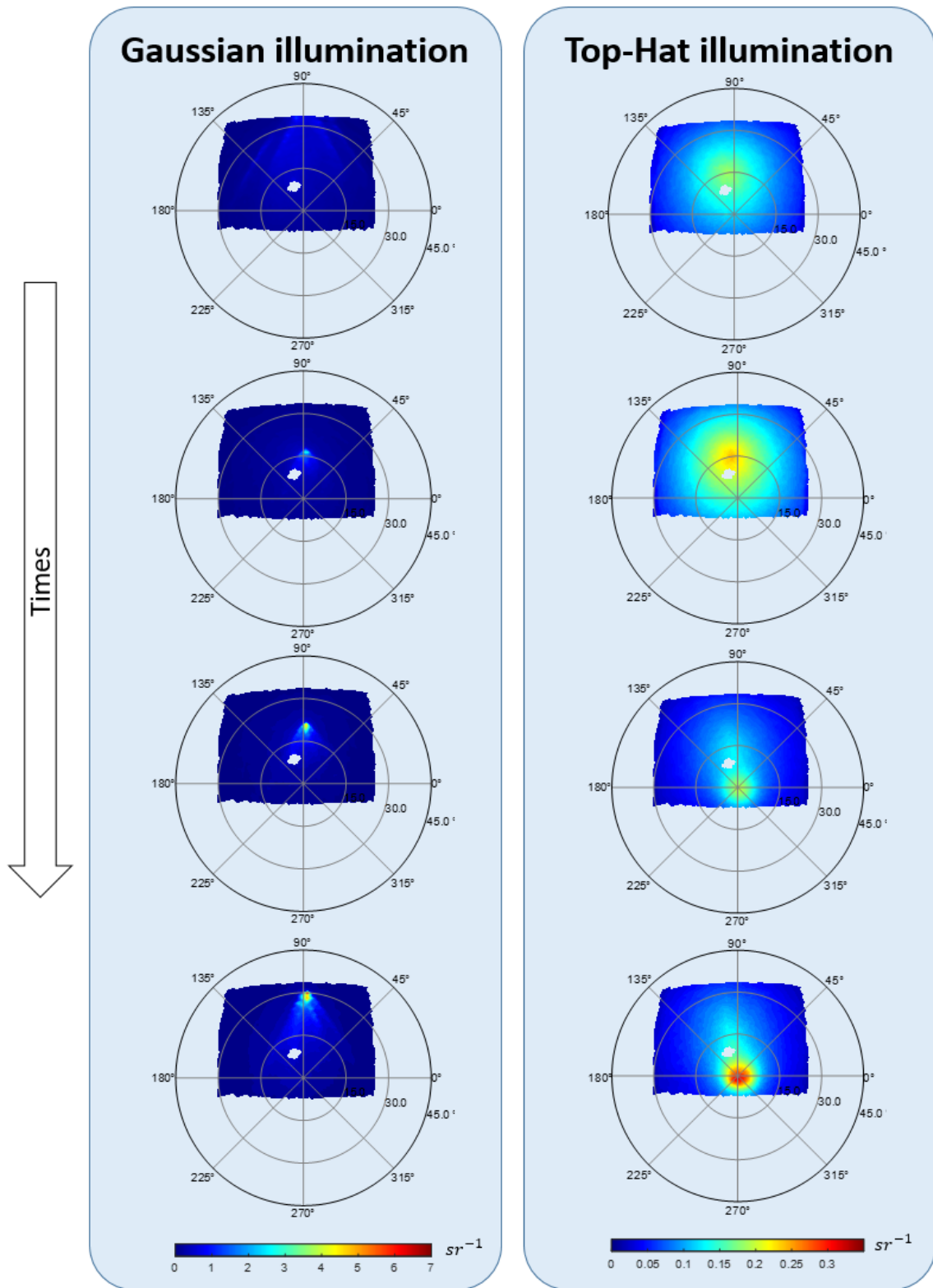


Figure 6.15: Measured BRDFs with top hat illumination (time step  $t=1.8$ ,  $t=2$ ,  $t=5$  s) and Gaussian illumination (time step  $t=0.3$ ,  $t=0.7$ ,  $t=0.9$  and  $t=1.4$  s).

#### 6.3.7 Summary of dynamic BRDF measurement

In conclusion, the radiative balance characterisation between reflected and absorbed radiative LASER energy and the quantification of the reflected part are of the utmost importance.

In this study, a complete work bench is developed. This set-up is a work in progress and has many avenues for optimisation. First, all results depend on the shape of the screen's BRDF, which is considered Lambertian based on our results. Second, the complex set-up (number of instruments, spectral filters, synchronisation, etc. ), the amount of data generated by the trials (10 GB), and the number of steps needed to obtain the final results make measurements quite difficult. Above all, the luminous flux delivered by the laser requires special attention to avoid saturating the various instruments.

Despite these difficulties, the methods developed in this study allow quantitative measurement of dynamic image-based BRDF under HEL illumination. This set-up has shown good results and highlights BRDF differences for different illumination shapes (top hat/Gaussian). The HEL-matter interaction's BRDF is of the utmost importance for defence applications to estimate eye safety.

## 6.4 Application of ATR for dynamic cases

### 6.4.1 Introduction

In this section, ATR is used to determine a material's absolute temperature during its interaction with an HEL without knowing the material's surface emissivity. The method presented in Chapter 4 is applied under extreme conditions, and the front face of the sample changes phase from solid to liquid as the surface is melted by the laser.

The robustness of the method is proven for two cases. First, the method is evaluated under extreme conditions involving the sample's phase change, and second, the sample has a particularly low emissivity to complicate the studied case.

### 6.4.2 Experimental set-up and sample description

As a reminder, the complete set-up used to measure the normal radiative intensity leaving a sample is described in Figure 6.16. The experimental bench is composed of a multi-spectral black body source (1, CN-MT, Prisma Instrument) whose temperature range extends from 20 °C to 400 °C. In this study, the temperature set point is 400 °C. A chopper (2) is used to modulate the intensity of the beam in lock-in mode. Typically, the frequency modulation ( $f_{BB}$ ) is set to 60 Hz, whereas the camera frequency acquisition ( $f_{acq}$ ) is set to double this value. A pair of parabolic mirrors (3 and 4) is used as an optical doublet to image a plane of the black body cavity onto the sample plane. The black body cavity is imaged on the sample's imaging plane with a magnification of 2. The first parabolic mirror (3) is a 15° gold-coated OAPM with a focal length of 645,92 mm, whereas mirror (4) is a 15° OAPM with a focal length of 542,92 mm and a silver coating. The IR camera (5, model A6753sc SLS) is synchronised with the optical chopper:  $f_{acq} = 2 f_{BB}$ . It has a SLS sensor (7,5  $\mu\text{m}$  – 11  $\mu\text{m}$ ) with a pixel area of 640  $\times$  512 equipped with a 50 mm focal lens. The beam splitter (6) (50% transmissivity, 50% reflectivity) is used both to normally illuminate the sample and to record the normal radiative intensity leaving the sample with the IR camera. A motorised rail (8) allows linear motion of the reference mirror (9) and the sample (10). Both are mounted with particular attention to coplanar alignment normal to the camera and beam axis.

## 6.4. APPLICATION OF ATR FOR DYNAMIC CASES

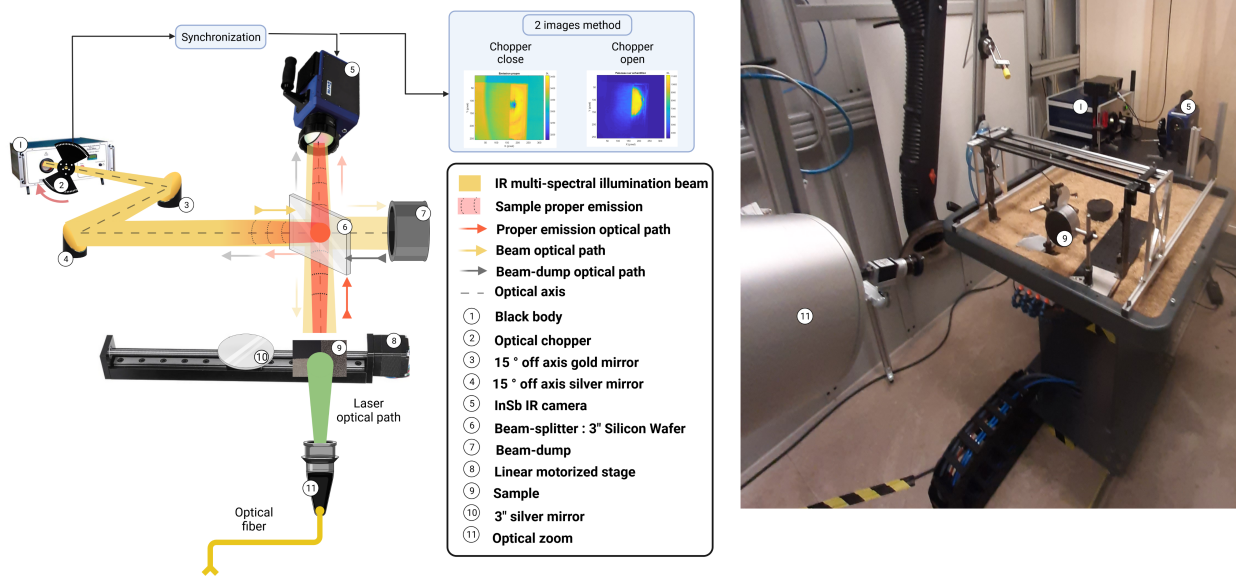


Figure 6.16: Schematic representation of the experimental set-up.

The studied material is an aluminium cylinder with a diameter of 10 cm and a thickness of 5 cm. The front face is painted black to absorb the laser. The rear face is hand polished to observe specular reflections. The surface roughness is measured with an optical profilometer, and the mean measured  $S_a$  is approximately  $0.98 \mu\text{m}$ . After the polishing process, half of the rear face of the sample is painted black.

Figure 6.17 shows surface topography measurements on the sample from the profilometer. Figure 6.18.a shows the rear face of the sample after polishing and before the trial, Figure 6.18.b shows the rear face of the sample after the trial, Figure 6.18.c shows the front face before the trial, and Figure 6.18.d shows the same face after the trial.

## 6.4. APPLICATION OF ATR FOR DYNAMIC CASES

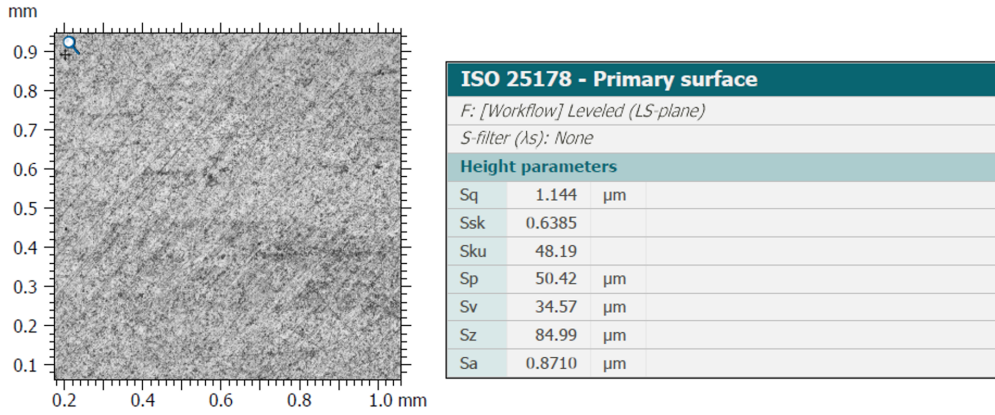


Figure 6.17: Surface roughness measurements.

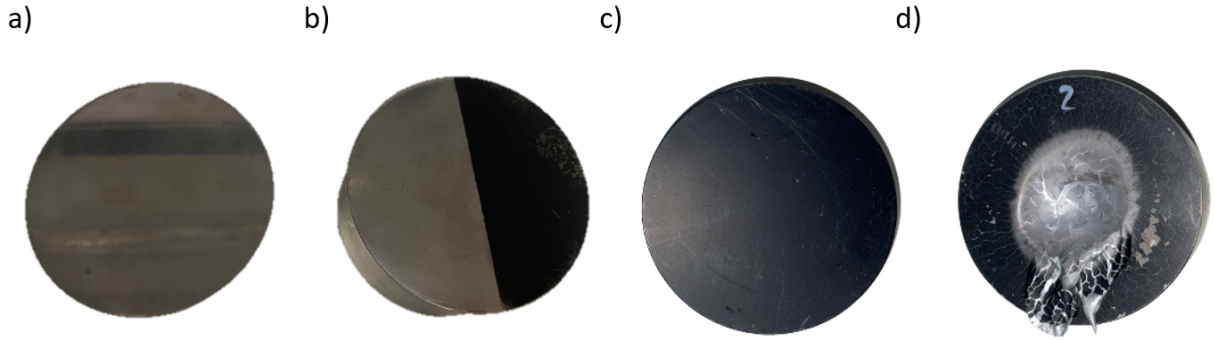


Figure 6.18: Sample presentation: (a) rear face after polishing and before the trial, (b) rear face after the trial, (c) front face before the trial and (d) front face after the trial.

### 6.4.3 Method reminders

Considering a transparent atmosphere, an opaque surface, specular reflections and a normal angle of view, the input radiation of any thermal camera ( $\dot{q}^l$ ) can be described as in Eq. 6.4. The integral represents the angular and spectral integrals of the camera sensor and objective. The first term describes the emission part of the signal, and the second term represents the reflected part of the signal.

$$\dot{q}^l(T(\vec{x}), \perp) = \int_{\Delta\Omega^\perp} d\vec{\omega}_r \int_{\lambda_1}^{\lambda_2} \left( [1 - \rho_F^\perp(T(\vec{x}), \lambda)] I_b(T(\vec{x}), \lambda) + \rho_F^\perp(T(\vec{x}), \lambda) I_{scn}^\perp \right) d\lambda \quad (6.4)$$

where  $T(\vec{x})$  is the temperature (K) at point  $\vec{x}$ ,  $\Omega$  is the solid angle (sr),  $\rho_F^\perp$  is the Fresnel bidirectional reflection normal to the sample (-),  $I_b$  represents Planck's law ( $W \cdot m^{-3} \cdot sr^{-1}$ ),  $I_{scn}^\perp$  represents the nearby



## 6.4. APPLICATION OF ATR FOR DYNAMIC CASES

---

surrounding sources to the normal of the sample ( $W \cdot m^{-3} \cdot sr^{-1}$ ) and  $\lambda$  is the wavelength (m).

The goal of the ATR method is to identify  $T(\vec{x})$  from the radiometric model of Eq. 6.4. To achieve this goal, the proposed method includes 6 steps:

1. Determine a black body calibration method to link  $\int \int I_b(T(\vec{x}), \perp, \lambda) d\lambda d\vec{\omega}_r$  to  $T(\vec{x})$ ,
2. acquire a raw image of the sample:  $\dot{q}_{s,1}(T(\vec{x}), \perp)$ ,
3. estimate the scene's reflection on the sample:  $\int \int \tau_{bs} I_{scn} d\lambda d\vec{\omega}_r$ ,
4. estimate the sample's normal-normal reflectivity:  $\rho_{Fs}^\perp$ ,
5. compute the sample's transmitted black body emittance:  $\dot{q}_s^b$ , and
6. infer the sample's true temperature from its emissivity and black body calibration.

For the **first step**, the reader can refer to the work of Burggraaf et al. [86]. The **second step** is the acquisition of  $\dot{q}_l$  from the raw image produced by the IR camera. In the **third step**, the radiative contribution ( $I_{scn}$ ) of reflections from the surroundings is estimated. Since the sample is assumed to be specular, we introduce  $\dot{q}_{m,1}$ , which corresponds to the pixel-based camera response when the chopper is in the closed position (Figure 6.16) when imaging the reference mirror. Here, we take advantage of the high reflectivity of the mirror ( $\rho_{F,m}^\perp \approx 1$ ); thus, the thermal part is neglected. As  $I_{scn}$  is considered constant, this operation is performed only at the beginning of the experiment. For  $\dot{q}_{m,1}$ , the reference mirror has to be placed in the exact same position and orientation as the sample. For the **fourth step**, we introduce  $\dot{q}_{m,2}$ ,  $\dot{q}_{s,1}$  and  $\dot{q}_{s,2}$ , which correspond to the pixel-based camera response during the open (2) or closed (1) chopper positions when imaging the reference mirror (s) or the sample (m). The ratio between these two parameters is used to evaluate the specular normal-normal reflectivity of the sample ( $\rho_{Fs}^\perp$ ) as described in Eq. 6.5. This ratio corresponds to the averaged sample reflectivity weighted by the radiative intensity of the black body source and is denoted by  $\tilde{\rho}_{Fs}^\perp$ .

$$\frac{\dot{q}_{s,2} - \dot{q}_{s,1}}{\dot{q}_{m,2} - \dot{q}_{m,1}} = \frac{\int_{\lambda_1}^{\lambda_2} \tau_{bs} \rho_{Fs}^\perp(T(\vec{x}), \lambda) I_{BB} d\lambda}{\int_{\lambda_1}^{\lambda_2} \tau_{bs} I_{BB} d\lambda} = \tilde{\rho}_{Fs}^\perp(T(\vec{x})) \quad (6.5)$$

To achieve the **fifth step**, the radiometric equation (Eq. 4.23) needs to be solved. As a result, the black body radiative intensity of the sample is obtained (see Eq. 6.6).

$$\dot{q}_s^b = \frac{\dot{q}_{s,1}(T(\vec{x}), \perp) - \tilde{\rho}_{F,s}^\perp(T(\vec{x}))\dot{q}_{m,1}}{1 - \tilde{\rho}_{F,s}^\perp(T(\vec{x}))} \quad (6.6)$$

The **last step** makes use of the first and fifth steps to obtain the absolute temperature.

*Remark:* The measurement of  $\dot{q}_{m,1}$  and  $\dot{q}_{m,2}$  is performed only once, as the surrounding contribution and the illumination beam are considered constant. The measurement of  $\dot{q}_{s,1}$  and  $\dot{q}_{s,2}$  as the temperature is increased to 400 °C and the frequency of the chopper and the camera lead to a succession of quasistatic cases.

#### 6.4.4 Application of the ATR method during 4 kW continuous laser–material interaction

Choosing the camera IT is a key step of the experiment. In fact, the camera’s dynamic range is coded with 14 bits, so it has a maximum DL of 16,000. Nevertheless, the camera sensor is not reliable below 2,000 DL or above 12,000; therefore, it is mandatory to work between those limits. In addition to the high-temperature shift (and therefore the DL) of the sample as it is heated by the laser, we must also take into account the reflected beam intensity. Thus, with regard to the calibration curves presented in Figure 6.19, the IT selected for this trial campaign is 0.03 ms.

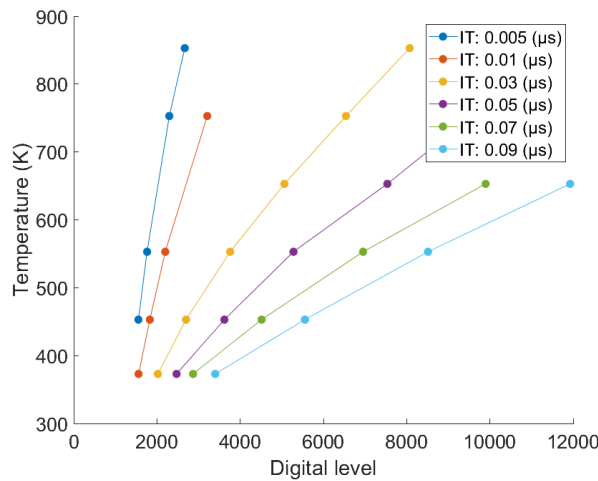


Figure 6.19: Camera calibration curves for multiple ITs.

The calibration is performed at the beginning of the experiment. At the chosen IT, the camera response is not sensitive to the ambient temperature, and a specific calibration [16] procedure is

#### 6.4. APPLICATION OF ATR FOR DYNAMIC CASES

---

performed for  $\dot{q}_{m,1}$ . As the DL is assumed to be a linear function for each IT, multiple acquisitions at over many ITs are obtained to determine the linear dependency with great sensitivity. This linear assumption is then fitted to project those measurements to lower ITs used for sample measurements. A fit is performed considering each pixel for different IT values (e.g., 0.1, 0.15, 0.2 and 0.2501 ms). The obtained images with the open chopper ( $\dot{q}_{m,1}$ ), closed chopper ( $\dot{q}_{m,2}$ ), and the difference ( $\dot{q}_{m,2} - \dot{q}_{m,1}$ ) are given in Figure 6.20.a, 6.20.b, and 6.20.c, respectively.

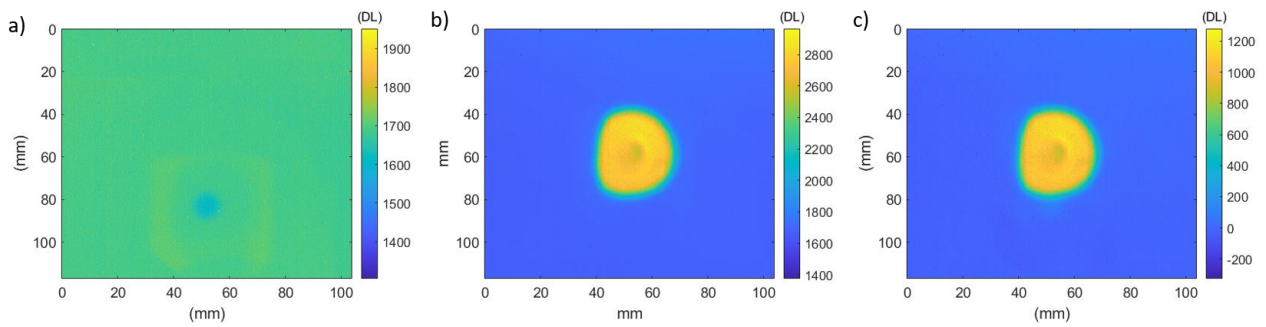


Figure 6.20: Calibration for (a)  $\dot{q}_{s,1}$ , (b)  $\dot{q}_{s,2}$  and (c)  $\dot{q}_{s,2} - \dot{q}_{s,1}$ .

Table 6.1 shows the image correction process at different time steps. The reflectivity on the polished part is approximately 0.93 (-), whereas the reflectivity of the black painted section is approximately null. The correction is performed on a disk with a radius of 2 cm. As shown in the last row of Figure 6.1, the ATR method corrects the gap between the polished and painted sections of the cylinder. This appears to be a more realistic case for measuring the temperature.

## 6.4. APPLICATION OF ATR FOR DYNAMIC CASES

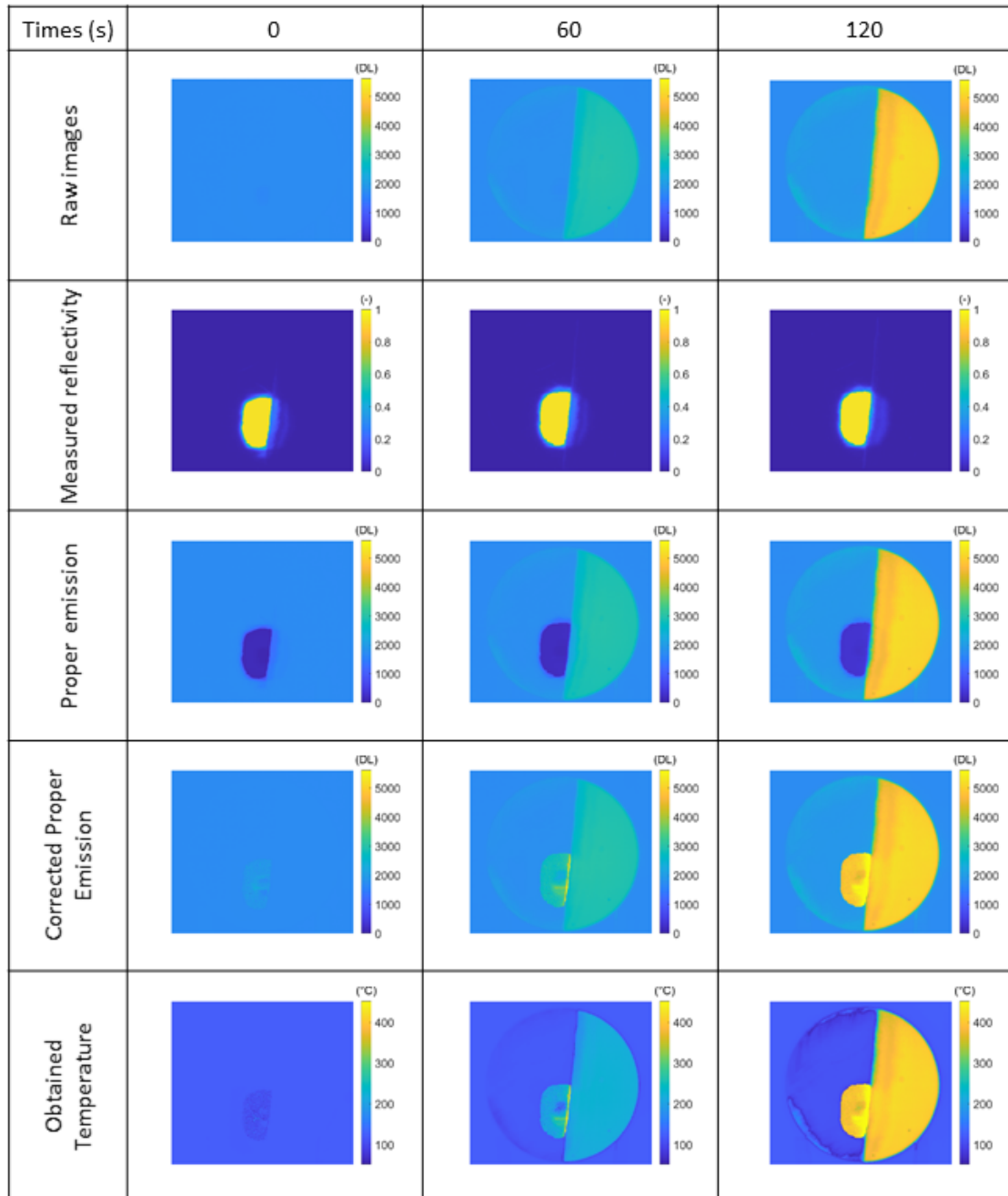


Table 6.1: Steps of the ATR method for multiple experimental times.

Figure 6.21.a shows the measured reflectivity field at the end of the experiment and highlights the 4 pixels from which the temporal plots in Figure 6.21.b are drawn. Two pixels are extracted from the polished part ( $X_1$  and  $X_2$ ), one pixel is extracted from the painted part where the correction is

## 6.4. APPLICATION OF ATR FOR DYNAMIC CASES

performed ( $X_3$ ), and the last pixel is extracted from the painted part where the correction cannot be done ( $X_4$ ). Figure 6.21.b shows the reflectivity temporal measurements for each point. There is no variation for points  $X_1$ ,  $X_2$  and  $X_4$ . Nevertheless, the reflectivity for point  $X_3$  increases in the last thirteen seconds of the experiment.

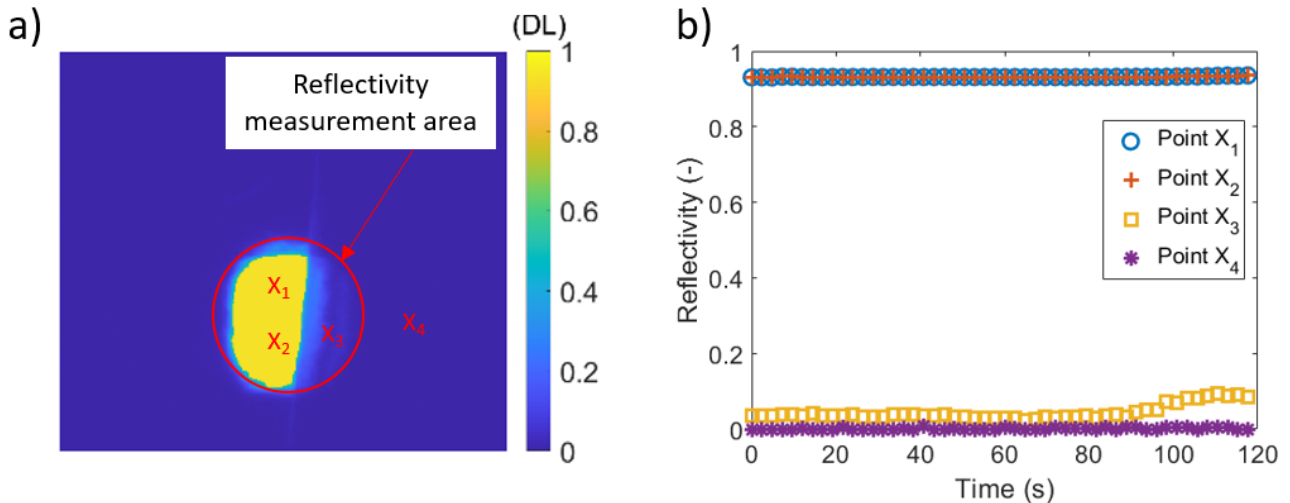


Figure 6.21: Measured reflectivity: (a) reflectivity field measured at the beginning, (b) temporal plot of reflectivity for different pixels.

Figure 6.22.a and 6.22.b and Figure 6.22.c and 6.22.d show the temporal and spatial variations in the measured raw DL and the corrected DL, respectively. As shown in Figure 6.22.a, point  $X_3$  is mismatched with point  $X_4$  at the end of the curves. The hump at point  $X_3$  can be explained by thermal expansion of the sample. Therefore, the pixel does not appear to represent the same physical position on the sample during the experiments. Moreover, as the paint is not perfectly homogeneous (Figures 6.18 and 6.22), the reflectivity can vary. This could also explain the hump on the reflectivity curves (Figure 6.21). Moreover, the measured DLs on  $X_1$  and  $X_2$  appear low in comparison to those of  $X_3$  and  $X_4$  before the correction. After the ATR method is applied (Figure 6.22.b), all points of the surface follow the same increase in DL. The variation in each curve is attributed to noise. Figure 6.22.c and 6.22.d represent the raw and the corrected DL fields at the end of the laser illumination, respectively. The vertical lines on the painted part in Figure 6.22.c are again attributed to uneven paint coatings. In Figure 6.22.d, the gap between the painted and polished parts is filled after the ATR method is applied.

Finally, using the calibration curves presented in Figure 6.19 and the corrected proper emission

## 6.4. APPLICATION OF ATR FOR DYNAMIC CASES

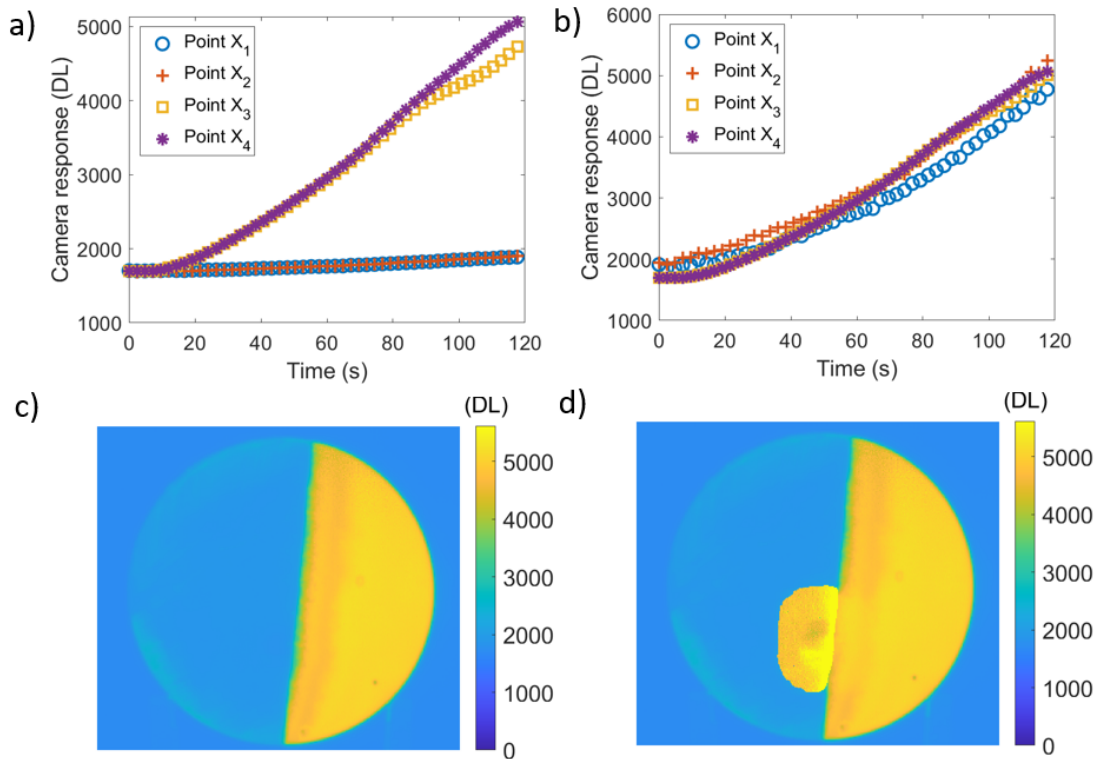


Figure 6.22: DL correction: (a) temporal plot of the raw DL, (b) temporal plot of the corrected DL, (c) last image of the raw DL, (d) last image of the corrected DL.

field presented in Figure 6.22, the absolute temperature field can be obtained. Figure 6.23 shows the temporal plot of temperature measurements before (Figure 6.23.a) and after (Figure 6.23.b) correction. As observed in Figure 6.22.a, the DLs of the first two points do not exceed 2200, as they are near the lower limits of the calibration, and the measured temperatures at this point do not change in Figure 6.23. Nevertheless, one can observe a temperature increase greater than 400 °C at the pixels pertaining to the painted surface. This phenomenon includes completely incorrect temperature fields. On the other hand, using the corrected DL (Figure 6.22.b), the obtained temperature after applying the correction is coherent. Figure 6.23.c and 6.23.d show the measured temperature field without and with the emissivity corrections, respectively. As can be observed in Figure 6.23.d, the obtained temperature for the polished part is nearly the same as for the painted part.

By taking point X<sub>4</sub> as a reference, the error from the utilisation of the ATR method can be obtained (Figure 6.24). In doing so, one can consider that all points have the same temperature during the experiment.

## 6.4. APPLICATION OF ATR FOR DYNAMIC CASES

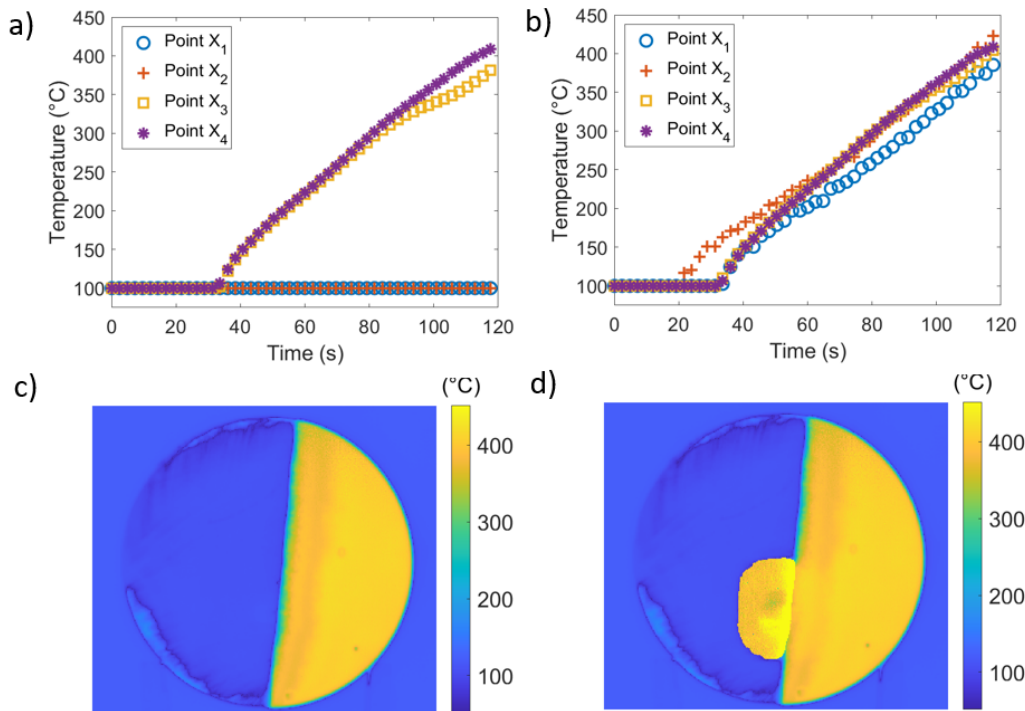


Figure 6.23: DL correction: (a) temporal plot of apparent temperature, (b) temporal plot of corrected temperature, (c) last image of the apparent temperature, (d) last image of the corrected temperature.

Figure 6.24.a shows that points  $X_1$  and  $X_2$  are superimposed. The error before the temperature increase is low because of the radiative equilibrium between emissivity and reflections presented in Section 4.7.3. Then, once the contribution from emissions exceeds that of the reflections, the error increases.

Figure 6.24.b shows the DL error with the application of the ATR method. Here, points  $X_1$  and  $X_2$  do not overlap as they do without the correction applied. Point  $X_1$  has a higher mean error than Point  $X_2$ . Through comparison of Figures 6.22 and 6.23, and considering that point  $X_1$  is closer to the heat source than other points, the point may not undergo the exact same temporal variations that the other points do. The hump at point  $X_3$  then decreases from 10 to 3%.

Figure 6.24.c shows the error in the temperature without corrections. Figure 6.24.d shows the temperature error after corrections are applied. The error for point  $X_1$  displays a positive peak at the beginning of the experiment. Point  $X_2$  is slightly underestimated during the experiment and has a maximum error of 8%. The maximum error of point  $X_3$  goes from 4% before correction to 2% after correction, which is under the calibration error. This quantity must be compared to the calibration

## 6.4. APPLICATION OF ATR FOR DYNAMIC CASES

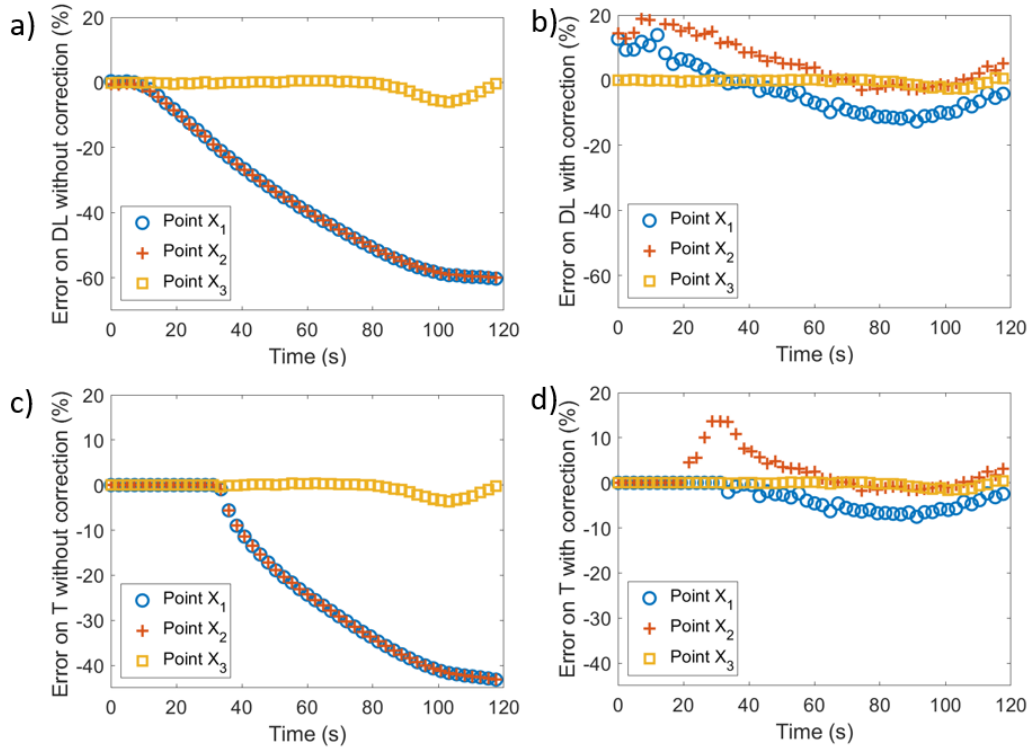


Figure 6.24: Error obtain through the application of ATR method: (a) DL error without correction, (b) DL error with correction, (c) temperature error without correction, (d) temperature error with correction.

precision, which is estimated to be  $\pm 2.5\%$ .

### 6.4.5 Summary of ATR temperature measurement during HEL illumination

The ATR method is tested to measure the absolute temperature under extreme conditions. The measured spatial emissivity displays heterogeneity, as it varies from 0.05 to 0.95 - almost the entire range of variation for the emissivity. Measuring the temperature under these conditions is extremely complicated. The two major difficulties in this case are as follows:

- The extreme thermal conditions involve a change from ambient temperature to  $400\text{ }^{\circ}\text{C}$  on the rear surface of the sample and a much larger range on the front face, which is not analysed. The thermal expansion of the material tends to disrupt the optical alignment necessary for the method.
- The high reflectivity of the sample means that 95% of the signal must be subtracted to remove



#### 6.4. APPLICATION OF ATR FOR DYNAMIC CASES

---

reflections. Then, to correct the emissivity, the remaining signal is divided by the emissivity, which corresponds here to a 20-fold change in the measured signal. It is important to highlight that an error of 1% for the reflectivity is negligible during the reflection subtraction (30 DL from 1500 DL in this case). However, an error of 1% is much more sensitive to division when changing the multiplier from 20 to 25.

Despite the experimental difficulties, the obtained temperature fields are relevant, and the ATR method shows good results for this case. Finally, despite the high temperature measured during the experiment, consideration of the reflections is essential to obtain the absolute temperature for this studied case.

## 6.5 Heat flux measurement during HEL material interaction

In this section, the heat flux absorbed by the sample is determined through quantitative thermal imaging. This is one major interest for MBDA and the motivation behind this thesis. Accurately identifying the flux absorbed by the sample during the laser–matter interaction is challenging. Our attempt to quantify the heat flux utilises the inverse method described in Chapter 5.5 and is used in an extremely complex case.

One of the issues during heat flux measurement is measurement precision. The precision falls drastically while working on high-power sources. The power meter (Gentec (Pronto-10K)) used to monitor the output of the laser beam has a  $\pm 5\%$  uncertainty. The power meter’s measured values are used as a point of comparison to the data presented later.

### 6.5.1 Reminders regarding the inverse method

As described previously (Chapter 5.5), the temperature field of any sample in thermal diffusion problems corresponds to the spatio-temporal convolution between the heat flux ( $\dot{q}(x, y, z = 0, t)$ ) and the impulse response of the system ( $\mathcal{H}(x, y, z = Lz, t)$ ), as presented in Eq. 6.7. To match the experimental set-up, the excitation is on the front face ( $\dot{q}(x, y, z = 0, t)$ ), and measurements are performed on the back face ( $\mathcal{H}(x, y, z = Lz, t)$ ). Thus, Eq. 5.48 can be written as follows. 6.7.

$$T(x, y, z = lz, t) = \dot{q}(x, y, z = 0, t) \underset{s,t}{\circledast} \mathcal{H}(x, y, z = Lz, t) \quad (6.7)$$

where  $\underset{s,t}{\circledast}$  represents the spatio-temporal convolution (s,t).

In this equation, one seeks to identify  $\dot{q}(x, y, z, t)$  based on temperature measurements ( $T(x, y, z = lz, t)$ ). To change the spatio-temporal convolution, two spatial Fourier transforms are performed along the x- and y-axes (by applying the integral transform method [133, 126]), and the impulse response is replaced by a Toeplitz matrix, as presented in the following equation.

$$\{T(\alpha_n, \beta_m, z = Lz)\} = [\tilde{\mathcal{H}}(\alpha_n, \beta_m, Lz)]\{\dot{q}(\alpha_n, \beta_m, z = 0)\} \quad (6.8)$$

where  $\alpha_n = \frac{n\pi}{Lx}$ ,  $n \in \mathbb{N}$ ,  $\beta_m = \frac{M\pi}{Ly}$ ,  $M \in \mathbb{N}$  represents the spatial Fourier modes and  $[\tilde{\mathcal{H}}(\alpha_n, \beta_m, Lz)]$  is the Toeplitz matrix of the impulse response.

Finally, the temporal variation in the heat flux can be estimated in the Fourier space by the following equation:

$$\{\dot{q}(\alpha_n, \beta_m, z = 0)\} = [\tilde{\mathcal{H}}^t \tilde{\mathcal{H}} - \nu \Gamma]^{-1} [\tilde{\mathcal{H}}]^t \{T(\alpha_n, \beta_m, z = Lz)\} \quad (6.9)$$

where  $\Gamma$  is a temporal derivation matrix,  $\nu$  is the regularisation coefficient [142, 143] and the exponent  $\underline{t}$  represents the transpose matrix.

Finally, once the spatio-temporal heat flux is completely identified in the Fourier space, two inverse transforms are performed to express it in the real space. Specific attention must be paid at this step. The impulse response  $[\tilde{\mathcal{H}}]$  is obtained by applying Fourier's law of thermal diffusion to the system. To solve this equation, the integral transform method is used with respect to the boundary conditions of the sample. In this study, only the heat flux is considered, and it is assumed that all other faces of the sample are insulated. By doing so, the obtained solution includes only the real components remaining from the Fourier transform. Thus, only the real part of the inverse Fourier transform on  $\dot{q}(\alpha_n, \beta_m, z = 0)$  is kept.

### 6.5.2 Modelling the heat transfer

To use the method presented in Chapter 5.5, an impulse response of the system must be computed. This is the objective of this section. The HEL material interaction implies a large increase in temperature, which leads to the emergence of the liquid phase. Due to the thermal gradient inside of the melted part, some convection and the Marangoni effect [152, 153] are expected to appear. At this stage, the surface tension holds the melted area in place, and the gravity force causes a droplet to form and fall off the sample. This entire phenomenon occurs simultaneously with oxidation and corrosion due to the high temperature of the material. The more complex the model becomes, the more parameters and associated assumptions are incorporated, thereby increasing the computation time as well. All these phenomena that consume energy are negligible in comparison to the major unknown parameter in this study: the absorption of the material. For those reasons, the experimental and numerical cases do not incorporate fusion, as illustrated in Figure 6.25.

Based on this assumption, the thermal model can be written as follows:

## 6.5. HEAT FLUX MEASUREMENT DURING HEL MATERIAL INTERACTION

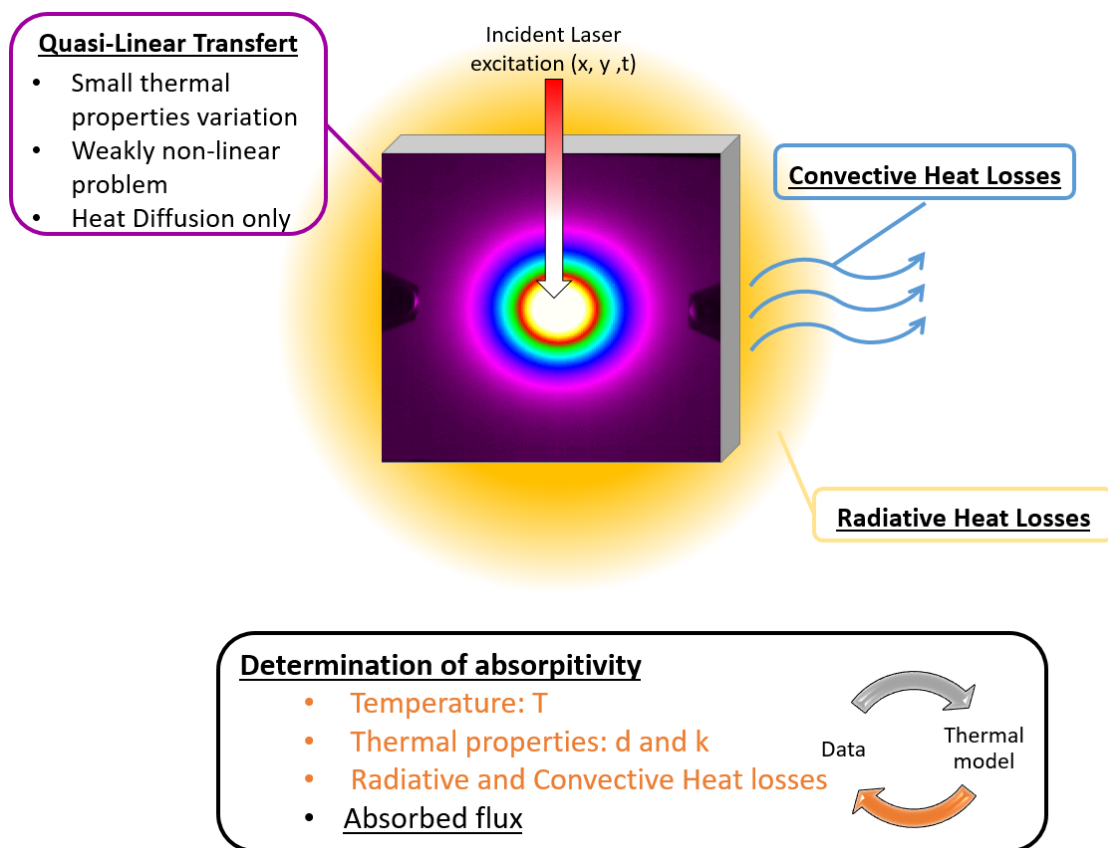


Figure 6.25: Thermal problem positioning.

$$\left\{ \begin{array}{l}
 \rho_v C_p \frac{\partial T(x, y, z, t)}{\partial t} = k \left[ \frac{\partial^2 T(x, y, z, t)}{\partial x^2} + \frac{\partial^2 T(x, y, z, t)}{\partial y^2} + \frac{\partial^2 T(x, y, z, t)}{\partial z^2} \right] \\
 -k \frac{\partial T(x, y, z, t)}{\partial x} \Big|_{x=0} = -h_c \left[ T(x=0, y, z, t) - T_{out} \right] - \varepsilon \sigma \left[ T(x=0, y, z, t)^4 - T_{out}^4 \right] \\
 -k \frac{\partial T(x, y, z, t)}{\partial x} \Big|_{x=L_x} = h_c \left[ T(x=L_x, y, z, t) - T_{out} \right] + \varepsilon \sigma \left[ T(x=L_x, y, z, t)^4 - T_{out}^4 \right] \\
 -k \frac{\partial T(x, y, z, t)}{\partial y} \Big|_{y=0} = -h_c \left[ T(x, y=0, z, t) - T_{out} \right] - \varepsilon \sigma \left[ T(x, y=0, z, t)^4 - T_{out}^4 \right] \\
 -k \frac{\partial T(x, y, z, t)}{\partial y} \Big|_{y=L_y} = h_c \left[ T(x, y=L_y, z, t) - T_{out} \right] + \varepsilon \sigma \left[ T(x, y=L_y, z, t)^4 - T_{out}^4 \right] \\
 -k \frac{\partial T(x, y, z, t)}{\partial z} \Big|_{z=0} = -h_c \left[ T(x, y, z=0, t) - T_{out} \right] - \varepsilon \sigma \left[ T(x, y, z=0, t)^4 - T_{out}^4 \right] + \dot{q}(x, y, t) \\
 -k \frac{\partial T(x, y, z, t)}{\partial z} \Big|_{z=L_z} = h_c \left[ T(x, y, z=L_z, t) - T_{out} \right] + \varepsilon \sigma \left[ T(x, y, z=L_z, t)^4 - T_{out}^4 \right] \\
 T(x, y, z, t=0) = 0
 \end{array} \right. \quad (6.10)$$

where:

- $\rho_v$  is the density ( $kg \cdot m^{-3}$ ),
- $C_p$  is the thermal capacity ( $J \cdot kg^{-1} \cdot K^{-1}$ ),
- $k$  is the thermal conductivity ( $W \cdot m^{-1} \cdot K^{-1}$ ),
- $T$  the temperature ( $k$ )
- $h_c$  is the heat transfer coefficient ( $W \cdot m^{-2} \cdot K^{-1}$ ),
- $\varepsilon$  is the total emissivity (-),
- $\sigma \approx 5.670 \times 10^{-8} W \cdot m^{-2} \cdot K^{-4}$  is the Stefan–Boltzmann constant (see Section 2.7),
- $\dot{q}$  is the heat flux ( $W \cdot m^{-2}$ ),
- $l_x = 0.1$  is the sample length ( $m$ ),
- $l_y = 0.1$  is the sample width ( $m$ ),
- $l_z = 0.025$  is the sample thickness ( $m$ ), and
- $T_{out} \approx 293$  is the ambient temperature ( $K$ ).

## 6.5. HEAT FLUX MEASUREMENT DURING HEL MATERIAL INTERACTION

To simplify the model, one can take a closer look at heat losses. To approximate heat losses due to thermal radiation and convective effects, the mean temperature (denoted by  $\langle T \rangle$ ) of the sample is computed.

Based on  $\langle T \rangle$ , the heat losses ( $Q_{out}$ ) can be expressed as follows:

$$\begin{aligned} Q_{out} &= \iint_{\partial D} \left( h_c [\langle T \rangle - T_{out}] + \varepsilon \sigma [\langle T \rangle^4 - T_{out}^4] \right) dS \\ &= \left[ 2L_x L_y + 2L_x L_z + 2L_z L_y \right] \left[ h_c [\langle T \rangle - T_{out}] + \varepsilon \sigma [\langle T \rangle^4 - T_{out}^4] \right] \end{aligned} \quad (6.11)$$

where  $\partial D$  represents the external surface of domain  $D$ .

By considering a black body ( $\varepsilon = 1$ ) and a large heat transfer coefficient (i.e.,  $h_c = 25$ ), heat losses of  $Q_{out} \approx 13$  W are calculated. This overestimation of heat losses represents less than 1 % of the incident laser beam of 1 kW. Thus, both convective and radiative heat losses can be neglected. Consequently, Eq. 6.10 can be written as follows:

$$\left\{ \begin{array}{l} \rho_v C_p \frac{\partial T(x, y, z, t)}{\partial t} = k \left[ \frac{\partial^2 T(x, y, z, t)}{\partial x^2} + \frac{\partial^2 T(x, y, z, t)}{\partial y^2} + \frac{\partial^2 T(x, y, z, t)}{\partial z^2} \right] \\ -k \frac{\partial T(x, y, z, t)}{\partial x} \Big|_{x=0} = 0 \\ -k \frac{\partial T(x, y, z, t)}{\partial x} \Big|_{x=L_x} = 0 \\ -k \frac{\partial T(x, y, z, t)}{\partial y} \Big|_{y=0} = 0 \\ -k \frac{\partial T(x, y, z, t)}{\partial y} \Big|_{y=L_y} = 0 \\ -k \frac{\partial T(x, y, z, t)}{\partial z} \Big|_{z=0} = \dot{q}(x, y, t) \\ -k \frac{\partial T(x, y, z, t)}{\partial z} \Big|_{z=L_z} = 0 \\ T(x, y, z, t = 0) = 0 \end{array} \right. \quad (6.12)$$

The impulse response to such 3D thermal diffusion problems presented in Chapter 5 can be written in the transformed Fourier Laplace space as follows:

$$\begin{cases} \tilde{\mathcal{H}}(\alpha_n, \beta_m, z, p) = Ae^{\sqrt{k}z} + Be^{-\sqrt{k}z} \\ A = \frac{e^{-2\sqrt{k}L_z}}{\sqrt{k}(e^{-2\sqrt{k}L_z} - 1)} \\ B = \frac{1}{\sqrt{k}(e^{-2\sqrt{k}L_z} - 1)} \end{cases} \quad (6.13)$$

where  $k = \frac{\nu}{\alpha} + \alpha_n^2 + \beta_m^2$  is the solution of the characteristic equation of Eq. 5.55.

### 6.5.3 Estimation of the absorbed heat flux under HEL illumination

In this section, two experiments are described. The first involves a calibration of the regularisation factor ( $\nu$ ). To ensure suitably high absorbance on the front face of the sample, this face is painted black. Consequently, the adapted regularisation factor can be identified. The second involves a sample without any particular surface treatment, and the sample's absorbance is thus estimated based on the estimated flux and the calibrated regularisation factor ( $\nu$ ).

#### 6.5.3.1 Experimental set-up

The experimental set-up is presented in Figure 6.26. The laser illuminates the sample on the front face, and an IR camera is positioned to image the rear face. Laser excitation of the material occurs at the front face of the sample, and the IR camera simultaneously measures the temperature field of the rear surface.

As the inverse method requires temperature measurements along the whole rear surface, the sample is clamped on the sides. Figure 6.27.a illustrates the clamping system on the front face, and Figure 6.27.b shows a raw image taken with the IR camera.

The laser head produces a 30 mm laser spot with a top hat profile. The laser profile is visualised with a visible camera and is illustrated in Figure 6.28. The spatial repartition of energy is nearly flat, with some random peaks and valleys. This is attributed to the fact that the laser is multimodal. The laser is used to illuminate the centre of the sample.

To simplify the temperature measurements, the rear face is painted with a highly emissive coating. The sample is prepared by MBDA as a square plate with the following dimensions: 100 mm × 100 mm and 2.5 mm thickness. The material used is aluminium 2024, for which the thermal properties are

6.5. HEAT FLUX MEASUREMENT DURING HEL MATERIAL INTERACTION

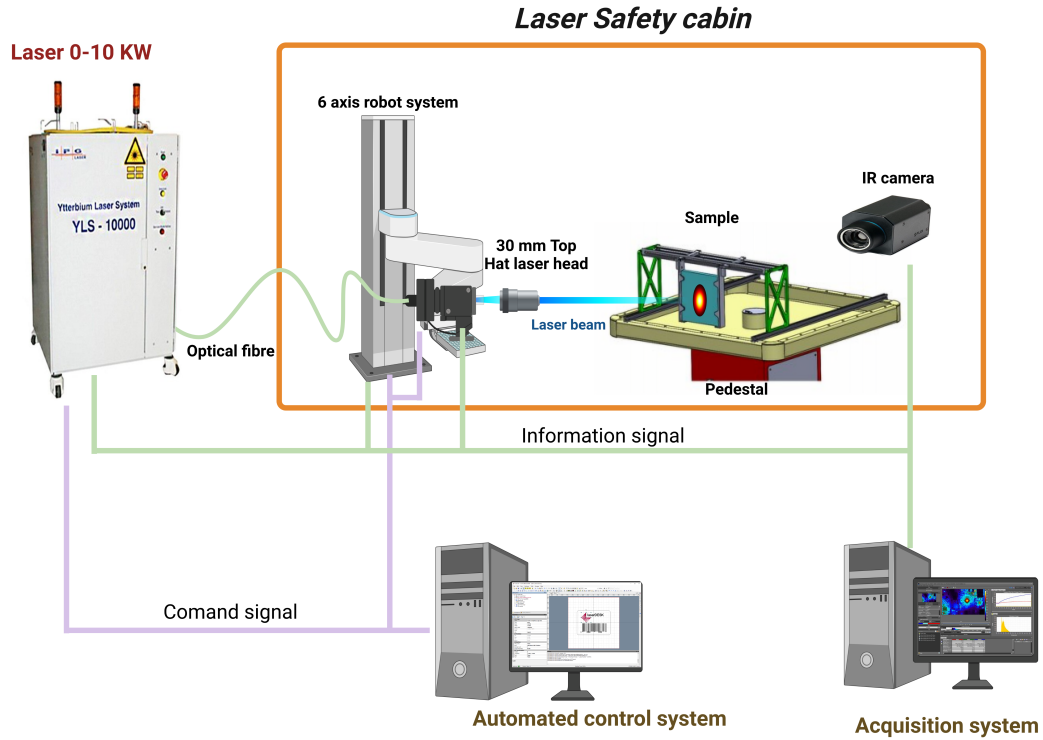


Figure 6.26: Thermal problem positioning.

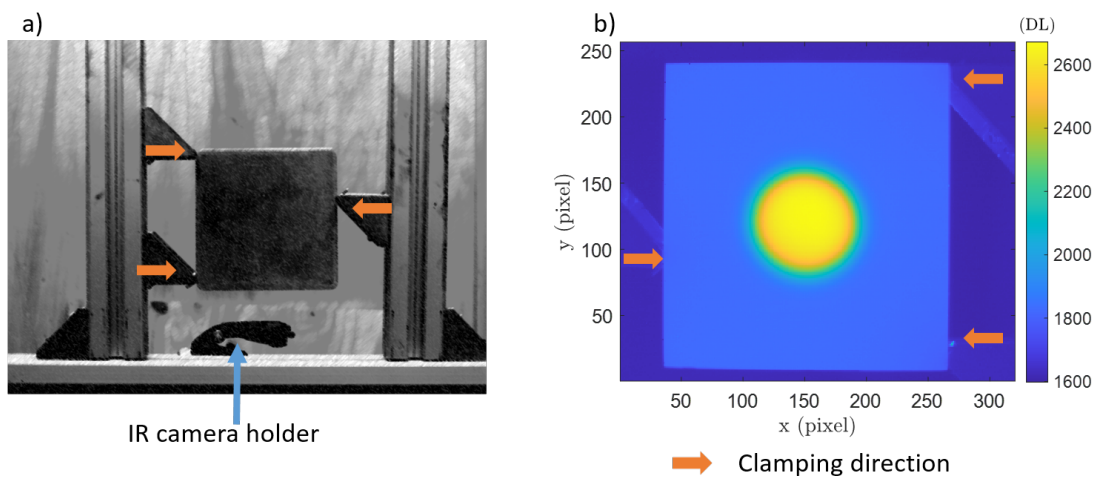


Figure 6.27: Illustration of the clamping system: (a) image in visible light (front face) and (b) raw image captured by the IR camera.



## 6.5. HEAT FLUX MEASUREMENT DURING HEL MATERIAL INTERACTION

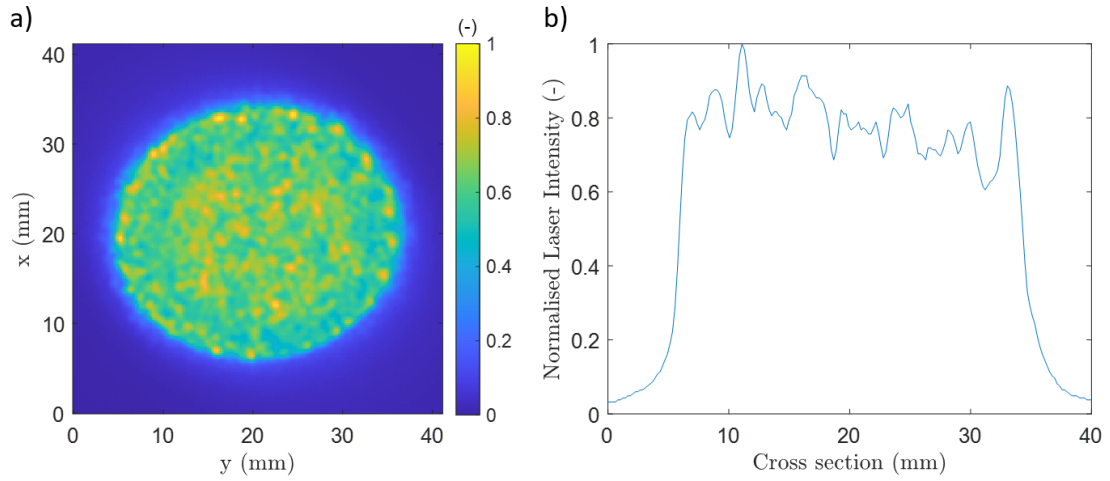


Figure 6.28: Measured laser beam spatial repartition of (a) the measured beam and (b) a profile of the cross section.

presented in Table 6.2 [154, 155, 156, 157, 158].

Density ( $\rho_v$ $kg \cdot m^{-3}$ )	Specific heat capacity ( $C_p$ $J \cdot kg^{-1} \cdot K^{-1}$ )	Thermal conductivity ( $k$ $W \cdot m^{-1} \cdot K^{-1}$ )	Thermal diffusivity ( $mm^2 \cdot s^{-1}$ )
2550	764	180	92.3

Table 6.2: Thermal properties of AL2024.

The camera used in this study is an SC7300L MCT (Flir) equipped with a 50 mm focal length objective. The camera frame rate is set to 150 Hz, the integration is 100  $\mu s$ , the pixel size is approximately  $435 \times 435 \mu m^2$ , and the spectral range of the camera is 7.7  $\mu m$  - 9.3  $\mu m$ .

### 6.5.3.2 Case of a front-painted aluminium plate

For this study, the front face of the sample is painted black to ensure good absorbance (RAL9005). The reflectance of the paint used in this study is measured under an integrating sphere in a commercial Fourier-transform infrared spectroscopy provided by [159] with a value of  $\mathcal{R}_p \approx 6\% \equiv \mathcal{A}_p \approx 94$  at the laser wavelength ( $\lambda = 1.074 \mu m$ ).

The temporal shape of the excitation is presented in Figure 6.29a. It is a single 1 s pulsed square signal with 1 kW power. The Figure 6.29b shows the maximum temperature increase measured on each pixel for the rear surface. A large thermal gradient is observed where the temperature of the

## 6.5. HEAT FLUX MEASUREMENT DURING HEL MATERIAL INTERACTION

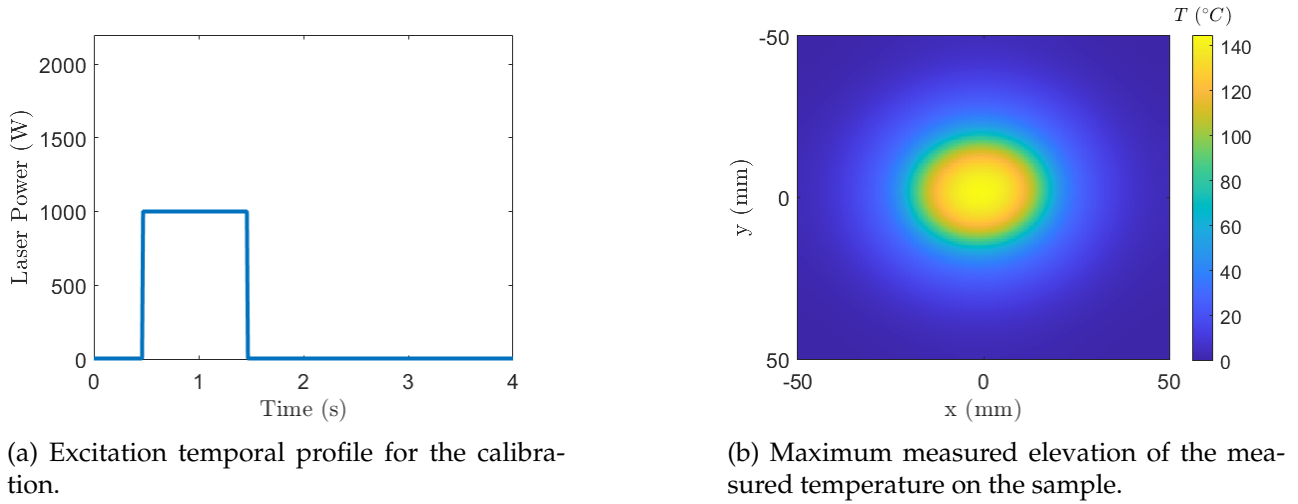


Figure 6.29: Laser temporal profile and the measured maximum temperature on each pixel.

pixels located at the centre of the sample exceeds  $140\text{ }^{\circ}\text{C}$ , whereas the edges of the sample exhibit nearly no shift in temperature.

Figure 6.30b shows the temperature evolution of the pixel at the centre of the laser spot. The temperature linearly increases during laser excitation, and after the laser is switched off, the heat diffuses through the material. Figure 6.30b shows the cross section of the temperature fields at different time intervals.

Based on those measurements, the inverse method previously presented and the pixel size, one can estimate the heat flux absorbed by the material. The material absorptivity is taken into account to make comparisons with the laser output power.

As a spatio-temporal estimation is targeted, the temporal aspect must be considered. To do so, the heat flux ( $\dot{q}_{est}(x, y, z = 0, t)$  W) is estimated, integrated over the entire image, multiplied by the pixel resolution ( $S_{pixel}$ ) and divided by the paint absorbance  $\mathcal{A}_p$  to determine the total estimated power  $Q_t$  as described in Eq. 6.14. The results are illustrated for multiple regularisation factors ( $\nu$ ) in Figure 6.31. The estimated  $Q_t$  is not relevant for regularisation factors ( $\nu$ ) below  $10^{-8}$ . With lower regularisation factors, the estimations approach the imposed power, down to  $\nu = 10^{-14}$ . For regularisation factors near the relative numerical accuracy of the computer ( $\nu = 10^{-16}$ ), the solution converges through coherent results but contains substantial noise. To conclude, the method shows relatively accurate estimations of the imposed power for  $10^{-8} \geq \nu \geq 10^{-14}$

## 6.5. HEAT FLUX MEASUREMENT DURING HEL MATERIAL INTERACTION

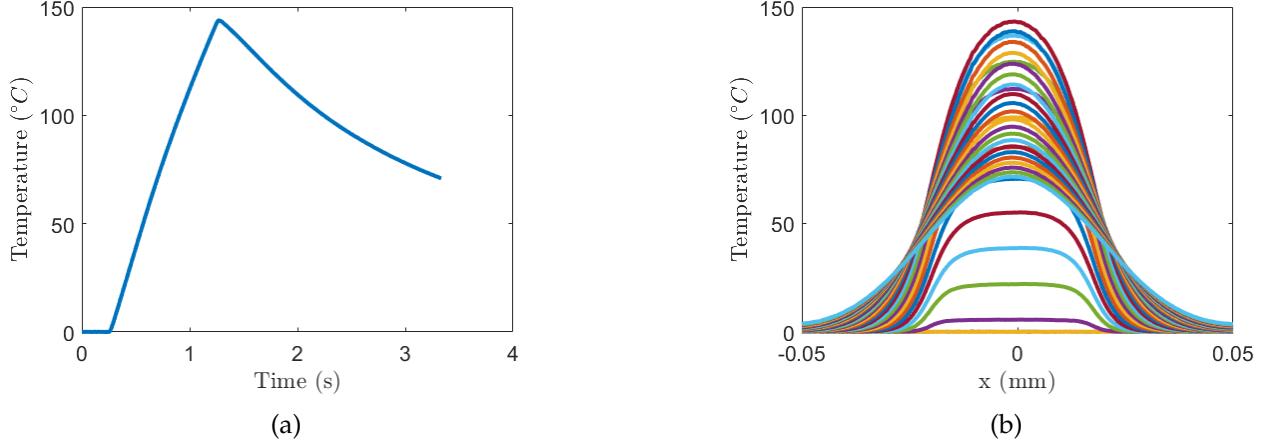


Figure 6.30: a) Temporal temperature profile for the central pixel and (b) cross section of temperature across the centre row of the sample.

$$Q(t) = \frac{S_{pixel}}{\mathcal{A}_p} \sum_x \sum_y \dot{q}_{est}(x, y, z = 0, t) \quad (6.14)$$

To study the spatial estimation, the heat flux ( $\dot{q}_{est}(x, y, z = 0, t)$  W) estimation is multiplied by the pixel resolution ( $S_{pixel}$ ) and divided by the paint absorbance  $\mathcal{A}_p$  to determine the estimated spatial power  $Q(x, y)$  as described in Eq. 6.15. The results are shown for  $t=1$  s and multiple regularisation factors in Figure 6.32. The estimated  $Q(x, y)$  is not relevant for regularisation factors ( $\nu$ ) below  $10^{-8}$  where no power is measured. For lower regularisation factors  $\nu$  ( $10^{-8} - 10^{-12}$ ), the estimation of the spatial distribution of power becomes sharper. Around  $10^{-14} \geq \nu$ , some random eigen-modes appear in the image. The mean value of those modes must be near 0 because they do not introduce much error to the temporal estimation of  $Q(t)$ .

$$Q(x, y, t) = \frac{S_{pixel}}{\mathcal{A}_p} \dot{q}_{est}(x, y, z = 0, t) \quad (6.15)$$

Based on Figure 6.32, the best regularisation factor for the spatial reconstruction is approximately  $10^{-6} \geq \nu \geq 10^{-12}$ . To better visualise the spatial reconstruction, Figure 6.33 shows a cross section of the reconstructed flux and a cross section of the laser beam weighted by the laser power for a pixel size of  $2.5 \cdot 10^{-4}$  (Figure 6.28). The solution matches the imposed profile for  $10^{-8} \geq \nu \geq 10^{-10}$ .

To conclude, considering both spatial and temporal aspects, the best regularisation factors identified are approximately  $10^{-8} \geq \nu \geq 10^{-12}$ . The method applied in this case nearly perfectly matches

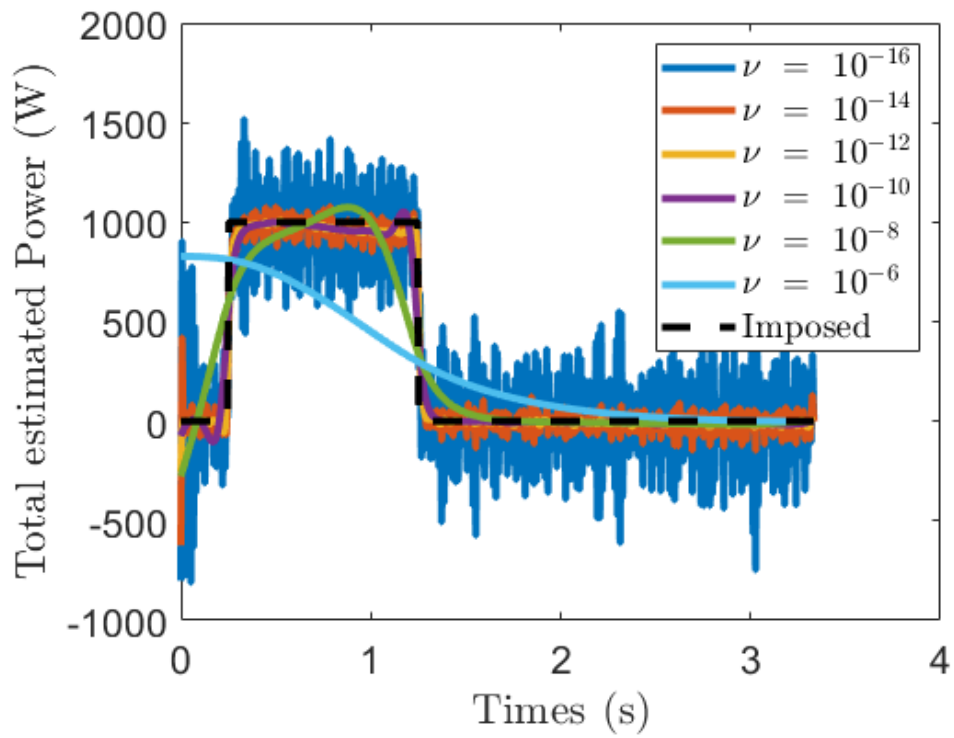


Figure 6.31: Estimated power ( $Q(t)$ ) as a function of time.

6.5. HEAT FLUX MEASUREMENT DURING HEL MATERIAL INTERACTION

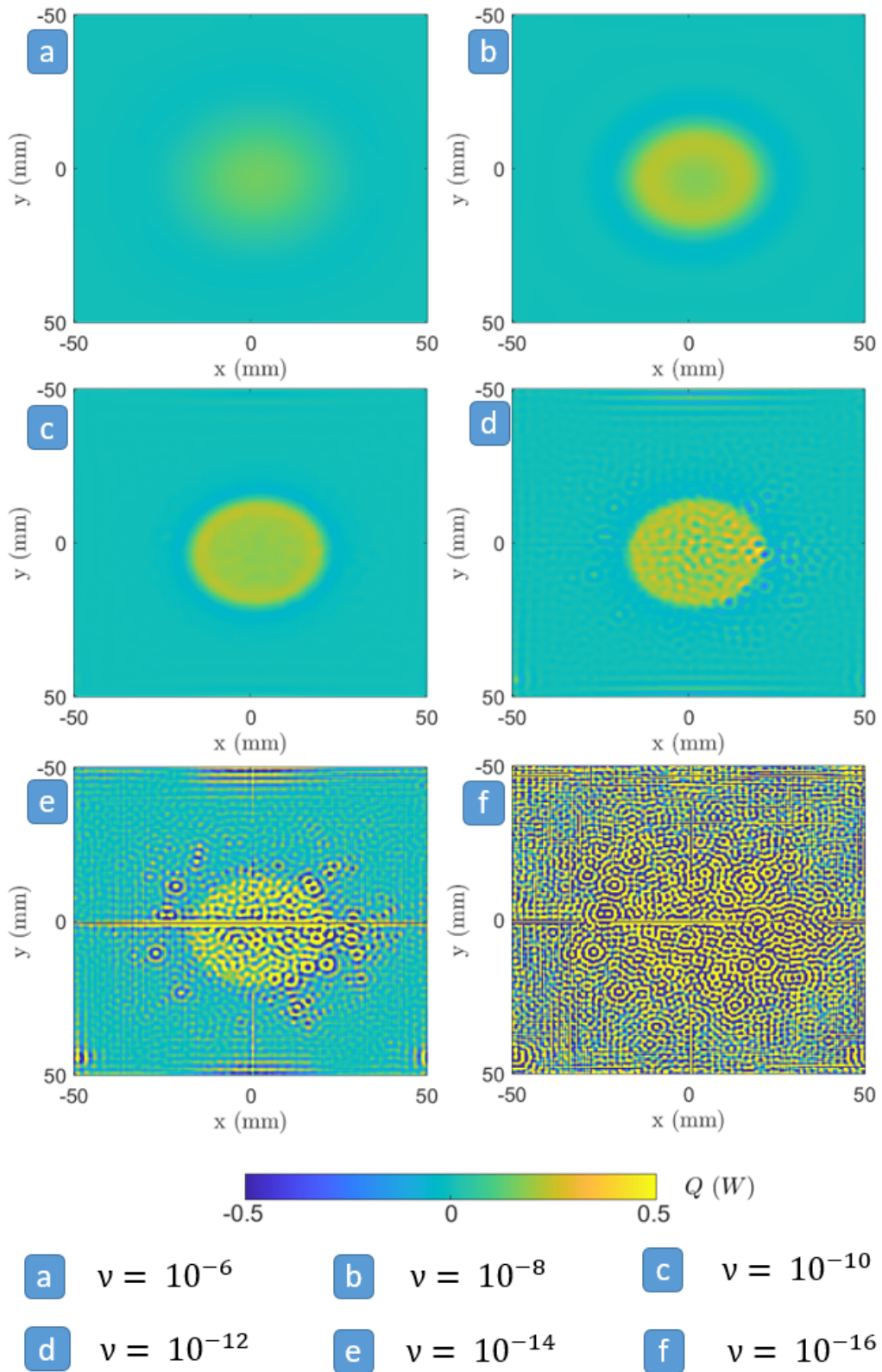


Figure 6.32: Estimated power:  $Q(x, y, t = 1)$ .

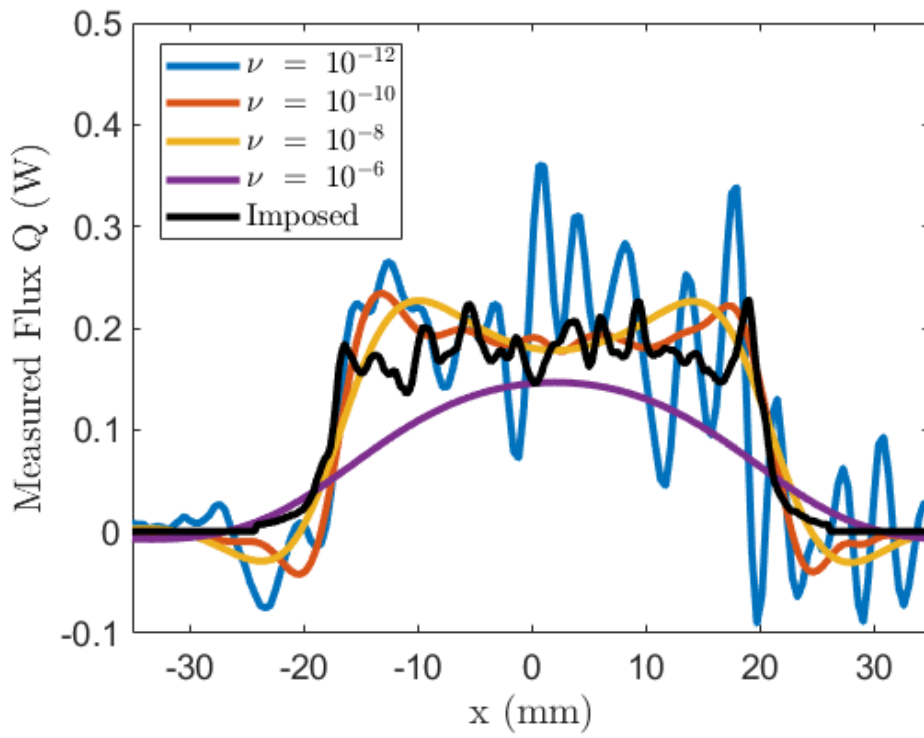


Figure 6.33: Cross section of the estimated power:  $Q_{xy}(t = 1)$ .

## 6.5. HEAT FLUX MEASUREMENT DURING HEL MATERIAL INTERACTION

---

the temporal reconstruction of the excitation. However, a few reservations have to be taken for the spatial aspect, as it does not perfectly resemble the expected top-hat-shaped signal. Nevertheless, the presented case is difficult due to the high power of the laser and the spatial repartition, which is sharp and hard to identify.

### 6.5.3.3 Case of a bare aluminium plate

For the second experiment, the temporal profile of the excitation is presented in Figure 6.34a. It is a 1 s pulsed square signal with a 1 kW power, immediately followed by a second square pulse of 2 kW for another 1 s. Figure 6.34b shows the maximum temperature increase measured on each pixel for the rear surface. A large thermal gradient is observed where the temperature of the pixels located at the centre of the sample exceeds 100 °C, whereas the edges of the sample exhibit nearly no shift in temperature.

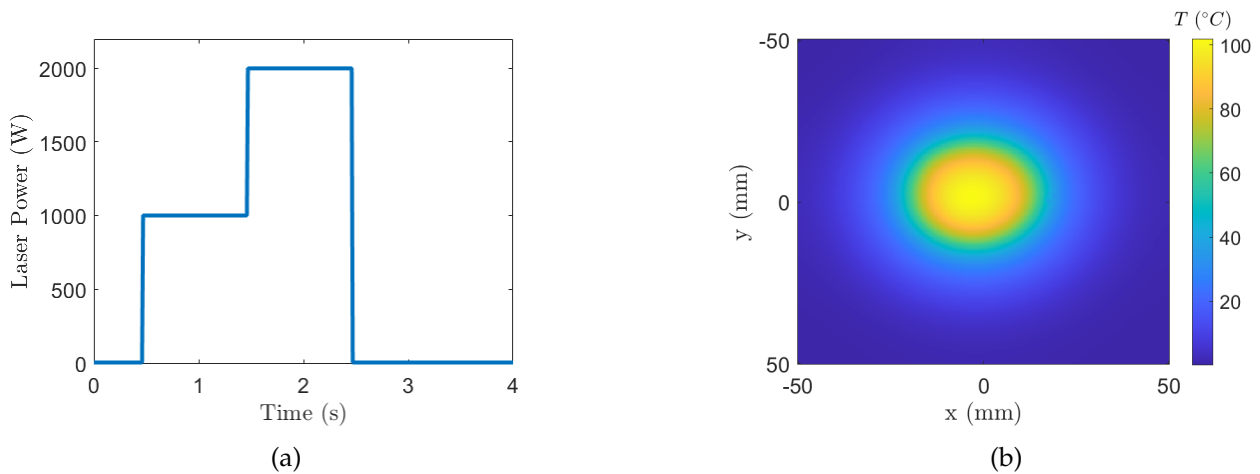


Figure 6.34: a) Excitation temporal profile for the calibration and (b) image of the maximum measured temperature.

Figure 6.35 shows the temperature profile of the centre pixel as a function of time. The temperature increases linearly during the laser shot, but the slope increases when the laser amplitude changes. Once the laser is switched off, the temperature begins to decrease.

Figure 6.36 shows (a) the maximum temperature measured on each pixel and (b) a cross section of the temperature field for different time steps. In Figure 6.36.a, a magnified region is shown to highlight a paint defect that introduces some error of temperature measurements. These errors are also visible in Figure 6.36.b with a small gap in the different curves of the figure at  $x \approx 18$  mm.

Based on the previous regularisation coefficient calibration, the coefficient used in this study is  $\nu = 10^{-10}$ . The spatial estimation is illustrated in Figure 6.37 for multiple time steps. The top hat distribution of intensity can be properly identified. Nevertheless, there is a large peak at  $x \approx 18$  followed by some wavelet rebounds on every image. This numerical artefact, which has no physical



6.5. HEAT FLUX MEASUREMENT DURING HEL MATERIAL INTERACTION

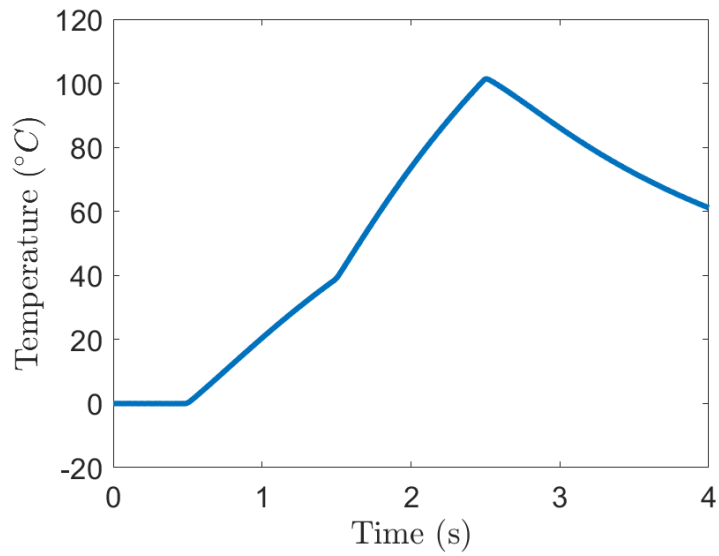


Figure 6.35: Temperature temporal profile of the central pixel.

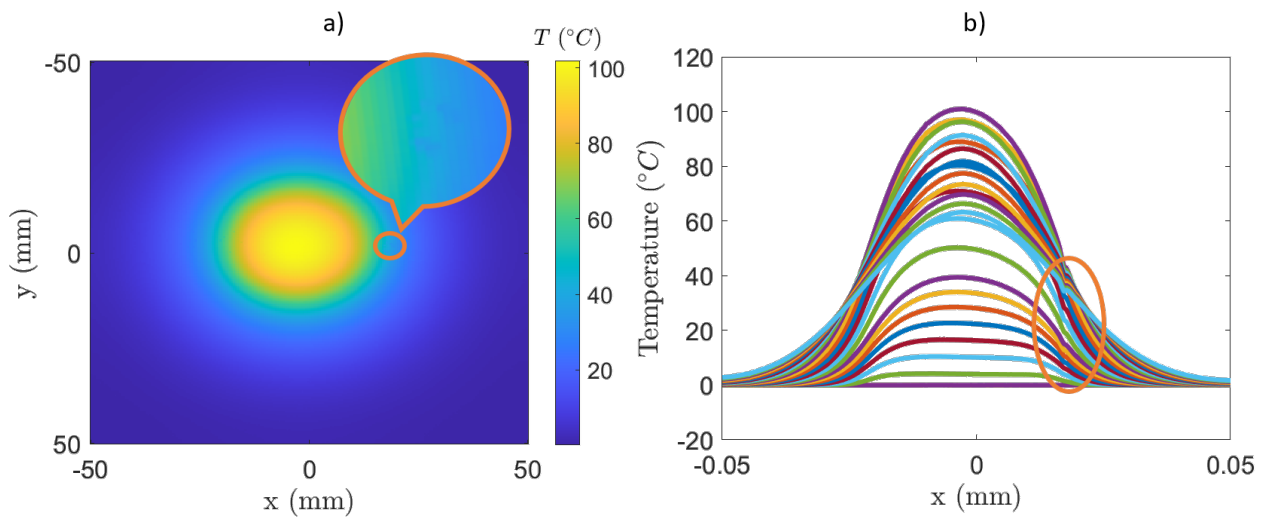


Figure 6.36: Illustration of the temperature field: (a) maximum measured temperature and (b) cross section of the temperature field for different time steps.

## 6.5. HEAT FLUX MEASUREMENT DURING HEL MATERIAL INTERACTION

---

meaning, is attributed to paint defects located in the same place.

Based on Eq. 6.15, the flux absorbed at each time step can be computed as presented in Figure 6.38. The temporal shape of the excitation is properly identified. The absorbed flux is composed of two square signals of one second each with amplitudes of 250 W and 500 W. The second square signal immediately follows the first.

By linking the temporal (Figure 6.38) and spatial estimations (Figure 6.37), one can conclude that the estimated heat flux seems more than coherent. It is assumed that the sum of the spatial artefact data presented in Figure 6.37 trends towards 0 and does not affect the temporal estimation of the heat source.

Based on this measurement, the absorbance of the sample can be computed and is presented in Figure 6.39. The absorbance is nearly a flat curve where  $\mathcal{A} \approx 0.2$ . Some points affect the measurement due to the temporal reconstruction, which does not perfectly match the imposed flux. A maximum error is observed over the 0.02 s duration, where the absorbed power shifts from 250 W to 500 W. This can be seen in Figure 6.39 at  $t \approx 1.5$  s.

6.5. HEAT FLUX MEASUREMENT DURING HEL MATERIAL INTERACTION

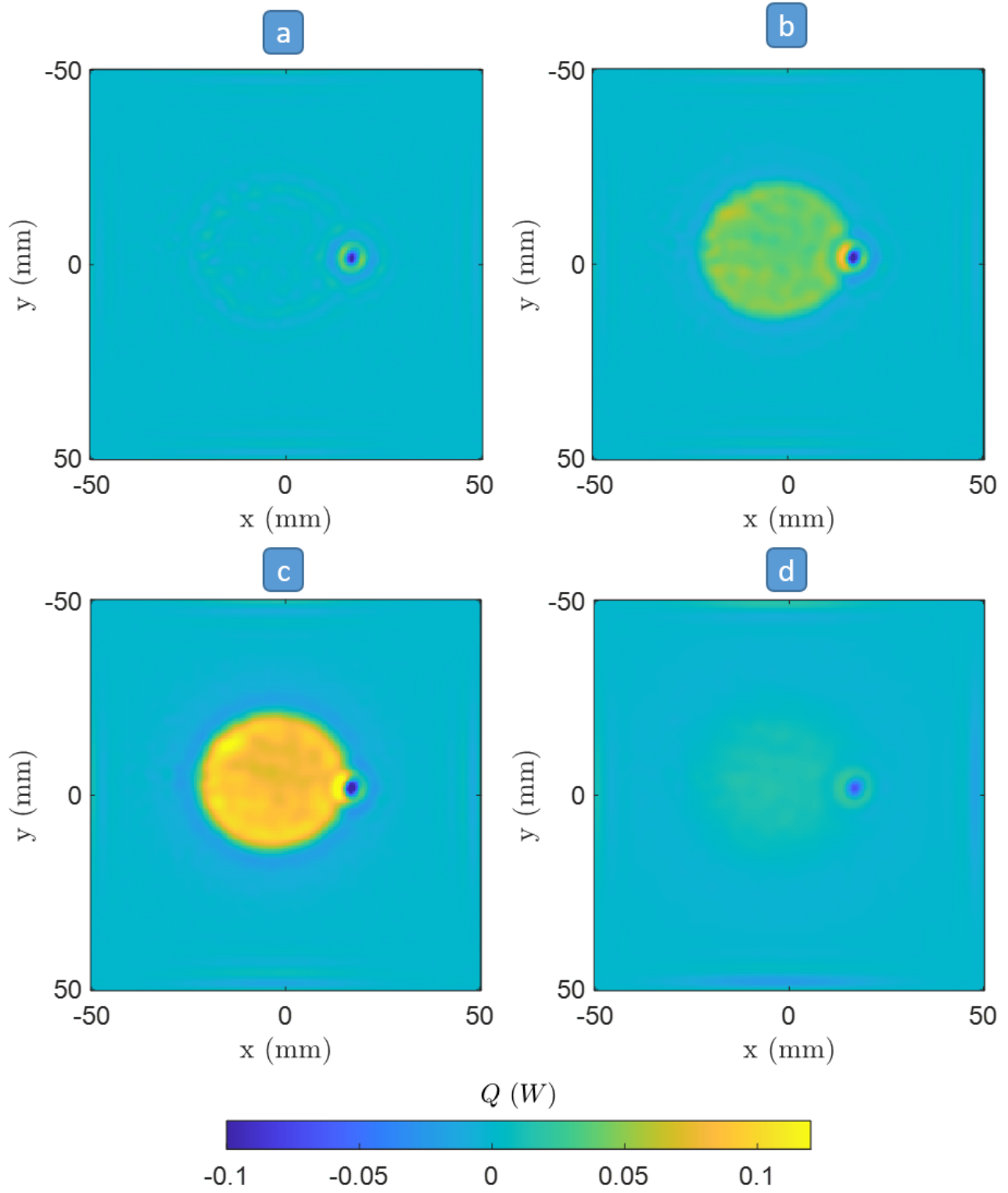


Figure 6.37: Spatial estimation of the absorbed power at (a)  $t=0.2$  s, (b)  $t=1$  s, (c)  $t=2$  s and (d)  $t=3$  s.

## 6.5. HEAT FLUX MEASUREMENT DURING HEL MATERIAL INTERACTION

---

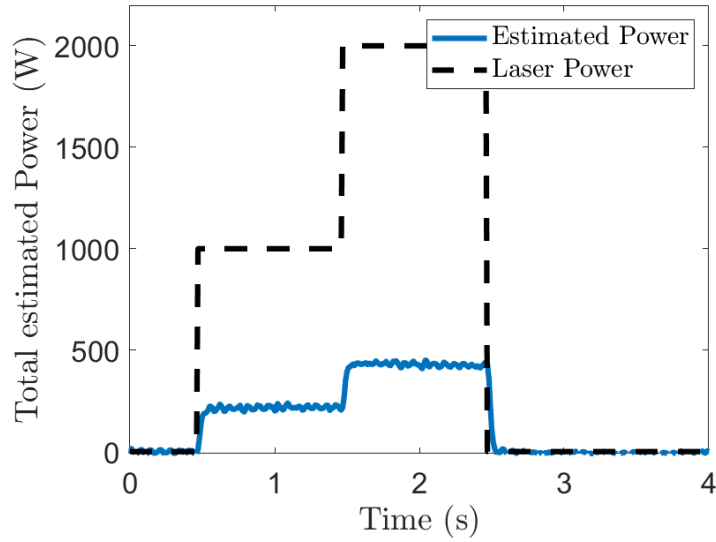


Figure 6.38: Temporal behaviour of the absorbed power.

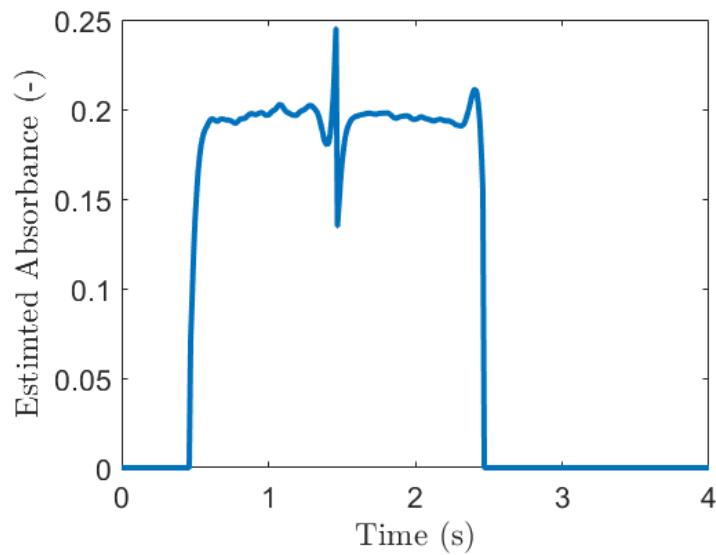


Figure 6.39: Sample absorbance as a function of time.

### 6.5.4 Summary of heat flux reconstruction

The inverse method that allows the estimation of spatio-temporal heat flux is tested and validated under extreme conditions. In this study, no denoising methods (moving average, SVD, etc.) or Fourier filters are used to prove the robustness of the method (neither on the input data nor the estimated flux). As the presented method uses only thermal signals and properties, the heat flux can be estimated for any material under applied heat fluxes.

## 6.6 Chapter summary

Multiple **experimental set-ups** including imaging systems in the **visible and near- and far-infrared** ranges have been used. **Data processing, different models (thermal and radiative)** and the **inverse method** are addressed to quantify different aspects of the laser–matter interactions.

Based on the method developed in Chapters 3 and 5 and the dedicated experimental set-ups shown in this chapter, one can completely characterise the HEL–material interactions in terms of reflection and absorption. Both methods are studied in this chapter under HEL illumination.

The measurement of this radiative balance is integral for the foundation of laser direct energy webs and can lead to accurate system dimensioning and a better understanding of ocular risks.

Accessing radiometric measurements of surface temperatures for a sample under laser illumination is a complex process. The **ATR** method has shown good results on complex cases with emissivities ranging from 0.08 to 0.95. Despite the difficulties encountered, the method leads to coherent spatial and temporal temperature measurements. However, this method remains at a low technology readiness level (TRL), and the experimental set-up developed in this study is not at a stage where it can easily be popularised.

# Chapter 7

## Conclusion and perspectives

### Table of Contents

---

7.1 Conclusion . . . . .	223
7.2 Perspectives . . . . .	224

---

### 7.1 Conclusion

As lasers continue to be implemented in various facets of modern technology, the rate at which their respective safety measures improve must be evaluated in tandem. The most dangerous applications pertain to the military sector, where high-powered lasers are being adapted as extremely potent weapons. Laser vulnerability, a specific military application, must also be considered. Specifically, laser vulnerability refers to the susceptibility of a system, device, or material to be damaged from exposure to laser radiation. Laser vulnerability can vary depending on the wavelength, power, and duration of the laser exposure, as well as the characteristics of the system or the exposed material. Consequently, the objective of the work presented in this thesis was to develop tools to quantify direct energy laser weapon vulnerability.

The first chapter of this thesis discussed an overview of the basic laws and quantities governing radiative heat transfer. These fundamental equations are important for describing the complex nature of light–matter interactions on opaque materials. From this summary, 3 major quantities that drive laser–material interactions were highlighted: reflectance, absorbance and temperature. This thesis is based on measuring these quantities using experimental set-ups, models and numerical methods to

elucidate the evolution of these parameters. These parameters were first evaluated at the laboratory scale (Chapters 3, 4 and 5) and then under HEL illumination (Chapter 6).

In Chapter 3, we presented a new experimental set-up to measure multi-spectral reflection shapes (BRDFs) in infrared wavelengths. This set-up allowed image-based acquisition of BRDFs for spectral ranges of  $2.7 \mu\text{m}$  and  $5.5 \mu\text{m}$ , with more than 60,000 simultaneously acquired points.

The fourth chapter presented an Active Thermo-Reflectometry method, which was used to capture in situ measurements of emissivity and estimations of reflections occurring in a thermal scene. This set-up was used to measure the absolute temperature through contactless methods.

Chapter 5 discussed two approaches for the estimation of the spatio-thermal heat flux from temperature measurements. These approaches are based on the modelling of conductive heat transfer of materials and on the formalism of inverse methods in thermal science.

Finally, Chapter 6 presented a synthesis of all previous chapters in this thesis. The different methods developed previously for laser-matter interactions were presented, and the experimental and numerical difficulties under these extreme conditions were presented.

The elements provided in this thesis work are summarised as follows:

- Instrumentation
- Data processing
- Radiative and thermal modelling
- Inverse and optimisation methods
- Applications of HEL illumination
- Multi-party (MBDA, ALPhANOV, I2M) and multidisciplinary approaches

## 7.2 Perspectives

The perspectives gained from this thesis are addressed from two perspectives: research laboratories and industry:

**Multi-spectral infrared BRDF measurement:**

- Laboratory scale: The BRDF measurement methods from this thesis provide a plethora of information for laser–material interactions and are a great starting point for future work. Improving the instrumentation would expand the spectral range and range of materials for which these measurements can be acquired, greatly contributing to the literature in the infrared domain.
- Industrial transfer: thermal simulations are key for the improvement and robustness of recognition algorithms. Thus, acquiring BRDFs on representative coatings or materials may unveil the next steps for improving infrared sensor modelling. The hot spot identification of HEL reflections from weaponized lasers is expected to clarify the range of applications for these weapons.

### **Temperature measurement:**

- Laboratory scale: The developed ATR method can be further developed to apply to more complex cases than the specular model or even to non-planar geometries.
- Industrial transfer: the development of a reliable and robust method for contactless temperature measurement is still ongoing throughout the field and would address many industrial needs.

### **Heat flux measurement:**

- Laboratory scale: The developed method is an extension of previous studies by the TIFC-I2M team. Other developments are required to simplify the process, and automated methods for determining the regularisation factor are of interest.
- Industrial transfer: The studied cases are relevant to industrial and manufacturing applications.





# Bibliography

- [1] The U.S. National Archives. Left side view of an NKC-135 airborne laser laboratory (ALL) aircraft in flight. The aircraft is the test bed for the Air Force Weapons Laboratory's laser tests in an airborne environment. (Substandard image), September 1982.
- [2] Bernd Mohring, Stephan Dietrich, Leonardo Tassini, Rudolf Protz, Franz Geidek, and Jürgen Zoz. High-energy laser activities at MBDA Germany. page 873304, Baltimore, Maryland, USA, May 2013.
- [3] Electromagnetic Spectrum Diagram |.
- [4] Dimitrios Biliouris, Willem Verstraeten, Phillip Dutré, Jan Van Aardt, Bart Muys, and Pol Coppin. A Compact Laboratory Spectro-Goniometer (CLabSpeG) to Assess the BRDF of Materials. Presentation, Calibration and Implementation on *Fagus sylvatica* L. Leaves. *Sensors*, 7(1):1846–1870, September 2007.
- [5] Jefferson Y. Han and Ken Perlin. Measuring bidirectional texture reflectance with a kaleidoscope. *ACM Transactions on Graphics*, 22(3):741–748, July 2003.
- [6] Kristin J. Dana and Jing Wang. Device for convenient measurement of spatially varying bidirectional reflectance. *JOSA A*, 21(1):1–12, January 2004. Publisher: Optica Publishing Group.
- [7] Dominique Pajani. Thermographie - Principes et mesure. *Techniques de l'Ingénieur*, V2(2740):21, March 2013.
- [8] Pierre Bourdon. *Technologies laser pour applications militaires*. Optique / photonique, Université Paris Sud, Paris, September 2016.
- [9] Carlo Kopp. High Energy Laser Directed Energy Weapons. Technical Report APA-TR-2008-0501, Air Power Australia, May 2008.
- [10] Jason D.Ellis. *Directed Energy Weapons Promise and Prospects*. 20YY series. Washington : New York, center for a new america security edition, April 2015.
- [11] Kosta Tsipis. Could orbiting lasers defend a nation against missile attack? The technological obstacles are insurmountable; furthermore, such weapons would be vulnerable to simple countermeasures. *SCIENTIFIC AMERICAN*, page 7, 1981.
- [12] Yann Cochenec. Armes laser : MBDA inaugure un laboratoire d'essai à Bordeaux. *Air et Cosmos*, April 2019.

## BIBLIOGRAPHY

---

- [13] Réjean Baribeau, William S. Neil, and Éric Côté. Development of a robot-based gonireflectometer for spectral BRDF measurement. *Journal of Modern Optics*, 56(13):1497–1503, July 2009. Publisher: Taylor & Francis \_eprint: <https://doi.org/10.1080/09500340903045702>.
- [14] Phillip R. Mattison, Mark S. Dombrowski, James M. Lorenz, Keith J. Davis, Harley C. Mann, Philip Johnson, and Bryan Foos. Handheld directional reflectometer: an angular imaging device to measure BRDF and HDR in real time. In Zu-Han Gu and Alexei A. Maradudin, editors, *SPIE's International Symposium on Optical Science, Engineering, and Instrumentation*, pages 240–251, San Diego, CA, October 1998.
- [15] M. Romano, C. Pradere, and J.C. Batsale. Simultaneous spectroscopic and temperature imaging by IR monochromator and camera. In *Proceedings of the 2014 International Conference on Quantitative InfraRed Thermography*. QIRT Council, 2014.
- [16] Sara Kirchner, Sebastien Narinsamy, Alain Sommier, Marta Romano, Meguya Ryu, Junko Morikawa, Jacques Leng, Jean-Christophe Batsale, and Christophe Pradère. Calibration Procedure for Attenuation Coefficient Measurements in Highly Opaque Media Using Infrared Focal Plane Array (IRFPA) Spectroscopy. *Applied Spectroscopy*, 72(2):177–187, February 2018. Publisher: Society for Applied Spectroscopy.
- [17] C. Pradere, M. Ryu, A. Sommier, M. Romano, A. Kusiak, J. L. Battaglia, J. C. Batsale, and J. Morikawa. Non-contact temperature field measurement of solids by infrared multispectral thermotransmittance. *Journal of Applied Physics*, 121(8):085102, February 2017. Publisher: American Institute of Physics.
- [18] M. Ryu, J. A. Kimber, T. Sato, R. Nakatani, T. Hayakawa, M. Romano, C. Pradere, A. A. Hovhannisyanyan, S. G. Kazarian, and J. Morikawa. Infrared thermo-spectroscopic imaging of styrene radical polymerization in microfluidics. *Chemical Engineering Journal*, 324:259–265, September 2017.
- [19] M. Romano, C. Ndiaye, A. Duphil, A. Sommier, J. Morikawa, J. Mascetti, J.C. Batsale, L. Servant, and C. Pradere. Fast infrared imaging spectroscopy technique (FIIST). *Infrared Physics & Technology*, 68:152–158, January 2015.
- [20] Marine Garcia, Alain Sommier, Dominique Michau, Gérald Clisson, Jean-Christophe Batsale, and Stéphane Chevalier. Concentration field imaging in microfluidic fuel cells based on operando visible spectroscopy, September 2022. arXiv:2209.14704 [physics].
- [21] Coline Bourges, Stéphane Chevalier, Jérémie Maire, Alain Sommier, Christophe Pradere, and Stefan Dilhaire. Infrared thermotransmittance-based temperature field measurements in semi-transparent media, November 2022. arXiv:2211.00275 [cond-mat, physics:physics].
- [22] D. Hernandez. A concept to determine the true temperature of opaque materials using a tricolor pyroreflectometer. *Review of Scientific Instruments*, 76(2):024904, February 2005. Number: 2.
- [23] G. Llauro, D. Hernandez, F. Sibieude, J. M. Gineste, R. Verges, and D. Antoine. In situ characterization of surfaces at high temperature by using simultaneously a pyroreflectometer and an X-ray diffractometer. *Applied Surface Science*, 135(1):91–96, September 1998.

## BIBLIOGRAPHY

---

- [24] A. Sommier, J. Malvaut, V. Delos, M. Romano, T. Bazire, J. C. Batsale, A. Salazar, A. Mendioroz, A. Oleaga, and C. Pradere. Coupling Pulsed Flying Spot technique with robot automation for industrial thermal characterization of complex shape composite materials. *NDT & E International*, 102:175–179, March 2019.
- [25] A. Bedoya, J. González, J. Rodríguez-Aseguinolaza, A. Mendioroz, A. Sommier, J. C. Batsale, C. Pradere, and A. Salazar. Measurement of in-plane thermal diffusivity of solids moving at constant velocity using laser spot infrared thermography. *Measurement*, 134:519–526, February 2019.
- [26] L. Gaverina, A. Sommier, J. L. Battaglia, J. C. Batsale, and C. Pradere. Pulsed Flying Spot Elliptic method for the estimation of the thermal diffusivity field of orthotropic materials. *International Journal of Thermal Sciences*, 125:142–148, March 2018.
- [27] Jeremie Girardot. *Interaction laser/matière en régime de perçage par percussionalanalyse expérimentale, modélisation et simulation numérique*. PhD thesis, ENSAM, Paris, 2014.
- [28] Francisco Chinesta, Elias Cueto, Emmanuelle Abisset-Chavanne, Jean Louis Duval, and Fouad El Khaldi. Virtual, Digital and Hybrid Twins: A New Paradigm in Data-Based Engineering and Engineered Data. *Archives of Computational Methods in Engineering*, 27(1):105–134, January 2020.
- [29] Rubén Ibáñez, Emmanuelle Abisset-Chavanne, David González, Jean-Louis Duval, Elias Cueto, and Francisco Chinesta. Hybrid constitutive modeling: data-driven learning of corrections to plasticity models. *International Journal of Material Forming*, 12(4):717–725, July 2019.
- [30] Abderezak Aouali. *Tomographie thermo-spectroscopique par imagerie 3D pour l'étude des torches à plasma*. PhD thesis, Université de Bordeaux, Bordeaux, France, January 2022.
- [31] G. Kirchhoff. On the relation between the radiating and absorbing powers of different bodies for light and heat. *The London, Edinburgh, and Dublin Philosophical Magazine and Journal of Science*, 20(130):1–21, July 1860.
- [32] 14:00-17:00. Thermal insulation — Heat transfer by radiation — Physical quantities and definitions ;, 1989.
- [33] Michael F. Modest. *Radiative heat transfer*. Academic Press, New York, 3d edition edition, 2013.
- [34] Jean-Jacques Greffet, Patrick Bouchon, Giovanni Brucoli, Emilie Sakat, and François Marquier. Generalized Kirchhoff law. *Physical Review X*, 8(2):021008, April 2018. arXiv:1601.00312 [physics].
- [35] P.-M Robitaille. Kirchhoff's Law of Thermal Emission: 150 Years. *Progress in Physics*, October 2009.
- [36] J.-F. Daigle, D. Pudo, and F. Théberge. Standoff high energy laser induced oxidation spectroscopy (HELIOS). *Journal of Applied Physics*, 122(17):173102, November 2017.
- [37] Claude Amra. Diffusion de la lumière par les rugosités d'interface et les hétérogénéités de volume. Application à la caractérisation de microstructure dans les composants interférentiels.

## BIBLIOGRAPHY

---

- In *Élaboration et caractérisation des cristaux massifs et en couches minces pour l'optique*, volume 8, pages 203–226, Les Houches, France, 2003. EDP Sciences.
- [38] Sheldon M. Smith. Far-Infrared (FIR) Optical Black Bidirectional Reflectance Distribution Function (BRDF). In *Radiation Scattering in Optical Systems*, volume 0257, pages 161–168. SPIE, March 1981.
- [39] Till W Liepmann. Hemispherical Reflectance Measurement Field Instrument Design. Test Facilities, Equipment and Methods Biology ADA289671, Pacific-Sierra Research Corporation Los Angeles, CA, Pacific-Sierra Research Corporation Los Angeles, CA, July 1991.
- [40] Mark J Proctor. ACTIVE MULTISPECTRAL BIDIRECTIONAL DISTRIBUTION FUNCTION MEASUREMENT SYSTEM. Technical report, AIR FORCE INST OF TECH WRIGHT-PATTERSON, 2000.
- [41] Samuel I. Harkiss. *A Study of Bi-Directional Reflectance Distribution Functions and Their Effect on Infrared Signature Models*. PhD thesis, DEPARTMENT OF THE AIR FORCE AIR UNIVERSITY, Wright-Patterson Air Force Base, Ohio, March 2007. Section: Technical Reports.
- [42] Fred E Nicodemus. Directional Reflectance and Emissivity of an Opaque Surface. *Applied Optics*, 4:776–775, 1965.
- [43] R. P. Young and B. E. Wood. BiDirectional Reflectance Distribution (BRDF) of NASA Shuttle Tiles. Technical Report ADA235115, Arnold Engineering Development Center, Arnold Engineering Development Center, January 1991. Section: Technical Reports.
- [44] Uri P. Oppenheim, Mary G. Turner, and W. L. Wolfe. BRDF reference standards for the infrared. *Infrared Physics & Technology*, 35(7):873–879, December 1994.
- [45] D. Rod White, Peter Saunders, Stuart J. Bonsey, John van de Ven, and Hamish Edgar. Reflectometer for measuring the bidirectional reflectance of rough surfaces. *Applied Optics*, 37(16):3450–3454, June 1998. Publisher: Optica Publishing Group.
- [46] S.R. Sandmeier and K.I. Itten. A field goniometer system (FIGOS) for acquisition of hyperspectral BRDF data. *IEEE Transactions on Geoscience and Remote Sensing*, 37(2):978–986, March 1999. Conference Name: IEEE Transactions on Geoscience and Remote Sensing.
- [47] Zhongyi Zhao, Chao Qi, and Jingmin Dai. Design of multi-spectrum BRDF measurement system. *Chinese Optics Letters*, 5(3):168–171, March 2007. Publisher: Chinese Optical Society.
- [48] Bradley Balling. *A Comparative Study of the Bidirectional Reflectance Distribution Function of Several Surfaces as a Mid-wave Infrared Diffuse Reflectance Standard*. PhD thesis, Air Force Institute of Technology Air F, Wright-Patterson Air Force Base, Ohio, March 2009.
- [49] Gregory J. Ward. Measuring and modeling anisotropic reflection. *ACM SIGGRAPH Computer Graphics*, 26(2):265–272, July 1992.
- [50] Gerard Serrot, Madeleine Bodilis, Xavier Briottet, and Helene Cosnefroy. Presentation of a new BRDF measurement device. In *Atmospheric Propagation, Adaptive Systems, and Lidar Techniques for Remote Sensing II*, volume 3494, pages 34–40. SPIE, December 1998.

## BIBLIOGRAPHY

---

- [51] Dmitri Lanevski, Farshid Manoocheri, and Erkki Ikonen. Gonioreflectometer for measuring 3D spectral BRDF of horizontally aligned samples with traceability to SI. *Metrologia*, 59(2):025006, March 2022. Publisher: IOP Publishing.
- [52] A. M. Rabal, A. Ferrero, J. Campos, J. L. Fontecha, A. Pons, A. M. Rubiño, and A. Corróns. Automatic gonio-spectrophotometer for the absolute measurement of the spectral BRDF at in-out-of-plane and retroreflection geometries. *Metrologia*, 49(3):213–223, February 2012. Publisher: IOP Publishing.
- [53] G. B. Airy. On the Diffraction of an Object-glass with Circular Aperture. *Transactions of the Cambridge Philosophical Society*, 5:283, January 1835. ADS Bibcode: 1835TCaPS...5..283A.
- [54] Thomas Lafargue-Tallet, Romain Vaucelle, Cyril Caliot, Abderezak Aouali, Emmanuelle Abisset-Chavanne, Alain Sommier, Raymond Peiffer, and Christophe Pradere. Active thermo-reflectometry for absolute temperature measurement by infrared thermography on specular materials. *Scientific Reports*, 12(1):7814, May 2022. Number: 1 Publisher: Nature Publishing Group.
- [55] Benjamin P. Keller, Shawn E. Nelson, Kyle L. Walton, Tushar K. Ghosh, Robert V. Tompson, and Sudarshan K. Loyalka. Total hemispherical emissivity of Inconel 718. *Nuclear Engineering and Design*, 287:11–18, June 2015.
- [56] Abdelmagid El Bakali, Rémi Gilblas, Thomas Pottier, and Yannick Le Maoult. A fast and versatile method for spectral emissivity measurement at high temperatures. *Review of Scientific Instruments*, 90(11):115116, November 2019. Number: 11.
- [57] M. R. Bhat. Some illustrations of the theory of the Christiansen optical filters. *Proceedings of the Indian Academy of Sciences - Section A*, 38(1):67–76, July 1953.
- [58] B. Rousseau, J. F. Brun, D. De Sousa Meneses, and P. Echegut. Temperature Measurement: Christiansen Wavelength and Blackbody Reference. *International Journal of Thermophysics*, 26(4):1277–1286, July 2005.
- [59] Robin Lucile, Delmas Agnès, and Lanternier Thomas. Surface temperature measurement of semitransparent ceramics at high temperature Comparison between pyrometry at the Christiansen frequency and infrared thermography. *Quantitative InfraRed Thermography Journal*, 4(2):165–186, December 2007. Publisher: Taylor & Francis \_eprint: <https://doi.org/10.3166/qirt.4.165-186>.
- [60] T Ohji, N Yoshioka, T Shiwaku, and A Okubo. Temperature measurement by UV thermal radiation. *Welding International*, 9(3):185–190, January 1995.
- [61] Lorris NAVELLO-HUON. *Developpement d'un Pyromètre Bichromatique impulsional pour la mesure de température de surfaces solides et liquides en milieux perturbés*. PhD thesis, Université Paris-Ouest, Paris, October 2015.
- [62] Benjamin Javaudin. *Modélisation de la diffusion optique pour la mesure de température par thermorélectométrie polychromatique*. PhD thesis, IMT – École Nationale Supérieure des Mines d'Albi-Carmaux, Albi, February 2021.

## BIBLIOGRAPHY

---

- [63] Mihai Chirtoc, Austin Fleming, Nicolas Horny, and Heng Ban. Nonlinear heterodyne photothermal radiometry for emissivity-free pyrometry. *Journal of Applied Physics*, 128(15):153101, October 2020.
- [64] F. E. Nicodemus. Reflectance Nomenclature and Directional Reflectance and Emissivity. *Applied Optics*, 9(6):1474–1475, June 1970. Publisher: Optica Publishing Group.
- [65] A. Seiffter, M. Grover, D. B. Holtkamp, A. J. Iverson, G. D. Stevens, W. D. Turley, L. R. Veaser, M. D. Wilke, and J. A. Young. Emissivity measurements of shocked tin using a multi-wavelength integrating sphere. *Journal of Applied Physics*, 110(9):093508, November 2011.
- [66] David C. Deisenroth, Leonard M. Hanssen, and Sergey Mekhontsev. High temperature reflectometer for spatially resolved spectral directional emissivity of laser powder bed fusion processes. In Leonard M. Hanssen, editor, *Reflection, Scattering, and Diffraction from Surfaces VII*, page 18, Online Only, United States, August 2020. SPIE.
- [67] Leonard M. Hanssen, Claus P. Cagran, Alexander V. Prokhorov, Sergey N. Mekhontsev, and Vladimir B. Khromchenko. Use of a High-Temperature Integrating Sphere Reflectometer for Surface-Temperature Measurements. *International Journal of Thermophysics*, 28(2):566–580, June 2007.
- [68] Carolyn A. Paddock and Gary L. Eesley. Transient thermorefectance from thin metal films. *Journal of Applied Physics*, 60(1):285–290, July 1986. Number: 1.
- [69] Susanne Sandell, Emigdio Chávez-Ángel, Alexandros El Sachat, Jianying He, Clivia M. Sotomayor Torres, and Jeremie Maire. Thermorefectance techniques and Raman thermometry for thermal property characterization of nanostructures. *Journal of Applied Physics*, 128(13):131101, October 2020.
- [70] J L Gardner and T P Jones. Multi-wavelength radiation pyrometry where reflectance is measured to estimate emissivity. *Journal of Physics*, 13(306):6, June 1979.
- [71] D. Hernandez and E. Milcent. Pyro-réfectomètre bicolore à fibres optiques pour mesures “in situ”. *Journal de Physique III*, 5(7):999–1011, 1995. Number: 7 Publisher: EDP Sciences.
- [72] D. Hernandez, J. L. Sans, and M. Pfänder. Pyroreflectometry to Determine the True Temperature and Optical Properties of Surfaces. *Journal of Solar Energy Engineering*, 130(3):031003, August 2008. Number: 3.
- [73] R. Gilblas, T. Sentenac, D. Hernandez, and Y. Le Maoult. New approach on determination of emissivity fields using bicolor reflectometry technique. In *Proceedings of the 2010 International Conference on Quantitative InfraRed Thermography*. QIRT Council, 2010.
- [74] Thierry Sentenac, Rémi Gilblas, Daniel Hernandez, and Yannick Le Maoult. Bi-color near infrared thermorefectometry: A method for true temperature field measurement. *Review of Scientific Instruments*, 83(12):124902, December 2012.
- [75] B. Javaudin, R. Gilblas, T. Sentenac, and Y. Le Maoult. BRDF (Bidirectional Reflectivity Distribution Function) modelling for accuracy enhanced thermorefectometry. In *Proceedings of the 2018 International Conference on Quantitative InfraRed Thermography*. QIRT Council, 2018.

## BIBLIOGRAPHY

---

- [76] Benjamin Javaudin, Rémi Gilblas, Thierry Sentenac, and Yannick Le Maout. Experimental validation of the diffusion function model for accuracy-enhanced thermoreflectometry. *Quantitative InfraRed Thermography Journal*, 18(1):18–33, January 2021.
- [77] Zdeněk Peřina, Jaroslav Solař, Filip Čmiel, and Radek Fabian. The Elimination of Reflected Radiation in an Infrared Thermographic Measurement in the Exterior. *Advanced Materials Research*, 923:187–190, April 2014.
- [78] Björn Zeise and Bernardo Wagner. Temperature Correction and Reflection Removal in Thermal Images using 3D Temperature Mapping:. In *Proceedings of the 13th International Conference on Informatics in Control, Automation and Robotics*, pages 158–165, Lisbon, Portugal, 2016. SCITEPRESS - Science and and Technology Publications.
- [79] M.-H. Aumeunier, M. Kočan, R. Reichle, and E. Gauthier. Impact of reflections on the divertor and first wall temperature measurements from the ITER infrared imaging system. *Nuclear Materials and Energy*, 12:1265–1269, August 2017.
- [80] Larbi Moulla, Patrick Gougeon, and Christian Coddet. Influence of reflected atmospheric plasma spraying torch radiations on long wavelength IR radiometry temperature measurement. *Infrared Physics & Technology*, 46(5):364–369, June 2005.
- [81] Vincent Guériaux. *Contribution à l'étude expérimentale et théorique des photodétecteurs infrarouge a multipuits quantiques couvrant la bande spectrale 3-20um*. PhD thesis, Université de Paris Diderot, Paris, June 2010.
- [82] François Cabannes. Pyromètre Optique. *Techniques de l'Ingénieur*, 1990.
- [83] J L Tissot, C Trouilleau, B Fieque, A Crastes, and O Legras. Uncooled microbolometer detector: recent developments at ULIS. *Infrared Photoelectronics*, 14(1):8, 2006. Number: 1.
- [84] LEGRAND, Anne-Claire. *Thermographie Multispectrale, Haute et Basse Température, Application au Contrôle Non Destructif*. PhD thesis, Université de Bourgogne, 2002.
- [85] Bruno Aragon, Kasper Johansen, Stephen Parkes, Yoann Malbeteau, Samir Al-Mashharawi, Talal Al-Amoudi, Cristhian F. Andrade, Darren Turner, Arko Lucieer, and Matthew F. McCabe. A Calibration Procedure for Field and UAV-Based Uncooled Thermal Infrared Instruments. *Sensors*, 20(11):3316, June 2020.
- [86] Olivier Burggraaff, Norbert Schmidt, Jaime Zamorano, Klaas Pauly, Sergio Pascual, Carlos Tapia, Evangelos Spyrakos, and Frans Snik. Standardized spectral and radiometric calibration of consumer cameras. *Optics Express*, 27(14):19075, July 2019. Number: 14.
- [87] Rasim Caner Calik, Emre Tunali, Burak Ercan, and Sinan Oz. A Study on Calibration Methods for Infrared Focal Plane Array Cameras. In *VISIGRAPP*, pages 219–226, 2018.
- [88] S. Lagüela, H. González-Jorge, J. Armesto, and P. Arias. Calibration and verification of thermographic cameras for geometric measurements. *Infrared Physics & Technology*, 54(2):92–99, March 2011. Number: 2.
- [89] Graham Machin, Rob Simpson, and Marc Broussely. Calibration and validation of thermal imagers. *Quantitative InfraRed Thermography Journal*, 6(2):133–147, December 2009. Number: 2.



## BIBLIOGRAPHY

---

- [90] Titti Malmivirta, Jonatan Hamberg, Eemil Lagerspetz, Xin Li, Ella Peltonen, Huber Flores, and Petteri Nurmi. Hot or Not? Robust and Accurate Continuous Thermal Imaging on FLIR cameras. In *International Conference on Pervasive Computing and Communications (PerCom)*, pages 1–9, Kyoto, Japan, March 2019. IEEE.
- [91] Frédérick Marcotte, Pierre Tremblay, and Vincent Farley. Infrared camera NUC and calibration: comparison of advanced methods. *International Society for Optics and Photonics*, 8706:870603, June 2013.
- [92] Núria Playà-Montmany and Glenn J. Tattersall. Spot size, distance and emissivity errors in field applications of infrared thermography. *Methods in Ecology and Evolution*, 12(5):828–2840, 2021.
- [93] Daniel Herrera C., Juho Kannala, and Janne Heikkila. Joint Depth and Color Camera Calibration with Distortion Correction. *IEEE Transactions on Pattern Analysis and Machine Intelligence*, 34(10):2058–2064, October 2012.
- [94] Youssef Souhar. *Caractérisation thermique de matériaux anisotropes à hautes températures*. Doctoral dissertation,, Institut National Polytechnique de Lorraine, Nantes, May 2011.
- [95] Brandon M. Lane and Eric P. Whinton. Calibration and Measurement Procedures for a High Magnification Thermal Camera. Technical Report NIST IR 8098, National Institute of Standards and Technology, January 2016. Issue: NIST IR 8098.
- [96] P. Saunders, J. Fischer, M. Sadli, M. Battuello, C. W. Park, Z. Yuan, H. Yoon, W. Li, E. van der Ham, F. Sakuma, J. Ishii, M. Ballico, G. Machin, N. Fox, J. Hollandt, M. Matveyev, P. Bloembergen, and S. Ugur. Uncertainty Budgets for Calibration of Radiation Thermometers below the Silver Point. *International Journal of Thermophysics*, 29(3):1066–1083, June 2008.
- [97] F Sakuma and S Hattori. Establishing a practical temperature standard by using a narrow-band radiation thermometer with a silicon detector. *Temperature: Its Measurement and Control in Science and Industry*, 5:421–427, 1982.
- [98] F Sakuma. Interpolation equation of scales of radiation thermometers. In *Proceedings of Tempmeke*, volume 1, pages 305–310, Torino, 1996. Symposium on Temperature and Thermal Measurements in Industry and Science in Torino.
- [99] Kenneth Levenberg. A method for the solution of certain non-linear problems in least squares. *Quarterly of Applied Mathematics*, 2(2):164–168, 1944.
- [100] Donald W. Marquardt. An Algorithm for Least-Squares Estimation of Nonlinear Parameters. *Journal of the Society for Industrial and Applied Mathematics*, 11(2), June 1963. Publisher: Society for Industrial and Applied Mathematics.
- [101] Achille Messac. *Optimization in practice with MATLAB for engineering students and professionals*. Cambridge University Press, New York, NY, 2015.
- [102] Baltes. On the Validity of Kirchhoff'S Law of Heat Radiation for a Body in a Nonequilibrium Environment. In E. Wolf, editor, *Progress in Optics*, volume 13, pages 1–25. Elsevier, January 1976.

## BIBLIOGRAPHY

---

- [103] Cyril Caliot, Stéphane Blanco, Christophe Coustet, Mouna El-Hafi, Vincent Eymet, Vincent Forest, Richard Fournier, and Benjamin Piaud. Combined conductive-radiative heat transfer analysis in complex geometry using the Monte Carlo method. *hal-02096305ff*, page 9, 2019.
- [104] H. E. Bennett and J. O. Porteus. Relation Between Surface Roughness and Specular Reflectance at Normal Incidence. *Journal of the Optical Society of America*, 51(2):123, February 1961.
- [105] John R. Howell, M. Pinar Mengüç, Kyle Daun, and Robert Siegel. *Thermal Radiation Heat Transfer*. CRC Press, Boca Raton, 7 edition, December 2020.
- [106] Panuwa Yambangyang. Photo of Basalt stone background - - ID:59160725 - Royalty Free Image - Stocklib.
- [107] Florent Husson, Mathieu Valentin, Kamil Aouati, and Rainer Kling. Upscaling laser polishing of large 3D surfaces. In Stefan Kaierle and Stefan W. Heinemann, editors, *High-Power Laser Materials Processing: Applications, Diagnostics, and Systems IX*, page 4, San Francisco, United States, March 2020. SPIE.
- [108] James W. Howard and Irving R. Abel. Narcissus: reflections on retroreflections in thermal imaging systems. *Applied Optics*, 21(18):3393, September 1982.
- [109] Ivan Jandrić and Stoja Rešković. Choosing the optimal coating for thermographic inspection. *The Holistic Approach to Environment*, 5:127–134, 2015.
- [110] G. Crammond, S.W. Boyd, and J.M. Dulieu-Barton. Speckle pattern quality assessment for digital image correlation. *Optics and Lasers in Engineering*, 51(12):1368–1378, December 2013.
- [111] Artur Cebula and Jan Taler. Determination of transient temperature and heat flux on the surface of a reactor control rod based on temperature measurements at the interior points. *Applied Thermal Engineering*, 63(1):158–169, February 2014. Number: 1.
- [112] J. F. Bonnans, editor. *Numerical optimization: theoretical and practical aspects*. Universitext. Springer, Berlin ; New York, 2nd ed edition, 2006.
- [113] David Northershauser. *Résolution de problèmes inverses tridimensionnels instationnaires de conduction de chaleur*. PhD thesis, Ecole Nationale Supérieure de l’Aéronautique et de l’Espace, Toulouse, 2000.
- [114] M. Z. Nashed. A NEW APPROACH TO CLASSIFICATION AND REGULARIZATION OF ILL-POSED OPERATOR EQUATIONS<sup>11</sup>This research was partially supported by the United States Army Research Office under grant DAAG-29-83-K-0109. In Heinz W. Engl and C. W. Groetsch, editors, *Inverse and Ill-Posed Problems*, pages 53–75. Academic Press, January 1987.
- [115] Albert Tarantola. *Inverse Problem Theory and Methods for Model Parameter Estimation*. Society for Industrial and Applied Mathematics, January 2005.
- [116] Jianhua Zhou, Yuwen Zhang, J. K. Chen, and Z. C. Feng. Inverse Heat Conduction Using Measured Back Surface Temperature and Heat Flux. *Journal of Thermophysics and Heat Transfer*, 24(1):95–103, January 2010. Number: 1.

## BIBLIOGRAPHY

---

- [117] Denis Maillat, Yvon Jarny, and Daniel Petit. Problèmes inverses en diffusion thermique - Modèles diffusifs, mesures, sensibilités. *Techniques de l'Ingénieur*, page 32, 2018.
- [118] J.C. Batsale, D. Maillat, and A. Degiovanni. Extension de la méthode des quadripôles thermiques à l'aide de transformations intégrales—calcul du transfert thermique au travers d'un défaut plan bidimensionnel. *International Journal of Heat and Mass Transfer*, 37(1):111–127, January 1994.
- [119] Yvon Jarny, Denis Maillat, and Daniel Petit. Méthodes inverses appliquées à la convection forcée en thermique. *Techniques de l'Ingénieur*, page 38, 2015.
- [120] Krzysztof Grysa. Inverse Heat Conduction Problems. In Vyacheslav Vikhrenko, editor, *Heat Conduction - Basic Research*. InTech, November 2011.
- [121] C Charles. Introduction aux problèmes inverses, December 2014.
- [122] J. Hadamard. SUR LES PROBLÈMES AUX DERIVEES PARTIELLES ET LEUR SIGNIFICATION PHYSIQUE. *PRINCETON UNIVERSITY BULLETIN.*, 13(4):4, 1902.
- [123] M. Hadamard. Les problèmes aux limites dans la théorie des équations aux dérivées partielles. *J. Phys. Theor. Appl.*, 6(1):202–241, 1907. Number: 1.
- [124] Assia Benabdallah and Djamel Teniou. Exponential stability of a Von Karman model with thermal effects. *Electronic Journal of Differential Equations*, 1998(07):13, 1998. Number: 07.
- [125] Kurt BRYAN and Lester F. CAUDILL, Jr. An Inverse Problem in Thermal Imaging. *Journal on Applied Mathematics*, 56(3):715–735, June 1996. Number: 3.
- [126] D Maillat, Stéphane André, J C Batsale, Alain Degiovanni, and Christian Moyne. *Thermal quadrupoles: solving the heat equation through integral transforms*, volume 1. Wiley, Chichester Weinheim, 2000.
- [127] J. Toutain, J.-L. Battaglia, C. Pradere, J. Pailhes, A. Kusiak, W. Aregba, and J.-C. Batsale. Numerical Inversion of Laplace Transform for Time Resolved Thermal Characterization Experiment. *Journal of Heat Transfer*, 133(4):044504, April 2011.
- [128] H.K. Versteef and W. Malalasekera. *An introduction to computational fluid dynamics - The finite volume method*, volume 1 of *Longman Scientific & Technical*. Pearson, New York, longman scientific & technical edition, June 1995.
- [129] Sushas Patankar. *numerical-heat-transfer-and-fluid-flow.pdf*, volume 1 of *Computational Methods in Mechanics and Thermal Sciences*. Sparrow, Washington : New York, hemisphere publishing corporation edition, 1980.
- [130] C Pradere, J Toutain, J C Batsale, J Morikawa, E Hayakawa, and T Hashimoto. Micro-scale thermography of freezing biological cells in view of cryopreservation. In *9th International Conference on Quantitative InfraRed Thermography*, volume 1, page 10, Krakow, Poland, 2008. QIRT Council.
- [131] Matthieu Bamford. *Methode flash et thermographie infrarouge pour la cartographie de propriétés thermophysiques : application a la caractérisation en thermomécanique*. PhD thesis, L'UNIVERSITÉ BORDEAUX I, July 2011.

## BIBLIOGRAPHY

---

- [132] Marie-Marthe Groz. *Reconstruction 3D de sources de chaleur volumiques à partir des champs de température de surface mesurés par thermographie InfraRouge*. PhD thesis, Université de Bordeaux, Talence, 2019.
- [133] D Maillet, J.-C Batsale, A Bendada, and A Degiovanni. Méthodes intégrales et contrôle non destructif par thermographie infrarouge stimulée. *Revue Générale de Thermique*, 35(409):5–13, January 1996.
- [134] Hans Rademacher and Otto Toeplitz. *The Enjoyment of Mathematics: Selections from Mathematics for the Amateur*. Courier Corporation, January 1990. Google-Books-ID: Oj8mkvcOECwC.
- [135] Robert M. Gray. Toeplitz and Circulant Matrices: A Review. *Foundations and Trends® in Communications and Information Theory*, 2(3):155–239, 2005.
- [136] Michel Kern. Problèmes inverses. *Techniques de l'Ingénieur*, page 27, 2010.
- [137] C. Ibarra-Castanedo, D. González, F. Galmiche, X. P. Maldague, and A. Bendada. Discrete signal transforms as a tool for processing and analyzing pulsed thermographic data. In Jonathan J. Miles, G. Raymond Peacock, and Kathryn M. Knettel, editors, *Conference: Defense and Security Symposium*, page 620514, Orlando (Kissimmee), FL, April 2006.
- [138] Daniel Petit and Denis Maillet. Techniques inverses et estimation de paramètres. Partie 1. *Techniques de l'Ingénieur*, 1(1):21, 2008.
- [139] L. Rondi. Uniqueness and stability for the determination of boundary defects by electrostatic measurements. *Proceedings of the Royal Society of Edinburgh: Section A Mathematics*, 130(5):1119–1151, October 2000. Number: 5.
- [140] A. N. Tikhonov. Solution of incorrectly formulated problems and the regularization method. *Soviet Math. Dokl.*, 4:1035–1038, 1963.
- [141] A. N. Tikhonov and V. IA Arsenin. *Solutions of ill-posed problems*. Scripta series in mathematics. Winston ; distributed solely by Halsted Press, Washington : New York, 1977.
- [142] Oleg M. Alifanov, Evgenij A. Artjuchin, Sergej V. Rumjancev, Oleg Mikhaïlovich Alifanov, Evgeniï Alekseevich Artiukhin, Sergeï Vladimirovich Rumiantsev, Oleg M. Alifanov, and Oleg M. Alifanov. *Extreme methods for solving ill-posed problems with applications to inverse heat transfer problems*. Begell House, New York, NY, 1995.
- [143] Helcio R B Orlande. Inverse Problems in Heat Transfer: New Trends on Solution Methodologies and Applications. In *International Heat Transfert Conference*, page 20, Washington : New York, 2010. IHTC.
- [144] Maximilian Taillandier, Raymond Peiffer, Benjamin Colomer, Rafael Ortiz, Emmanuel Chalumeau, and Matthieu Pommies. High-energy laser experiments for vulnerability studies in the context of the European TALOS program. In David H. Titterton, Robert J. Grasso, Mark A. Richardson, Harro Ackermann, and Willy L. Bohn, editors, *High-Power Lasers and Technologies for Optical Countermeasures*, page 8, Berlin, Germany, November 2022. SPIE.
- [145] Keith A. Snail and Leonard M. Hanssen. Integrating sphere designs with isotropic throughput. *Applied Optics*, 28(10):1793–1799, May 1989. Publisher: Optica Publishing Group.

## BIBLIOGRAPHY

---

- [146] Raymond J. Castonguay. New generation high-speed high-resolution hemispherical scatterometer. In John C. Stover, editor, *SPIE's 1993 International Symposium on Optics, Imaging, and Instrumentation*, pages 152–165, San Diego, CA, December 1993.
- [147] Kenneth J. Voss, Albert Chapin, Marco Monti, and Hao Zhang. Instrument to measure the bidirectional reflectance distribution function of surfaces. *Applied Optics*, 39(33):6197, November 2000.
- [148] Leonard M. Hanssen and Keith A. Snail. Integrating Spheres for Mid- and Near-Infrared Reflection Spectroscopy. In John M. Chalmers and Peter R. Griffiths, editors, *Handbook of Vibrational Spectroscopy*, page s2405. John Wiley & Sons, Ltd, Chichester, UK, December 2001.
- [149] Daniel F. Huantes, Kenneth S. Keppler, Robert A. Gallaway, Albert W. Bailey, Justin J. Zohner, Edward A. Early, Paul K. Kennedy, and Robert J. Thomas. An approach to high energy laser safety in open environments. In *International Laser Safety Conference*, pages 241–242, San Francisco, California, USA, 2007. Laser Institute of America.
- [150] Jean-François Daigle, Dominik Pudo, Francis Théberge, and Marc Châteauneuf. Laser safety evaluation for high-energy laser interaction with solids. *Optical Engineering*, 56(2):026106, February 2017.
- [151] Roberto Sabatini, Mark A. Richardson, Alessandro Gardi, and Subramanian Ramasamy. Airborne laser sensors and integrated systems. *Progress in Aerospace Sciences*, 79:15–63, November 2015.
- [152] T. Fuhrich, P. Berger, and H. Hügel. Marangoni effect in laser deep penetration welding of steel. *Journal of Laser Applications*, 13(5):178–186, October 2001.
- [153] C Limmaneevichitr and S Kou. At high Peclet numbers, the pool bottom can be flat or even convex instead of concave. *WELDING JOURNAL-NEW YORK*, 79(8):8, 2000.
- [154] Jun Du, Guangxi Zhao, and Zhengying Wei. Effects of Welding Speed and Pulse Frequency on Surface Depression in Variable Polarity Gas Tungsten Arc Welding of Aluminum Alloy. *Metals*, 9(2):114, January 2019.
- [155] Benjamin Turquais, Jean-Louis Sans, Laurent Davoust, Jules Delacroix, Christophe Journeau, Pascal Piluso, and Nourdine Chikhi. Métrologie à très haute température (1300-2500°C) en pyroréfectométrie pour des applications nucléaires. *Société Française de Thermique*, 1(1), 2021. Publisher: Société Française de Thermique.
- [156] Mir Zahedul H. Khandkar, Jamil A. Khan, Anthony P. Reynolds, and Michael A. Sutton. Predicting residual thermal stresses in friction stir welded metals. *Journal of Materials Processing Technology*, 174(1-3):195–203, May 2006.
- [157] Ardeshir Sarmast, Siamak Serajzadeh, and Amir H Kokabi. A study on thermal responses, microstructural issues, and natural aging in gas tungsten arc welding of AA2024-T4. *Proceedings of the Institution of Mechanical Engineers, Part B: Journal of Engineering Manufacture*, 228(3):413–421, March 2014.

- [158] Juan J Valencia and Peter N Quested. Thermophysical Properties. *ASM International*, 15(1):468–481, 2008.
- [159] Sandra Potin. *Spectrophotométrie de la matière extra-terrestre*. PhD thesis, Université Grenoble Alpes, Grenoble, 2020.

## BIBLIOGRAPHY

---

# Chapter 8

## Annexe reflection

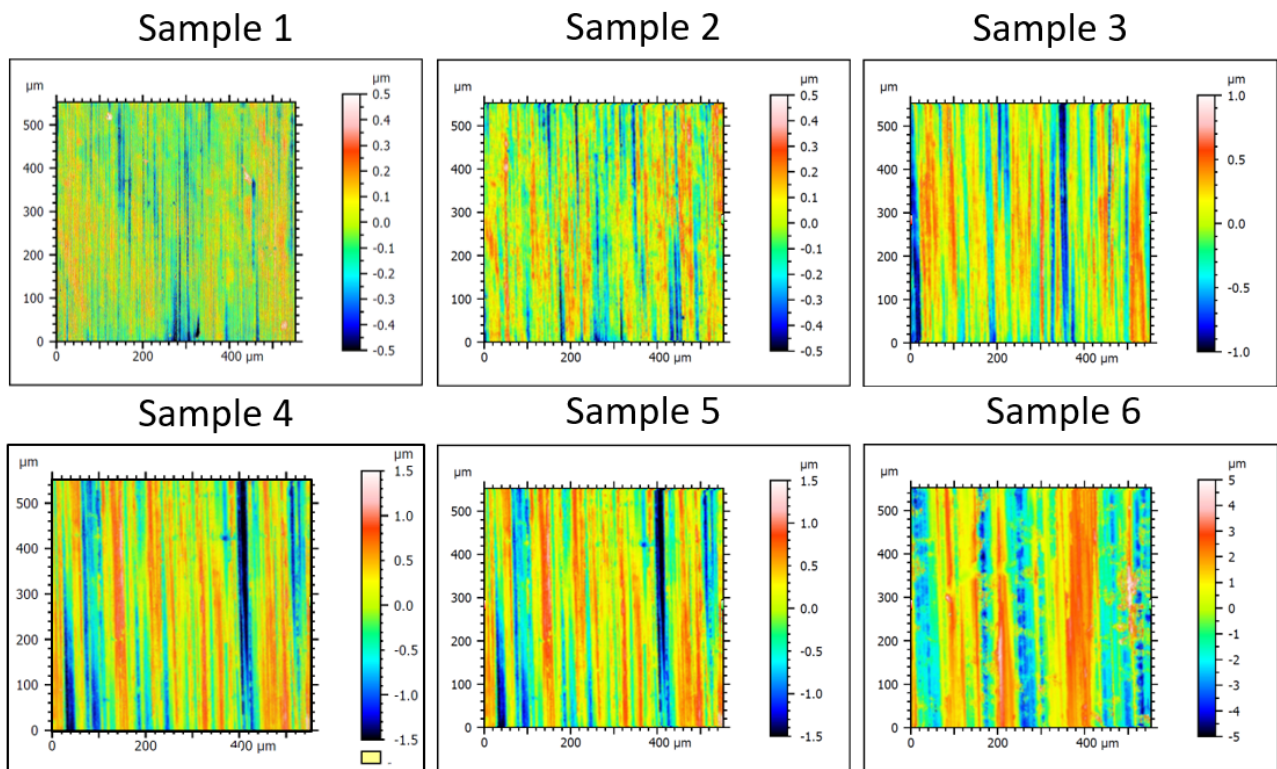


Figure 8.1: Measured samples surface topography

This annexe shows the measured multi-spectral of the samples presented in [.3.4.2.](#)



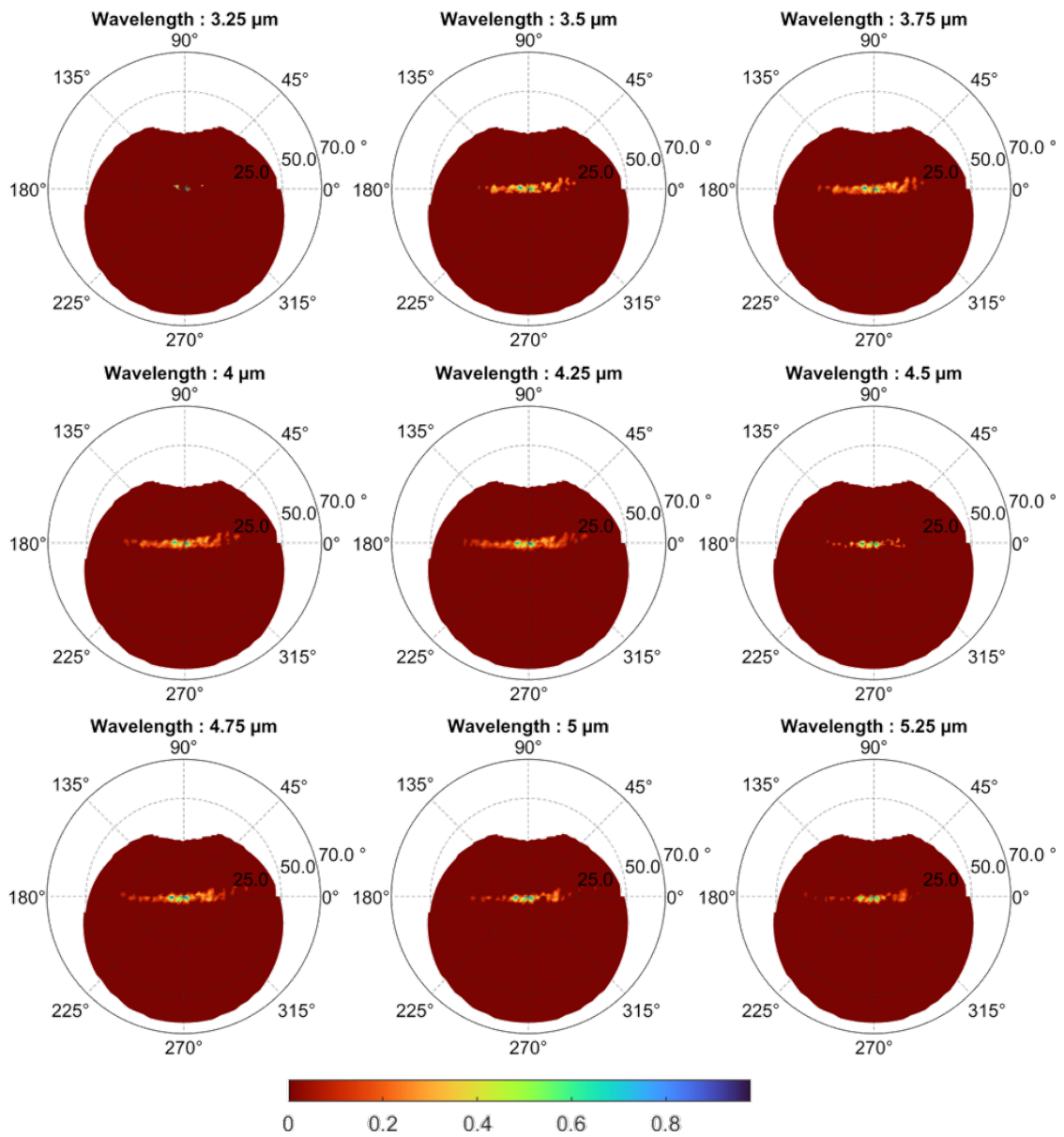


Figure 8.2: Measured Multi-Spectral BRDFs on sample 1

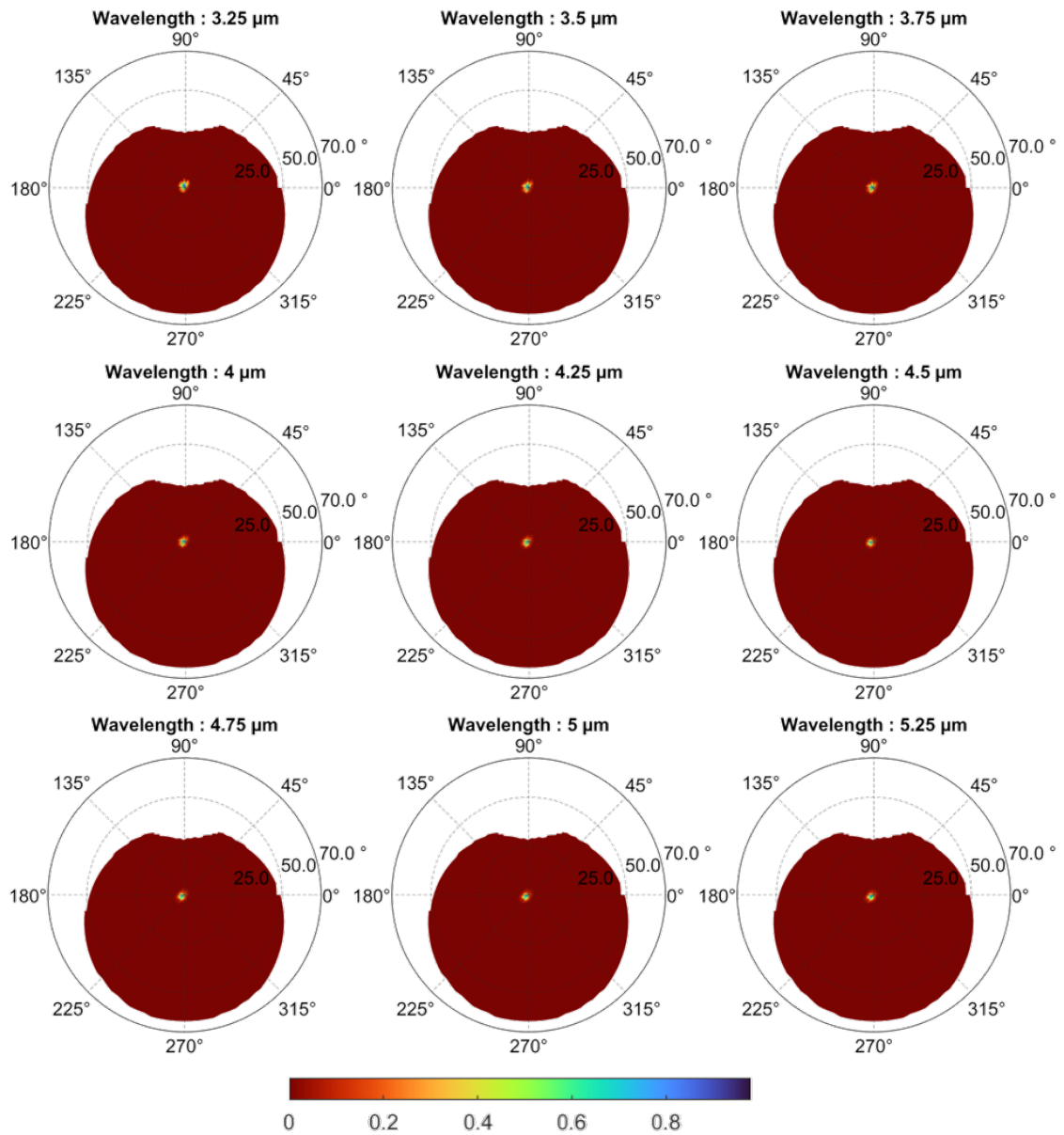


Figure 8.3: Measured Multi-Spectral BRDFs on sample 2

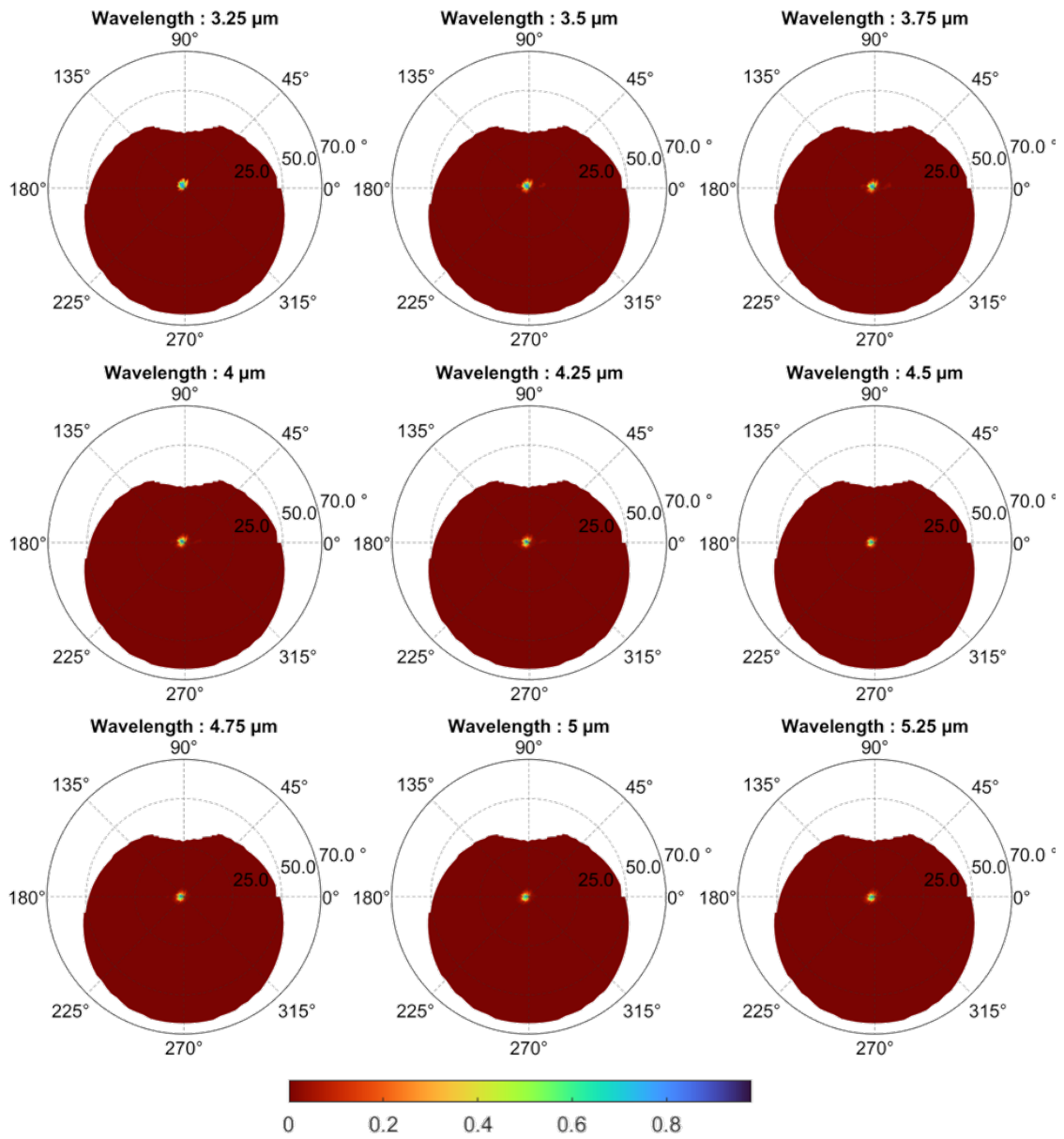


Figure 8.4: Measured Multi-Spectral BRDFs on sample 3

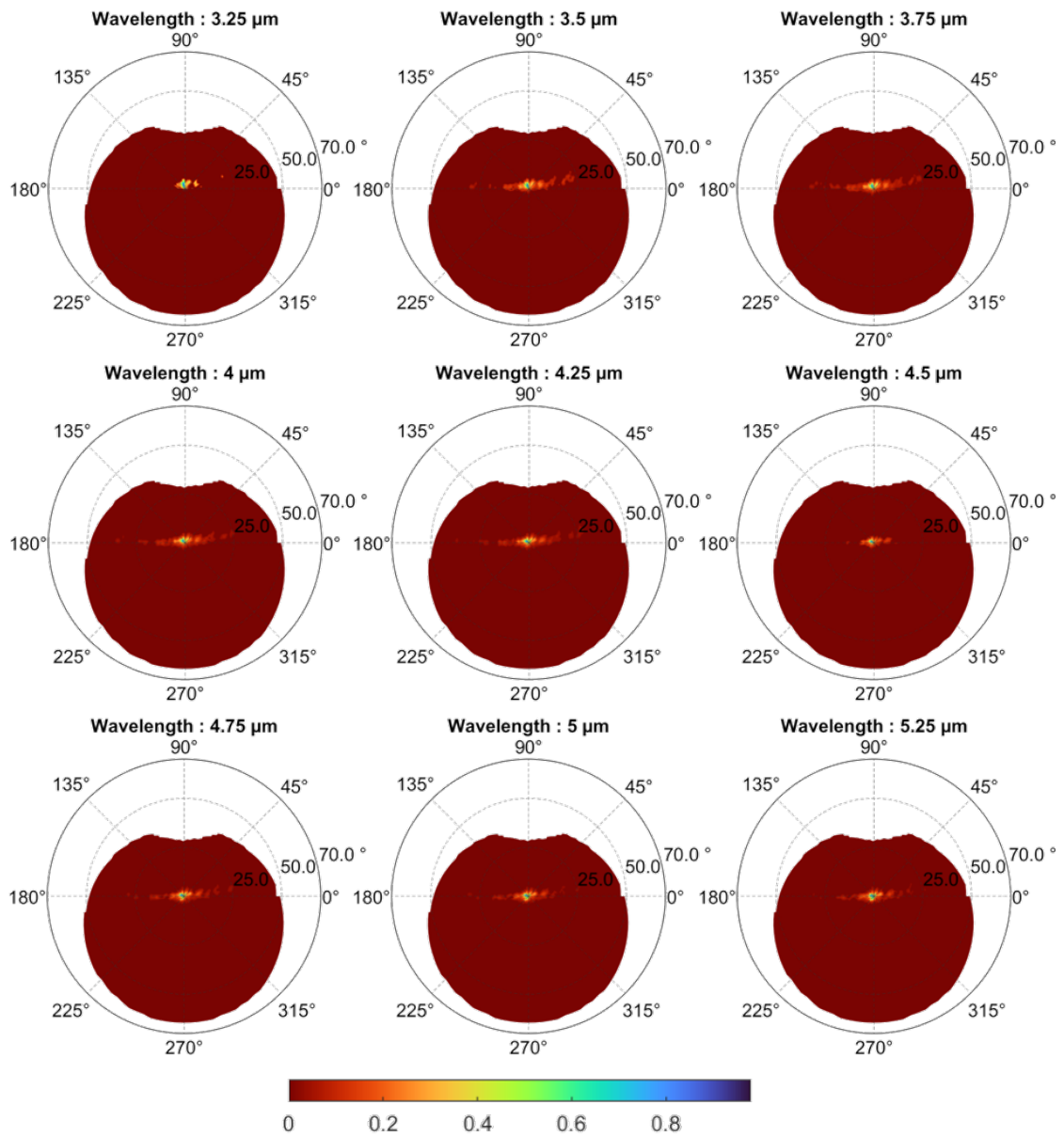


Figure 8.5: Measured Multi-Spectral BRDFs on sample 4

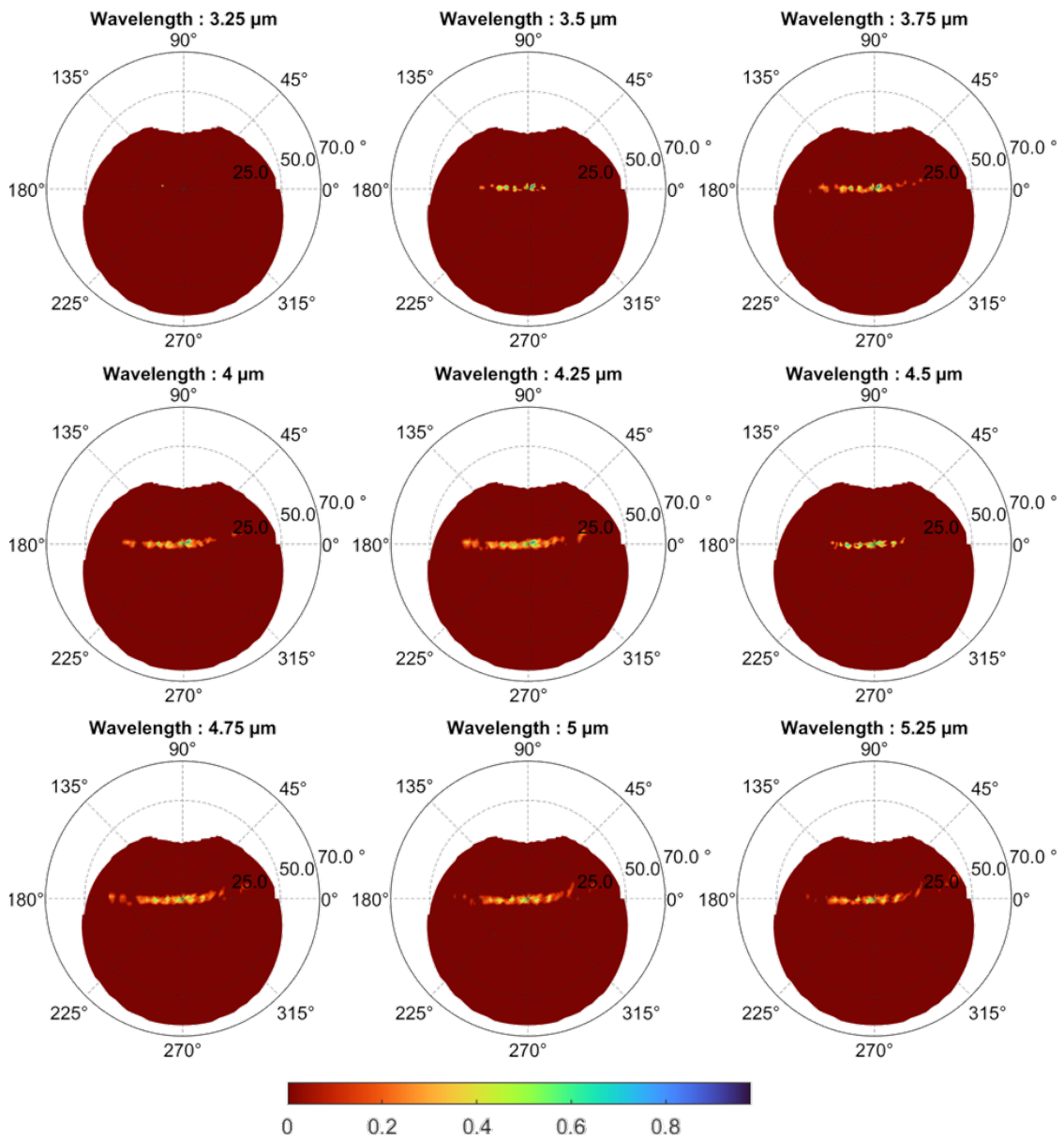


Figure 8.6: Measured Multi-Spectral BRDFs on sample 5

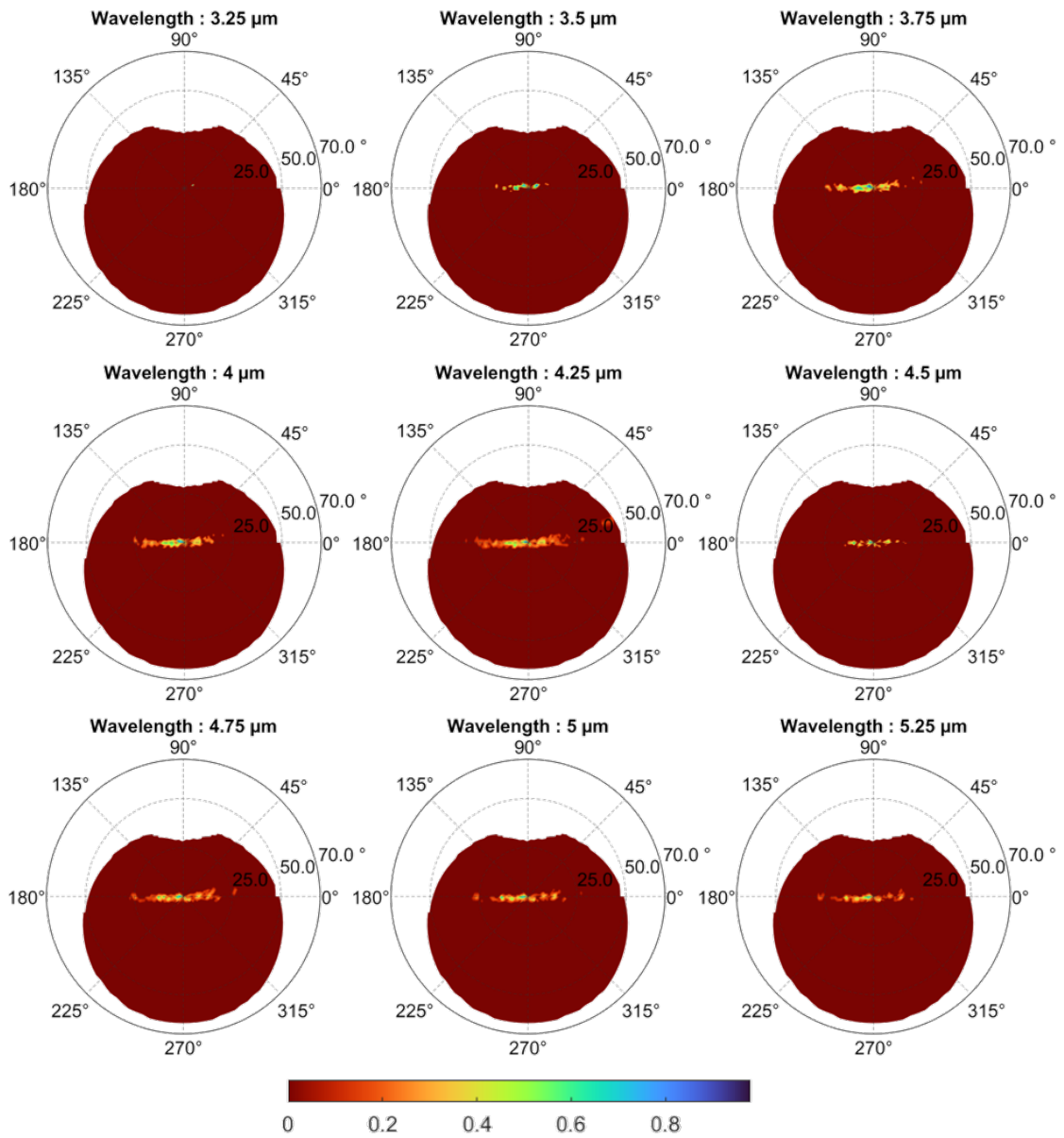


Figure 8.7: Measured Multi-Spectral BRDFs on sample 6





**Thomas Lafargue-Tallet**

**Étude du comportement de matériaux  
illuminés par des sources laser de fortes  
puissances**

**HESAM  
UNIVERSITÉ**

**Résumé :** Ce sujet de thèse se place dans le cadre d'un projet à moyen/long terme de recherche et développement d'armes laser de fortes puissances. En effet, suite à la diversification des menaces (cibles/modes opératoires) et aux risques futurs d'illuminations laser, MBDA France, en coopération avec ALPhANOV, développe des essais autour d'un laser continu haute puissance. L'objectif final de MBDA France est de pouvoir quantifier la vulnérabilité de cibles. Compte tenu de la variété des familles de matériaux d'intérêt, les mécanismes de dégradation intervenants dans ce type d'applications sont nombreux (fort couplage thermique, mécanique et chimique). De plus, ils sont peu documentés du fait de la rareté de moyens d'essais équipés de laser continu multi-kW. Le travail doctoral permettront d'acquérir de la connaissance et de la compréhension de ces phénomènes d'interaction laser-matière grâce à des approches expérimentales et analyses numériques.

**Mots clés :** Conditions Extrêmes, Infrarouge, Thermographie, Hautes températures, Hauts flux, Interaction Laser Matière, Réflexion, Absorption, BRDF.

**Abstract :** This thesis subject is part of a medium/long-term project for the research and development of high-power laser weapons. Indeed, following the diversification of threats (targets/operating modes) and the future risks of laser illuminations, MBDA France, in cooperation with ALPhANOV, is developing trials around a high-power continuous laser. The final objective of MBDA France is to be able to quantify the vulnerability of targets. Given the variety of families of materials of interest, the degradation mechanisms involved in this type of application are numerous (strong thermal, mechanical and chemical coupling). In addition, they are poorly documented due to the scarcity of test facilities equipped with multi-kW continuous lasers. The doctoral work will make it possible to acquire knowledge and understanding of these laser-matter interaction phenomena thanks to experimental approaches and numerical analyzes.

**Keywords:** Extreme Conditions, Infrared, Thermography, High Temperatures, High Flux, Laser Matter Interaction, Reflection, Absorption, BRDF.